Doctoral theses at NTNU, 2024:102

Jiali He

Electronic Property Engineering in a Ferroelectric Oxide

Nanostructuring and Advanced Characterization

Doctoral thesis

NTNU
Norwegian University of Science and Technology
Thesis for the Degree of
Philosophiae Doctor
Faculty of Natural Sciences
Department of Materials Science and Engineering

NTNU
Norwegian University of
Science and Technology

Jiali He

Electronic Property Engineering in a Ferroelectric Oxide

Nanostructuring and Advanced Characterization

Thesis for the Degree of Philosophiae Doctor

Trondheim, March 2024

Norwegian University of Science and Technology
Faculty of Natural Sciences
Department of Materials Science and Engineering

NTNU
Norwegian University of
Science and Technology

NTNU
Norwegian University of Science and Technology

Thesis for the Degree of Philosophiae Doctor

Faculty of Natural Sciences
Department of Materials Science and Engineering

ISBN 978-82-326-7798-6 (printed ver.)
ISBN 978-82-326-7797-9 (electronic ver.)
ISSN 1503-8181 (printed ver.)
ISSN 2703-8084 (online ver.)

Doctoral theses at NTNU, 2024:102

Printed by NTNU Grafisk senter

Preface

This dissertation has been submitted to the Norwegian University of Science and Technology (NTNU) in partial fulfillment of the requirements for the degree of Philosophiae Doctor.

This work has been carried out in the Functional Materials and Materials Chemistry (FACET) group at the Department of Material Science and Engineering. The supervision of the work was led by Professor Dennis Meier at the Department of Material Science and Engineering, with co-supervisor Professor Sverre Magnus Selbach at the same department.

This work was funded by the European Research Council (ERC) through a project entitled ATRONICS (project ID 863691), with Dennis Meier as the principal investigator.

PUBLICATIONS

Several of the results obtained during my PhD are published in articles in peer-reviewed journals, as listed below:

- **J. He**, M. Zahn, I. N. Ushakov, L. Richarz, U. Ludacka, E. D. Roede, Z. Yan, E. Bourret, I. Kézsmárki, G. Catalan, D. Meier. Non-destructive tomographic nanoscale imaging of ferroelectric domain walls. *Adv. Funct. Mater. 2314011 (2024).*
- U. Ludacka, **J. He**, S. Qin, M. Zahn, E. F. Christiansen, K. A. Hunnestad, Z. Yan, E. Bourret, I. Kézsmárki, A. T. J. van Helvoort, J. Agar, D. Meier. Imaging and structure analysis of ferroelectric domains, domain walls, and vortices by scanning electron diffraction. *To be published in njp Comp. Mater., pre-print available (2024).*
- L. Richarz, **J. He**, U. Ludacka, E. Bourret, Z. Yan, A. T. J. van Helvoort, D. Meier; Moiré fringes in conductive atomic force microscopy. *Appl. Phys. Lett. 122, 162903 (2023).*

Additionally, I have contributed work to the following articles (not included in this work):

- W. Sandvik, A. M. Müller, H. W. Ånes, M. Zahn, **J. He**, M. Fiebig, T. Lottermoser, T. Rojac, D. Meier, J. Schultheiß. Pressure control of nonferroelastic ferroelectric domains in $ErMnO_3$. *Nano Lett. 23, 6994 (2023).*
- H. Lu, Y. Tan, L. Richarz, **J. He**, B. Wang, D. Meier, L.Q. Chen, A. Gruverman. Electromechanics of domain walls in uniaxial ferroelectrics. *Adv. Funct. Mater. 33, 2213684 (2023)*.
- S. Luo, E. Lian, **J.He**, J.C. DeMello, Flexible transparent electrodes formed from template-patterned thin-film silver. *Adv. Mater. 2300058 (2023).*

In preparation:

- **J. He**, U. Ludacka, D. M. Evans, T. S. Holstad, E. D. Roede, K. A. Hunnestad, K. Shapovalov, Z. Yan, E. Bourret, A. T. J. van Helvoort, S. M. Selbach, D. Meier. Controlling local electronic properties by electric-field driven splitting of anti-Frenkel defects. *In preparation (2024).*
- **J. He**, G. Catalan, Z. Yan, E. Bourret, D. Meier. Electronic responses of charged domain walls in a fully depleted ferroelectric semiconductor. *In preparation (2024).*

AWARDS

I have received the following honors during my PhD, awarded by international committees:

- Best poster elected by the UFFC Ferroelectric School committee in Lyon, France (2022).
- Best poster at the Ferroelectrics Workshop, Hurtigruten, Norway (2023).

CONFERENCE CONTRIBUTIONS

I made the following contributions to scientific conferences:

- *Non-invasive imaging of hidden ferroelectric domain walls and their electronic properties*. Poster at Ferroelectrics Workshop, Hurtigruten, Norway (2023).
- *Revealing hidden ferroelectric domain walls in sub-surface regions and their electronic properties via non-destructive conductance mapping*. Oral presentation at DPG Meeting of the Condensed Matter Section, Dresden, Germany (2023).
- *Electric-field control of oxygen defects and local transport properties in* $ErMnO_3$*.* Oral presentation and poster at the first TNNN conference, Trondheim, Norway (2022).
- *Controlling local electronic properties by electric-field driven splitting of anti-Frenkel defects.* Poster at UFFC Ferroelectric School, Lyon, France (2022).
- *Time-voltage dependent evolution of anti-Frenkel defects in* $ErMnO_3$*.* Oral presentation at MRS Spring Meeting, Digital (2022).
- *How to probe nanoscale electronic properties? A revealing guide.* Poster and Joint tutorial presentation at Nordic Nanolab Network, Gothenburg, Sweden (2022).
- *Electric-field-driven evolution of anti-Frenkel defects in* $ErMnO_3$. Poster at DPG conference of the Condensed Matter Section, Digital (2021).
- *Local conductivity control in a functional ferroelectric oxide.* Oral presentation at the sustainable Materials Workshop and PhD seminar, Digital (2021).

Acknowledgments

Looking back at the three and half years of my PhD, I was fortunate to receive extensive support and help from people around me. I would like to express my sincere appreciation to everyone who has helped me in this journey.

First and foremost, I want to thank my main supervisor, Professor Dennis Meier, for the guidance, patience, and inspirations throughout my PhD. Thanks for the diverse group social activities, which gave me many chances to join a lot of activities I had never tried before. I greatly appreciate the positive atmosphere he fostered in our group, encouraging us to collaborate together and learn from each other. I also want to thank my co-supervisor, Professor Sverre Magnus Selbach, for his support and his profound knowledge. His guidance in discussions, emphasizing the connection of new and old knowledge, has been invaluable.

I would like to express my gratitude to all members of our team. Firstly, to those who were here when I joined: Mariia, Jan, Erik R., Kasper, Ivan, Erik L., Longfei, and Payel, thanks for welcoming me to the group and creating a friendly and helpful atmosphere. Special acknowledgement goes to Erik R. for his guidance and demonstrations for FIB work, and for always being available to assist. Thanks for the collaborations with Erik R. and Kasper on Mibot and Tripod polishing. I am grateful to Jan for insightful scientific discussions, including experiments, manuscript, and thesis, and for his clear thinking and precise questions. Ivan's assistance with SPMs and good explanations have been greatly appreciated. A heartfelt thank you goes to Ursula for the time we sat together beside Cypher and the passion for TEM that shines in her eyes. I also warmly thank those who joined along the way: Leonie, Katharina, Gustau, and Ruben. Our time together has been truly enjoyable. Additional thanks are given to Leonie, Ruben, Jan, Ivan, and Katharina for reading my thesis and offering their valuable feedback.

I would like to extend my appreciation to the FACET group, which provides a larger research group, allowing us to share our work and gain insights into a wide range of topics. My sincere thanks to Per-Erik Vullum for sharing and demonstrating his expertise in TEM lamella techniques. My gratitude also goes to Yingda Yu for his assistance with EBSD. Additionally, I am grateful to the staff at Nanolab for maintaining the instruments, which ensured the smooth progress of our research.

I would also like to express my gratitude to my supervisor during the internship before my Ph.D., Professor Merete Tangstad and Karin Fjeldstad Jusnes. I appreciate all the support and guidance at the beginning of my academic journey at NTNU.

Finally, I want to express my gratitude to my family and my friends for their support. To my family, thank you for your unconditional trust and love. I am especially thankful to my parents, brothers, and my sister-in-law. Most importantly, my deepest thanks go to my husband Jianmeng, and my daughter Emma Ziyi. Your constant accompaniment, love, and encouragement have been my greatest source of strength. I could not have completed this work and enjoyed my life without your companionship and encouragement.

Abstract

The advancement of electronic nanotechnology hinges on the use of innovative materials and new conceptual approaches for devices to meet the demand of miniaturization, energy efficiency, and sustainability. Ferroelectric domain walls, with their sub-nanometer feature size and unique properties, are promising candidates as active building blocks of future electronics. By utilizing their intrinsic properties, the walls themselves can function as devices, capable of emulating key electronic components such as transistors and diodes at a bulk level. **This thesis addresses different fundamental challenges associated with the utilization of ferroelectric domain walls, including advanced characterization of domain walls, their behavior in systems with reduced physical dimensions, and the creation of basic device structures.**

Using $ErMnO_3$ as the model system, SPM (scanning probe microscopy) and SEM (scanning electron microscopy) are combined with FIB (focused ion beam), the electronic property is engineered on the local scale under the influence of the electric field, as well as at domain walls under different sample thicknesses.

Going beyond domain walls, the functional properties of $ErMnO_3$ can further be enhanced at the nanoscale via electric-field written oxygen defects, which is also explored. The creation and evolution of these defects are systematically investigated under varying conditions, including electric field strength and exposure time, probe tip radius, and environmental conditions. One key result is the observation of specific regions where oxygen vacancy and oxygen interstitials separate, forming npn-like junctions. The findings provide a guideline and novel opportunities for the construction of complex functional networks and circuitry at the local scale.

The fundamental electronic properties of domain walls are investigated systematically across a wide range of sample thicknesses, ranging from 1000 nm to sub-10 nm, using different sample preparation processes. Correlated SPM characterization of the nanostructured samples reveals that the domain walls in $ErMnO_3$ preserve their bulk-like functionality and stability down to about 200 nm in thickness, whereas the emergence of new physical phenomena are observed for wedge lamella. We observe emergent electronic depletion effects and domain wall response, providing quantitative guidelines for the design of domain wall test devices for the next steps toward future applications.

A non-destructive imaging technique for materials with functional charged domain walls and domain-wall-based devices is introduced based on SEM scans. Based on SEM surface measurements and cross-sectional data, a model is developed, relating the probed intensity to domain walls in near-surface regions. This SEM-based approach facilitates non-destructive high-throughput screening of materials and is compatible with future fabrication processes for real-time monitoring of the domain wall properties.

Finally, applying the new findings and processes, an elementary device is fabricated by integrating a domain wall lamella into a customized setup that bridges different length scales, making the domain wall compatible with conventional circuitry. Preliminary tests by SPM were conducted, providing valuable insights for the next steps to fabricate devices for further investigation.

The different projects addressed in this work are part of the ERC project “ATRONICS”, contributing to the team’s goal to provide novel functional systems for the development of atomic-scale electronics.

Contents

1. Introduction

Digital technology influences many aspects of our lives, forming the backbone of communication, healthcare, education, entertainment, and scientific research. The increasing demand sets new requirements for future electronic components and device miniaturization, energy efficiency, and sustainability have become critical aspects for device design. The scientific community is actively exploring opportunities beyond traditional semiconductor-based technologies, seeking innovative materials and conceptually new approaches for device advancement.

The groundbreaking works of Herbert Kroemer, the 2000 Nobel laureate, highlighted the unique functionalities at the interface between different semiconductor materials, surpassing the capabilities of the individual single-material semiconductors. This led to the development of novel transistors, lasers, and other electronic and optoelectronic devices, reflected by his famous sentence: "The interface is the device" [1].

Over the past two decades, advancements in thin film growth techniques have revealed that oxide interfaces exhibit exotic physical phenomena going beyond those of conventional semiconductor interfaces [2–4]. These oxide interfaces, exemplified by the $LaAlO_3/SrTiO_3$ interface, demonstrate remarkable properties such as coexisting ferromagnetism and superconductivity, which are absent in the bulk form of the individual constituents [5,6]. The fabrication of field-effect transistors based on $LaAlO_3/SrTiO_3$ [7], along with the possibility of controlling electronic transport and inducing novel phenomena through epitaxial strain, underscores the versatility of oxide interfaces [8–10].

In the past decade, ferroelectric domain walls have attracted increasing attention, as functional interface, offering new opportunities for nanoelectronics. A key discovery was the experimental observation of enhanced electrical conductance at domain walls in $BiFeO_3$ in 2009. This unusual electronic response at domain walls and its importance for devices has been theoretically predicted as early as 1973 [11]. Similar to the $LaAlO_3/SrTiO_3$ interface, ferroelectric domain walls represent quasi-2D systems with distinct symmetry and unique electronic properties, exhibiting novel functional phenomena. These include photovoltaic effects [12], enhanced electromechanical response [13], net magnetism at ferroelectric domain walls in otherwise antiferromagnetic systems [14], and unusual electronic transport behaviors[15–19]. While interfaces in oxide heterostructures, such as $LaAlO_3/SrTiO_3$, are engineered by layer-by-layer growth [14], and, hence, spatially fixed, ferroelectric domain walls stand out due to their remarkable dynamics. The position of ferroelectric domain walls can be controlled by an external electric field, and domain walls can be created, moved, and erased on demand. This mobility, combined with their unique properties, fuels the outstanding technological potential

of ferroelectric domain walls, facilitating, reconfigurable device architectures. One example is domain-wall memory cells, which utilize the presence or absence of domain walls to define the ON and OFF states, respectively [20] (section 2.1.3). Here, the domain walls act as rewritable wires.

To utilize the diverse electronic properties of ferroelectric domain walls beyond their application as conductive channel, other concepts have been explored. A particularly intriguing discovery in this context was the anisotropic conductance [16] and electronic components-like behavior [21,22] at the ferroelectric domain walls in hexagonal manganites. Due to the improper nature of the ferroelectricity in hexagonal manganites, different types of domain walls naturally form in the as-grown state, including electrically charged domain walls [23,24]. These walls are explicitly stable and persist even when their bound charges are not completely screened [10,25,26], making them an ideal model system for domain-wall related studies. Notably, the domain walls in hexagonal manganites exhibit rectifying[22] and gating[21] behaviors. Thus, the domain walls themselves function as devices, capable of controlling electronic signals, which is a fascinating alternative compared to the more traditional strategies that rely on moving, deleting, and inserting domain walls.

With a solid understanding of the basic physics in place and continuous advancements in characterization and nanostructuring methods, it is now possible to go the next step from proof-of-concept experiments on bulk samples towards device-relevant physical dimensions and device achitectures. This Ph.D. thesis is part of a larger research project financed by the European Research Council (ERC), entitled ATRONICS. The overall goal of ATRONICS is to create building blocks for atomic-scale electronics based on ferroelectric domain walls, integrating them into circuitry and extended networks for electric signal control in ultra-small and energy-efficient devices.

As the first stage of ATRONICS, the goal of my Ph.D. was to establish a fabrication process of a prototype device structure that is compatible with existing circuitry, using $ErMnO_3$ as model system. Furthermore, to lay the groundwork for more complex networks and extended circuit paths in the next step, I explore the possibility of altering the material's local electronic transport behavior based on the electric-field driven injection of oxygen defects. This approach not only allows for writing connecting wires between different domain walls but also opens up possibilities for inducing new functionalities in the material for circuit design.

The prototype device fabrication process involves the targeting of specific functional domain walls and incorporating them into circuits that are accessible for future macroscopic device testing. As part of this process, two main objectives were tackled: understanding the behavior of domain walls in nanostructured samples of reduced dimension and bridging the gap

between different length scales to facilitate the incorporation functional domain walls into conventional circuits.

For the first objective, the influence of the physical dimensions of the host material on the domain wall properties will be studied. This aspect is crucial, as previous studies on domain wall electronic properties predominantly probed behaviors at the surface of millimeter-thick bulk samples, ignoring the impact of the subsurface region and the network of the domain walls.

For the second objective, a custom PCB (printed circuit board)-carrier chip-lamella stack setup is optimized starting from the microelectronic setup developed by Dr. E. Lysne [27] and Dr. E. D. Roede [28] in our group.

Concerning the design of extended circuit paths and enhancemennnnnt of functional responses of $ErMnO_3$, I focused systematic writing of oxygen defects, varying key parameters, such as electric field strength, exposure time, and environmental conditions.

This thesis is structured as follows:

Chapter 2 provides the scientific background. Starting from the basics of ferroelectrics, domains and domain walls, I will discuss key aspects related to domain wall conductance and domain wall nanoelectronics. I then introduce our model system, the improper ferroelectric hexagonal manganites, their domain structure and domain walls, emphasizing emergent domain wall properties and property engineering using oxygen defects.

Chapter 3 describes the instruments used in this work for sample preparation and characterization, outlining the important underlying principles. FIB (focused ion beam) is the main technique for nanostructuring and fabrication. SEM (scanning electron microscopy) is the main imaging technique for both bulk and nanostructured samples, complemented by different modes of SPM (scanning probe microscopy).

Chapter 4 presents the experiment results, addressing the enhancement of the functional properties of hexagonal manganites at the nanoscale controlling local electronic transport phenomena via oxygen defects. It covers the creation and evolution of these defects under different parameters, followed by the surface characterization and atomic scale compositional and structural characterization of the modified region.

In **Chapter 5**, different methods for preparing domain wall samples with different geometries are discussed, along with subsequent characterization of the domain wall electronic response using correlated SEM and SPM techniques.

Based on the experimental observation that the subsurface domain wall structure affects the domain wall electronic behavior, **Chapter 6** introduces an SEM-based method for non-destructive imaging of the 3D structure of charged domain walls in near-surface regions. This

technique provides valuable insights and a strategy for real-time imaging during future device fabrication.

Building on the results gained from the effect of geometry confinement and SEM imaging of domain walls in near-surface regions, **Chapter 7** moves towards device fabrication. The elementary device setup is built up, and the basic device fabrication process is demonstrated.

Chapter 8 summarizes the overall results and findings of this thesis and discusses the challenges and outlook for future studies.

2. Scientific background

Ferroelectric materials are crucial in a variety of applications, such as sensors, actuators, and memory devices, due to their ability to switch their polar state in response to external stimuli [29]. In recent decades, ferroelectric domain walls have attracted increasing attention due to their unique electrical, structural, and functional properties, offering the potential for innovative applications in nanoelectronics [30–34].

This chapter introduces ferroelectric materials, providing a general overview of their domains and domain walls, with a focus on charged domain walls and their applications in nanoelectronics. In the second part, the improper ferroelectric material class of hexagonal manganites is introduced, with emphasis on its domain wall properties and functionalities, as well as defect chemistry.

2.1. Ferroelectrics

Ferroelectrics are materials that exhibit a spontaneous electric polarization from aligned dipole moments, and the orientation state of the polarization can be switched between two or more allowed directions by an external electric field [35,36]. The field dependence of the polarization in ferroelectric material is typically described by a hysteresis loop [37,38], which will be shown in section 2.1.2.

2.1.1. Proper and improper ferroelectrics

Ferroelectric phases can arise when inversion symmetry is broken during the phase transition, e.g., by a distortion of a high symmetry phase below the Curie temperature. Ferroelectric materials can be categorized into two types: proper and improper ferroelectrics. In proper ferroelectrics, the spontaneous polarization is the primary order parameter. Typical examples are $BaTiO_3$, where the displacements of cations with respect to the anion sublattice stabilized by the partial covalency between B-site cation empty d-states and oxygen 2p states[39], and $BiFeO_3$, where ferroelectricity arises due to electron lone-pairs [40,41]. In improper ferroelectrics, the spontaneous polarization emerges as a secondary effect of the symmetry-breaking caused by, e.g., charge ordering, magnetism, or geometric instability [42–44]. The geometric improper ferroelectrics will be introduced in section 2.2.1 in more detail, as the model system of this work falls into this category.

2.1.2. Domain and domain walls in ferroelectrics

Ferroelectric materials tend to split into domains, which form to minimize the energy associated with the electronic dipole moments [45]. Accompanying the spontaneous polarization, the surface perpendicular to the polar direction is associated with surface charge. This surface charge generates an electric field in the opposite direction to the polarization, termed depolarization field E_d, as depicted in Figure 2-1a. Having a uniformly oriented

polarization throughout the entire sample is energetically unfavorable, and the depolarization field can reduce or even cancel the spontaneous polarization. To minimize the strong depolarization field, ferroelectric materials form domains. The polarization orientation in each domain is uniform, and the overall macroscopic polarization of all domains ideally averages to zero [33,35]. Figure 2-1b illustrates such a multidomain state in a uniaxial ferroelectric material.

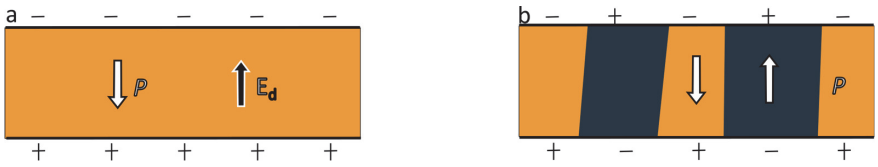

Figure 2-1 Domain formation in ferroelectrics. (a) Monodomain state: bound charge on the surface generating a big depolarization field. (b) Multidomain state: the material splits into multiple domains to minimize the electrostatic energy. Due to energy costs associated with the domain walls, the material divides into a finite number of domains.

The boundary separating the two domains is the domain wall. The formation of domain walls also costs energy, resulting in the material dividing into a finite number of domains. The domain size is determined by the competition between the energy of the domain and the energy of the domain wall [46]. In general, the domain size follows Kittel's scaling law, where the domain width w is proportional to the square root of the thickness of the ferroelectric material d: $w \propto \sqrt{d}$ [33,47]. This scaling law was proposed to describe the behavior of magnetic domains in ferromagnetic materials, which was later expanded to ferroelectrics [37,48].

Macroscopically, the polarization of ferroelectric material can be switched to two or more symmetry-allowed orientations by an external electric field. At the domain level, this process involves the growth of domains with polarization aligned with the field direction at the expense of domains antiparallel to the field. The dynamics of domain switching are complex, involving nucleation and growth of new domains, and the motion of existing domain walls. The switching process of a uniaxial ferroelectric material is illustrated in Figure 2-2, based on ref. [28,49].

For the microscopic process of ferroelectric domain switching, Li et al. [49] summarized a wide range of complex switching phenomena observed by in-situ TEM techniques. A more comprehensive overview is provided in a recent review article [50]. Due to the capability of conversion between two or more stable polarization states, ferroelectric materials have a high potential for applications, such as high-density and non-volatile ferroelectric random-access memory (FeRAM) [51]. Here, using an electric field to inject or switch domains, the polarization states represent binary bits, and the states remain after the power is turned off due to the remanent polarization. The injection and creation of domains are processes intrinsically linked to the movement of domain walls, which will be discussed next.

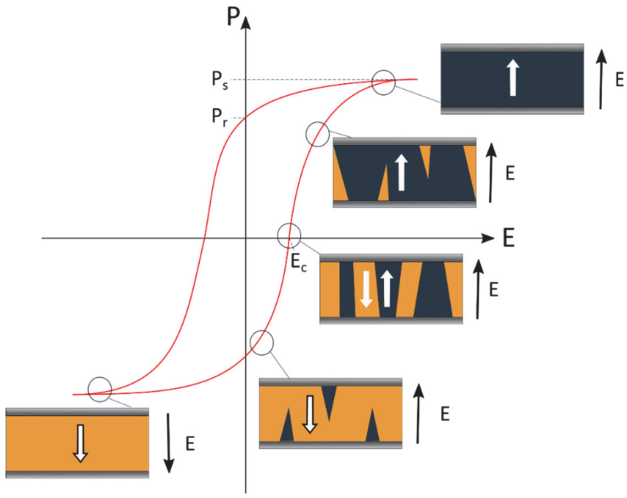

Figure 2-2 Sketch illustrating domain switching in a uniaxial ferroelectric material. Beginning from the lower left, the material is initially polarized downwards in a negative electric field. With the increasing positive electric field, the polarization is reoriented through the three-step switching process [49]: nucleation, forward propagation, and lateral growth of the domains with polarization parallel to the applied electric field. Key points such as coercive field (E_c), remanent polarization (P_r), and saturation polarization (P_s) are indicated. Inspired by ref. [28,49].

2.1.2.1. Domain walls and domain wall conductance

Domain walls are the interfaces between domains with different polarization directions, which means the order parameter changes from one direction to another across the domain walls. Depending on how polarization changes, there are three main types of domain walls: Ising, Bloch, and Néel domain walls [52]. Ising domain walls are characterized by a gradual reversal in polarization magnitude and are typically found in ferroelectric materials with the polarization of adjacent domains that are antiparallel. [28,53]. In Bolch and Néel domain walls, the polarization direction rotates gradually from one domain to the other in a spiral fashion, either out-of-plane or in-plane of the domain wall, respectively. These types of domain walls are more common in ferromagnets because polarization rotation in ferroelectrics comes with more cost in elastic energy. However, they have recently been found to exist also in some standard perovskite ferroelectrics [54,55].

Depending on the relative change of the order parameter across the wall, the domain walls can be defined as neutral or charged domain walls [10,38]. For simplification, a uniaxial ferroelectric system is used as a reference. At neutral domain walls, the polarization vectors on either side of the wall are antiparallel, resulting in zero net charge at the wall (Figure 2-3a). These walls are often almost atomically sharp, e.g., 0.5 nm for $Pb(Zr_{0.2}Ti_{0.8})O_3$ [56], representing the energetically most stable configuration [57]. In contrast, charged domain walls carry a nonzero net bound charge, including negatively charged tail-to-tail (Figure 2-3b) and positively charged head-to-head configurations (Figure 2-3c), resulting in diverging electrostatic potentials. Also, the width of the charged domain wall is, in general, larger than that of the neutral walls due to the bound

charge, e.g., 5 nm for $Pb(Zr_{0.2}Ti_{0.8})O_3$ [56]. The bound charge density ρ_b is the change in the polarization components normal to the domain wall, and can be calculated as [35,58]:

$$\rho_b = \left(\overrightarrow{P_1} - \overrightarrow{P_2}\right) \cdot \overrightarrow{n_1} \qquad \textit{Equation 2-1}$$

where $\overrightarrow{n_1}$ is the domain wall normal as illustrated for the more general case of a curved domain wall in Figure 2 3d.

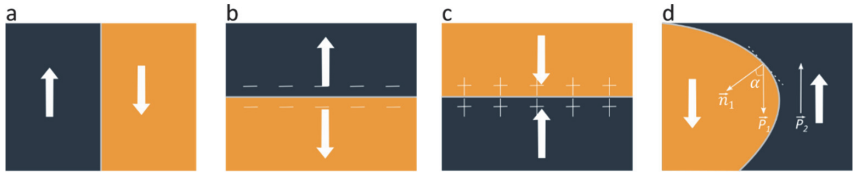

Figure 2-3 Domain walls in uniaxial ferroelectric materials. (a) Neutral domain wall: polarization direction side-by-side. (b) Negatively charged tail-to-tail domain wall. (c) Positively charged head-to-head domain wall. (d) Illustration of a meandering domain wall in a uniaxial ferroelectric material. The bound charge at the domain wall can be calculated using Equation 2-1. The angle between the domain wall normal $\overrightarrow{n_1}$ and the polarization $\overrightarrow{P_1}$ is termed as α. Inspired by ref. [28,34].

In proper ferroelectrics, charged domain walls are electrostatically very costly and can only stabilize if the bound charge at the domain wall is sufficiently screened. The existence of strongly charged domain walls in proper ferroelectrics can be facilitated by means of, for example, specialized poling procedures [18,59,60], defects [61], and strains [62].

In improper ferroelectrics, the ordering is driven by an order parameter other than the polarization, which is only a secondary effect. Consequently, the depolarization field impacts the ferroelectric behavior much less, leading to unique properties that differ significantly from those observed in proper ferroelectrics. The domain wall profiles and width are determined by the primary order parameter of the phase transition, across which ferroelectricity occurs independent of the polarization. Consequently, charged domain walls can also occur naturally and can stably exist, such as in geometrically driven improper systems, for instance, h-$R$$MnO_3$ (R= Er, Ho, Y) [16,63,64] (section 2.2.1), and $(Ca,Sr)_3Ti_2O_7$ [65].

The presence of bound charges at domain walls generally leads to intriguing screening effects by mobile charges, such as electrons, holes, and/or mobile ions, resulting in distinctive electronic transport behaviors at the domain walls in comparison to the surrounding domains [10,38]. For example, electrons tend to accumulate at positively charged head-to-head domain walls and are depleted at negatively charged tail-to-tail domain walls, giving rise to enhanced or reduced conductance of the domain walls relative to the domains.

The distinct electronic transport behavior at charged domain wall and potential applications have been discussed already in 1970s. Vul et al. [11] considered that a domain wall between two domains with mutually opposite polarization directions could exhibit metallic conductivity, because of high concentrations of free charges. In 2009, Seidel et al. [15] experimentally demonstrated enhanced conductance at charged domain walls in $BiFeO_3$, using conductive atomic force microscopy (cAFM) (Figure 2-4). The enhanced conductance at the 180° and 109° domain walls was attributed to an increased carrier density due to the electrostatic potential step at the walls and a decrease in the bandgap at the wall due to structural changes. Since then, conductive charged domain walls have been discovered in various ferroelectrics, both proper ferroelectrics (like $LiNbO_3$ [19], $BaTiO_3$ [60], $Pb(Zr_{0.2}Ti_{0.8})O_3$ [17], $KTiOPO_4$ [66]), and improper ferroelectrics (such as h-$R$$MnO_3$ (R= Er, Y, Ho) [16,63,64], $Cu_3B_7O_{13}Cl$ [67,68], and $(Ca,Sr)_3Ti_2O_7$ [65]), as well as non-oxide ferroelectric GaV_4S_8 [68].

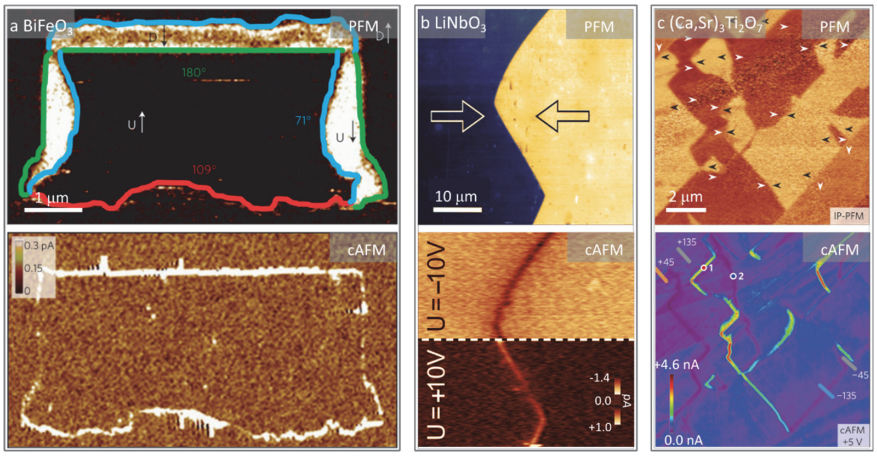

Figure 2-4 Conductive domain walls revealed by PFM images (top row) and cAFM images (bottom row). (a) $BiFeO_3$. Adapted from [15] with permission. *(b) $LiNbO_3$. Adapted from* [19] with permission. *(c) $(Ca,Sr)_3Ti_2O_7$. Adapted from* [65] with permission.

2.1.2.2. Conduction mechanisms at ferroelectric domain walls

Building up on ref. [52], the fundamental mechanisms behind domain wall conduction have been intensively studied and are classified into intrinsic and extrinsic mechanisms. The first is a fundamental reduction in the local electronic band gap at the domain wall (Figure 2-5a). The second involves a band bending induced by domain wall-bound charge (Figure 2-5b). These intrinsic mechanisms are preferred when resistivity is controlled by the injection and depletion of domain walls as they facilitate fast response time [10]. In addition, the domain wall conductance can be extrinsically varied by driving point defects toward or away from the wall (Figure 2-5c). In reality, all these mechanisms may be playing a role at the same time.

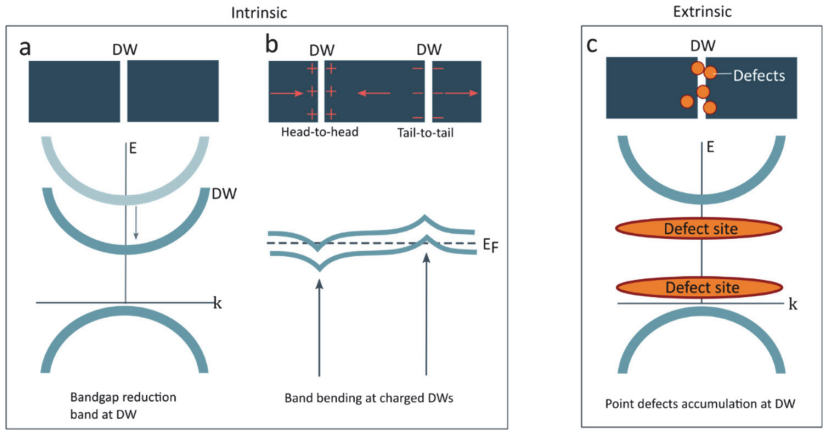

Figure 2-5 Typical mechanisms of domain-wall conduction. (a) Intrinsic different electronic band structures at the domain wall lead to a bandgap reduction. The top semicircle represents the conduction band, and the bottom semicircle represents the valence band. (b) Band bending due to local bound charges at domain walls (DW). (c) Intra-bandgap defects states between the conduction band (top semicircle) and the valence band (bottom circle). E and k indicate the energy and the wave vector, respectively. E_F is the Fermi energy. (a)-(c) adapted from [52] with permission.

In hexagonal manganites (h-*R*MnO_3), for example, the conductivity at the charged domain walls originates from the redistribution of free charges and the related electrostatic potential locally modifying the electronic band structure (Figure 2-5b). Meanwhile, the electrostatic potential can also drive the defects toward or away from the domain wall (Figure 2-5c). For instance, positively charged oxygen vacancies tend to accumulate at negatively charged tail-to-tail domain walls and deplete at positively charged head-to-head domain walls. In contrast, at neutral domain walls, the electronic structure is similar to the bulk, but its conductivity can differ due to extrinsic contribution from oxygen defects induced by local strain [22,69].

2.1.3. Domain wall nanoelectronics

Ferroelectric domain walls, with their intriguing electronic properties and ultra-small feature size (frequently with width at the unite cell level [52]), as well as the fact that they can be created, moved, and erased by an electric field [38,52], have been exploited as functional entities that can be integrated into electronic devices for signals control, a field known as domain wall nanoelectronics [33]. This section is mainly based on the review article by Meier et al.[10].

Inspired by the proof-of-concept work on $BiFeO_3$ for device applications [15], the domain walls can serve as a reconfigurable conductive channel, i.e., controlling conductivity through the injection, movement, and erasure of domain walls, providing a dynamic way to reconfigure the electronic circuitry [10]. A typical example is the prototype non-volatile ferroelectric domain wall memory in $BiFeO_3$ thin film [20], in which the ferroelectric sample is contacted with planar electrodes. By modulating the bias voltage between the electrodes, the domain wall can be injected and erased, corresponding to the binary state low and high resistance, respectively. This, therefore, realizes the concept of two-terminal non-volatile domain wall memory (Figure

2-6a), where the ON and OFF states are associated with the presence or absence of a conducting domain wall. This concept was further expanded to achieve three distinct addressable resistance states by precisely controlling the charge state of the injected domain wall [70]. Based on the domain wall injection, in $LiNbO_3$ single crystal, varying the magnitude of the electric field pulse allowed for systematic control of the density of injected conducting head-to-head domain walls, leading to a range of conductance states varying by nearly 12 orders of magnitude, realizing a ferroelectric domain wall memristor [71]. This makes ferroelectric domain walls well-suited for integrating into neuromorphic computing architectures to emulate synaptic plasticity mechanisms like STDP (Spike-Timing-Dependent Plasticity) [72]. Moreover, based on the redirection of conducting domain walls between the drain, gate, and source by controlling gate/source voltage, a non-volatile ferroelectric $LiNbO_3$ transistor was created [73]. In these applications, the injected domain walls are stabilized by the majority carrier in the material.

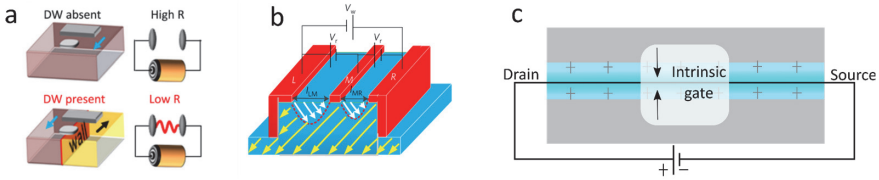

Figure 2-6 Domain wall-based devices. (a) Domain wall memory cell with high resistance (High R) and low resistance (Low R) binary states, determined by the absence or presence of a conductive domain wall between two electrodes. Reprinted from [20] under a Creative Commons CC BY license. (b) Domain wall-based read-out ferroelectric memory device. Partial switching can transiently create highly conductive domain walls, enabling non-destructive read-out of the polarization information. Reprinted from ref. [74] with permission. *(c) Conceptual sketch of a domain-wall-based field-effect transistor using the bound charge at the head-to-head domain wall as the intrinsic gate. The domain wall is not a reconfigurable conductive wire in the device architecture but the device itself. Adapted from* [21] *with permission.*

Another approach in domain wall nanoelectronics involves using energetically unfavorable domain wall configurations that only transiently occur under external electric fields [10], facilitating non-destructive read-out technology with much higher read current under low operating voltage. As shown in (Figure 2-6b), in epitaxial BFO thin film [74], by controlling the voltage between the electrodes L, M, and R, the information (yellow arrows) can be effectively read out. This process is facilitated by the transient creation of a conductive charged wall (red dashed lines) via a partial domain reversal (white arrows) near the film surface, when the applied electric field is antiparallel to the in-plane polarization component. These charged walls disappear immediately after the removal of the read voltage because of the depolarization field. Conversely, when the in-plane polarization component aligns parallel to the applied field, no read-out current is produced. This approach was later expanded to $LiNbO_3$ thin films bonded to SiO_2/Si wafers, representing a big progress in terms of both memory functionality and mass production compatibility.

These applications rely on injecting, manipulating, and removing conducting domain walls to control the electronic signal. A second category of domain wall device concept utilizes the domain wall itself as a device (Figure 2-6c), exploiting the domain walls naturally present in the improper ferroelectrics. These domain walls offer additional functionalities beyond conduction, enabling the behavior of classical electrical components, such as diodes [22]and transistors [21]. The details of these domain walls and their functionalities, as well as devices based on exploiting the intrinsic properties of the domain walls, will be introduced in section2.2.3.

2.2. Hexagonal manganites

The hexagonal manganites belong to the class of geometrically improper ferroelectrics. These materials have attracted considerable interest in the scientific community due to their unusual ferroelectric properties (T_C) [75] and low temperature (T_N < 120 K) antiferromagnetism [76], serving as model system for multiferroic order.

The system used in this work is $ErMnO_3$, and the study focuses on the ferroelectric properties. It is worth noting that although many of the experimental and theoretical findings from previous studies discussed below are derived from different h-*R*MnO_3 members, such as $YMnO_3$ and $HoMnO_3$, many results are generally applicable across all h-*R*MnO_3, including $ErMnO_3$. For specific distinctions between different compounds in h-*R*MnO_3 family, readers are referred to references [76] and [77]. This section will describe the state-of-the-art, covering the crystal structure, ferroelectric domains and domain walls, and defect chemistry.

2.2.1. Crystal structure

The crystal structure of h-*R*MnO_3 consists of layers of *R*-cations separated by layers of corner-sharing MnO_5 bipyramids. Above the phase transition temperature (T_C = 1150 °C [78]), the paraelectric phase is centrosymmetric and belongs to the space group $P6_3/mmc$ (Figure 2-7a). Below the phase transition temperature, the structure has $P6_3cm$ space group symmetry (Figure 2-7b), driven by the buckling of the MnO_5 bipyramids and a corrugation of *R*-ions [28]. The latter results in a distortion that displaces the *R*-ions in either an up-up-down pattern for positive polarization or a down-down-up pattern for negative polarization [23].

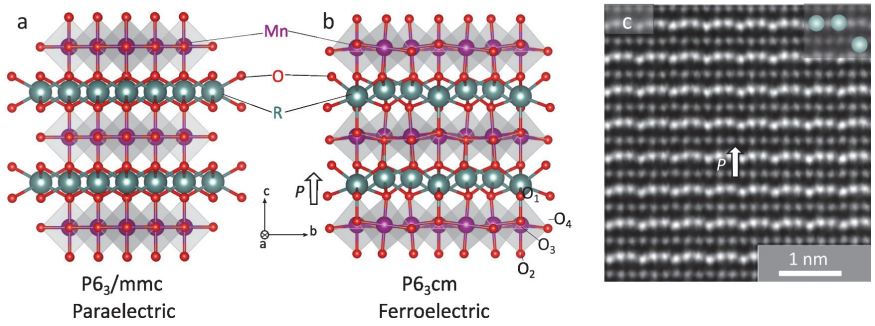

Figure 2-7 (a) The high-temperature paraelectric phase P63/mmc of $RMnO_3$. (b) The low-temperature ferroelectric phase P63cm of $RMnO_3$. (a, b) are rendered in Vesta [79] *using crystallographic data from* [80] *and* [81]*, respectively. (c) High-angle annular dark field scanning transmission electron microscopy (HAADF-STEM) image of an up-polarized domain with the up-up-down pattern of Er atoms, adapted from* [23] *under a Standard ACS Author Choice/ Editors' Choice usage agreement.*

The displacement pattern is shown in the HAADF-STEM image in Figure 2-7c taken by Holtz et al. [23], showing a domain with an up-up-down corrugation of Er ions in $ErMnO_3$. In this image, the brighter Er ion layers alternate with Mn layers, while oxygen as a light element is not resolved.

2.2.2. Phase transition and domain formation in h-*R*MnO_3

As the polarization in h-*R*MnO_3 is a secondary effect driven by a structural change, the ferroelectricity in h-*R*MnO_3 is categorized as geometrically improper ferroelectricity [82]. During the phase transition, the trimerization of MnO_5 bipyramids occurs, where groups of three bipyramids tilt towards or away from a central R^{3+} ion. This trimerization process triples the unit cell volume but does not yet induce polarization. The trimerization can occur at three different R^{3+} ion sites, resulting in antiphase domains with different trimerization states α, β, and γ. This trimerization [83] is defined by a two-dimensional primary order parameter (Q, Φ), involving the bipyramids tilting amplitude (Q) and the azimuthal orientation of the tilt (Φ), as sketched in Figure 2-8a [24]. The polarization arises as a byproduct of nonlinear coupling with the trimerization. The occurrence of polarization is associated with the vertical shift of the R^{3+} relative to the Mn [75], giving rise to a net dipole moment along the c-axis. The direction of polarization, either +P or -P, depends on whether the bipyramids tilt towards or away from the R^{3+} (Figure 2-8b).

Combing the three different antiphase domains (α, β, and γ) with two possible polarization directions results in six possible domain states $\alpha^{\pm}$, $\beta^{\pm}$, and $\gamma^{\pm}$ (Figure 2-8c) [23]. As supported by theoretical calculations [23,84,85], experimental observations [78,86,87] show that mutual locking of structural antiphase domains (α, β,and γ) and two electric polarization orientations form a "cloverleaf" pattern (Figure 2-8d), where six domains are converging at one point [86]. These meeting points, commonly referred to as six-fold vortices, are the most energetically favorable. Around each core, the domain configurations are arranged either counterclockwise (vortex: α^+, β^-, γ^+, α^-, β^+, γ^-) or clockwise (anti-vortex: $\alpha^+, \gamma^-, \beta^+, \alpha^-, \gamma^+, \beta^-$), as shown in Figure 2-8c. The vortex and anti-vortex always occur in pairs [78]. Figure 2-8d presents a TEM (transmission electron microscopy) dark-field image of $YMnO_3$, displaying a typical vortex and anti-vortex pair, in which the cycle of domain configuration is reversed. These vortices are topological defects formed during the ferroelectric phase transition [23,38,85,88].

As the spontaneous polarization in h-$RMnO_3$ arises only as a secondary effect, it is relatively small ($\sim 5.5\ \mu C\ cm^{-2}$ in $ErMnO_3$ [89]) compared to that in proper perovskite ferroelectrics ($BiFeO_3$: ~130 $\mu C\ cm^{-2}$ [90], $BaTiO_3$: 15-30 $\mu C\ cm^{-2}$ [91], PZT: 70 $\mu C\ cm^{-2}$ [92]).

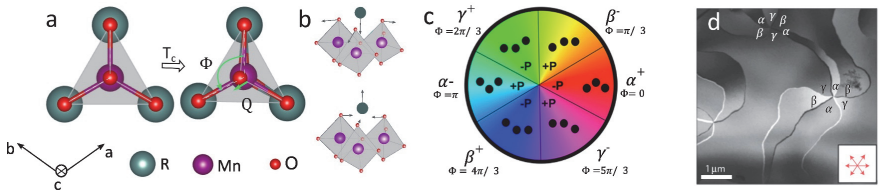

Figure 2-8 (a) Oxygen bipyramids tilt below the phase transition temperature (T_c), described by the angle Φ and the amplitude Q. (b) Two possible polarization directions depending on the bipyramid tilt towards or away from the R ion, adapted from [82] *with permission. (c) Six possible domains arise from different R ion configurations according to the different Φ, with the corresponding R-corrugation patterns sketched via the black dots in each segment, adapted from* [23]*. (d) TEM dark-field image recorded from $YMnO_3$ sample, showing a vortex (black texts) and anti-vortex (white texts) pair structure with six domains (α–β–γ– α–β–γ), adapted from* [86] *with permission.*

2.2.2.1. Domains

The domains in h-*R*MnO_3 were observed through optical microscopy with the assistance of chemical etching already in 1967 (Figure 2-9a). Today, with the advancements in characterization techniques, domains can be easily observed in high resolution using PFM (piezoresponse force microscopy) [93], cAFM[16], SEM (scanning electron microscopy)[94], STEM (scanning transmission electron microscopy) [87], etc., without the need for chemical etching. In h-*R*MnO_3, the equilibrium domain configuration is characterized by vortex and antivortex pairs as shown in Figure 2-8d. Interestingly, despite the highly anisotropic uniaxial structure of h-*R*MnO_3, the domain distribution is almost isotropic [77]. Jungk et al.[95] observed that these vortex-domain structures occur in all three spatial dimensions, with only a slight elongation of the domains along the c-axis on non-polar faces, as illustrated in Figure 2-9b. More recently, Roede et al. [96] used FIB tomography to reconstruct 3D domain structures in h-$ErMnO_3$, revealing vortex-domain structures in three spatial dimensions (Figure 2-9c).

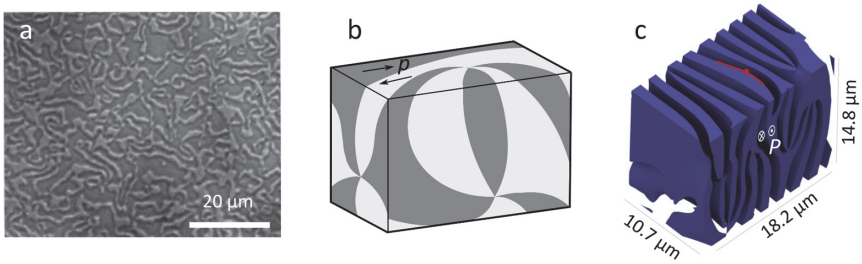

Figure 2-9 Isotropic vortex domains in h-$RMnO_3$. (a) The first observed domains in $YMnO_3$, revealed by optical microscopy, aided by H_3PO_4 etching, adapted from [99] *with permission. (b) Illustration of vortex domains occurring in all three spatial dimensions. (c) Reconstructed 3D domains in $ErMnO_3$ single crystal via FIB-tomography, with -P rendered transparent and +P in blue. (c) is adapted from* [96] *under the term of the Creative Commons CC BY license.*

It is important to note that stripe domains and loop domains can form when the crystal growth takes place below the phase transition temperature (T_c), as found in flux-grown h-$ErMnO_3$ single crystal by Chae et al. [78]. Subsequent annealing above T_c can transform these domains into typical vortex domains, but they cannot revert to stripe or loop domains once the vortex pattern

is established. Stripe domain formation was recently also observed in polycrystalline samples of $ErMnO_3$ and explained by the interaction between the vortex structure and elastic strain field [97,98]. In this work, neither stripe domains nor loop domains are relevant, so the focus is on the typical vortex domains.

2.2.2.2. Domain switching

Vortex and antivortex structures in h-*R*MnO_3 are topological defects and cannot be moved or erased by an external electric field. This results in distinct domain-switching behaviors. The unusual switching characteristics of h-*R*MnO_3 have been experimentally investigated by PFM [86,95], SEM [100], and TEM [88]. Under an applied bias voltage, domains with polarization parallel to the applied field expand while those antiparallel to the electric field shrink. Figure 2-10a and b show the same area on a $YMnO_3$ surface before (a) and after (b) voltage poling, demonstrating the bright domains contract to lines after the bias voltage is applied [95]. Similar domain-switching behavior in $ErMnO_3$ has been observed in TEM under positive and negative fields, as illustrated in Figure 2-10c [88]. For further details about the switching behavior at the level of the domains, the interested reader is referred to, e.g., ref. [101].

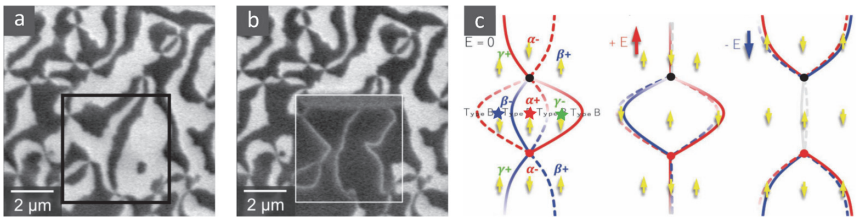

Figure 2-10 Domain switching in h-RMnO₃. (a) and (b) PFM images of an out-of-plane surface in YMnO₃ before (a) and after (b) tip-voltage poling within the highlighted region (black (a)/ white (b) frame). After the poling, the white domains shrink while the dark domains expand. Adapted from [95] *with permission. (c) Schematic of domain switching around a vortex observed in TEM. Domains with polarization parallel to the applied field expand while those antiparallel contract. Unbiased condition (left), under a positive applied field (middle), under a negative applied field (right). Adapted from* [88] *with permission.*

2.2.3. Domain walls and their functionalities

Due to the topologically protected vortex/anti-vortex structures in h-*R*MnO_3, which serve as six-fold anchor points for the domain walls, meandering domain walls of all possible orientations naturally occur. This leads to the spontaneous formation of stable ferroelectric domain walls, both neutral and charged domain walls. In recent years, these domain walls have garnered increasing attention because of their unique properties, holding significant opportunities for innovative nanoelectronics [23].

Figure 2-11 presents HAADF-STEM images of the three different types of domain walls in h-*R*MnO_3: (a) tail-to-tail, where the polarization vectors of adjacent domains point away from each other, resulting in negative bound charge at the wall; (b) head-to-head, characterized by polarization vectors pointing towards each other, leading to a positive bound charge state at the wall, and (c) neutral domain walls, where the polarization vectors in adjacent domains are

antiparallel, such that no net accumulation of bound charge occurs at the wall. In contrast to proper ferroelectric domain walls, these walls are very sharp and have similar widths to each other (charged walls 7.4 ± 0.2 Å, neutral walls 6.3 ± 0.1 Å for $ErMnO_3$ [23]). According to Holtz et al. [23], this uniformity is given by the structural stiffness of the system rather than charge properties, representing a striking example of the unique consequences of improper ferroelectricity at the atomic scale.

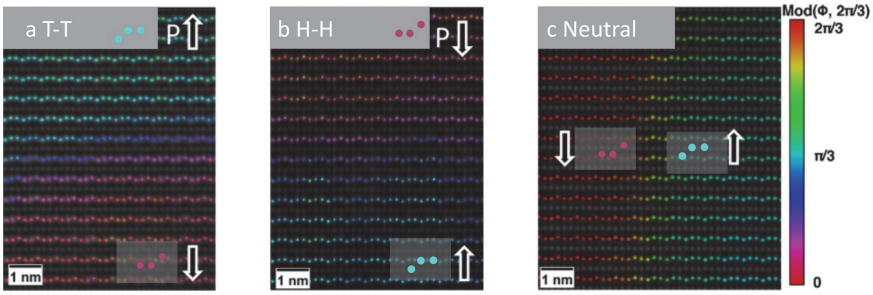

Figure 2-11 HAADF-STEM images of domain walls in $ErMnO_3$ (a, b) and $Er_{1-x}Zr_xMnO_3$ (c). (a) Negatively charged tail-to-tail (T-T) domain wall. (b) Positively charged head-to-head (H-H) domain wall. (c) Side-by-side neutral domain wall. The width of these domain walls is at unit-cell level, and both charged domain walls and neutral domain walls exhibit similar widths. adapted from [23] *under a Standard ACS Author Choice/ Editors' Choice usage agreement.*

Bound charges at the domain walls necessitate electrical screening, leading to the redistribution of intrinsic and extrinsic charge carriers. This section focuses on the intrinsic carriers, while the extrinsic ones will be discussed in the defects engineering part in section 2.2.4. The redistribution of intrinsic charge carriers gives rise to significantly different conduction phenomena at the domain walls compared to the bulk. For example, in p-type h-$RMnO_3$, negatively charged tail-to-tail walls attract the majority carriers (holes), enhancing p-type conductivity. Conversely, positively charged head-to-head domain walls are screened by a depletion of holes and exhibit suppressed conductivity. This anisotropic conductance at domain walls was first reported by Meier et al. [16] on an in-plane $ErMnO_3$ surface using cAFM (Figure 2-12a). Following this finding, similar behavior was found in other family members of h-$RMnO_3$, such as $HoMnO_3$ [63] and $YbMnO_3$ [102]. Since then, the domain walls in h-$RMnO_3$ have been intensively investigated both experimentally and theoretically, including the fundamental properties and applications. A few years later, Mundy et al. [21] found that the conductance of the head-to-head domain walls in p-type $ErMnO_3$ can be reversibly controlled between insulating and conducting states by adjusting the cAFM bias voltage. At low voltages (V_{DC} = 2.5 V), the image displays standard behavior with conducting tail-to-tail (bright) and insulating head-to-head (dark) domain walls [16,57], termed as the low voltage regime (Figure 2-12c). However, when the voltage is high enough ($V_{DC} \geq 6.0$ V), both tail-to-tail and head-to-head walls become more conductive than the surrounding domains, known as the high voltage regime (Figure 2-12d). Adjusting the applied electric field allows reversible switching between these

two states (Figure 2-12b). In this manner, the head-to-head domain wall turns into an electronic switch, providing additional functionality beyond just enhanced conduction, foreshadowing the possibility of designing an all-domain-wall device for nanotechnology.

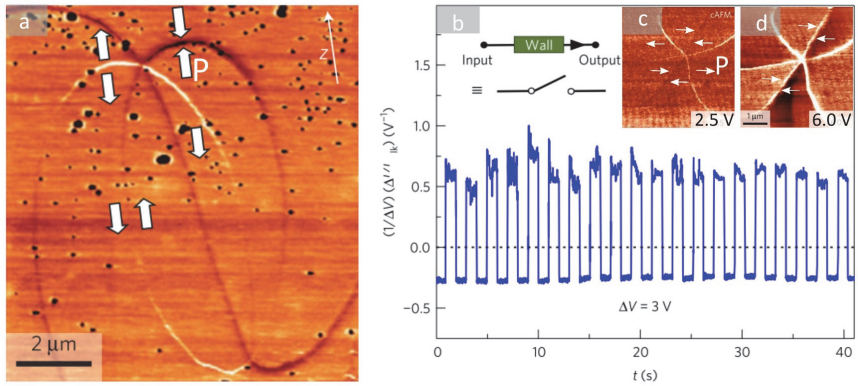

Figure 2-12 (a) A cAFM image showing anisotropic electrical conductance at ferroelectric domain walls in in-plane h-$ErMnO_3$. The white arrows indicate the polarization directions. Adapted from [16] *with permission. (b) Reversible switching between enhanced and reduced conductance over 20 cycles at head-to-head domain wall in $ErMnO_3$. (c) cAFM image of a six-fold meeting point recorded with a bias voltage of 2.5V on an in-plane $ErMnO_3$ sample, revealing conducting tail-to-tail (bright) and insulating head-to-head (dark) domain walls. (d) cAFM image obtained by a bias voltage of 6.0 V at the same position as shown in (c). Both head-to-head and tail-to-tail domain walls exhibit enhanced conductance. (b)-(d) are adapted from* [21] *with permission.*

The reversible conductance at the head-to-head domain walls was attributed to the formation of an inversion layer at the wall. The calculated band diagram (Figure 2-13a) shows that the potential is flat, and the Fermi level lies very close to the valence band maximum (VBM) in the bulk. At the tail-to-tail domain wall, the VBM shifts upward and generates more holes, which screen the negative bound charge at the wall and enhance the conductance. However, at the head-to-head wall, significant band bending occurs with the conduction band minimum (CBM) dipping below the Fermi level. This suggests that screening at the head-to-head domain wall is realized by both hole depletion around the wall and electron accumulation right at the wall. Theoretical calculations suggest that the accumulated electron layer is likely in a localized polaronic state, which does not contribute to conductance in the low voltage regime but becomes the primary source for charge carriers in the high voltage regime, facilitating the reversible switching from insulating to conductive behavior at head-to-head domain walls.

The corresponding calculated charge carrier density across a head-to-head domain wall is displayed in Figure 2-13b. The inset shows that the average carrier density is proportional to the conductance, with the color of each curve corresponding to different spatial resolution

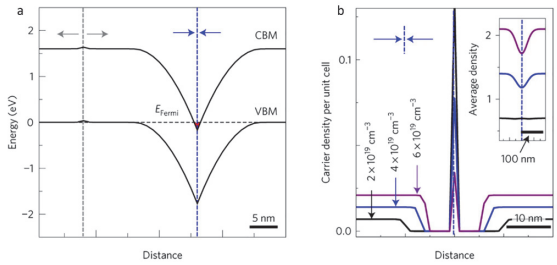

Figure 2-13 (a) Band bending at tail-to-tail domain wall and head-to-head domain wall. (b) Calculated carrier density at head-to-head walls. With decreasing average density (from purple curve to black curve), the screening by hole depletion becomes less and less efficient so that the electron density increases to aid in screening the positive bound charges at the wall. The inset displays the average carrier density (hole) in a realistic resolution for cAFM. (a) and (b) are adapted from [21] *with permission.*

plots in the main graph. In regions with high hole density (purple), the depletion of holes is efficient enough to screen the head-to-head walls. However, in areas with low bulk hole density (black), the screening is realized by both hole depletion and electron accumulation, which offers intriguing functionality, as described above.

In addition to the charged head-to-head domain walls, neutral walls in h-$ErMnO_3$ have also demonstrated the possibility of emulating electrical components. Figure 2-14a shows the input AC voltage and the corresponding I(V) curve of an out-of-plane $ErMnO_3$ sample. The asymmetry in the I(V) curve leads to the rectification of the AC voltage. Furthermore, the Schottky barrier between the tip and sample in the +P and -P domains differ, creating domain contrast in the low-frequency regime, which decreases and eventually disappears as the frequency increases to 2.1 MHz. Remarkably, neutral domain walls exhibit rectifying behavior, enabling the conversion of AC to DC over a frequency range from kHz to MHz (Figure 2-14c), and this behavior persists at higher frequencies than in the domains (Figure 2-14d). This rectification is attributed to the accumulation of oxygen interstitials at the neutral domain walls, which induces enhanced conductance and is energetically more favorable than in the bulk. As a result, these domain walls can act as nano-diodes with minimal size, facilitating the possibility of nanoscale electronic components.

Unlike conventional proper domain walls, which are typically used as reconfigurable conducting channels in the much larger device architecture, the improper domain walls in h-*R*MnO_3 become the device itself. These domain walls are stable and persist even when their bound charge is not fully screened [10], representing a conceptually new approach towards ultra-small and energy-efficient electronics. Beyond the intrinsic properties induced by the bound charges,

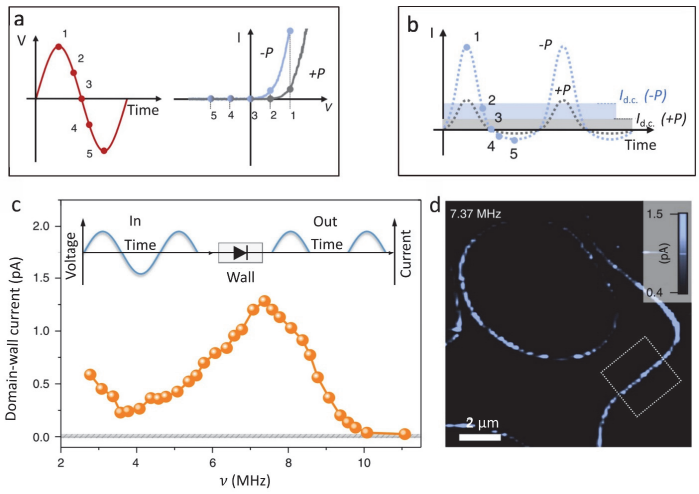

Figure 2-14 Rectifying behavior at neutral domain wall in $ErMnO_3$. (a) and (b) Illustration of AC input voltages (left) are transferred to DC current responses (b) due to the asymmetric I-V curve (right) in $ErMnO_3$. +P shows a higher Schottky-like barrier than -P (on the right of (a)), resulting in domain contrast in output DC signals (b). (c) Frequency-dependent half-wave rectification at neutral domain walls in $ErMnO_3$. Top panel: The inputted AC voltage can be half-wave rectified to DC current. Orange dot-curve: AC inputs are rectified at the neutral wall from ~2 MHz to 10 MHz. (d) Ac-cAFM image taken at a frequency 7.37 MHz, showing the position of the data shown in (c). (a)-(d) are adapted from [22] *with permission.*

the domain wall properties in h-*R*MnO_3 can also be modulated by extrinsic defects. This additional layer of control, which will be introduced in the next section, provides further opportunities for domain wall property engineering and the functionalization of the material at the nanoscale in general.

2.2.4. Defect engineering in hexagonal manganites

Hexagonal manganites exhibit considerable chemical flexibility in terms of cation and anion off-stoichiometry, making defect engineering a powerful method for tailoring properties at both bulk and domain wall levels. In this context, we focus on point defects, which are most relevant to this work.

Aliovalent substitution of R and Mn cations in h-*R*MnO_3 has been reported to be able to modulate the materials' conductivity [103,104], and the accommodated oxygen defects [105] sometimes even drive phase transitions that alter the crystal structure [106]. Cation doping typically requires adjusting the initial powder composition and calcination above the phase transition temperature before crystal growth. Once the crystal growth is complete, modifying the doping level becomes challenging. In contrast, modulating the oxygen defect concentration in h-*R*MnO_3 is done rather easily. Various methods can be employed, including thermal and atmospheric treatments, the application of an external electric field [107], and ion beam irradiation [108]. The thermal and atmospheric treatments can be performed by varying the growth atmosphere or conducting thermal annealing at a relatively low temperature (~200-400 °C [109]) in different atmospheres after growth (as also demonstrated in this work in

section 4.1.3). This flexibility makes oxygen defects an advantageous tool for engineering the properties of h-*R*MnO_3 materials. Due to the multivalency of Mn and its less densely packed structures, h-*R*MnO_3 can tolerate a substantial level of oxygen non-stoichiometry (h-*R*$MnO_{3\pm\delta}$) without significant alterations to its crystal structure. Oxygen vacancies and oxygen interstitials play an equally important role for its electronic transport properties [10].

Figure 2-15a and b illustrate a stoichiometric unit cell and an oxygen interstitial (red) sitting between the three Mn in the Mn-O planes, respectively. Skjærvø et al. [109] reported that in an oxygen-excess environment, the formation of oxygen interstitials causes subtle local structural distortions, oxidizing two Mn^{3+} to Mn^{4+} to compensate the charge (Equation 2-2). The process is following the chemical defect reaction [109]:

$$\frac{1}{2}\,O_2(g) + 2Mn_{Mn}^{x} \xrightarrow{YMnO_3} 2Mn_{Mn}^{\bullet} + O_i'' \qquad \textit{Equation 2-2}$$

where O_i'' is interstitial O^{2-}, and Mn_{Mn}^{X} and $Mn_{Mn}^{\bullet}$ represent Mn^{3+} and Mn^{4+} on Mn lattice sites, respectively. Mn^{4+} here is Mn with localized electron holes: $Mn^{4+} = Mn^{3+} + h^{+}$, which contribute to p-type conductance.

By alternating between O_2 and N_2 atmospheres, the oxygen stoichiometry δ in porous polycrystalline $YMnO_3$ bars can be reversibly adjusted between 0.00 to about 0.15 at temperatures ranging from 250 to 400 °C [109]. Based on both experimental and theoretical results, they found interstitial oxygen to be the dominating defect in $YMnO_3$, and it is responsible for the p-type electronic conductivity under ambient conditions [109].

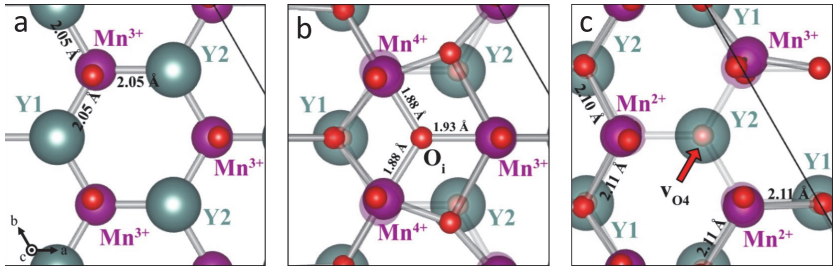

Figure 2-15 Illustration of local structure with and without oxygen defects. (a) Stoichiometric unite cell. (b) Oxygen interstitial (O_i'') situated in the middle of three Mn in the Mn-O plane. (c) Oxygen vacancy ($V_O^{\bullet\bullet}$) located at the planar O4 site. Images adapted from [110].

In contrast, oxygen deficiency often leads to the formation of oxygen vacancies, the most common defects in oxides, including h-*R*MnO_3. As illustrated in Figure 2-15c, an oxygen atom leaves its lattice position, resulting in an oxygen vacancy. According to Skjærvø et al. [111], under a finite concentration, vacancies are charge compensated by reducing two Mn, following the defects chemistry:

$$2Mn_{Mn}^{x} + O_O^{x} \xrightarrow{YMnO_3} 2Mn_{Mn}' + V_O^{\bullet\bullet} + \frac{1}{2}O_2\,(g) \qquad \textit{Equation 2-3}$$

where Mn_{Mn}^{x} and O_{O}^{x} represent lattice Mn and O, respectively. $V_{O}^{\bullet\bullet}$ is an oxygen vacancy with relative charge +2, and $Mn_{Mn}^{\prime}$ denote Mn^{2+} cation. Oxygen vacancies $V_{O}^{\bullet\bullet}$ can act as electron donors.

The formation of oxygen vacancies is favored by high temperature and low oxygen partial pressure [111]. Wang et al. [112] found that the oxygen vacancy concentration in bulk $YMnO_{3-\delta}$ crystal was about $\delta = 0.02$ after being quenched to room temperature in Ar flow from near phase transition temperature. Large oxygen deficiency in $YMnO_{3-\delta}$ with $\delta = 0.15$ has been obtained by topotactic reduction [113].

Skjærvø et al. [111] noted that oxygen vacancies preferentially form at the planar O_4 sites (shown in Figure 2-7b) in the bulk and are elastically screened by the surrounding Mn ions. In contrast to previous studies on selected proper ferroelectrics [114,115], oxygen vacancies in h-$RMnO_3$ are repelled from the neutral domain walls.

2.2.4.1. Oxygen defects for domain wall engineering

Both oxygen interstitials and oxygen vacancies have a significant impact on the behavior of domain walls, e.g., electrical conductivity. Schultheiß et al.[69] and Schaab et al. [22] found enhanced DC and AC conductance at the nominally neutral domain walls, respectively, attributed to the accumulation of oxygen interstitials at the neutral domain walls. Du et al. [64] found that the local conductivity at the domain walls increased significantly in $YMnO_{3-\delta}$ due to the oxygen vacancies. The local strain field and electrostatic potential can both act as the driving force for the redistribution of these charged point defects. For example, oxygen interstitials accumulated at the neutral domain wall due to lattice strain [22,69], while positive oxygen vacancies tend to gather at negatively charged tail-to-tail domain walls and deplete at positively charged head-to-head domain walls because of electrostatic potential [10,116]. Therefore, the concentration and types of oxygen defects, controlled by the thermal-atmospheric history, can significantly influence the domain wall properties. This opens up opportunities in sensor technology, where environmental changes can be detected as variations in domain wall conductance [10].

2.2.4.2. Oxygen defects induced domain switching

In addition to their influence on domain walls, oxygen defects also significantly impact the domain and local electrical properties. This section will explore the role of oxygen defects in domain switching.

The surrounding atmosphere at high temperatures could effectively influence the sample polarization orientation in the near-surface region because of the oxygen defect gradients; this is termed chemical switching. Wang et al. [117] observed that the surface domains in h-*R*MnO_3 (R= Lu, Ho, Yb) predominantly polarized in one direction, while the other shrank into a line after the sample was quenched to room temperature from nearly phase transition temperature in

Ar flow. This contrasts with the typical configuration, where domains with upward and downward polarizations are present in approximately equal proportions (see Figure 2-16a). This phenomenon was attributed to an internal self-electric-poling effect triggered by a gradient in oxygen off-stoichiometry near the surface, affecting regions to a depth in the order of 100 nm. Soon after, Lilienblum [77] systemically demonstrated that the in- or out-diffusion of oxygen causes polarization reversal in a depth of around 200 nm. For instance, an out-of-plane $YMnO_3$ sample with equilibrium domain configuration (Figure 2-16a) transitions to a surface domain configuration with expanded -P-polarized domains and shrunken +P-polarized domains in the near-surface region after annealing at 527 °C in an oxygen-deficient N_2 atmosphere (Figure 2-16b). This transition is due to an oxygen loss near the surface, which creates a gradient of oxygen vacancies. This gradient generates an internal electric field, as indicated in the top arrow in Figure 2-16c. Despite this internal electric field, the vortices remain in their original positions because of the aforementioned topological protection. Conversely, annealing in an oxygen-rich atmosphere results in a surface domain configuration where +P-polarized domains expand and -P-polarized domains contract, a result of the oxygen interstitial gradient in the near-surface region, as illustrated in the bottom row in Figure 2-16c.

The chemical switching induced by defect gradients yields a result similar to those caused by external field-induced switching (Figure 2-10b), typically characterized by the domain wall movement in the near-surface region, showing the significant role of oxygen defects in modulating the properties of ferroelectric hexagonal manganites.

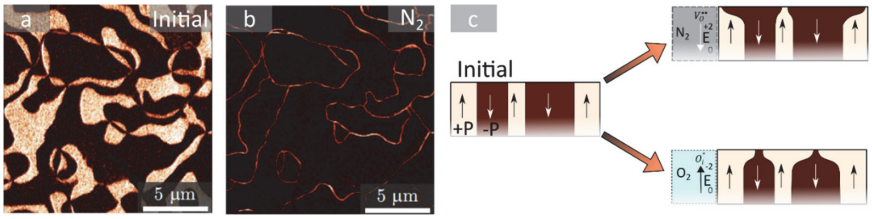

Figure 2-16 Domains in h-$YMnO_3$ switched by an oxygen defect gradient in the near-surface region. (a) PFM image of the domain structure on the out-of-plane sample surface. (b) The same sample as (a) after annealing at T= 527 °C in a N_2 atmosphere. (c) Sketch of the domain structure changes in the near-surface region after annealing in oxygen-deficient (N_2) and oxygen-excess (O_2) atmosphere. Adapted from [77].

2.2.4.3. Nanoscale local conductance control by oxygen defects

Oxygen defects enable the modulation of the domain and domain wall properties, offering substantial potential for technological applications. However, such effect applies simultaneously to the entire system, lacking site-specific precision. With the advancement of nanotechnology, which significantly relies on high spatial accuracy in order to facilitate device/circuit miniaturization and high energy efficiency, a method enabling local conductance control at the nanoscale using oxygen defects is highly desirable.

The SPM-tip-based method, using an electric field, is a powerful approach for this purpose. The sharp SPM tip strongly enhances the local electric field and allows for precise defect movement. This method has been successfully applied for nanoscale manipulation in various systems, such as $LaAlO_3$-$SrTiO_3$ heterostructures [118]and $BiFeO_3$ [119]. Wang et al. [112] demonstrated nanoscale conductance manipulation in $Y_{0.67}Lu_{0.33}MnO_3$ single crystals, induced by oxygen interstitial migration. As shown in Figure 2-17a, the area marked by the red frame was scanned with a 4.0 V bias voltage, followed by the green area being scanned with a -4.5 V bias voltage. The subsequent current map shows that the square ring region, which was scanned only by the positive bias, exhibits higher conductivity compared to the surrounding areas. Figure 2-17b displays the current profile along the purple line in (a). This effect was explained by the induced migration of the majority carrier oxygen interstitials under the electric field.

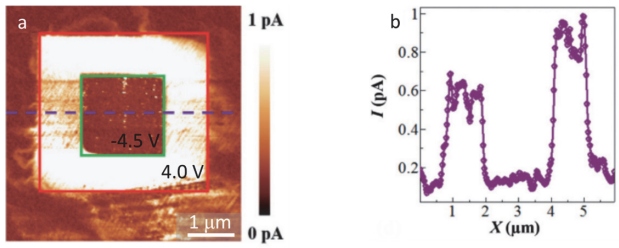

Figure 2-17 Oxygen vacancy-migration-induced local conductance change. (a) cAFM image in an area where oxygen defects have been manipulated using a cAFM scan. The red area was initially scanned with a 4V bias voltage first, followed by a -4.5V scan of the green area. (b) The current profile along the purple dashed line in (a), highlights that the area only scanned by positive voltage exhibits enhanced conductance. Adapted from [112] *with permission.*

It is important to note, however, that due to their effective electric charge, both oxygen interstitials and oxygen vacancies can have an impact on the ferroelectric properties of the material. Evans et al. [107] found a novel route to overcome this challenge using charge-neutral oxygen interstitial-vacancy pairs, which are termed anti-Frenkel defects.

Frenkel defects are common point defects in ionic solids [120], characterized by smaller ions (usually cations) leaving their regular lattice sites and moving to interstitial sites, which are positions in the lattice where atoms are normally not located. Anti-Frenkel defects refer to oxygen interstitial-vacancy pairs. The formation process is illustrated in Figure 2-18a for the case of hexagonal manganites. Under a biased cAFM tip, a lattice oxygen (yellow) migrates from its original lattice site to a neighboring planar oxygen lattice site (grey), which in turn is nudged into an interstitial site, resulting in the formation of oxygen vacancy and oxygen interstitial pair. To compensate for the charges, two of Mn^{3+} beside the oxygen vacancy are reduced to Mn^{2+},

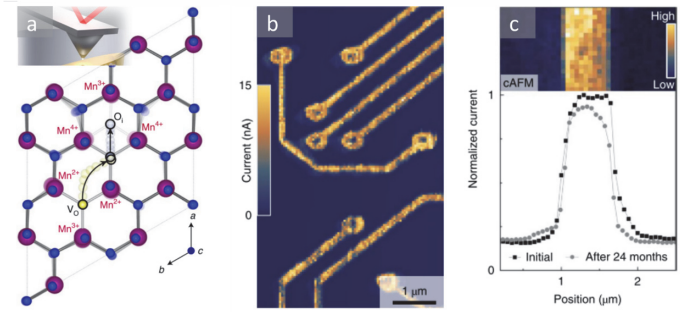

Figure 2-18 Anti-Frenkel defect formation and resulting conducting features in h-Er(Mn,Ti)O_3. (a) Formation of anti-Frenkel defects under electric field applied by SPM tip (inset). (b) cAFM image showing conducting nanowires (bright) on an out-of-plane semiconductor h-Er(Mn,Ti)O_3 surface. (c) Normalized current profile across a conducting bar right after writing (black) and after 24 months (grey). The data reflect the long-term stability of the conducting features created by the formation of anti-Frenkel defects. (a)-(b) adapted from [107] *with permission.*

while two others beside the oxygen interstitial are oxidized to Mn^{4+}. This process macroscopically enables the writing of conductive features based on the generation of the anti-Frenkel defects. Figure 2-18b displays a cAFM image of an out-of-plane h-Er(Mn,Ti)O_3 semiconductor surface, on which conducting wires with a width of 100 nm have been written. The enhanced conductance of the written wires persisted for more than 24 months in ambient conditions. Moreover, these created conducting features can be reset by thermal annealing to 300 °C [107].

This electric field-induced creation of anti-Frenkel defect offers a minimally invasive and non-volatile conductivity control with nanoscale spatial precision. Unlike conventional methods that accumulate/deplete charged particles, this technique allows for site-specific manipulation without changing the overall stoichiometry. It holds great potential for integrating multiple domain walls into circuits in domain wall-based nanoelectronics. In this work, the creation of anti-Frenkel defects will continue to be utilized, with an emphasis on exploring their potential functionalities beyond just writing conducting wires. These expanded applications and possibilities will be elaborated in Chapter 4.

3. Nanoscale characterizations

This chapter introduces the different characterization and nanostructuring tools used in this work, including SEM (scanning electron microscopy), FIB (focused ion beam microscopy), and SPM (scanning probe microscopy). Each part starts with the working principle, the system setup of the corresponding tool, and its application in ferroelectrics.

3.1. Scanning electron microscope (SEM)

The scanning electron microscope (SEM) is an instrument that generates magnified images of the sample surface by directing a focused electron beam onto a specific location on the specimen, subsequently collecting the outgoing electron signals. These outgoing electron signals provide rich information about sample topography, compositional microstructure, crystalline orientation, electrical properties, etc. Modern SEM has evolved into an extraordinarily flexible tool, capable of imaging a diverse range of samples, from metals over semiconductors to insulators, with dimensions spanning from millimeters to nanometers. Furthermore, SEM is compatible with other task-oriented systems, such as piezo-actuated micro-robots (Mibots by Imina Technologies) for highly localized site-specific electrical measurements [121].

This section starts with a description of the SEM column where the incident electron beam is formed, followed by an explanation of electron-sample interactions that create the outgoing signal. Following this, the SEM detectors, some common artifacts in SEM imaging, and the SEM imaging mechanisms for ferroelectric materials are presented.

The theory described here is mainly based on the books by Goldstein[122] , Reimer [123], and Hamid [124] unless otherwise specified.

3.1.1. Instruments

In SEM, the electron beam is generated from an electron source at an accelerated energy E_0, and a beam current I_b. As illustrated in Figure 3-1, the electron beam passes through a series of electromagnetic lenses and apertures, which focus it into a fine point on the sample surface. As the incident electron beam strikes the sample surface, different electron-sample interactions occur, emitting various signals. Some of the signals are collected by detectors and eventually visualized on a monitor. During SEM imaging, the incident electron beam is raster-scanned across the sample surface area with the assistance of electromagnetic scanning coils. Signals are collected from each pixel, thereby assembling a visual representation of the scanned area. The brightness at each pixel is directly proportional to the number of captured signal electrons from the corresponding position on the sample, resulting in an image that is essentially a convolution effect of the sample response and the SEM column system.

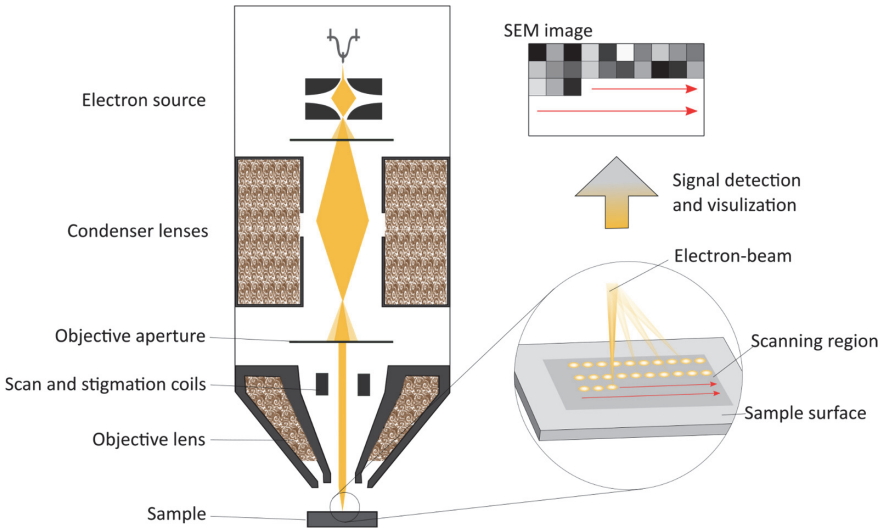

Figure 3-1. Illustration of an SEM column and SEM image formation. Left column from top to bottom: The electron beam is generated by the electron source, then focused by lenses and apertures, and precisely controlled by the scan coils. Right column from bottom to top: Scan coils deflect the electron beam to scan point by point across the scanning region in a controlled raster pattern. The signals generated from discrete locations of the scanning region are collected and synchronously displayed on corresponding pixels of the SEM image. The brightness of each pixel in the SEM image is proportional to the intensity or number of signals captured from each respective location. Inspired by references [123,125].

3.1.1.1. Electron source

The Electron source is located at the top of the SEM column, providing a stable electron beam, ideally with high brightness, small probe size, and small energy spread.

Energetic electrons emitted from an electron source impart sufficient energy to the material's electrons, enabling them to overcome the potential energy barrier that prevents them from escaping from the material's surface. Depending on the electron emission modality, the electron sources are categorized into three types: thermionic emission source, field emission source, and Schottky emission source. The mechanism underlying these emission processes is illustrated in Figure 3-2.

Thermionic emission sources generate electrons by thermionic excitation. As shown in the schematic diagram in Figure 3-2a, the V-shaped filament (tip diameter 100 μm) is resistively heated to a very high temperature (2500 °C) by a high-voltage supply. This heating process ensures that electrons at the tip receive sufficient thermal energy to overcome the barrier φ, as illustrated by the red line in Figure 3-2d. The filament is negatively biased, and the anode is grounded, thereby creating an electric field between the filament and the anode to extract and accelerate the electrons toward the anode. A slightly negative potential between the Wehnelt cup and the filament focuses the electrons only emitted from the filament tip area with a divergence angle α_0. Traditionally, tungsten was the most common filament material in thermionic emission sources due to its high melting temperature, ease of replacement, and low

vacuum requirement ($\sim 10^{-3}$ Pa). However, because of its high work function (4.5 eV), large energy spread, and low brightness, other filament materials, such as Cerium hexaboride (CeB_6) crystal and LaB_6 crystal [124], have also been explored. Despite the improvement, thermionic emission sources are still not suited for low voltage (≤ 5kV) applications, due to their inherently low gun brightness at low electron energy.

Field emission sources are usually referred to as field emission electron guns (FEG) and rely on the quantum mechanical tunneling effect at room temperature. As illustrated in Figure 3-2b, single crystal tungsten (W) wire with a very sharp tip is used. Dut to the small radius of the tip ($r \approx 0.1\ \mu m$), field emission occurs around the tip region when the electric field strength ($|\vec{E}| \approx \frac{U_1}{r}$) is large enough (~$10^7$ V/cm), where U_1 represents the potential difference between the cathode tip and the first anode. Such a high electric field narrows the width ω of the potential barrier, enabling electrons from the Fermi level E_F to penetrate the barrier by tunneling effect, as shown by the blue curve in Figure 3-2d. In contrast to the thermionic emission source setup, FEG uses two anodes. The potential difference U_1 between the first anode and the tip (a few kV) is used to extract the electrons from the tip, while the second anode accelerates the electrons to the final kinetic energy. The capacity to focus electron emission into a small region around the sharp tip results in height brightness and small beam size in FEG. This simplifies the focus procedure, requiring only one demagnified lens to achieve a probe size below 1 nm. Additionally, FEG operates at room temperature without heating up the metal, commonly referred to as cold field emission guns (CFEG), minimizing the energy spread. These features render FEG an ideal tool for high-resolution applications. However, challenges arise concerning its temporal stability. The accumulation of contaminations at the W tip, resulting from the adsorption of column gases at room temperature and charged molecules propelled by the large electric field, leads to unstable or fluctuating current and decreased emission over time. Therefore, the FEG source must be kept in an ultra-high vacuum environment (10^{-7} to 10^{-9} Pa) to ensure the emitter tip remains extremely clean. This makes the FEG source considerably more expensive and necessitates time-consuming service maintenance.

Schottky emission source is a hybrid of a thermionic and field emission source. It is essentially a field-assisted thermionic emission source, in which the electric field is used to reduce the work function but is not sufficient for the tunneling effect. Electrons overcome the potential barrier through thermal energy, as indicated by the yellow curve in the middle of Figure 3-2d. As illustrated in Figure 3-2c, the Schottky emitter is made of ZrO-coated tungsten wire welded to tungsten filament. The ZrO coating reduces the work function (from 4.5 eV to 2.7 eV[123,124]), lowering the potential required for emission. The wire tip has a radius of $r \approx 0.1 - 1\ \mu m$ [123]. The electric field ($|\vec{E}| \approx \frac{U_1}{r}$) at the cathode is strongly increased (~10^6 V/cm), resulting in a reduction of barrier height $\Delta\varphi \approx 0.4$ eV [123] (Figure 3-2d). The electric field is much higher than

for a thermionic cathode but is still ten times lower than in FEG. Additionally, the cathode is resistively heated by the applied electric field to a high temperature (1500 °C) to initiate electron emission.

As a combination of thermionic and field emission sources, the Schottky emission source strikes a good balance between brightness, energy spread, and temporal stability. Unlike the FEG described above, a Schottky emission source operates without the need for ultra-high vacuum conditions, simplifying the maintenance. These advantages make the Schottky emission source a popular choice in many advanced SEM systems. The SEM instrument used in this work is Thermo Fisher Scientific G4UX Dual-beam FIB-SEM, equipped with Schottky field emission source, allowing accelerating voltage ranges from 350 V to 30 kV and beam current ranges from 0.8 pA to 100 nA, ensuring stable, high-resolution analysis across a broad range of samples.

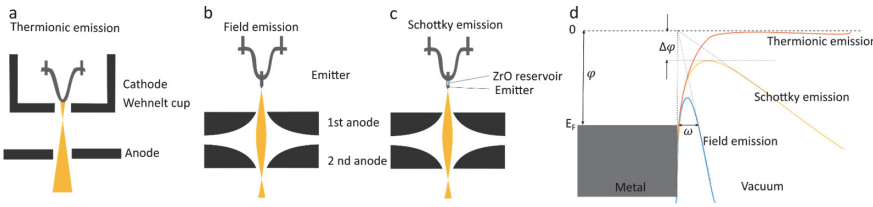

Figure 3-2. (a) Schematic of thermionic emission electron source. (b) Field emission source. (c) Schottky emission source. (d) Potential barrier (φ) that electrons need to overcome to escape the metal surface for different types of electron sources, adapted from reference [123] *with permission.*

3.1.1.2. Lenses

After being emitted from the source, the electron beam passes through the electron optical system, which shapes it into a fine-focused electron probe that scans the region of interest (ROI) on the sample surface. The final beam size at the sample surface is critical for the resolution of SEM imaging and analysis. Therefore, how the optical system focuses and demagnifies the electron beam directly affects the resolution of the image. In SEM, electromagnetic lenses are utilized to adjust the trajectories of the electrons.

Electromagnetic lenses are typically comprised of Cu coils enclosed in an iron casing with cylindrical pole pieces, as sketched in Figure 3-3. When a current is running through the coil, the magnetic flux of the coil is concentrated within a small volume between the polepieces, generating a magnetic field with rotational symmetry at the gap. Consequently, electrons travel along screw trajectories due to the Lorentz force. The electrons away from the optic axis are deflected towards the axis by the axial field component, creating a focusing effect. The degree of focus can be controlled by the current in the coil. Depending on their different purpose, different lens geometries can be used.

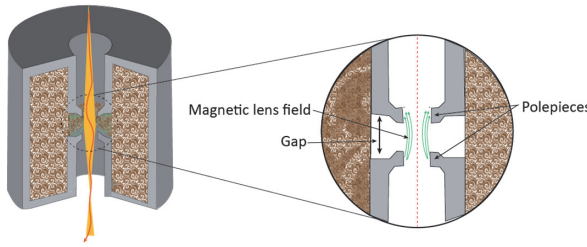

Figure 3-3. Schematic of electromagnetic lens used in SEM column. Adapted from reference [124] *with permission.*

3.1.1.3. Condenser lenses

Condenser lenses are designed to "condense" or converge the electron beam into a relatively parallel beam, directing it through a focal point. The condenser lens is mounted below the electron gun, with the arrangement and number of condenser lenses varying depending on the microscopy and the required extent of demagnification. By increasing the current of the coil, the electrons are focused closer to the center of the lens. Following that, an aperture is utilized to block the off-axis electrons, such that the beam proceeds to the next lens with a smaller probe size and current.

3.1.1.4. Objective lens

The objective lens is the final lens in the column and is used to focus the electron beam into a probe point on the sample surface. There are several types of objective lenses, each with its unique features and applications.

Pinhole Lens is the most commonly utilized one and is also referred to as the conventional or outer-lens objective lens. In this design, the magnetic field of the lens is confined within the polepiece and does not extend to the sample surface. This makes the Pinhole Lens suitable for imaging samples with large dimensions at large working distances with relatively low magnifications. It is versatile enough to characterize various samples, including magnetic ones.

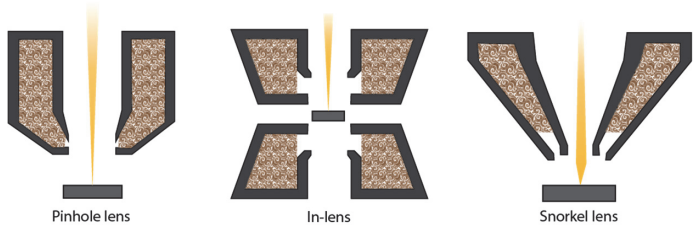

Figure 3-4. Illustration of different objective lenses. Adapted from reference [124] *with permission.*

In-lens is designed to place the specimen within the bore of the lens, allowing the lens magnetic field to engulf the sample. This configuration results in a small focal length, which significantly

reduces lens aberrations and provides the highest image resolution. However, this design considerably restricts the geometry between the specimen and the detector.

Snorkel lens combines the benefits of both types of lenses mentioned above. In this design, the specimen is positioned directly below the objective lens, and the magnetic field of the lens extends to the sample surface. This configuration enables high-resolution imaging for larger specimens, making it widely used in modern SEM. Throughout this work, we will refer to this as the immersion lens.

3.1.1.5. Lens aberrations

Lens aberrations refer to the distortions or imperfections in the image caused by the limitations of the lens system. In the optical system of the SEM, the aberrations can hinder the ability of lenses to focus the electron beam into a fine probe, thus limiting the imaging resolutions and quality.

Spherical aberration: Electrons far away from the optical axis are bent by the lens more strongly than those closer to the axis, leading the electron beam to converge into a disc rather than a point and subsequently causing image blur. Spherical aberration can be controlled by introducing a small aperture to remove the off-axis electrons, or using a short working distance.

Chromatic aberration occurs due to the energy spread ΔE of the electron beam E_0. Electrons of different energies are focused to different focal lengths, causing the electrons to converge in the form of a disc instead of a point. To reduce chromatic aberration and enhance the image resolution, one can use a source with a small energy spread

Diffraction error: Electron diffraction occurs at the edge of the small aperture, forming a diffraction pattern whose highest intensity is found at the optical axis. This diffraction error broadens the electron beam. Reducing the diffraction error can be achieved by increasing the convergence angle. However, this would increase the spherical aberration and chromatic aberration.

Astigmatism: Due to the imperfection of the lens, the electron beam is focused into a cylinder symmetry instead of a spherical symmetry, inducing the beam to be focused more in one direction than the other. This causes image distortion, making certain features appear stretched or blurred. Astigmatism is usually corrected using a stigmata consisting of an electromagnetic octupole lens within the objective lens.

3.1.2. Electron-sample interactions

When the incident electron beam, referred to as primary electrons (PE), focuses on the sample surface, it generates various signals that carry sample-related information. This section begins by describing the inelastic and elastic scatterings between the PE and sample. Following this, the secondary electrons (SE) and backscattered electrons (BSE) will be described in detail, with

a particular focus on the SE signals due to their significant relevance to the SEM results in this work. Furthermore, the discussion will include how these signals are influenced by variables such as the incident beam energy and material atomic numbers. Additionally, some image defects related to the results of this work will be discussed.

3.1.2.1. Inelastic scattering and elastic scattering

The interaction between PE and the sample can be collectively referred to as "scattering events", which can be categorized into inelastic and elastic scattering.

Inelastic scattering includes various physical processes wherein beam electrons interact with the weakly bound out-shell atomic electrons or tightly bound inner-shell atomic electrons, transferring beam energy to the specimen atoms. These processes include the emission of SE, characteristic X-rays, plasmons, and phonons. The energy loss in inelastic scatterings restricts the distance to which the beam electrons can travel within the sample before losing all their energy and being absorbed. Bethe [122] approached these energy loss processes through a continuous-slowing-down approximation, describing the rate of energy loss (incremental dE, measured in eV) with traveled distance (incremental ds, measured in nm) as [122]:

$$\mathrm{dE/ds(eV/nm)} = -\,7.8\,(\mathrm{Z}\rho/\mathrm{AE})\ln\,(1.166\,\mathrm{E/J}), \qquad \text{Equation 3-1}$$

where E is the beam energy (keV), Z is the atomic number, ρ is the density $(\mathrm{g/mol})$, and J is the mean ionization potential given by

$$\mathrm{J(keV)} = (9.76\,\mathrm{Z} + 58.5\,\mathrm{Z}^{-0.19}) \times 10^{-3} \qquad \text{Equation 3-2}$$

The maximum length that beam electrons traveled within the sample, termed the Bethe range $\mathrm{R_B}$, is derived by integrating over the range of energy from the incident energy down to a cut-off energy E [28,122]:

$$\mathrm{R_B} = \int_{\mathrm{E_{min}}}^{\mathrm{E_0}} \left(\frac{1}{-\mathrm{dE/ds}}\right) \mathrm{dE} \qquad \text{Equation 3-3}$$

It is important to note that the Bethe range $\mathrm{R_B}$ here represents the maximum distance that a beam electron can travel within the sample. This distance is measured along the complex trajectory of the electron and differs from the penetration depth, which will be discussed later.

Elastic scattering occurs when the beam electron is deflected by the nucleus of the sample, resulting in the electron deviating from its initial path onto a new trajectory. The elastic scattering is a complicate process. For instance, the scattering angle can vary in a broad range, from a few degrees to 180°; the landing point of the deflected electrons can happen in a 3D area; and more scattering steps can happen and deviate the electron to a new direction[126]. So, the individual trajectories can be significantly different, and calculating or simulating a small number of trajectories can not provide an adequate view of the interactions.

3.1.2.2. Interaction volume and imaging signals

Form a practical perspective, when the incident electron beam (PE) strikes the sample surface, elastic and inelastic scattering usually occur concurrently, further complicating the interaction. Moreover, a substantial number of beam electrons are involved during imaging, depending on the specific imaging parameters. These factors indicate that individual trajectories are unimportant [28]. Therefore, discussions typically focus on the electron interaction volume, which is the region where beam electrons travel and deposit energy within the sample. The Monte Carlo electron trajectory simulation [127] is a statistical method that can be used to calculate the numerical properties of the interaction volume and related processes.

While the Bethe range [122] gives the maximum length that a beam electron can travel within the sample, Kananya and Okayama [128] proposed a model to describe the interaction volume as a hemisphere centered at the beam impact point. Considering both inelastic and elastic scattering, the radius of this volume corresponds to the maximum PE penetration depth, with at least 95% of the trajectories contained within this region[126]. The radius can be calculated as [28,124]:

$$R_{KO} = \frac{0.0276\, A E_0^{1.67}}{\rho Z^{0.89}}, \qquad \text{Equation 3-4}$$

where A is the atomic mass, E_0 is the incident beam energy, and ρ is the density.

The Kananya-Okayama range, R_{KO}, provides penetration depth information to describe the spatial distribution of the signals produced within the interaction volume. As illustrated in Figure 3-5, indicated by the black arrow. Table 3.1 presents the Kananya-Okayama range R_{KO} of some elements under different beam energies, calculated by the Monte Carlo simulation, with data adopted from ref. [126]. It is consistent with Equation 3-4 that as the atomic number of the target material increases, its penetration depth decreases. Conversely, when the incident beam energy increases, the penetration depth increases.

In terms of SEM imaging, Secondary electrons (SE) and backscattered electrons (BSE) are the most important signals. Secondary electrons (SE) are ejected weakly bound outer-shell electrons from the sample atom generated by inelastic scattering events, which occur along the complete trajectories of beam electrons. In contrast, backscattered electrons (BSE) are deflected beam electrons resulting from elastic scattering interactions with the nuclei of the sample atoms, typically with negligible energy loss.

R_{KO} gives the information of the penetration depth of the beam electrons, only those generated within a certain escape depth and with sufficient energy can escape and be detected. An SEM image is essentially an intensity map of the inspected area, where a brighter shade indicates a higher level of electron emission. The distinct origins of SE and BSE result in their different kinetic energies, defining their respective escape depths. Figure 3-5 illustrates the

electron-sample interaction, showing the generation and escaping of SE and BSE signals. Due to their extremely low kinetic energy, SEs can only escape from a shallow depth t_{SE}, whereas BSE signals travel a significant fraction of the Kaneya-Okayama depth R_{KO} within the sample before escaping. The content here provides a general overview, and a detailed description of SE and BSE will be presented in the following sections.

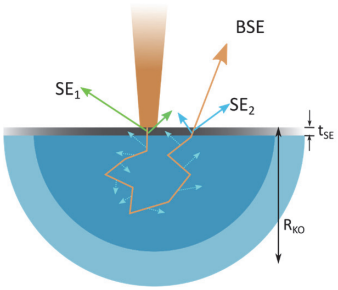

Table 3-1 Kanaya-Okayama range (R_{KO})

	5 keV	10 keV	20 keV	30 keV
C	450 nm	1.4 μm	4.5 μm	8.9 μm
Al	413 nm	1.3 μm	4.2 μm	8.2 μm
Fe	159 nm	505 nm	1.6 μm	3.2 μm
Ag	135 nm	431 nm	1.4 μm	2.7 μm
Au	85 nm	270 nm	860 nm	1.7 μm

Figure 3-5 Illustration of the interaction volume. R_{KO} represents the Kananya-Okayama range, defining the radius of the interaction volume hemisphere. t_{SE} denotes the maximum escape depth of SE. SEs are ejected weakly bound outer-shell electrons and are emitted along the entire trajectories of beam electrons, but only those within the escape depth (t_{SE}) can exit the sample surface. BSEs are deflected incident beam electrons, with their escape depth being a fraction of the Kaneya-Okayama depth (R_{KO}). Table 3-1 adapted from reference [126] *with permission.*

3.1.2.3. Backscattered electrons (BSE)

Backscattered electrons (BSE) refer to a fraction of the incident beam electrons that are elastically scattered and deflected by the nuclei through large angles and eventually find their way out of the sample. BSE usually possesses a broad energy range (50 keV <E ≤E_0). The surface of their entry and departure may or may not be the same.

In terms of escaping depth, BSEs travel a significant fraction of the Kaneya-Okayama depth R_{KO} (Table 3.1) within the sample, approximately 15% (high Z material) to 30% (low Z). Materials with higher atomic numbers tend to travel a smaller fraction of R_{KO} depth, and those with lower atomic numbers travel larger fractions. Consequently, BSE can emerge from depths of up to several micrometers within the sample.

The emission of BSE is quantified with the backscattered electron coefficient (η), which represents the number of BSE generated per incident PE. The BSE coefficient (η) exhibits a monotonic dependence on the atomic number Z of the material when the incident bean energy is above 5 keV. This correlation is critical for providing compositional contrast in BSE images, with materials of higher atomic number tending to show a higher BSE coefficient (η). For the incident energy above 5 keV, η varies little with the incident beam energy E_0[122,123]. In addition, η is also influenced by the incident angle, displaying a distinctive angular distribution that varies with the incident angle. For more detailed information on the BSE coefficient variation, readers are referred to references [122,123].

3.1.2.4. Secondary electrons (SE)

Secondary electrons (SE) are ejected weakly bound out-shell electrons due to inelastic scattering. As previously mentioned, SEs are generated along the whole trajectory of the PEs within the sample (R_B, Equation 3-3). However, only a small fraction of SEs generated near the surface with adequate kinetic energy can overcome the surface energy barrier and escape. This class of SE is commonly referred to as SE_1, which preserves the lateral spatial resolution information provided by the incident beam and is highly sensitive to the characteristics of the surface and near-surface region. Meanwhile, as the BSEs move towards the surface, they also excite SEs, termed SE_2. The energy and angular distribution between SE_1 and SE_2 are nearly indistinguishable. However, SE_2 carries the lateral spatial distribution of the BSE due to its origin. In addition, the third class, SE_3, is generated when the BSEs hit other metallic surfaces within the chamber, such as the objective polepiece and chamber wall. These SE_3, therefore, cannot convey the inherent properties of the sample and contribute to the noise in the image.

Escape depth of SE

The most important characteristic of SEs is their extremely low kinetic energy, conventionally, defined as emitted electrons with kinetic energy between 0-50 eV. For instance, a study on a copper target using 1 keV incident beam revealed that 90% of the SEs emitted from copper possess energies less than 8.4 eV [129]. This energy distribution is generally representative of many metals and other materials[126,130]. SEs that are generated away from the surface cannot escape the sample due to insufficient kinetic energy required for propagating through the solid and surpassing the surface energy barrier. This suggests that the escape depth of the SE is very shallow.

According to the Reimer et al.[123], the probability of a SE escaping from a depth z beneath the surface is described by:

$$p(z) = 0.5 \exp\left(-\frac{z}{t_{SE}}\right) \qquad \text{Equation 3-5}$$

with p being the escape probability, z denoting the depth below the surface where the SE is emitted, and t_{SE} being the depth that SEs can escape.

The escape depth of SE depends on the type of materials. It is about 0.5-1.5 nm for metals, 10-20 nm for insulators, and 1-30 nm for metal oxides and alkali halides[123]. This shallow depth is the reason that SEs are considered to constitute the most appropriate signal for the surface topography.

SE yield (δ) varies with incident beam energy E and atomic number Z

For the SE yield (δ) as a function of incident beam energy E, a general trend is observed for all materials, as shown by the curve in Figure 3-6*Figure 3-6 Universal curve*. The SE yield (δ) increases from 0 to a maximum value δ_m at an incident beam energy E_m, and subsequently

decreases with increasing E [130]. This is the so-called 'universal law for SE yield'. Lin et al.[131] describe this relationship using the ratio $\frac{\delta}{\delta_m}$ as a function of $\frac{E}{E_m}$:

$$\frac{\delta}{\delta_m} = 1.28\left(\frac{E}{E_m}\right)^{-0.67}\left(1-\exp\left(-1.614\left(-\frac{E}{E_m}\right)^{1.67}\right)\right), \qquad \text{Equation 3-6}$$

here E_m represents the incident beam energy corresponding to the maximum SE yield δ_m, such that $\delta(E_m) = \delta_m$. The value of E_m depends on the material and its surface conditions.

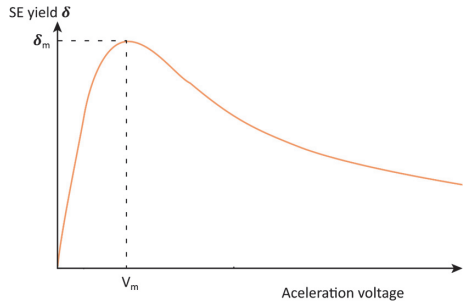

Figure 3-6 Universal curve for SE yield (δ) as described by Equation 3-6. With increasing beam energy, δ increases from 0 to its maximum δ_m, and then monotonically decreases. Adapted from reference [131] *with permission.*

The correlation between the SE yield (δ) and the atomic number (Z) of the target material has been a topic of study already for around 90 years[132]. However, a comprehensive review of SE yield (δ) profiles for incident electron energies up to 50 keV, was conducted by Joy et al.[133], reveals significant discrepancies in data published over 80 years from more than 100 different groups. The data recorded under ultrahigh-vacuum conditions from clean sample surfaces differ significantly from those under typical SEM environments. These findings suggest that the SE yield (δ) is highly sensitive to surface conditions such as oxidation, contamination, and roughness, leading to additional variation from sample to sample and potentially also over time.

SE yield (**δ**) varies with the incident angle

Incident angle θ is defined as the angle between the incident beam and the surface normal. When the beam is perpendicular to the surface, $\theta = 0°$. As the incident angle θ increases, the SE yield (δ) increases accordingly. The correlation between the SE yield (δ) and the tilt angle θ can be written as [124]:

$$\delta(\theta) = \delta_0 \sec\theta \qquad \text{Equation 3-7}$$

where δ_0 is the SE yield (δ) at zero tilting.

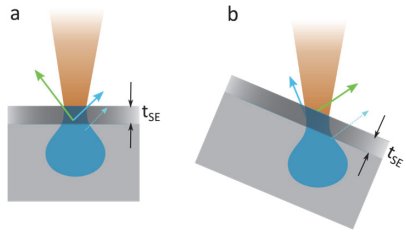

Figure 3-7. Illustration of the SE yield (δ) increase with sample tilting (increase in incident angle). (a) θ=0°. (b) $\theta > 0°$. A larger fraction of interaction volume being within escape length causes higher δ. Inspired by references [28,124].

This increase in SE yield (δ) can be understood from the geometric change, as illustrated in Figure 3-7a and b. A larger fraction of the interaction volume is closer to the surface, increasing the escape possibility. Moreover, since the BSE coefficient (η) increases with tilt, SE2 generated due to backscattering also boosts. This monotonic dependence of the SE yield (δ) on the tilting angle θ is the basis of the topographic contrast of SEs. However, when the energy beam is reduced significantly, all the SEs generated within the escape depth t_{SE}, and the incident angle no longer increases the SE yield (δ).

3.1.2.5. Electron-sample interactions in low beam energy SEM

Low beam energy SEM involves imaging samples at beam energy $E_0 \leq 5$ keV. It is particularly important for imaging insulating materials and semiconductors due to the reduced charging effect (see section 3.1.2.6). In this low-energy regime, the electron-sample interaction is markedly different from that in higher-energy settings[134], resulting in different interaction volumes, signal yields, and surface resolution.

According to Equation 3-4, within the low beam energy range, the electron penetration depth Kananya-Okayama range, R_{KO}, is rapidly reduced. This reduction strongly influences the SE yield (δ), as it increases the fraction of energy loss near the surface. Although BSE are still generated, their occurrence is much less than SE. Furthermore, as the incident beam energy is lowered, the lateral distribution of the SEs (SE2 and SE3) signals associated with BSE converges with the SE1 distribution, which is restricted to the beam footprint. Therefore, at sufficiently low beam energy, all of these signals carry high spatial resolution information similar to the SE1, providing more detailed surface morphology and enhancing sensitivity to surface chemistry. Morden high-performance SEMs equipped with high brightness sources, such as FEG or Schottky emission source, have made low beam energy SEM a popular choice for achieving high-resolution imaging. This technique is also predominantly used in my work.

3.1.2.6. Artifacts during imaging

SEM imaging is a powerful tool for investigating sample information based on the electron-material interaction described above. However, during imaging, the interaction between the electrons and sample is frequently influenced by several artifacts that interfere

with data analysis and interpretations, including charging, radiation damage [124], surface contamination, moiré fringe [135], and others. Charging is inevitable when imaging semiconductors or insulators. In addition, surface contamination has also been observed in this work (section 4.3.2). This section delves into the origins of these two types of artifacts and discusses methods of minimizing their impacts.

Charging

Due to the interaction between the incident electron beam and the sample, BSEs and SEs are emitted from the sample. Conceptually, the specimen can be likened to an electrical junction, where the beam current (I_B) flows in and the emitted BSE and SEs current flow out (I_{BSE} and I_{SE}). The remaining current (I_{sample}) must flow from the sample to the ground to avoid charge accumulation. This process can be written as:

$$\sum \mathrm{I_{in}} = \sum \mathrm{I_{out}} \qquad \text{Equation 3-8}$$

$$\mathrm{I_B} = \mathrm{I_{BSE}} + \mathrm{I_{SE}} + \mathrm{I_{sample}} \qquad \text{Equation 3-9}$$

The total electron yields can be written as a function of beam energy: $\sigma(\mathrm{E}) = \delta(\mathrm{E}) + \eta(\mathrm{E})$

The emitted current can be written in terms of beam current so that:

$$\mathrm{I_B} = \sigma(\mathrm{E})\mathrm{I_B} + \mathrm{I_{sample}} = \delta(\mathrm{E})\mathrm{I_B} + \eta(\mathrm{E})\mathrm{I_B} + \mathrm{I_{sample}} \qquad \text{Equation 3-10}$$

However, if the sample is not sufficiently conductive, such as semiconductors and insulating samples, $\mathrm{I_{sample}}$ cannot effectively flow to the ground. This causes electron accumulation and a consequent local increase in potential, leading to the phenomenon known as 'charging effect'. Such a charging phenomenon has been observed to be able to modify the imaging result of SEs [136], given that SEs are emitted at a lower kinetic energy and can be strongly influenced by the local potential difference. Meanwhile, the BSE yield $\eta(\mathrm{E})$ shows minor variation with E. Therefore, the conceptual charging analysis can be built on the same shape as the universal SE curve. The electron emission is a function of beam energy, as shown in Figure 3-8. For many insulating materials, the total electron emission $\sigma(\mathrm{E})$ can be higher than 1 (with δ_m values ranging from 2 to 20 based on the material [126]). This suggests that the number of emitted electrons surpasses the number of incident electrons. At two crossover energies $\mathrm{E_1}$ and $\mathrm{E_2}$, the total electron emission is equal to 1 ($\sigma = 1$). At these two points, the charges injected by the incident electrons are just balanced by the charges leaving as BSE and SEs. No charging occurs. If the beam energy is either less than $\mathrm{E_1}$ ($\mathrm{E} < \mathrm{E_1}$) or larger than $\mathrm{E_2}$ ($\mathrm{E} > \mathrm{E_2}$), the yield is less than 1 ($\sigma < 1$). This indicates that fewer electrons are emitted than those injected into the sample, leading to the accumulation of negative charges. Conversely, when the beam energy lies between $\mathrm{E_1}$ and $\mathrm{E_2}$ ($\mathrm{E_1} < \mathrm{E} < \mathrm{E_2}$), the yield exceeds 1 ($\sigma > 1$), resulting in positive charging.

To ideally image semiconductors and insulators, acceleration voltage close to V_1 and V_2, which corresponds to incident beam energy E_1 ($E_1 = qV_1$)and E_2 ($E_2 = qV_2$), are recommended. V_1 can be as low as about 200 V [130], which might compromise image quality, making V_2 a more practical choice. Table 3-3 lists some typical values of V_2. The voltage around V_2 enables a dynamic charging stabilization process, facilitating effective imaging on semiconductors and insulators without additional surface treatment.

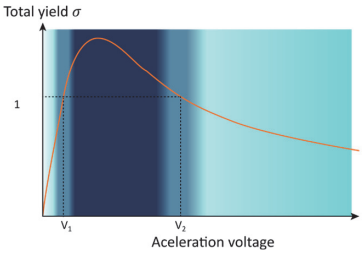

Table 3-3 Examples of V_2 values (V) for some materials

SiO_2	GaAs	NaCl	Pyrex	Teflon	PMMA	PE	Kapton
3.0	2.6	2.0	1.9	1.8	1.6	1.5	0.4

Figure 3-8. Schematic representation of the SE yield as a function of acceleration voltages during SEM imaging. V_1 and V_2 denote the two equilibrium points where the yield equals 1. For $V<V_1$ and $V>V_2$, the sample is negatively charged and appears bright. Conversely, for $V_1<V<V_2$, the sample is positively charged and appears dark. Both the figure and the table are adapted from reference [28].

In order to image an insulating sample or semiconductor sample with a minimized charging effect, several strategies can be used:

(1) Selection of appropriate imaging parameters.

When the electron beam scans a surface area, each scan point essentially acts as a local capacitor. Charging accumulates when the beam is placed there and partially decays as the beam moves to the next point[28,126]. Consequently, the charging dynamics are influenced by the scanning strategy (such as scan speed and size) and the beam conditions (beam energy and current). Therefore, the charging effect can be modulated based on these imaging parameters. Generally, utilizing a beam voltage around the charging balance points (V2), along with a lower current and faster scanning speed, helps reduce the charging effect. This is the main strategy utilized in this work.

(2) Coating the sample with a thin conductive layer.

This method is commonly used. One important aspect is that the conductive coating layer must be connected to an electrical ground, ensuring a charge dissipation path. A limitation of this approach is that the surface details and some surface-sensitive contrast might be lost after coating. Removal of this layer typically requires polishing. This approach has been used in this work in lamella fabrication in section 5.1.

Surface contamination

Surface contamination in SEM imaging refers to a variety of phenomena where unintended foreign materials, typically hydrocarbon, are deposited on the sample surface during SEM

imaging. A typical observation of contamination occurs when an area is first imaged at high magnification with a slow scan, and subsequently zoomed out for a broader view at lower magnification. The result is a discernible rectangular imprint on the lower magnification image, marking the area initially scanned at high magnification. Two examples are provided in Figure *3-9*, which displays two SEM images of the $ErMnO_3$ sample surface. Figure 3-9a is the typically observed rectangular imprint described above. Figure 3-9b presents a more extreme example, wherein the surface on the left part was scanned by 20 keV electron beam with 20 nA current (large beam diameter) during EBSD (electron backscatter diffraction) measurement.

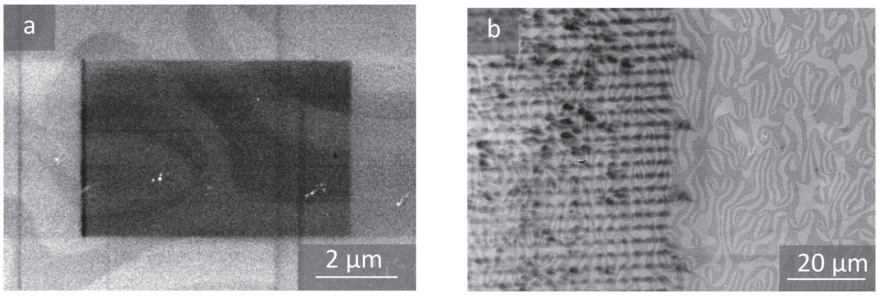

Figure 3-9. Examples of surface contamination in SEM images. (a) Typical rectangular scan imprint. (b) The left part of the image was scanned by an electron beam with a large diameter (acceleration voltage: 20 kV, current: 20 nA, distance 15 mm).

This black contamination layer is usually ascribed as a deposited carbon layer, which forms when the electron beam interacts with hydrocarbon residues in the system. Under the bombard of the electron beam, hydrocarbon molecules may break down into gaseous components, leaving behind the nonvolatile carbon[126]. Potential sources of the hydrocarbon include the sample itself, outgassing components in the chamber, and the pumping system of SEM[137].

The presence of contamination can modify the SE coefficient, obscure the surface details, compromise the image quality, or even distort the feature size[138]. However, it is difficult to eliminate contamination entirely. There are some strategies to reduce the contamination, basically based on maintaining clean instruments and clean samples. Furthermore, controlling the electron dosage for the region of interest during imaging and implementing in-chamber plasma cleaning in the SEM before pumping down are practical approaches for reducing contamination[139]. For heavily contaminated samples, plasma cleaning has been acknowledged as an efficacious remediation method in both this work and earlier studies [138]. However, one must proceed cautiously: plasma cleaning can induce undesirable influence on certain samples. For instance, samples sensitive to oxygen should not be exposed to oxygen plasma. Instead, argon plasma can be a suitable alternative.

3.1.3. Detection, imaging, and analysis

Incident electrons interact with the sample, generating signals like SEs and BSEs. This section introduces the detectors used for capturing SEs and the contrast formation mechanisms specific to the ferroelectric domain and domain walls in SEM images.

3.1.3.1. Detectors

The SEM chamber is furnished with multiple detectors to capture the emitted electron signals. Depending on the kinetic energy response and the position of the detector, they can be sensitive to SEs, BSE, or both. Most BSEs possess high enough kinetic energy to be directly detected by semiconductor and scintillation detectors. In contrast, most SEs exit the sample with energy below 10 eV, necessitating additional acceleration for their detecting. This energy differential also dictates distinct collection methods for SEs and BSE. SEs are electrostatically gathered from different angles using a bias voltage, whereas the location of the BSE detector directly affects its collecting efficiency. As the images from this work all utilize SEs signals, only the SEs detectors will be introduced below.

Everhart-Thornley Detector (ETD)

Everhart-Thornley Detector (ETD) is the most frequently used detector in SEM. It is named after the designers T. E. Everhart and R. F. M. Thornley.[140], primarily designed for detecting SEs and mounted on the side of the chamber.

This detector consists of three main components: the collector grid (Faraday cage) in the chamber, collecting electrons; the scintillator, converting the electron signal into photons; and the photomultiplier tube (PMT) outside the SEM chamber, converting photons back to electrons and amplifying the number of electrons. Figure 3-10 provides an illustration of an ETD detector positioned on one side of the sample.

The collector grid is a metal wire mesh that covers the face of the detector. It is known as the Faraday cage, isolating the SEM chamber from the strong electric field emanating from the Scintillator within the detector. Meanwhile, a bias voltage in the range of -50 V to +250 V is applied to attract electron signals through the grid to the scintillator surface. The scintillator, made of phosphorescent material, is responsible for converting electron energy into photons. A high positive voltage (+10-12 kV) is applied in the vicinity of the scintillator to accelerate the collected secondary electrons towards the scintillator, ensuring the electrons possess enough energy to produce a multitude of photons. The photons then subsequently travel through a light pipe to the PMT, which amplifies the photons into a detectable electron signal. The amplified electron signals are finally directed to image processing.

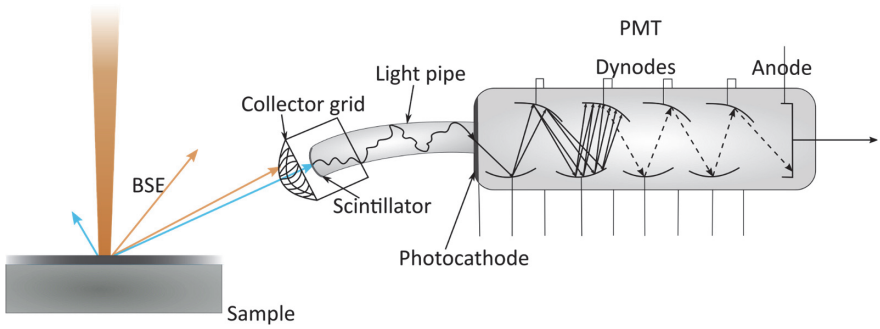

Figure 3-10 Illustration of the ETD detector mounted on the side of the sample inside the SEM chamber.

Adjusting the bias voltage of the collector can modulate the signal captured by the ETD. A positive voltage setting collects all SEs alongside a small fraction of BSEs. At neutral or slightly negative voltage, all SEs are rejected, and only those BSEs that are emitted within the detection range are captured. Although ETD is also able to detect BSE signals, the signal is rather weak due to its asymmetrical position. However, for SE imaging, this unique placement enhances the topographic contrast based on the feature position relative to the detector.

Through-the-lens detector (TLD)

TLD, also known as ILD (In-lens detector) and TTL (Through-the-lens), is an ETD-type detector placed above the objective lens at a slight off-axis distance inside the SEM column, providing high-resolution SE imaging. This TLD type of detector is used in microscopes equipped with In-lenses or Snorkel objective lenses, which project a magnetic field into the sample chamber. Our instrument uses the Snorkel objective lens. SE_1, and SE_2 are collected and spiraled up by the magnetic field through the lens and subsequently captured by the TLD detector. In contrast, low-resolution signal SE_3 can effectively be filtered out since it originates far from the optic axis. Moreover, by combining electric field and magnetic field, the majority of high-energy BSE can be filtered out as well. As a result, an image with a high signal-to-noise ratio is obtained, providing detailed insights into the sample surface and near-surface region with high magnifications.

In Chamber Electronic Detector (ICE)

ICE detector is a detector positioned near the end of the SEM/FIB column, specifically designed to enhance the collection efficiency and signal-to-noise ratio of secondary electrons and secondary ions.

The ICE detector belongs to the ETD type, as shown in Figure 3-11a, which uses a scintillator to detect electrons and convert them into photons. These photons are then transformed back into electrical signals by a transducer such as a photomultiplier tube (PMT). The improvement of the ICE detector is that both the scintillator and the transducer are positioned entirely within

the SEM chamber. Contrasting traditional designs where a long light pipe transmits signals to the PMT positioned outside the chamber, this ICE detector incorporates a very short light guide that connects directly to a PMT situated near the scintillator in the chamber, thereby significantly enhancing the signal-to-noise ratio and eliminating signal loss associated with the mating light pipe[141].

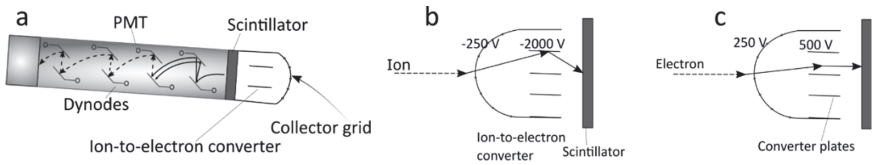

Figure 3-11 Illustration of ICE detector. (a) Mounted on the opposite side of ETD. (b) Positive ion collection mode. (c) Electrons collection mode. Adapted from reference [141].

The ICE detector is commonly mounted on the opposite side of the ETD detector (Figure 3-11a). Besides the difference in collecting directions with the ETD, this ICE detector is capable of both collecting secondary electrons and secondary ions. This is realized by incorporating an ion-to-electron converter in front of the scintillator. In the positive ion collection mode (Figure 3-11b), the collector grid is negatively biased to attract low-energy positive ions generated at the sample. Meanwhile, the converter plates are biased -2000V relative to the FIB target. The strong potential attracts and accelerates positive ions to strike the converter plates, causing the emission of electrons toward the scintillator. While in the electron collection mode, positive bias are applied, as marked in Figure 3-11c, to guide the electrons toward the scintillator.

Among all the detectors described above, the TLD detector is more sensitive to low-energy SEs, offering more pronounced contrast, especially for those associated with subtle energy variations, compared to the ETD detector, such as charging. However, the ETD and ICE detectors are more sensitive to the topography[142]. In the practical operation, simultaneously using ETD, ICE, and TLD detectors can be beneficial as the total yield of SE is fixed. For instance, combining the outputs of these three detectors at the same time can suppress charging artifacts while keeping the image details [124,142].

3.1.4. SEM imaging of ferroelectric domains and domain walls

SEM contrast is caused by the varying intensity/number of the electron signals emitted when the beam electrons strike different parts of the sample. There are multiple mechanisms that can cause variations in the electron signal, often with several factors simultaneously contributing to the obtained image, including topographic contrast, compositional contrast, channeling contrast, electrical and magnetic contrast, and strain contrast. Therefore, it is crucial to carefully interpret the obtained image, and this should be done by combining different imaging strategies, such as utilizing different detectors and adjusting beam parameters. For a

comprehensive understanding of image formation and interpretations in SEM imaging, readers are referred to ref. [122].

This part introduces the mechanisms of SEM imaging ferroelectric domains and domain walls, mainly based on references [94]and [28].

SEM has been used for contact-free and non-destructive imaging of the ferroelectric domains and domain walls since the 1970s across various materials systems. The first reported SEM imaging of ferroelectric domains was carried out on $BaTiO_3$ [143]. Preferential chemical etching was used to obtain corresponding surface topography, followed by coating the sample with a metal layer to prevent charging. The domain contrast obtained in this way was thus purely due to the surface topography. Soon after, Le Bihan et al. [136,144–146] observed ferroelectric domains in SEM without modifying the sample surface, neither chemical etching nor metal coating. At this point, the domain contrast was due to an electrical phenomenon rather than a topographic effect. These contrasts were achieved at low voltage (5 kV) in the secondary electron mode. In addition to the domain imaging, Aristov et al. [147] also observed ferroelectric domain walls in $LiNbO_3$ using SEM, and both domain and domain wall contrasts can be captured on the same sample surface under different imaging parameters.

With the improved low-accelerating voltage performance, SEM is now one of the mainstream methods for analyzing ferroelectric domains and domain walls, as it does not require additional sample preparation except polishing and cleaning. However, the imaging mechanisms can be complex, as various factors often interact and affect the image simultaneously. Hunnestad et al. [94] have done commendable work summarizing and classifying the non-topographic imaging mechanisms involved in domain and domain wall imaging.

It is important to note that the discussion here focused on SE contrast, which is the most commonly used imaging mode in various previous studies, as well as this work. However, BSE is also possible to image domain or domain walls in some material systems, especially when compositional change, topographic variation, or crystallographic orientation changes are involved [94].

3.1.4.1. Out-of-plane polarization

For samples with antiparallel ferroelectric domains and spontaneous polarization $\pm P$ pointing out-of-plane, both domain contrast and domain wall contrast can be observed[69,136,147,148]. Figure 3-12 presents an example of an out-of-plane TGS (triglycine sulfate) sample, which exhibits a domain contrast at $\mathrm{V} = \mathrm{V}_2$ (Figure 3-12a), and domain wall contrast at $\mathrm{V} < \mathrm{V}_2$ (Figure *3-12*b) and $\mathrm{V} > \mathrm{V}_2$ (Figure 3-12c). Here, V_2 is referred to as one of the equilibrium accelerating voltages, as discussed earlier. The detailed mechanisms will be discussed in the following part.

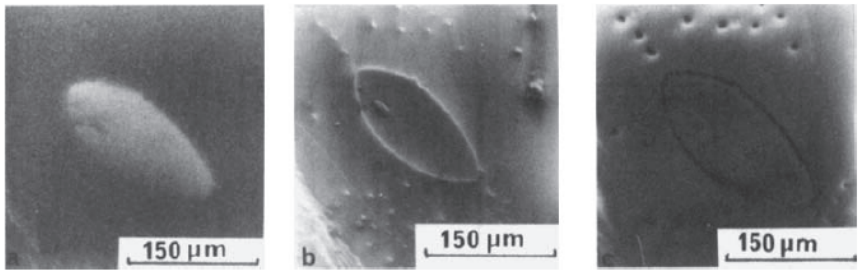

Figure 3-12. Voltage contrasts of the same antiparallel domains in a TGS sample under different accelerate voltages in SE mode. (a): $V = V_2$ domain contrast, negative domain appears bright, and the positive domain appears dark; (b): $V < V_2$, domain wall appears bright; (c): $V > V_2$, domain wall appears dark. Reproduced from [136] *under the terms of the Creative Commons CC BY license.*

For the domain contrast, three main mechanisms are possible, as illustrated in Figure 3-13 a-c.

Polarization contrast (Figure 3-13a): this mechanism relies on the interaction of the surface-bound charges and SEs produced in the SEM. Domains with negative bound charge ($-P$) repel SEs, increasing the SEs yield and making the domain appear brighter. Conversely, the $+P$ domain appears dark. A good example is shown in Figure 3-12a. This mechanism requires an unscreened charge on the surface. However, the uncompensated surface-bound charge can be altered by factors such as free charge carriers in the material, dynamic charging during primary electron irradiation, and external adsorbents on the surface. All these possibilities can alter the SEs yield and, thereby, the obtained contrast.

Pyroelectric effect (Figure 3-13b): The spontaneous polarization decreases when the ferroelectric material is locally heated by an electron beam due to the pyroelectric effect, resulting in the formation of pyroelectric potential U_{Pyro}, change the surface potential. This change is different for domains of opposite polarization, specifically, $\pm U_{Pyro}$ for $\mp P$ domains[28]. This results in a change in the surface potential of $2U_{Pyro}$ between the two types of domains, which is not instantaneously screened, leading to a domain-dependent surface potential. Notably, the contrast resulting from the pyroelectric effect is inverted compared to that from the polarization contrast.

Emission contrast (Figure 3-13c): This contrast arises from variations in the SEs yield due to differences in material physical properties, such as work function or permittivity[136].

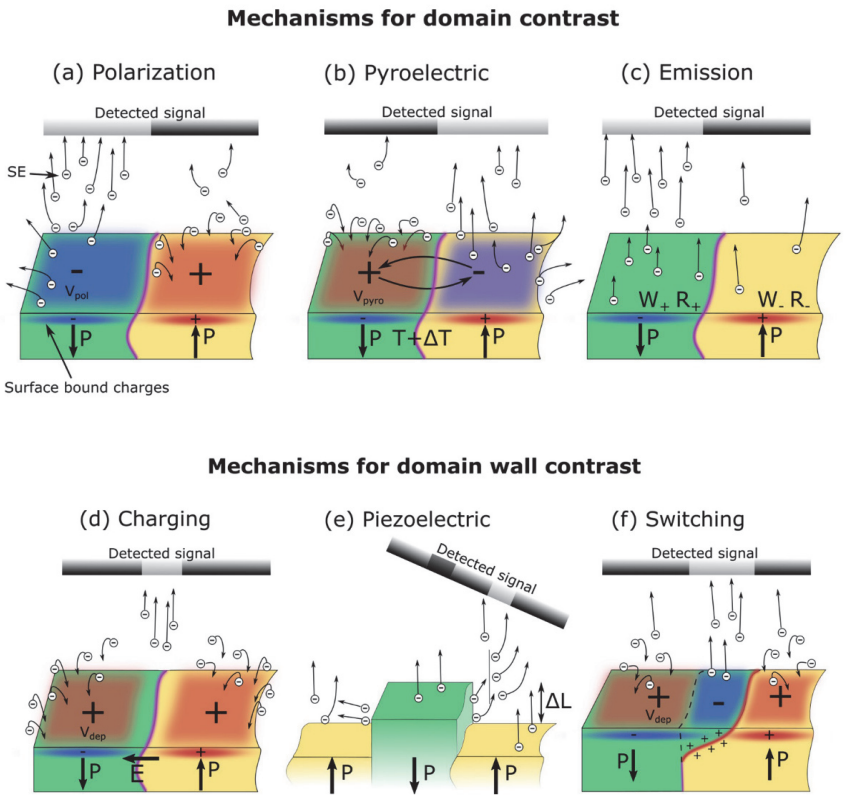

Figure 3-13. Main mechanisms for domain contrast (top row) and domain wall contrast (bottom row) on out-of-plane surfaces. Reproduced from reference [94] *under the terms of the Creative Commons CC BY license.*

For the domain wall contrast on the surface of out-of-plane samples, i.e., nominally neutral domain walls, the SEM imaging mechanism is also classified into three main types.

Charging contrast (Figure 3-13d): This contrast arises from the charging difference between the domains and the domain walls. The potential difference between the two domains raises a strong electric field across the domain wall. This strong electric field deflects both the incident and secondary electrons away from the wall, making the wall always appear less charged than the domains. Thereby, their contrast appears oppositely. When $V < V_2$, the surface is positively charged (dark), the wall appears bright (Figure 3-12b). For $\mathrm{V} > \mathrm{V}_2$, the wall is darker than the domains (Figure 3-12c).

Piezoelectric contrast (Figure 3-13e): This contrast is due to topographic changes in ferroelectric domains as a result of the converse piezoelectric effect: charging leads to domain contraction or expansion, causing variations in surface topography. This phenomenon results in differential SEM contrast based on domain orientations, especially when using side-mounted detectors.

Switching contrast (Figure 3-13f): Domain switching due to electron beam heating and charging. In a positively charged condition, this results in a negative surface potential in the switched area, altering both the PE and SE behavior and giving a bright contrast at the switched area. This switching involves the domain wall moving on the surface and bending underneath, as illustrated in Figure 3-13f. This induced bound charge at the domain wall, causing additional contrast contributions on an in-plane surface, which will be described next.

3.1.4.2. In-plane polarization

For samples with polarization lying in the surface plane, domain contrast and its inversion were observed in 1984 [147], and the mechanism was attributed to the difference in secondary electron emission (Figure 3-13c). The SEM imaging of domain walls contrasts on the non-polar surface is particularly interesting as both the neutral and charged domain walls are now being intensively studied for functional applications. The contrast mechanisms for charged domain walls in SEM images can also be classified into three main types:

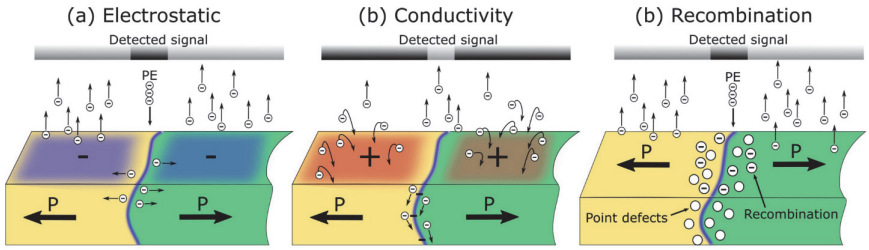

Figure 3-14. Contrast mechanisms in SEM imaging for charged domain walls on the in-plane sample surface. Reproduced from reference [94] *under the terms of the Creative Commons CC BY license.*

Electrostatic contrast (Figure 3-14a): Domain walls act as potential barriers that inhibit charge accumulation, similar to the charging contrast for out-of-plane samples mentioned above. Tail-to-tail domain wall appears dark under negative charging, while head-to-head walls are not visible. Conversely, the head-to-head wall becomes brighter under positive charging conditions, and the tail-to-tail wall is not visible.

Conductivity contrast (Figure 3-14b): The conductivity difference between the domain wall and the domain results in different surface potentials, with the same consequence as in the neutral domain walls.

Recombination contrast (Figure 3-14c): Point defects or impurities accumulate at charged domain walls, increasing the recombination of electrons and holes, and subsequently decreasing the SEs yield.

These mechanisms have been proposed by different researchers and from different systems. However, there is not yet a comprehensive understanding of the underlying contrast

mechanism for ferroelectric domain and domain wall imaging in SEM. Roede [28] demonstrated how the domain contrast in out-of-plane $ErMnO_3$ can be inverted with only a change in scan speed and how domain contrast can be replaced by domain wall contrast with only a change in acceleration voltage. Additionally, the imaging results are highly sample and condition-dependent, making it difficult to reproduce the exact same result under identical parameters. These phenomena suggest that SEM imaging is a dynamic process and cannot be fully explained by any single mechanisms described above, indicating several contrast mechanisms can play a role simultaneously.

Despite these challenges, SEM remains a valuable technique for investigating ferroelectrics. Beyond imaging, SEM also offers the capability for domain polarization alteration. This phenomenon has been widely observed in proper ferroelectrics since the first published work on SEM imaging of ferroelectric domains in $BaTiO_3$ in 1967 [143], which was observed through an optical microscope mounted in SEM chamber. Recently, it has also been observed in improper ferroelectric $ErMnO_3$ that the electron beam in SEM can be used to manipulate the domain configuration by combining it with the ion beam of FIB [100], a task often not feasible by electrodes at room temperature [25,95,149]. This offers new opportunities for contact-free manipulation of domains and domain walls in improper ferroelectrics.

In this work, taking full advantage of the rapid, convenient, and high-resolution characteristics of SEM imaging, combined with complementary SPM techniques, SEM is frequently used for the investigation of electronics transport behaviors in both the surface and sub-surface regions of $ErMnO_3$.

3.2. Focused ion beam

The FIB instrument and its principles are very similar to those of SEM, with the primary difference being that FIB utilizes an ion source instead of an electron source. The significant difference in mass between electrons and ions (specifically Ga^+ here) results in different interactions with the sample, most importantly the sputtering of the target material. FIB is capable of not only milling the sample surface but also imaging the target region with high resolution. In conjunction with the gas injection capabilities, FIB can perform ion-beam-induced deposition and enhanced etching, allowing for various sample fabrication processes. This aligns with the technologies envisioned by Richard Feynman in 1959 [150], where he described that the "eyes" and "hands" in the microscopic realm guarantee us the ability to observe and manipulate on a small scale. FIB is often complemented with SEM to form a FIB/SEM dual beam system, perfectly integrating non-inversive imaging with effective manipulation on demand.

In this section, the difference between a FIB instrument and a SEM, including the ion source and lenses, will be described. Following this, the ion-matter interaction and the general functions of FIB will be outlined, as well as some important examples of the application of FIB in the field of ferroelectrics. The content in this section is primarily based on the books of Giannuzzi et al.[151] and Orloff et al.[152], unless otherwise specified.

3.2.1. FIB Column

The FIB column resembles an SEM column but differs primarily in its use of electrostatic lenses instead of the electromagnetic lenses found in SEM. As illustrated in Figure 3-15, the ion beam originates from the ion source and is subsequently focused and directed toward the sample surface through a series of electrostatic lenses.

Morden FIB tools are typically combined with an SEM column to create an FIB-SEM dual-beam system. In such systems, the FIB column is usually mounted at an angle relative to the vertical SEM column, 52° in our instrument. When the sample stage is adjusted to the coincidence position (Figure 3-15) at the eucentric height [153], both columns can focus precisely on the same location on the sample. This alignment allows for SEM imaging of the FIB-processed at high resolution in real-time, enabling advanced material characterizations and manipulations, such as site-specific sample preparation [154], in-situ analysis [155], and 3D reconstruction [156].

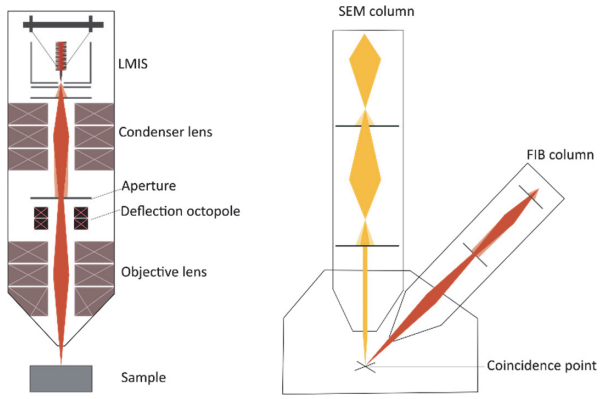

Figure 3-15. Illustrations of the FIB column (left) and dual beam FIB-SEM system (right). The FIB column utilizes a Ga+ liquid metal ion source (LMIS) to generate an ion beam. This beam is then focused by a series of electrostatic lenses, apertures, and eventually scans across the sample surface controlled by deflection octupole. The FIB-SEM dual beam system (right) allows both columns to focus on the same spot on the sample surface, facilitating sequential imaging and processing for site-specific manipulations. Inspired by reference [28].

3.2.1.1. Liquid metal ion source (LMIS)

The development of innovative ion sources has significantly advanced FIB tools. Currently, most commercial FIBs are equipped with LMIS[154], including the instrument used in this work. The accelerating voltage in our instrument (Thermo Fisher Scientific G4UX Dual-beam FIB-SEM) ranges from 500 V to 30 kV, and beam current ranges from 7 pA to 65 nA. This section outlines the basic principle of the LMIS, while a more detailed description of the physics of LMIS can be found in the book by Orloff et al.[152].

As illustrated in Figure 3-16, an LMIS consists of a tungsten needle (radius 1-5 µm) attached to a reservoir that contains the metal source material (Gallium in our case). The reservoir is resistively heated to bring the metal to its liquid state so that a thin film of liquid metal forms over the tungsten needle and is continuously replenished. A strong electric field between the tip and the extractor electrode induces a combination of electric and hydrodynamic forces. These forces pull the liquid metal at the tip into a cone shape. In LMIS, the cone-jet apex intensifies the extraction field enough to undergo field evaporation, leading to the simultaneous ionization and extraction of species from the liquid. Ions are then ejected from the tip of the cone, forming the ion beam. The suppressor electrode helps control and stabilize the ion beam generation.

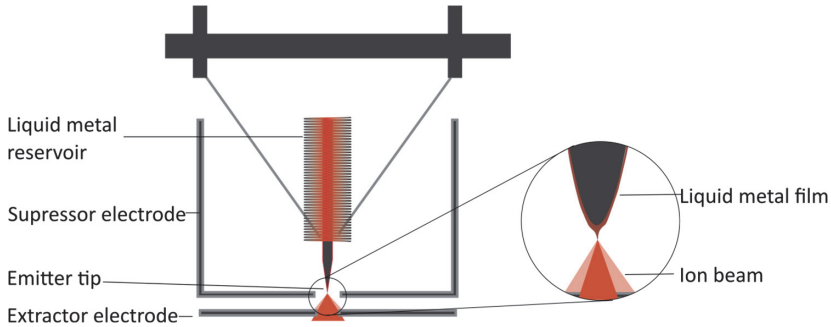

Figure 3-16. Schematic diagram of a Liquid metal ion source. A tungsten needle (emitter) with a sharp tip is attached to the liquid metal reservoir, which holds the metal source material, Ga, in our instrument. The reservoir is heated to maintain the metal in a liquid state, ensuring a continuous feed to the tip of the emitter. The strong electric field between the sharp emitter tip and the extractor facilitates ion emission through field evaporation.

Compared to electron sources, the virtual source size of an LMIS is generally larger due to the pronounced space charge effect [157]. This effect arises from the mutual repulsion among the positively (negatively) charged ions (electrons) that are emitted from the ion (electron) source. In an ion beam, the significantly heavier mass of ions, compared to the electrons, results in slower velocities for a given accelerating voltage. This slower movement extends the time that ions spend in close proximity to each other, intensifying the space charge effect. Consequently, this leads to a wider energy spread of the ion beams and ultimately limits their resolution compared to electron-based tools. The space charge effect is particularly pronounced near the ion source for three main reasons [158]: (1) high charge density leads to strong mutual interactions; (2) slow particle movement results in prolonged interaction times; (3) random particle positions give rise to a nonzero net force on each particle. To minimize the space charge effect, the strategies are based on reducing the ion concentration, shortening the interaction time, and optimizing the lens design. Practically, this means operating the ion beam at high energy and low current, as well as designing lenses that minimize beam travel time [28], hence enhancing the overall performance.

There are several metallic elements or alloy sources that can be used in LMIS, such as Au [159] and In[160]. Currently, Ga is the most used LMIS (Ga LMIS) for commercial FIBs. Its low melting point (29.8 °C) minimizes any potential interaction between the metal film and the tungsten needle. Additionally, its low volatility at melting point and low vapor pressure yield a long source life. However, a significant limitation of Ga LMIS is the beam damage caused by Ga^+ implantation, which will be discussed later on.

Liquid metal alloy ion source (LMAIS)[161] utilizes different metals mixed at their low-temperature eutectic composition to achieve a liquid state easily. This approach offers versatility and potential improvements in performance for specific applications, such as target

ion implantation. However, it also introduces additional complexity to the system, such as the Wien mass filter for ion species segregation.

In addition to LMIS, there are now several alternative ion sources available for FIBs, including gas field ionization sources (GFIS) used in helium ion microscope (HIM)[162], inductively coupled plasma (ICP) used in plasma FIB[163], and very recently developed laser-cooled low-temperature ion source (LoTIS)[164]. HIM and plasma FIB are both commercialized. Each ion source and microscopy technique has its own advantages and disadvantages. The best tool often depends on the specific requirements of a target application.

3.2.1.2. Lenses

Once the Ga^+ is extracted from the LIMS, electrostatic lenses are used to control the trajectory of the ion beam precisely to achieve the desired focus and resolution. The preference for electrostatic lenses instead of electromagnetic lenses is primarily due to the significantly heavier mass of ions, which is less susceptible to deflection by magnetic field compared to electrons. Specifically, an electron has a mass of approximately 10^{-31} kg, whereas a Ga^+ ion has a mass of 10^{-25} kg. Therefore, electrostatic lenses are more practical in FIB systems.

Figure 3-17 illustrates an electrostatic lens consisting of three-cylinder electrodes with gaps in between. The central electrode is at a different potential than the outer two electrodes.

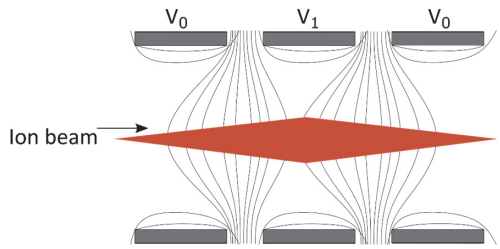

Figure 3-17. Illustration of an Einzel les (Electrostatic lens). The central electrode is at a different potential (V_1) with the outer two electrodes(V_0), enabling the focusing of the beam without changing its energy. The grey lines represent equipotential lines.

If a negative voltage V_0 is given to the outer two electrodes relative to the inner V_1, ions entering the lens will encounter the field between the first and central electrodes. Depending on the voltage difference, they might be decelerated. Upon reaching the central electrode, they experience the opposite effect, being re-accelerated. This deceleration and acceleration cause ions that were initially farther from the axis to bend more than those closer to the axis, bringing the ions into focus at a point on the optical axis downstream without changing the beam energy. This type of lens is called 'Einzel' lens. Einzel lens can function as both a condenser lens [165] and an objective lens in FIB columns [166,167]. In contrast, by applying a different voltage to the final electrode, the ions are "immersed" in a continuous electric field. This configuration is known as immersion lens. Due to the asymmetric electric field, the ions energy changes as it passes

through the lens, resulting in simultaneous acceleration/deceleration and focusing of the ions. Immersion lenses are particularly effective in reducing chromatic aberration (section 3.1.1.5) in the ion beam, and are commonly used in low-energy ion beam tools[168].

As mentioned above, the ion column typically contains two types of lenses: condenser lens and objective lens. The condenser lens gathers and focuses the ion beam, preparing the beam for further refinement and precise manipulation. This concentrated and focused beam is subsequently directed toward the objective lens, which further refines the beam and precisely focuses it onto the sample surface. Between these two types of lenses, a series of apertures is used to control the beam current, allowing for a range of ion currents from a few pA to 20 or 30 nA, and blocking out stray ions to enhance the beam quality.

Similar to SEM, different kinds of lens aberration can occur in the ion column. Due to the aforementioned space charge effect, which causes significant beam broadening and energy spread widening, chromatic aberration and astigmatism are even more pronounced in FIB. Cylindrical octupole lenses, commonly located near the objective lens, are used to perform beam deflection, alignment, and astigmatism correction. To prevent inadvertent sample damage, beam blankers are used to deflect the beam away from the center of the column.

3.2.2. Ion-matter interactions

Ion-matter interactions occur when the ion beam strikes the sample surface. Due to the large mass of Ga^+ ions, the incident ions transfer a considerably higher momentum to the target atoms compared to electron impact, triggering the occurrence of different scattering events.

Elastic scattering and inelastic scattering are the two basic classes of interaction processes between the incident ions and target atoms. Elastic scattering induces surface sputtering, displacement of lattice atoms, and the formation of defects. Inelastic scattering results in the generation of SEs, X-rays, and optical photon emissions. Figure 3-18 illustrates the key aspects of ion-matter interactions investigated in FIB.

Sputtering is the core process in FIB, during which the incident ions transfer their momentum to the atoms of the target material, causing some atoms to be knocked out of their initial positions and initiating a collision cascade. Target atoms can be ejected if they receive sufficient kinetic energy to overcome the surface binding energy. This is the key process that FIB is used for milling.

Secondary ion emission occurs when target atoms are ionized due to the ion impact and obtain sufficient energy to escape from the surface. Secondary ions can be collected and utilized for SIM imaging, as described in section 3.2.3.1. For a more comprehensive and quantitative analysis, a mass spectrometer can be employed, which can provide information on the elemental composition of the sample. A well-known technique based on this is Time-of-Flight

Secondary Ion Mass Spectrometry (ToF-SIMS[169]), which is capable of 3D chemical mapping at the nanoscale.

Secondary electrons are also emitted from the surface as a result of energy transfer from the incident ions. According to Orloff et al. [152], the secondary electron yield (i.e., the number of SEs generated per incident ion) on a metallic surface is 10-1000 times greater than that of the secondary ion. These ion beam-induced secondary electrons can be used for imaging, termed as iSE image, as detailed in section 3.2.3.1.

Atom displacement occurs when Ions of sufficient energy enter the solid and cause internal dislocation within the bulk material. This displacement of atoms causes amorphization in crystals.

Implantation refers to the process by which incident ions lose all their energy due to collisions and become trapped in the solid.

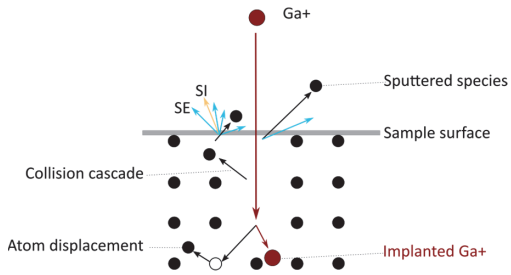

Figure 3-18. Schematic of the ion-matter interactions. Many events occur when the energetic ions bombard the sample surface, including sputtering, SI and SE emission, atom displacement, and incident ion implantation. These interactions facilitate various functionalities in material processing, such as imaging and milling. Meanwhile, ion implantation and atom displacement are typically considered to disturb material analysis and properties.

Similar to the electron-sample interaction, the interaction between the ion and material also has a specific volume. The size of this interaction volume is fundamentally determined by the stopping power, which quantifies the energy loss as incident ions transfer energy to the solid. As ions are stopped by collisions with atoms in the solid, they lose energy in two main channels: nuclear collisions and electronic collisions. Nuclear collision occurs between the incident ion and the target atoms, and these interactions are generally considered to be elastic. Electronic collisions result from interactions between the incident ions and lattice electrons, resulting in excitation and ionization, which are inelastic by nature. The details of these collision processes can be complicated and commonly calculated by the Monte-Carlo simulations[170], which facilitate the extraction of statistical quantities, i.e., ion penetration depth. Note that the penetration depth of a 30- 50 keV Ga^+ beam is limited to only a few tens of nanometers[171]. Specifically, ~ 40 nm for 30 keV Ga^+ beam on Si[172].

3.2.3. FIB basic functions

This section introduces the basic functions of FIB, including FIB imaging, deposition, and milling. The examples of each basic function are presented, with more emphasis on the milling due to its relevance in the sample fabrication process in this work. Typically, the practical applications of FIB involve a synergistic combination of these basic functions.

3.2.3.1. Imaging

The emitted SEs and SIs can be detected for ion beam-induced secondary electron (iSE) and secondary ion (SI) imaging, respectively. It is important to mention that the sample is being sputtered during the ion beam imaging process, which is destructive compared to standard SEM. Therefore, it is recommended to use a beam current of less than 100 pA for ion beam imaging to limit the induced beam damage. Depending on the detector settings, the image can be based on secondary electrons and secondary ions, providing a range of contrast mechanisms, which is able to offer some advantages over the standard SEM imaging, including stronger grain orientation contrasts (iSE) and fewer charging artifacts (SI).

Notably, iSE images often display a more pronounced grain orientation contrast compared to the SEM image obtained by an electron beam. This enhanced contrast arises from the channeling effect in crystalline materials, where incident ions travel deeper along crystallographic directions with lower atomic density. This deeper penetration occurs without undergoing too many scattering events, leading to the generation of fewer secondary ions and electrons in these directions. Although the channeling effect can be exhibited in both iSE and SI images, iSE yield is significantly greater than that of SI for most materials [173]. Figure 3-19a and b present standard SEM and iSE images from the same location, respectively, providing a clear comparison of the channeling effect of ions[174]. The SEM image in Figure 3-19a displays only the topography contrast, whereas the iSE image in Figure 3-19b reveals clear grain orientation contrast on the cross-section of a polycrystalline sample.

In addition to providing enhanced grain orientation contrast, iSE and SI imaging can also reduce charging artifacts compared to standard SEM imaging, due to the positive incident ions that help neutralize the accumulated negative charge on the sample surface. Particularly in SI imaging, the detection of secondary ions requires the ejection of atoms or molecules from the surface, effectively removing the charged layer and thereby reducing charging effects. Figure *3-19*c and d present the SE and SI images of a sample composed of a tungsten (W) wire, human hair, and the background. The SEM image (Figure 3-19c) displays noticeable charging effects around the human hair on a somewhat blurred background. In contrast, the SI image exhibits no charging artifacts on the human hair, revealing more surface detail across both the human hair and the background. This difference highlights the advantages of SI imaging in reducing charging in semiconducting or insulating materials over standard SEM images. However, the

invasive nature of the interaction between the surface atoms and the incident ions can not be neglected.

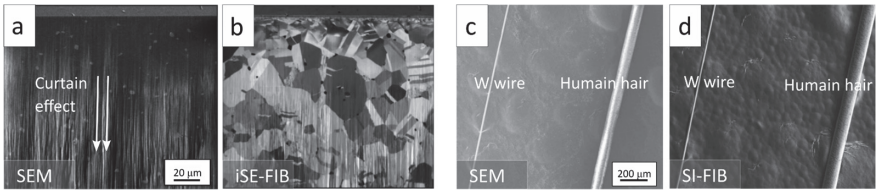

Figure 3-19. Comparison of SEM images with iSE and SI images. (a) SEM image of an FIB-cut cross-section in a brass sample, displaying only topography and some stripes caused by the curtain effect along the milling direction, indicated by white arrows. (b) iSEM image from the same position as (a), showing pronounced grain orientation contrast. (c) SEM image of a sample consisted of a W wire and a human hair on a background, exhibiting a noticeable charging effect around the human hair. (d) SI image from the same sample as (c) reveals enhanced surface detail and diminished charging artifacts. (a) and (b) are adapted from reference [174] *with permission. (c) and (d) are adapted from reference* [126] *with permission.*

3.2.3.2. Deposition

Focused ion beam-induced deposition (FIBID) can be used for precise material addition, complementing the sputtering used to remove the material. These techniques have been commercially used for IC failure analysis and precise nanofabrication [175,176].

FIBID involves chemical vapor deposition processes that are assisted by ion beams (Figure *3-20*a). Specifically, a precursor gas, typically an organometallic compound, flows from the gas injection system (GIS) towards the ion-beam impact area on the sample surface. The precursor gas molecules ideally form a monolayer upon adsorption on the surface. As the ion beam strikes the surface, the precursor gas molecules decompose, leaving behind a solid deposit, while the volatile constituents of the molecule are pumped away by the vacuum system. During the deposition, there is a competition between the rate of deposition of new material and the sputtering of new material by the primary ion beam. In general, too high beam current under the normal operation voltage will result in sputtering instead of deposition. By carefully controlling the deposition parameters, such as ion beam current and gas flow rate, it is possible to deposit material in precise patterns or shapes [177].

The electron beam can also be used to induce the deposition based on the same mechanism, which is known as focused electron beam-induced deposition (FEBID) [177]. The FEBID is capable of more precise control due to its relative shaper beam size, and it avoids the sample damage associated with ion beam irradiation. Figure 3-20 presents an example of electron beam-induced C deposition on the surface of an $ErMnO_3$ single crystal. The main difference between the material deposited by FIBID and FEBID lies in the presence of Ga^+ in the former, introduced by the ion beam[177].

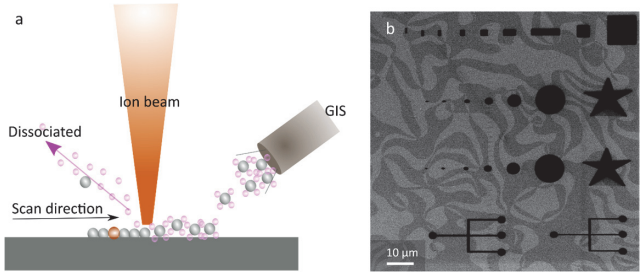

Figure 3-20. (a) Illustrations of ion beam-induced Pt deposition. (b) Electron beam-induced carbon deposition on the surface of an $ErMnO_3$ single crystal.

This difference results in varying electrical resistance of the deposited material. Specifically, Pt deposited by FEBID was found to be approximately two to four orders of magnitude more resistive than its FIBID counterpart. Even so, the resistivity of FIBID Pt deposits was significantly higher than that of the bulk Pt [178,179]. For a detailed comparison between FEBID Pt and FIBID Pt, please refer to ref. [179].

The advent of the dual-beam system enables the deposition of a protective layer using FEBID before the FIBID, proving to be a useful strategy in preventing undesirable damage to the target material. This method is now a standard way of making a protective layer for TEM lamella preparation [180], APT needle preparation[181], and FIB nanolithography [177].

A diverse range of materials can be deposited in FIB using precursor gases, including metals like Pt, W, and Au, utilizing precursors $(CH_3)_3(CH_3C_5H_4)$ Pt, $(W(CO_6))$, and $(C_7H_{13}AuO_2)$, respectively. In addition, insulators such as SiO_2 can be deposited using precursor $((CH_3O)_4Si$, or $(C_2H_5O_4)Si)$. Carbon deposition is also possible, typically using a precursor $(C_{22}H_{14})$ [177]. As carbon is usually contained inside the precursor, it is common for it to also be present in the other material that is deposited. For example, when using a Ga^+ ion beam with a beam energy of 35 keV to deposit Pt, the resulting deposit had a composition with a mass ratio of Pt:C:Ga:O equal to 45:24:28:3 [152].

3.2.3.3. Milling

When the incident ion beam strikes the target material, atoms in the target are knocked out and can be ejected from the material if the transferred energy surpasses the surface binding energy. Sputtering is the major mechanism for material removal and can be controlled with high precision, providing precise control for high-resolution milling of the target material. The milling efficiency is directly determined by the sputtering efficiency. The sputtering efficiency $Y(E_0)$, often termed the sputter yield, refers to the average number of atoms ejected from the target material per incident ion. The efficiency and profile of sputtering can be influenced by various factors, including the incident ions, the properties of the target material, and the angle of ion incidence.

Incident ion energy and species

For the same ion types, the sputtering efficiency $Y(E_0)$ increases with increasing beam energy.[182]. For different ion species with the same beam energy, the sputtering efficiency $Y(E_0)$ varies across different target materials. Brogden et al.[183] tested five different ion species (O^+, Ar^+, N^+, Xe^+, and Ga^+) on four different materials, observing that the sputtering efficiency $Y(E_0)$ difference changes at different beam energies and different materials, without any regular trend depending on the ion species.

Target material properties

During electron beam imaging, the yield of backscattered electrons is closely tied to the atomic number of the material, providing clear element contrast in BSE image. However, such a clear trend does not extend to the sputtering efficiency. As shown in Figure 3-21, a graph of the sputtering efficiency for the elements up to Au, no specific trend can be deduced based on changes in the atomic number. This observation aligns with the theory from Orloff [152] that the sputtering efficiency depends on both the mass and binding energy of the material. Consequently, materials composed of the same elements but synthesized in different processes will exhibit different sputtering efficiencies due to differences in bond strength, atomic configuration, etc. Referring to the channeling effect mentioned in the imaging part, different orientations of the same crystal can lead to varying sputtering efficiencies.

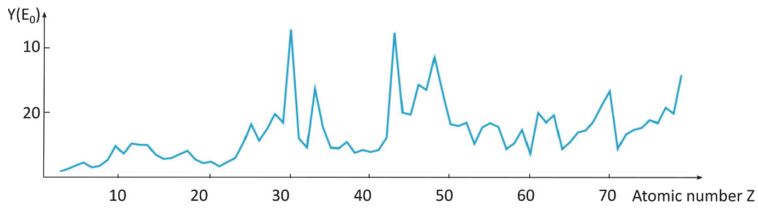

Figure 3-21. sputtering efficiency $Y(E_0)$ of the elements up to Au for 30 kV Ga+ at normal incidence. Reproduce from reference [28].

The angle of the ion incident

The angle of the ion incident plays a significant role in determining the sputtering efficiency [184]. Analogous to the SE yield in SEM, when the ion beam is incident perpendicular to the sample surface, the incident angle is zero (θ= 0°), and the sputtering efficiency is often at a minimum. As the incident angle increases, the ions-matter interaction volume moves closer to the surface, similar to the illustration in Figure 3-7, subsequently increasing the sputtering efficiency until a maximum. Beyond this maximum, often above 80°, as shown in Figure 3-22, the sputtering efficiency decreases rapidly as the ions tend to skim the surface rather than penetrate it. For TEM lamella preparation via FIB, sample polishing is commonly performed at a glancing angle[185,186] to enhance surface smoothing and reduce damage due to the decreased penetration depth[172,187]. In this work, different glancing angles (2°-7° less than 90°) are used

during the sample preparation process. It is important to note that the angle dependency described here assumes an amorphous sample.

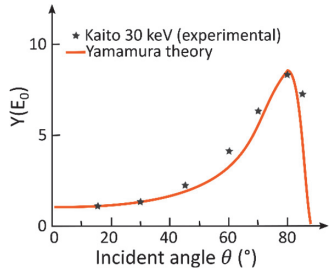

Figure 3-22. Variation of sputtering efficiency with incident angle. Both the Yamamura theory (represented by the orange curve) and Kaito's experimental data (depicted as grey stars) exhibit a consistent trend: the sputtering efficiency increases as the incident angle increases from 0° to a maximum around 80°, and then decreases as the angle approaches a glancing incident near 90°. Reproduced from reference [152] *with permission.*

3.2.4. Artifacts during FIB processes

As described above, FIB is capable of imaging, milling, and deposition, providing a highly precise means of fabrication. Meanwhile, it is important to note that the FIB process can be subject to various artifacts. This section outlines common artifacts encountered during sputtering milling in FIB, including redeposition, curtain, charging, and beam damage.

3.2.4.1. Redeposition

During FIB milling, most of the sputtered material is evacuated away by the vacuum system. However, some sputtered material can re-deposit onto other areas of the sample or nearby surface in an amorphous state, reducing the net sputtering rate (number of atoms being sputtered from the target per unit time). This is termed redeposition. Redeposition can sometimes be problematic if the redeposited material interferes with subsequent analyses or processing, such as causing surface contamination or hindering precise milling.

Despite redeposition being an inevitable aspect of FIB milling, its extent can be significantly altered by adjusting the milling approach. A trench milled with the ion beam trends to be wide at the top surface and tapers down to a point at the bottom, forming a classical "V-shape" (Figure 3-23a). As the trench is milled deeper, the effect of redeposition increases significantly until the rate of redeposition equals the rate of sputtering such that the aspect ratio is limited. Previous studies revealed that the magnitude of redeposition is strongly dependent on the aerial geometry of the target region, i.e., the aspect ratio of sidewall depth to width and length of the sputtered region[152]. Moreover, the milling strategy also plays a significant role. In practical, there are single-pass and multi-pass milling strategies. In multi-pass milling (Figure *3-23*b), the entire pattern is processed at each layer, allowing for the continuous removal of redeposited material by the next scan. However, the redeposition adheres on the sidewalls

tends to accumulate over time, and the resulting roughness of the sidewall varies with the ion beam current. In contrast, single-pass milling (Figure 3-23c) involves milling line by line towards the region of interest. In this case, the volume milled away might redeposit on the side opposite to the milling direction, but the final profile is clean and free from redeposition [28,188,189].

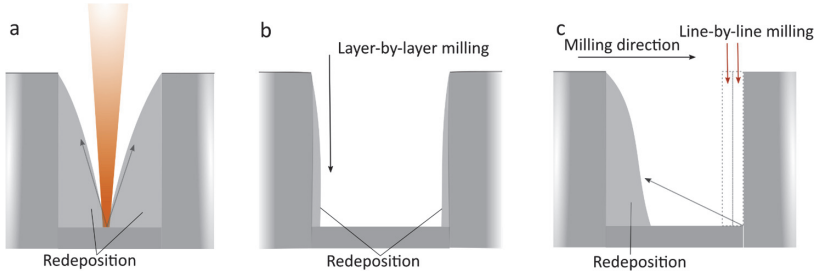

Figure 3-23. Illustrations of redeposition during different milling processes. (a) Milling into a deep, narrow trench typically results in a "V-shape" due to redeposition. (b) Multi-pass milling in a broader trench. Redeposition can be continually removed by the next scan, but these adheres on the sidewall is inevitable and accumulate progressively. (c) Single-pass milling in the broader trench. Redeposition lands on the side opposite the milling direction, leaving the newly milled side clean.

3.2.4.2. Curtain effect

The curtain effect, also known as the waterfall effect, is a well-known artifact in FIB-milled samples. It appears as vertical stripes along the milling direction on the milled surface, i.e., indicated by white arrows in Figure 3-19a, and is usually attributed to insufficient milling or masking due to topography or composition variations [28]. Several strategies can be employed to reduce the curtain artifacts, including using a lower ion beam current, adjusting the polishing angle, and depositing a protective layer to cover the topography variations [190].

3.2.4.3. Charging

The bombardment of ions (Ga^+) on the surface of a sample with insufficient conductance or insulator will cause excess charges to accumulate. These charges are usually positive and can cause unwanted deflection of the incident beam as well as secondary ions and electrons, leading to drift during milling or deposition. The two common ways of reducing charging are conductive layer coating and electron beam neutralization. In a FIB-SEM dual beam system, electron beam neutralization can be conducted by simultaneously using both ions and electrons to irradiate the surface. Coating with a conductive layer is straightforward and effective, and it is frequently utilized in this work during lamella fabrication, as detailed in section 5.1.

3.2.4.4. Beam damage

FIB is increasingly being used for sample milling, deposition, and imaging because of its high output and site-specific capabilities. However, FIB-fabricated samples inevitably suffer from ion beam damage, which is a fundamental limitation of the technique.

Ion beam damage, in principle, can be divided into two types: ion implantation and amorphization. Ion implantation occurs when the incident ions penetrate into the material and become embedded. This has been observed for Ga^+, Xe^+, and Ne^+ fabricated samples. However, Ga^+ ions have additional chemical influence due to their higher chemical reactivity compared to those inert ions[191,192]. Amorphization occurs in almost all ion beam-milled samples, as the incident ions cause displacement of the atoms from their lattice site, disrupting their crystalline structure. These two kinds of beam damage usually occur concurrently and manifest as a damage layer with a 20-30 nm thickness on each side of the milled surface. The specific damage layer thickness depends on the ion species, beam energies, and target material properties[193,194].

Different strategies have been used to remove or reduce the damaged layer, including thermal annealing, chemical etching, and low-energy beam/plasma polishing. Previous studies showed both recrystallization of the amorphous layer and expulsion of implanted gallium could be achieved by thermal annealing (700 °C [195] or 450 °C [196]) in air for a specific time (1 hour [195]). Ar/O plasma cleaning can remove remaining gallium oxide platelets after annealing. On the other hand, wet etching in a mixture of nitric and hydrofluoric acid can markedly reduce the beam-induced damage layer. By controlling the etching time and temperature, it is possible to remove the amorphous layer thoroughly [197]. Recently, Turner et al. [198] developed a method that combines FIB and wet-chemical etching to prevent beam damage on FIB-cut TEM lamella of a nanopillar sample. They encapsulated nanopillars in a sacrificial oxide, which acts as a protective layer during FIB milling. After cutting the TEM lamella to the desired thickness, the sacrificial oxide layer was removed by wet-chemical etching, leaving the nanopillars free. While these two kinds of strategies are all able to remove the damage layer, it is important to note that the additional sample treatments introduce complexity and potential risks to the process. Additionally, these methods are limited in their applicability to specific materials and geometries.

The use of a low-energy ion beam, as utilized in this work, represents the most convenient strategy[172]. It has been established that the damage layer is shallower at lower beam energies across various ion species[172]. Kato et al.[197] observed that a 10 keV beam reduced the amorphous layer thickness on a B-doped Si TEM lamella to 10 nm, which is half of that achieved with a 30 keV beam. Similar results have been observed by Kelley et al. [199], as shown in Figure 3-24 a-c. Consistently, Mosberg et al.[200] demonstrated that the conductance at tail-to-tail domain walls in a FIB lift-out $ErMnO_3$ lamella (700 nm-thick) was improved after polishing with a 5 keV ion beam compared to that of 30 keV. The conductance after milling with the 5 keV beam closely resembles that of a normal bulk sample, suggesting the low-energy beam can effectively preserve the electric properties of the domain walls by minimizing ion beam damage.

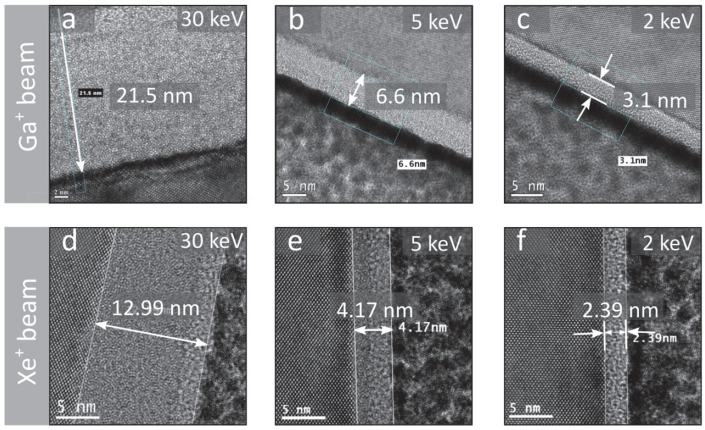

Figure 3-24. HRTEM images of beam-damaged layer on TEM lamellas. The top row is polished by Ga^+ FIB, and the bottom row is polished by Xe^+ FIB, each using different beam voltages, as specified in the images. Images (a)-(c) and (d)-(f) consistently exhibit that polishing with a lower energy beam results in a significantly reduced thickness of the damaged layer compared to those polished by high beam voltage. A comparative analysis between (a)-(c) and (d)-(f) suggests that the Xe^+ beam generally causes a thinner damaged layer than the Ga^+ beam, highlighting the impact of ion type on beam damage. Adapted from ref. [199] with permission.

Besides the Ga^+ ion beam, Kelley et al. [199] also compared the damaged layer thickness on TEM lamella surface finial polished by Ga^+ and Xe^+ ion beams of different beam energies at glancing angles, as shown in Figure 3-24 d-f. The result consistently showed that lower ion energy effectively reduces the thickness of the ion-damaged layer. Furthermore, the thickness of the damaged layer introduced by Xe^+ plasma FIB in silicon was found to be 20% (at 2 keV) to 40% (at 30 keV) less than that from a Ga^+ FIB prepared surface.

It is important to note that different ion species induce varying degrees of beam damage, with some inherently causing less damage than others due to the mass difference of the ions. A comparison of the damage induced by Ga^+, Ne^+, and He^+ ion beams revealed that low-energy Ne^+ and He^+ beams (10 keV) offer higher spatial resolution, avoid Ga implantation, and result in a much less damaged layer [191,201,202]. These benefits can complement the drawbacks of the Ga^+ beam, which exhibits a broader beam and lower resolution at low beam energies. Besides focused ion beams, broad Ar^+ ion milling can substantially reduce the thickness of the damaged layer when combined with focused ion beams [193,197,203]. In practice, taking the milling efficiency into consideration, a high-energy beam of one species may be combined with a low-energy beam of another species to achieve the desired outcome. For instance, Ga is used for the large volume milling, and another inert ion is used for the final cleanup step. This strategy is employed in this work to reduce the damage layer for FIB-cut cAFM lamellas, as described in chapter 5.

3.2.5. FIB application on ferroelectrics

The application of FIB to material science is rapidly expanding due to its flexibility and user-friendly working procedure. Even though FIB may introduce artifacts, as with all sample preparation techniques, it offers fascinating opportunities for both fundamental research and practical applications.

The general applications of FIB in material science include cross-sectioning, TEM sample preparation, APT sample preparation, and FIB 3D tomography. This section will focus specifically on the application of FIB in the study of ferroelectrics. Detailed significant results in the nanostructuring ferroelectrics by FIB have been reviewed by Burns et al.[204].

Firstly, FIB can be used to correlate surface properties with internal nanostructures, as the ferroelectric properties are highly dependent on local surrounding structures. FIB allows for precise, location-specific cross-sectioning, opening the area beneath the region of interest and enabling inspection of internal structures. By serial cross-sectioning and imaging procedure at the target region, the 3D reconstruction of internal nanostructures is possible, serving as the basis for reliable quantification of complex microstructures. Since the work of Holzer et al. [156] on 3D microstructures of $BaTiO_3$ ceramic using FIB-SEM, this technique has evolved into a mainstream tool for 3D tomography in nanometer scale. Recently, Roede et al. [96] utilized FIB 3D tomography to reveal the 3D structure of ferroelectric domain walls in $ErMnO_3$ single crystal in high resolution, enabling quantification of geometry-related domain wall properties. In addition to 3D morphology, FIB-SEM is a standard tool for preparing needles for atom probe tomography (APT) [205]. This technique enables the construction of a 3D atomic-scale compositional map, providing valuable insights into the defects, domain walls, and grain boundaries in the ferroelectric material. FIB is also commonly used to prepare lamellas for TEM, allowing the observation of atomic structures, as well as in-situ manipulations[206,207], such as observing the behavior of ferroelectric materials under bias voltage, heating, etc., in TEM chamber.

Furthermore, FIB has also been utilized to cut samples into specific geometries for domain configuration analysis. As early as 2006, Schilling et al.[208] cut lamella of a wedge shape, with a thickness range from 530 nm to 70 nm from $BaTiO_3$ single crystal using FIB and found the domain periodicity varied consistently with Kittel's law. Shortly after, they [209–211] found that domain configurations are influenced by the morphological confinement achieved by FIB cutting. Building upon these observations, they proceeded to extract lamella from bulk samples, mount them onto the substrate, pattern into specific geometries, and subsequently investigate their switching behavior under bias voltages. Their findings revealed that FIB-created morphologic notches, antinotches, and even structural holes can influence the domain wall mobility primarily by altering the local distribution of the applied electric field [212–214], offering

a novel method for controlling domain injection and switching through sample geometry manipulation.

This morphological confinement was then utilized in device-like functionality design. In 2015, from the same team, Whyte et al. [215] created a ferroelectric domain wall diode where domain walls were constrained to move only along one direction regardless of their polarity. This functionality was realized by the sawtooth morphology of the ferroelectric KTP lamella, based on the notion that the energy of a domain wall is proportional to its area. The domain walls could ascend the shallow slope of the sawtooth but were prevented from moving opposite due to the steep potential gradient.

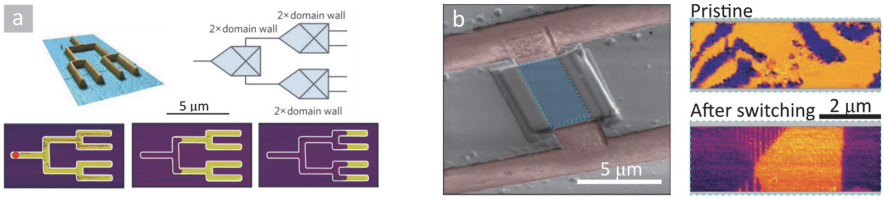

Figure 3-25 Examples of FIB applications in ferroelectrics. (a) Controlling domain wall motion, adapted from reference [216] *with permission. (b). A relevant application to this work. Extraction of lamella from a bulk sample for subsequent SPM characterization and manipulations, adapted from reference* [220] *under a Creative Commons license.*

Around the same time, with the assistance of the electron beam-induced deposition technique in FIB, McGilly et al. [216] demonstrated high-level control and manipulation of domain walls in ferroelectric thin film $Pb(Zr,Ti)O_3$ (Figure 3-25a). By giving bias voltages to the Pt electrode using a PFM tip, they were able to precisely control the domain wall displacement within the region covered by the Pt line electrode. This method was further extended to complex electrode structures as domain wall multipliers, opening up new possibilities for using domain wall motion in devices. In 2017, in contrast with the previous example that used only the electron beam in FIB, McGilly et al. [217] successfully utilized the ion dose in FIB to engineer the defect density in thin film $Pb(Zr,Ti)O_3$. The result revealed a dependency of the ferroelectric polarization switching and domain wall roughness on the ion dose. Recently, Chouprik et al.[218] used ion irradiation to induce Ga doping into HfO_2 thin film. This process involved introducing Ga ions into the amorphous thin film through ion beam irradiation, followed by annealing to crystallize the film. The resulting Ga-doped HfO_2 thin film exhibited a remarkable increase in remnant polarization (13 $\mu C/cm^2$), compared to the 0.5 $\mu C/cm^2$ of the undoped film. This example represents a typical process of ion beam implantation in semiconductors, as reviewed by Li et al.[219]. The key information here is that ion beam irradiation can be a controllable way for material property engineering rather than a mere undesirable side effect.

Another important application of FIB nanostructuring relevant to this work involves extracting lamella samples from bulk samples for subsequent SPM investigations. In 2011, McQuaid et

al.[220] machined lamella sample using FIB from bulk $BaTiO_3$ single crystal and investigated it with SPM. After retracting the poling voltage, they observed a unique mesoscopic flux-closure domain pattern (Figure 3-25b), which is uncommon in ferroelectric materials. Inspired by this sample preparation strategy, a previous study [200] from our group demonstrated an FIB workflow to extract a 700 nm thick lamella from an $ErMnO_3$ single crystal sample and then characterized it by different SPMs, setting the stage for investigating properties of domain walls in samples of different thicknesses. In this work, this sample preparation strategy is continuing to be used, optimized with some variation to achieve a new geometry.

In summary, FIB is an invaluable tool in the field of ferroelectrics, offering great opportunities for both fundamental characterization and device fabrication.

3.3. Scanning probe microscopy (SPM)

Scanning probe microscopy (SPM) refers to imaging techniques that use a sharp physical probe to raster-scan the surface of samples and locally collect information with nano or even atomic resolution[221,222].

In contrast to the SEM and FIB, which utilize high energy electrons or ion beams to raster scan over the sample surface, generating signals based on the interaction between these electrons or ions with the sample, SPM brought a solid probe close to, or in contact with, the sample surface to monitor changes. This allows us to obtain information on both the surface topography and the surface properties. This section is mainly based on the books from Voigtlander [221], Brandon et al.[223], and Lanza [224] unless otherwise specified.

Scanning tunneling microscopy (STM) and atomic force microscopy (AFM) are the two main classes of SPM. As the prototype of the SPM, STM was invented by Gerd Binnig and Heinrich Rohrer, who were awarded the Nobel Prize in 1986 for this invention. STM is based on the quantum tunneling current between the sharp metal tip and a conductive surface, which is exponentially dependent on the distance between them. This relationship is utilized in the feedback loop to maintain a constant current, enabling surface topographic measurements with atomic resolution. One of the main limitations of STM is its constraint to electrically conducting samples. In order to overcome this, AFM has been invented, where atomic force is used as a process variable, rather than quantum tunneling current. Since atomic forces are displayed by all materials, AFM can be applied to almost all samples, including conductive and insulating samples.

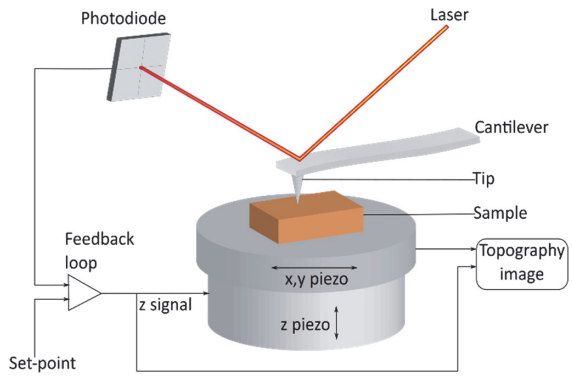

Figure 3-26 Schematic of atomic force microscopy (AFM). The feedback loop maintains a constant tip-sample distance.

Figure 3-26 illustrates the main setup of AFM. A tip is brought close to or in contact with the sample surface. A laser is then focused on the reflective backside of the cantilever, and a photodiode is used to detect the position or the vibrational amplitude of the reflected laser point, thereby, the displacement or vibration of the cantilever. The relative position between

the tip and sample is controlled by the piezo elements (x, y piezo, and z piezo). Once the cantilever displacement or vibration information is detected by the photodiode, this information is sent to the feedback loop, where it is compared with the desired value (setpoint). The z piezo continuously receives signals to keep the process variable (displacement or vibration) equal to the setpoint value, maintaining constant tip-sample distance. Meanwhile, this z signal is combined with the x and y signals to generate a topography image.

The SPM instrument used in this work is Oxford Instruments Cypher ES environmental AFM.

3.3.1. Tip-sample interactions

The idea behind the AFM is to utilize the forces between the surface and the tip to track the surface topography. The force between the tip and sample is composed of several long-range and short-range interactions. The overall tip-sample interaction can be qualitatively described by a Lennard-Jones potential. This potential describes the interaction between two neutral atoms by two terms: one term describes the long-range attractive part of the interaction, and another term describes the short-range repulsive interactions. It can be written as:

$$U_{LJ}(r) = 4U_0\left[\left(\frac{r_a}{r}\right)^{12} - \left(\frac{r_a}{r}\right)^{6}\right], \qquad \text{Equation 3-11}$$

where U_0 is the depth of the potential well, r is the distance between the atoms, and r_a corresponds to the distance at which $U_{LJ}(r)$ is zero.

As shown in Figure 3-27, the Lennard-Jones potential is represented by the red line, the attractive contribution ($-1/r^6$) by the yellow line and the repulsive contribution ($1/r^{12}$) by the black line.

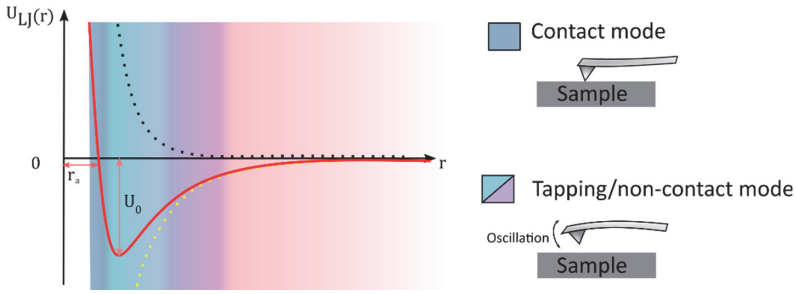

Figure 3-27. Lennard-Jones potential and its implications in AFM operation. The Lennard-Jones potential describes the overall tip-sample interactions in AFM. At larger separation (r), the attractive part (illustrated by the yellow dotted curve) predominantly influences the interaction, while at closer proximity, the repulsive contribution (presented by the black dotted curve) becomes dominant. Depending on these regimes, AFM operates in different modes: In contact mode, the tip maintains continuous contact with the surface, causing cantilever deflection due to repulsive interaction. In non-contact mode, the tip oscillates above the surface at a small amplitude, primarily influenced by attractive contributions. In tapping mode, an intermediate state, the tip oscillates at a large amplitude driven by a specific frequency, transitioning between attractive and repulsive interactions. Inspired by references [77]*and* [222].

Based on the tip-sample interaction force, AFM can be operated in three different modes: contact mode, semi-contact, and non-contact modes, all of which are capable of obtaining the

topographical information. Each mode has its own advantages and disadvantages, and should be selected based on the specific requirements of the investigation.

In contact mode, the interaction force between the tip and the sample falls within the repulsive regime. The force leads to the deflection of the cantilever according to Hooke's law. This cantilever deflection causes the laser beam deflection, which is eventually detected by the photodiode. The feedback loop responds to this deflection signal by generating a signal to adjust the probe height, maintaining a constant cantilever deflection and, thus, a constant tip-sample distance. Contact mode is generally used for hard material due to the constant load applied by the tip[77]. Beyond mapping topography, contact mode serves as the basis for various secondary mapping modes that sensor different physical quantities. For instance, in this work, piezoresponse force microscopy (PFM) is used to sense the piezoelectric response, and conductive AFM (cAFM) is utilized for local conductance mapping.

In noncontact mode, the tip oscillates with a small amplitude above the sample surface without physical contact during the scanning. The driving frequency is at or near its natural resonance frequency. The force now is in the attractive regime. As the tip approaches the sample, the resonance frequency of the cantilever changes, the amplitude of the oscillation thus decreases, and the phase shift changes. The feedback loop adjusts the tip height to maintain the constant amplitude. Non-contact mode is particularly useful for studying soft or sticky surfaces, as it avoids the direct physical contact between the tip and sample.

In semi-contact mode (or tapping mode), the cantilever is also excited at a driving frequency by a shaking piezo. The tip oscillation amplitude is larger, typically from several tens of nanometers above the sample surface to intermittently contact with the sample, which leads to the force changing between attractive force to repulsive force contribution. The constant driving frequency is usually selected at or very close to the resonance frequency of the free cantilever. Figure 3-28a illustrates the amplitude change as the oscillating tip approaches the sample surface, with the amplitude being a monotonic function of the tip-sample distance, enabling a stable feedback control. The phase shift in response to changes in the tip-sample distance is presented in Figure 3-28b. When the tip enters the attractive regime, the phase rises to above 90°. Bringing the tip closer to the sample surface increases the contribution from repulsive forces, inducing a discontinuous jump to the repulsive solution below 90°. Notice that as the amplitude approaches 0, the phase becomes undefined, introducing noise. The detected signal now is the amplitude of the cantilever oscillation instead of the deflection in contact mode. The tapping mode is the most frequently used mode, allowing high-resolution topographic imaging with minimal wear on delicate samples. In chapter 5 of this work, the tapping mode (AC mode) is first used to locate the surface of a lamella sample without causing any damage.

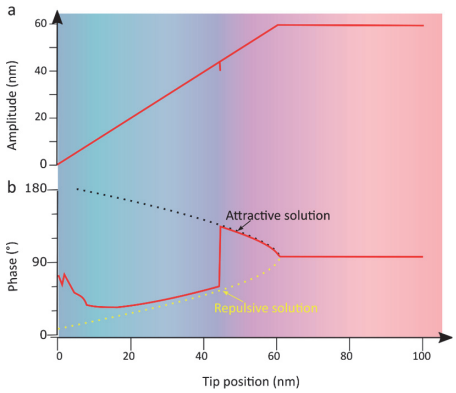

Figure 3-28 Cantilever amplitude and phase as a function of tip-sample separation in AC mode. The free-air amplitude at resonance frequency is assumed to be 60 nm. Reproduced from reference [225].

3.3.2. Conductive AFM (cAFM)

Conductive AFM (cAFM), a technique based on contact mode AFM, allows for spatially probing the electric current passing between the conductive tip and the sample. This is achieved by applying a voltage to the sample, creating a potential difference between the sample and tip, while a trans-impedance amplifier converts the input current signal into an output voltage signal that can be detected by the computer. Using this setup, as shown in Figure 3-29, either a current map of the sample surface or current-voltage spectra at predefined pixels can be obtained. The setup shown here is based on the instrument used in this work. The bias voltage can also be applied to the tip, while the sample is grounded depending on the specific instrument setup. In this work, cAFM is mostly used for collecting current maps.

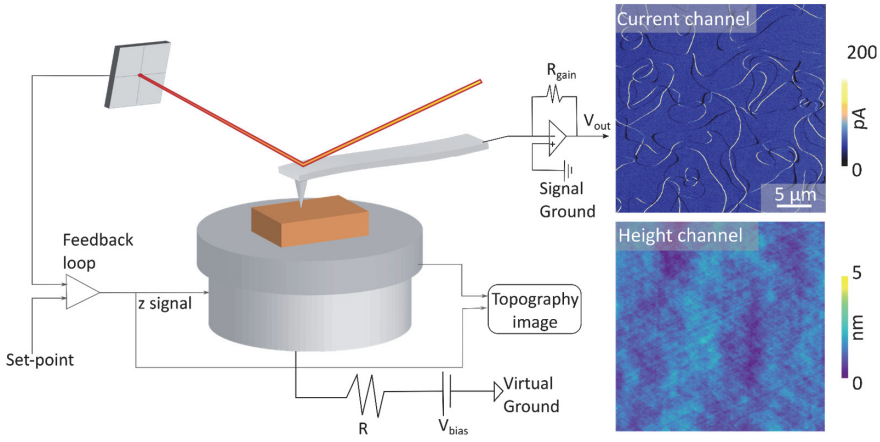

Figure 3-29 Schematic of a cAFM setup based on contact AFM. The bias voltage here is given to the sample with the tip grounded. Data on the right show domain walls in $ErMnO_3$ (bright lines and dark lines in top panel, see section 2.2.3 for details.) and the corresponding topography (bottom panel).

The first cAFM was performed by Murrell et al. [226] on a 12-nm-thick VLSI quality SiO_2 in 1993.

Since its invention, cAFM has usually been used to study ultra-thin dielectrics and some related phenomena. With the development of the technology, it is now not only widely used for imaging different nanomaterials and electronic phenomena, but also used for high-precision control processes, such as resistive switching of memristors based on different mechanisms, performing the set-reset processing, as reviewed by Yang et al.[227].

The mechanism of cAFM is straightforward, but it is subject to some limitations as discussed below.

(1) The first uncertainty is the tip-sample contact area. The Hertz contact theory is the most accepted method to estimate the physical contact area between the tip and sample [224], in which the tip radius and the applied force play a much larger role than the elasticity properties of the tip materials. However, the actual force is complicated to calculate as it involves additional factors, such as contamination, liquid layer, and micro-roughness of the tip and the sample. In addition, the tip radius may vary when the tip is worn out, and the effective area can change with the sample geometry.

(2) The electric-field distribution under a tip can be estimated, as theoretically analyzed by Molotskii [228] and recently demonstrated through Finite Element Modeling by Rieck et al. [229]. However, the actual field distribution can be even more complex due to factors such as changes to the tip geometry and surface contamination, which can alter the local field distribution. A good example of this complexity is evident in the first cAFM experiment conducted by Murrell et al. [226]. During this experiment, some sample regions exhibited much larger breakdown voltage than those measured by conventional macroscopic-scale methods. This deviation later turned out to be the issue of tip contaminations that affect the applied electric field instead of the initial hypothesis of a defect-free region.

(3) The nature of tip-sample contact must also be considered [28]. When the tip makes contact with a metallic surface, it is theoretically assumed to become electrically connected to all points of the sample. As a result, cAFM cannot perform strictly local measurements with a nanometric lateral resolution, and the collected currents apply to larger areas[224]. In contrast, when the tip is placed on a semiconductor surface, a depletion barrier may form in the semiconductor due to the mismatch in work function, leading to a Schottky contact at the interface. The cAFM result thus can only depict the relative changes and not provide intrinsic conductivity values. The junction between the conductive tip and an insulating sample is distinct from that of metal and insulating material.

In this work, the p-type semiconductor $ErMnO_3$ sample is investigated by cAFM, forming a Schottky barrier at the tip-sample interface based on previous works on $ErMnO_3$ sample [16,148,149,230] and $HoMnO_3$ [231].

3.3.3. Piezoresponse force microscopy (PFM)

Piezoresponse force microscopy (PFM) is designed to detect the local piezoelectric deformations in the sub-picometer regime with nanometers-scale lateral resolution. PFM is carried out in contact mode while an AC voltage is supplied to the tip (or the sample) to induce the periodic vibrations of the sample surface based on the converse piezoelectric effect. This, in turn, leads to the deflection of the tip cantilever, which is collected by the system and analyzed using a lock-in amplifier (LIA).

PFM is valuable for studying a wide range of electromechanical systems, such as piezoelectric, biological, and molecular-based mechanical systems. Since all the ferroelectrics are also piezoelectrics, and the ferroelectric and piezoelectric parameters are coupled, this makes PFM a perfect tool for ferroelectric domain imaging.

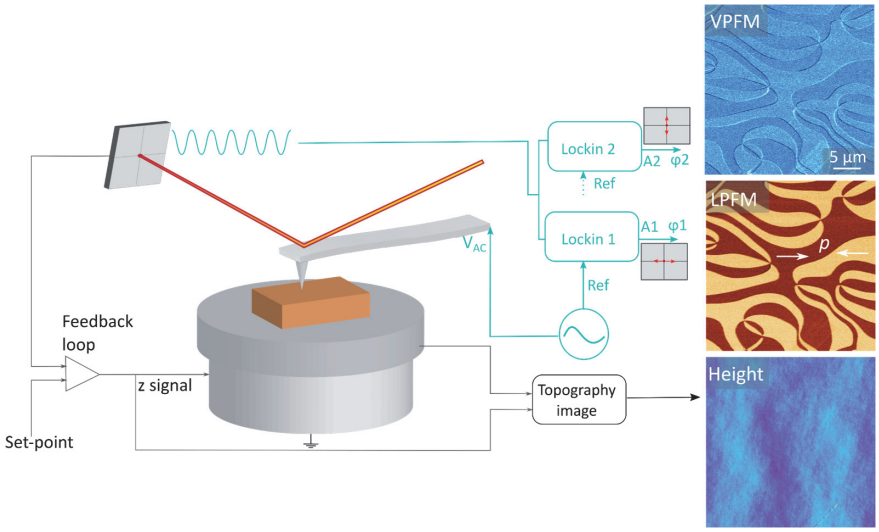

Figure 3-30 Schematic of a PFM setup based on contact AFM. The AC voltage of frequency f is applied to the tip, inducing vibrations in the sample surface at frequency f. These vibrations result in movements of the cantilever, which are detected and sent to the Lockin amplifier. These Lockin amplifiers extract the relevant frequency components, capturing the movements in both vertical (Lockin 2) and lateral (Lockin 1) directions. This generates the corresponding signals of vertical PFM (VPFM) and lateral PFM (LPFM), respectively.

Figure 3-30 illustrates the setup of PFM. Based on the setup of a standard contact AFM, additional components are shown on the right in blue color. An alternating voltage V_{ac} (with an amplitude of V and frequency of f) is applied through the conductive tip to the sample. This alternating voltage results in the expansion or contraction of the sample and subsequent cantilever deflection. At a common oscillation frequency of 40 kHz for standard PFM, the induced tip deflection is typically a few picometers, which would not affect the feedback loop[77]. Instead, the periodic tip displacement causes laser defections detected by the PSD. This PSD information will be sent to LIA, where it is compared with the reference signal of the supplied AC voltage. The piezoelectric strength and domain orientation can thus be determined by

analyzing the deformation amount and the phase shift between the PSD signal and the reference signal. Simultaneously, the sample topographic information is also obtained.

In uniaxial ferroelectrics, such as $ErMnO_3$, the samples are typically cut in a way such that the polarization directions are either perpendicular or parallel to the surface plane. These polarization orientations induce forces that are normal or parallel to the surface plane. This results in the laser beam deflecting along the vertical direction or horizontal directions of the PSD, leading to the vertical PFM(VPFM) and lateral PFM(LPFM) signals (Figure 3-30), respectively. For samples with uncertain polarization direction, the vector PFM, involving repeated scans and rotations, is necessary to distinguish different forces acting on the tip, as detailed in ref. [232].

In order to obtain quantitative information, such as the polarization direction and the piezoelectric strength, careful calibration is mandatory, as explained by Soergel [232]. This is typically performed on a uniaxial proper ferroelectric $LiNbO_3$, where both VPFM and LPFM can be calibrated simultaneously.

Resonance PFM

In order to improve the signal-to-noise ratio, resonance PFM is conducted with a driving frequency that matches the tip-sample contact resonance frequency. The concept of resonance PFM is to synchronize the tip driving frequency with that of the sample, thereby amplifying the cantilever deflection for a given tip displacement[77] and improving the system sensitivity. The driving frequency in our system ranges from a few tens kHz to about a few MHZ. However, the resonance PFM signal could also contain other information, e.g., topographical information, as the driving frequency is heavily dependent on the contact between the tip and the sample. In addition, non-piezoelectric effects can also contribute to the electromechanical response, as reviewed in ref. [233]. Thus, while the resonance PFM can resolve relative changes in electromechanical/piezo response, data interpretation requires careful consideration.

3.3.4. Kelvin Probe Force Microscopy (KPFM)

Kelvin Probe Force Microscopy (KPFM), also known as Scanning Kelvin Probe Microscopy (SKPM), is an SPM technique for imaging surface potentials across a diverse range of materials, spatially resolved at a nanometer scale. The term “Kelvin force” refers to similarities between this microscopic technique and the macroscopic “Kelvin probe” method.

As the technique is sensitive to topographical crosstalk, the KPFM (Figure 3-31) uses a two-pass method for operation, meaning that the tip scans twice over the same path. The first pass uses a standard tapping mode to determine the surface topography on a line-by-line basis, and the second pass measures the surface potential while following the topography path obtained in the first pass, typically on an elevated tip-sample distance (a few tens of nanometers).

The surface potential is measured by applying an AC bias (V_{AC}) with a frequency (ω) to the tip. A capacitive force is induced between the surface and the cantilever, making the cantilever oscillate. This capacitive force depends on the potential difference (V_{sp}) between the tip and the sample, and a DC bias (V_{DC}) can be used to decouple the surface potential contribution in the capacitive tip oscillation signal.

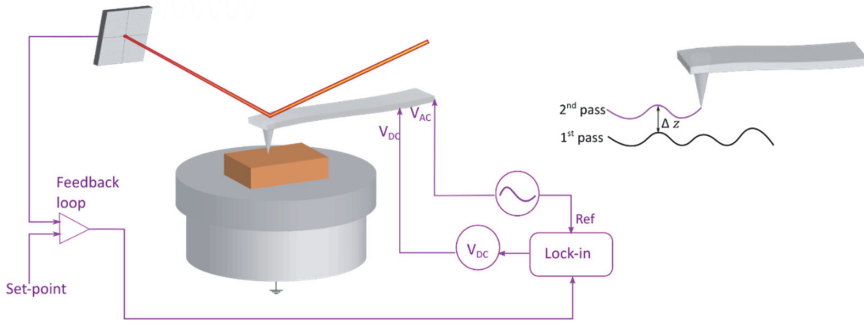

Figure 3-31 Schematic of the setup for the second pass in KPFM. The tip is raised to a fixed distance (Δz) above the surface determined in the first pass (illustrated in black). An AC bias is applied to the tip, which causes the tip mechanically oscillate due to the potential difference between the tip and the sample. These oscillations are detected, and the feedback loop adjusts the DC voltage to nullify them. The nullification of this force component by the DC voltage directly reveals the potential difference.

To see how this can be done, we approximate the tip-sample system as a parallel plate capacitor. The capacitive force is given by[234–236]:

$$F = \frac{1}{2}\frac{\partial C}{\partial z}V^2 \qquad \text{Equation 3-12}$$

where F is the attractive force between the plates, V is the voltage across the capacitor (that is, the potential difference between the two plates), and $\frac{\partial C}{\partial z}$ represents the change in capacitance C concerning the separation distance between the plates.

The total potential difference in our system is then given as the potential difference between the tip and the sample. With both AC and DC bias applied, this gives:

$$V = (V_{DC} - V_{sp}) + V_{ac} \sin(\omega t) \quad \text{Equation 3-13}$$

Combining Equation 3-12 and Equation 3-13, and using the identity $sin^2\,\theta = \frac{1}{2}(1 - cos\,2\theta)$, we get:

$$F = \frac{1}{2}\frac{\partial C}{\partial z}\left\{\left[(V_{DC} - V_{sp})^2 + \frac{1}{2}{V_{AC}}^2\right] + 2\left[(V_{DC} - V_{sp})V_{AC}\sin(\omega t)\right] - \left[\frac{1}{2}V_{AC}^2\cos(2\omega t)\right]\right\} \quad \text{Equation 3-14}$$

Due to the non-linear relation between force and potential, we thus get 0ω, 1ω, and 2ω harmonics in the signal, and by using a lock-in amplifier, one can qualitatively see how these change across the sample surface. At the same time, the 1ω harmonic vanishes when the applied DC voltage is equal to the surface potential ($V_{DC} - V_{sp} = 0$), enabling us to quantitatively measure the surface potential by introducing a feedback loop with V_{DC} as the output parameter, and the first harmonic as the process variable with the setpoint equal to 0. Accordingly, the value of V_{DC} is acquired by the feedback loop on a point-by-point basis during the second pass, composing a map of the surface potential across the scanned area.

Finally, it should be noted that multiple factors can contribute to the real potential difference, such as the work function difference between the tip and surface[235], trapped charges[237], and applied voltages between the tip and the sample[236]. Therefore, KPFM is often considered a pseudo-quantitative technique, providing accurate potential differences but not necessarily identifying the specific contributors. In this work, KPFM is utilized for assessing relative variation in surface potential.

4. Controlling local electronic transport phenomena by oxygen defects in $ErMnO_3$

The outstanding chemical flexibility (section2.2.4) of $ErMnO_3$ makes defect engineering a powerful tool to manipulate its electronic properties. Oxygen defects have been proven to have a significant impact on the electric conductance of metal oxide semiconductors [238,239], including $ErMnO_3$ [109,111]. These defects can be locally generated and mobilized by an electric field [240–242], offering exceptional control over electronic transport behaviors with nanoscale spatial resolution. Charge-neutral interstitial-vacancy pairs, anti-Frenkel defects (section 2.2.4.3) have gained attention as a minimally invasive type of defect that allows for controlling the electronic transport behavior of $ErMnO_3$ [107]. It has been demonstrated that their creation makes it possible to enhance the electronic conductance by orders of magnitude while preserving its initial ferroelectric properties in $ErMnO_3$, enabling minimally invasive defect-based property engineering [107,240].

In this chapter, building up on the previous study [107] of creating anti-Frenkel defects to write nanoscale conducting features, we explore the evolution of the anti-Frenkel defects under electric fields and their potential functionality beyond enhanced conductance. This chapter starts with the creation and response of anti-Frenkel defects under varying experimental conditions and the temporal stability of the associated electronic changes (section 4.1). By combining surface characterization (section 4.2) with atomic scale local composition and structure analysis (section 4.3), it is shown that anti-Frenkel defects undergo spatial separation under long-term exposure to electric fields, foreshadowing the generation of more advanced electronic components such as n-p-n bipolar junction.

4.1. Creation and manipulation of anti-Frenkel defects

Anti-Frenkel defects have been successfully generated using the electric field under a cAFM tip, allowing the writing of highly conductive features on the surface of otherwise poorly conducting $ErMnO_3$ single crystal [107]. This section starts by revisiting the creation process of anti-Frenkel defects using the cAFM tip and further tuning the applied writing voltage and duration to investigate time-voltage-dependent variations. This aspect involves assessing local conductance changes to understand the defect dynamics under the electric field (section 4.1.1). To figure out the determinants of this process and establish a comprehensive understanding on the electric field driven evolution of the defects, SPM tips with different radii (section 4.1.2), samples with diverse atmospheric histories (section 4.1.3), and different writing atmospheres (section 4.1.4) are used for the writing process. In the end, the temporal stability of the written structures is investigated.

4.1.1. Time-voltage dependence

This section presents the systematic creation and evolution of anti-Frenkel defects under applied electric fields.

The experiments are performed on $Er(Mn_{0.998},Ti_{0.002})O_3$ single crystals with (001) orientation (out-of-plane polarization), denoted $Er(Mn,Ti)O_3$ in the following. The samples were grown by Yan et al. [243] using the pressurized floating-zone method and subsequently prepared using the standard sample preparation procedure: oriented by Laue diffraction, and cut into 1mm-thick small pieces with polarization directions along one of the surface edges, which yields specimen with well-defined out-of-plane polarization. The samples were lapped with an Al_2O_3 (9 µm grain size) fluid on a cast iron lapping plate, and polished with silica suspension (Logitech, SF1 polishing suspension, pH= 9.0-10.5) on a polyurethane plate. Following this, the samples were annealed in 5% H_2/N_2 atmosphere at 300 °C for 48 hours, analogous to the procedure applied in our previous study [107].

An electrically bias cAFM tip is used to write anti-Frenkel defects. Figure 4-1a illustrates the experimental setup with the key components. During the writing process, the tip is grounded while the voltage is applied to the sample disk. For all the writing procedures, a negative bias voltage (U^{write}) is applied. Positive writing voltages were also tested but mainly resulted in surface damage under excessively high voltages, visible in AFM topography scans (not shown). This finding agrees with previous studies [107], where it was ascribed to an asymmetric response caused by the formation of a Schottky barrier at the tip-sample interface[148,244]. Conversely, for all the cAFM reading scans, positive voltages U^{read} are applied.

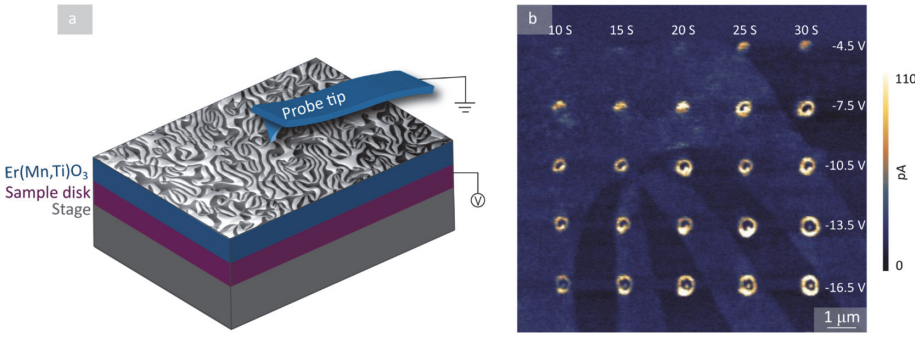

Figure 4-1. Time-voltage dependent writing of anti-Frenkel defects. (a) Illustration of the experimental setup for defect writing, in which the bias voltage is given to the sample disk and the tip is grounded. (b) cAFM image of a defect matrix written by tip 1 (DCP 20, 100nm) using a range of voltages and times on an out-of-plane $Er(Mn,Ti)O_3$ sample under ambient conditions. The detailed applied writing voltages and times are indicated in the image. The image is recorded with a positive reading voltage of 15V with the same tip.

To learn about the time-voltage evolution of the anti-Frenkel defects, we write a defect matrix where the writing time (contact duration) varies along one axis and the writing voltage along the other. This is done by programming the cAFM such that the tip lands on the sample surface

to apply a certain bias voltage for a designated time period, retracts, and then moves to the next location to repeat the process. Once the writing procedure is finished, a standard cAFM scan is conducted on the modified area, yielding a conductance map as shown in Figure 4-1b.

Figure 4-1b displays a representative conductance map of a 5×5 defect matrix, written with varying time and voltage by cAFM using a diamond-coated probe tip DCP 20 (curvature radius: 100 nm). The writing time (t^{write}) ranges from 10 s to 30 s along the horizontal axis, while the writing voltage (U^{write}) is -4.5 V to -16.5 V (vertical axis). The image, recorded with a positive voltage of U^{read}= 15 V, reveals two qualitatively different regimes on the standard out-of-plane oriented domain contrast [22] of the background. For low U^{write} (-4.5 V and -7.5 V) and short durations (<20 s for U^{write}=-7.5 V), a conducting dot appears. This is qualitatively the same feature as the conducting wires/dots, presented previously (section 2.2.4) [107]. For high U^{write} (-7.5 V and -16.5 V) and longer times (≥25 s for U^{write}=-7.5 V), a more complex structure appears, which consists of a conducting central dot and a conductive outer ring, separated by an insulating intermediary region. This pattern will be referred to as conducting dot-ring structure in the following. The diameters of the conducting dot-ring structures in Figure 4-1b are between 190 nm and 310 nm. Both the duration and voltage are able to trigger the evolution from the dot structure into the dot-ring structure, indicating that the lateral dimension is tunable by controlling the writing parameters.

The previous publication [107] has explained the origin of the conductive dot structure, attributing its formation to the anti-Frenkel defects pair induced by the electric field. Such defect pairs are composed of an oxygen interstitial O_i'' and an oxygen vacancy $V_O^{\bullet\bullet}$. In order to gain additional insight into the origin of the dot-ring structure, further writing experiments are conducted using different AFM tips, samples, and atmospheric environments.

4.1.2. The effect of tip radius and tip material

To understand how the tip radius and tip material affect the writing of the dot-ring structures, different SPM probe tips were tested. Firstly, two diamond-coated tips with different radii are used for writing and the subsequent reading:

Tip 1: Nitrogen-doped diamond probe tip DCP 20, with curvature radius: 100 nm.

Tip 2: Boron-doped diamond probe tip DEP-01, with curvature radius: 10 nm.

More information about tips 1 and 2 can be found in the Appendix. A dot-ring structure written by tip 1 (100 nm) with U^{write}= -21.0 V and t^{write}=60s is shown in Figure 4-2a, with an outer diameter of about 450 nm is observed, similar to the structures written by high voltage and long duration in Figure 4-1b. Figure 4-2b presents the defect structure written by tip 2 (10 nm) with similar parameters: U^{write}= -22.5 V and t^{write}=60. This tip also produced a qualitatively similar dot-ring structure, but with a notably larger diameter of about 950 nm compared to the

450 nm written by tip 1. The larger diameter obtained under similar parameters suggests that the emergence of the defect structure is determined by the contact area between the tip and the sample surface. The sharper tip gives rise to a higher electric field for the same applied voltage, thereby causing different defect migration and diffusion behaviors[245,246].

According to the Hertz contact model, the cAFM tip is approximated as a sphere in contact with the $ErMnO_3$ surface. The radius (a) of the contact area between the tip and sample can be calculated using Equation 4-1 [247]:

$$a^3 = \frac{3FR}{4E^*} \qquad \textit{Equation 4-1}$$

where F represents the applied force, R denotes the tip radius, and E^* the effective elasticity modulus. The value of E^* is determined to be 119 GPa, based on setting Young's modulus at 220 GPa and Poisson's ratio at 0.277 [248] for both the tip and the sample.

For tip 1 (100 nm), the spring constant was calibrated as 92.68 nN/nm, with a deflection inverse optical lever sensitivity (InvOLS) of 17.73 nm/V, and a setpoint of 1V applied. Based on these parameters, the radius of the contact area is calculated to be approximately 10.11 nm. In the case of tip 2 (10 nm), using a spring constant of 2.39 nN/nm, an InvOLS of 86.71 nm/V, and a setpoint of 1V, the radius of the contact area is calculated to be about 2.35 nm.

Nardi et al. [249] conducted a finite-element calculation on a metal-insulator-metal (MIM) device, revealing that reducing the contact area from 50 nm to 5 nm doubles the maximum electric field. This finding is consistent with the more pronounced effect, i.e., the larger lateral dimension of the dot-ring structure, observed in our experiment. Thus, the data in Figure 4-2 leads to the conclusion that the transition of dot-like conducting regions to dot-ring structures strongly depends on the electric-field strengths, consistent with the matrix in Figure 4-1, revealing the tip radius as an additional important degree of freedom in the writing process.

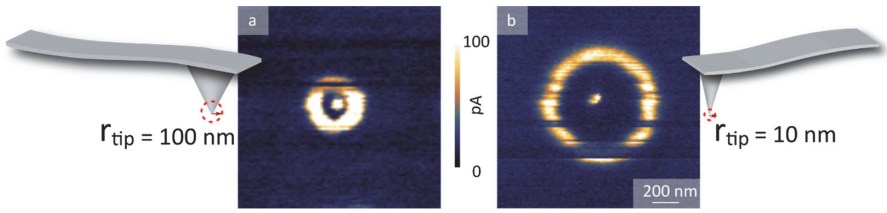

Figure 4-2. Defects written by two kinds of tips with different radii. (a) Defect structure written by tip 1, tip curvature radius: 100 nm; U^{write}=-21.0 V, and t^{write}=60s, U^{read}=16.5 V.(b) Defect structure written by tip 2, tip curvature radius: 10 nm; U^{write}= -22.5 V and t^{write}=60s, U^{read}=12.0 V. The scale bars for the size and current value are identical in a and b.

Beyond tip radius variations, we also tested tips coated with different materials for the writing process, such as Ti/Ir (ASYELEC.01-R2, Oxford Instruments) and W_2C (HA_FM/W2C+, NTMDT Spectrum Instruments). The writing processes were identical, but acquiring good cAFM contrast for the subsequent reading scan proved challenging as we lost the current contrast after long

exposure to a negative voltage (not shown). The result can, however, be monitored by a complementary technique such as SEM (section 4.1.4).

4.1.3. Atmospheric history

The defect matrix displayed in Figure 4-1 is representative, and qualitatively equivalent patterns can be written in different regions on the same sample, as well as on different samples with the same thermal and atmospheric history. Up to this point, all the samples used for the defect writing were annealed in 5% H_2/N_2 atmosphere, analogous to the previous study [107]. In the next step, the atmosphere was changed to a pure N_2 atmosphere, following the same temperature profile, allowing us to test if the hydrogen plays a specific role in the defect writing. Figure 4-3a illustrates the temperature profile of the annealing procedure: heat up from room temperature (RT) to 300 °C at a ramp rate of 5 °C/min, hold at 300 °C for a dwell time of 48 hours, then cool to RT at a rate of 5 °C/min. The blue line represents the 5% H_2/N_2 atmosphere annealing program, while the orange dashed line corresponds to the pure N_2 atmosphere annealing.

For reference, Figure 4-3b shows the cAFM data obtained from $Er(Mn,Ti)O_3$ after annealing in 5% H_2/N_2 atmosphere. It displays a typical out-of-plane contrast of the two domain types, with -P domains seeing more conductive than +P domains due to different Schottky barriers at the tip-sample interface (-P bright, +P dark) [148]. In contrast, the sample annealed in a pure N_2 atmosphere (Figure 4-3c) reveals conductive domain walls and less pronounced domain contrast compared to Figure 4-3b. The appearance of conducting domain walls is surprising since the charge state of the walls is neutral. This phenomenon agrees, however, with findings from previous studies [69,148], where it was observed that the conductance of out-of-plane $ErMnO_3$ samples can be either dominated by domain contrast or domain wall contrast, depending on their thermal history. This emphasizes the significant role of defects chemistry for the charge transport characteristics in $ErMnO_3$. The cAFM data in Figure 4-3 corroborate this finding, showing qualitatively different cAFM contrast after different annealing schemes. This intriguing defect chemistry warrants further investigation, but the key information here for defect writing is that the defect chemistry and electric response differ between the N_2 annealed sample and the 5% H_2/N_2 annealed sample in the near-surface region probed by cAFM.

Following annealing, the defect writing process (as described in section 4.1.1) is repeated on the sample annealed in a pure N_2 atmosphere, leading to similar conducting features to those observed in the initial 5% H_2/N_2 annealed sample. Figure 4-3d and e compare the dot-ring structures written on both samples. Figure 4-3d presents a dot-ring structure from the 5% H_2/N_2 annealed sample, written with U^{write}= -12 V and t^{write}= 5 s. This written structure is considerably more conductive compared to the surrounding domains, as indicated by the current profile on the right of Figure 4-3d. Figure 4-3e shows a dot-ring structure written on the sample annealed

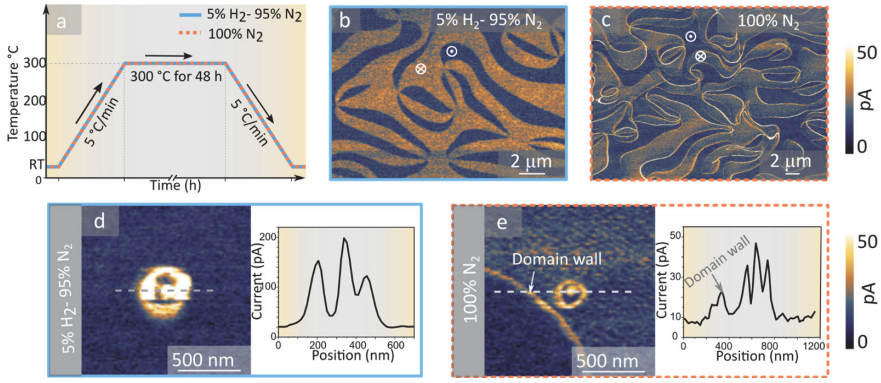

Figure 4-3. Samples annealed in different atmospheres and written defect structures. (a) Annealing procedure, blue line: 5% H_2/N_2 atmosphere; orange dashed line: 100% N_2 atmosphere. (b) cAFM image of sample after annealing in 5% H_2/N_2 atmosphere. Recorded by a DCP 20 tip, with 13.5 V reading voltage. (c) cAFM image of sample after annealing in 100% N_2 atmosphere. Recorded by a DCP 20 tip, with 12 V reading voltage. (d) cAFM image (left) and the current profile (right) of the defect structure written on the 5% H_2/N_2 annealed sample. (DCP 20 tip, Uwrite=-12.0 V, and t^{write}=5s, U^{read}=15.0 V). (e) cAFM image (left) and the current profile (right) of the defect structure written on the N_2 annealed sample. (DCP 20 tip, U^{write}=-30.0 V, and t^{write}=5s, U^{read}=16.5 V).

in pure N_2 atmosphere with U^{write}= -30 V and t^{write}= 5 s (different writing voltages have been tested, and for this experiment, a voltage has been chosen that leads to a well-defined dot-ring structure). Here, a conducting domain wall is visible, consistent with Figure 4-3c, but the conductance of the written structure is higher, as shown by the current profile on the right of Figure 4-3e. Upon closer inspection of the generated defect structure, both 5% H_2/N_2 and pure N_2 atmosphere annealed samples exhibit similar written defects. From this experiment, it can be inferred that hydrogen in the annealing atmosphere is not the driving mechanism, although it possibly promotes the writing process.

In addition to the experiments performed on samples annealed in reducing atmospheres (H_2/N_2 and N_2), the same defect writing process was applied to as-grown single crystal samples. In this case, no significant changes can be observed in cAFM and SEM even after applying significantly higher writing voltages of up to U^{write}= -135 V with t^{write}= 30 s. This implies that the applied annealing is crucial to facilitate efficient defect writing, providing additional insight into the underlying mechanism.

Considering the annealing temperature of 300°C, cation diffusion seems unlikely to happen [109] and can, therefore, be excluded as the driving force. However, it is well-established that the oxygen stoichiometry in hexagonal manganites can be tuned via thermal and atmospheric history [109,111,113,250]. As the structure of h-$RMnO_3$ can accommodate both oxygen vacancies and interstitials (section 2.2.4) [111], the different responses of annealed and as-grown samples likely lie in the concentration of oxygen defects. Skjærvø et al.[109] demonstrated a reversible control of the oxygen stoichiometry $3+\delta$ by alternating between O_2 and N_2 atmosphere at 300 °C for porous polycrystalline $YMnO_3$. It was found that the oxygen stoichiometry decreased when

switching to N_2 atmosphere. In this context, H_2/N_2 annealing could further decrease the oxygen stoichiometry, possibly through reducing oxygen interstitial concentration, as inferred from the p-type conductivity after annealing. The identification of p-type conductivity [22] is based on observations that the downward polarized domains are more conducting than upward ones. Considering the crystal growth process of our samples, the growth chamber was pressurized to 0.8 MPa with an Ar gas flow balanced with 5% O_2 during the whole growth process in order to prevent the Mn from evaporating [243]. This suggests that the samples progressively reduced relative to the as-grown sample and that the reduced oxygen content promotes the writing on anti-Frenkel defects and their electric-field driven splitting. The finding indicates that the formation of anti-Frenkel defects in $Er(Mn,Ti)O_3$ requires a specific starting concentration of oxygen defects, which explains why the effect is not observed in all hexagonal manganite samples. The latter points toward a complex defect chemistry that requires further experimental investigation and theoretical calculation for more quantitative information, which, however, is beyond the scope of this work.

4.1.4. Writing environments

For the writing processes discussed so far, we used our Oxford Cypher ES AFM working in an ambient atmosphere. To exclude potential extrinsic effects that arise from the writing environment after sample annealing, we further wrote defects in vacuum. The respective writing process was implemented together with Dr. Erik D. Roede and Dr. Kasper A. Hunnestad.

Figure 4-4 illustrates the experimental setup for the writing process in vacuum using a FIB-SEM chamber. Two micromanipulators (nanoprober miBot™, IMINA technologies) outfitted with tungsten probes are used to realize the electrical writing. As depicted in Figure 4-4, a glass panel (illustrated in green color) is used as an isolator, preventing any undesired current flow through the sample stage. Subsequently, an out-of-plane $ErMnO_3$ sample mounted on a conducting disk is positioned on top of the glass panel. Two micromanipulators are connected to the source/measure unit (SMU), terminating in the two tungsten (W) probes, which are positioned to connect to the sample surface (illustrated with green and white stripes) and the sample disk (in blue), respectively.

After identifying the region of interest (ROI) using the electron beam, the micromanipulators are used to control the landing of the W probe within the ROI. A noticeable change in SEM contrast can be observed in the e-beam channel due to different surface charging once the W probe 1 makes contact. Following this, as illustrated in Figure 4-4, probe 2 is connected to the sample disk, establishing an electric connection through which the bias voltage from the SMU is given to probe 2. In this configuration, the resulting circuit is comparable to the circuit in cAFM, where the bias voltage is applied to the sample disk while grounding the surface probe tip.

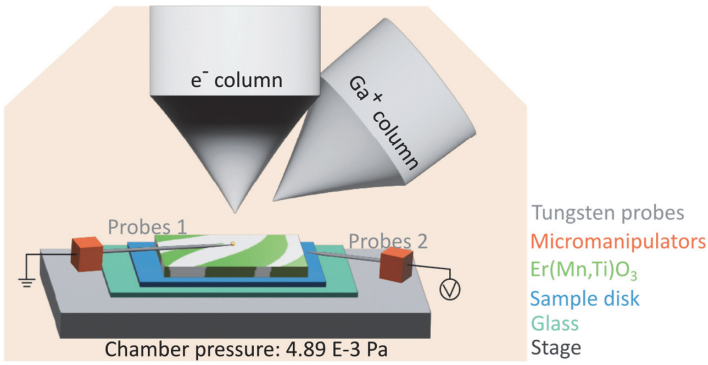

Figure 4-4. Illustration of the setup for writing conducting features using Mibot within a FIB chamber in a vacuum environment. The two W probes (gray color): one for applying bias voltage (Probe 2) and one for grounding the sample (Probe 1). The W probes have a tip radius of 1 µm, a shank diameter of 0.5 mm, and a length of 20 mm.

To write conducting feature analogous to the cAFM experiments discussed before, a negative bias voltage is applied via probe 2 for a certain time, with probe 1 grounded. The electron beam is then used to visualize the written structures (see Figure 4-5d-f). Using a sufficient bias voltage (U^{write}= -100 V) and varying the time for which the voltage is applied, we observed a defect structure evolution consistent with the cAFM experiments. The higher writing voltage required here, compared to that used in the cAFM writing process, can be attributed to the large radius of the probe, which is 1 µm.

For reference, Figure 4-5s a-c display again cAFM-based data, showing how written defect structures evolve from a conducting dot to a complex dot-ring structure with an insulating intermediate region, and the dot and the ring separate further with increased writing time t^{write}. Defect structures written in vacuum are revealed by the SEM images (Figure 4-5 d to f) and subsequent cAFM scans (Figure 4-5g-i). The cAFM images reveal an evolution from a single conductive dot (t^{write}= 5 s) to a characteristic conductive dot-ring structure as the writing time expands to 30 s and 240 s. Figure 4-5j presents the current profiles for the different stages of defect structure evolution, as marked by the dashed lines in Figure 4-5g-i. To a better visibility, the y-axis values for the structures written with 30 s and 240 s have been offset, increased by 150 and 300, respectively. The evolution from a single peak to a tri-peaked profile is visible as the writing time extends, showing qualitatively the same behavior as observed under ambient conditions. This finding confirms that defect formation is a process intrinsic to the material system, excluding that it originates from extrinsic effects related to the writing procedure. The primary hypothesis is that longer exposure time to the electric field leads to the spatial splitting of the O_i'' and $V_O^{\bullet\bullet}$ that from anti-Frenkel defects, causing the evolution of the written structures from conducting dot to dot-ring structure.

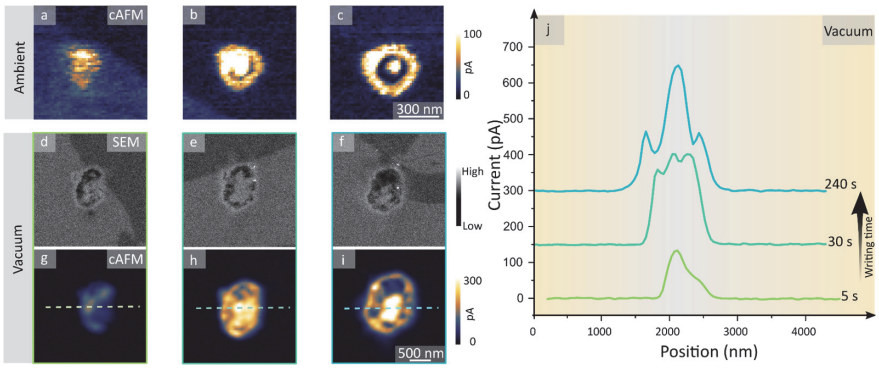

Figure 4-5. Evolution of defect structures in different writing environments. (a-c) Defect structures written by cAFM in ambient environment. The structures evolve from a conducting dot to a dot-ring structure as the writing time increases. (a) U^{write}= -12.0 V, and t^{write}= 1 s; (b) U^{write}= -12.0 V, and t^{write}= 5 s; (c) U^{write}= -12.0 V, and t^{write}= 30 s. (a)-(c) are recorded by a DCP-20 tip with 15V reading voltage. (d-f) SEM images of defect structures written by a tungsten probe in the FIB-SEM chamber, with U^{write}= -100.0 V, and t^{write}= 5 s, 30s, and 240 s, respectively. The image was captured by a TLD detector at 3.0 kV and 0.1 nA after plasma cleaning (Ar plasma for 1 minute) to remove potential contaminants on the sample surface after the writing process. (g-i) Subsequent cAFM image of the written structures, using a CDT-NCHR-10 tip with U^{read} of 13.5 V. (j) Current profiles for defects structures written by different t^{write}, showing an evolution from a single peak to a triple peak. For better visibility, profiles for 30 s and 240 s have been offset, with their y-axis values increased by 150 and 300, respectively.

4.1.5. Temporal stability

The comprehensive investigation of the writing parameters of conducting defect structures, including the time-voltage evolution, tip radius, and environment, reveals a general trend, which is the progression from a conductive dot to a dot-ring structure. To understand the physical properties of the evolving dot-ring structure and potential applications opportunities, the temporal stability of the dot-ring structure is investigated in this part.

The written defect structures keep their initial shape and transport behavior after writing and are stable under SPM scans and SEM characterization on the timescale of days, which can be inferred from correlated cAFM, PFM, and SEM scans (section 4.2). We remeasured the written dot-ring structure using cAFM after keeping it in an ambient environment in our lab for six months. Figure 4-6a displays a cAFM image of a defect structure immediately after writing, appearing as an enhanced dot-ring structure with the outer ring highlighted by a red dotted circle. The diameter of this as-written structure was 0.54 µm, and a clear intermediate insulating region is visible. After six months, a cAFM scan of the same region reveals a significant change in the structure. As indicated by the red dotted circle, displaying the diameter of the original dot-ring structure in Figure 4-6b, the local transport properties have changed substantially. Instead of a well-defined dot-ring structure, our investigations find a blurred conductive dot after six months, and the enhanced conductance has noticeably degraded. Figure 4-6c compares the current profiles across the as-written defects structure and the six-month-old structure. The once-pronounced tri-peak profile has evolved into a broader region of slightly enhanced conductance. This degradation trend is corroborated through observation

of other dot-ring structures, exhibiting qualitatively the same evolution as a function of time (not shown). For reference, time-dependent data obtained on a written nanowire adapted from the previous study [107] is presented in Figure 4-6d.

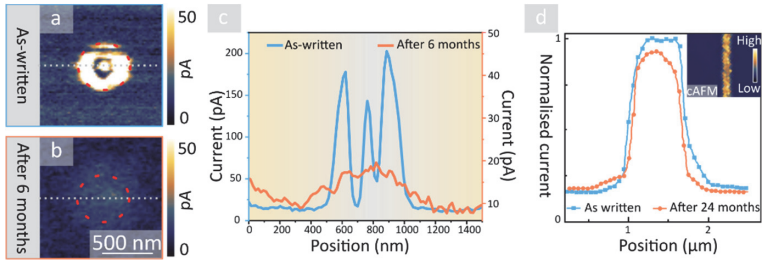

Figure 4-6. Stability of the written defect structure. (a) As-written state of the conducting dot-ring structure written. (b) After 6 months. (c) Current profile of the as-written defect structure and the degraded structure after 6 months. (d) Current profile of the as-written conducting line, and after 24 months, no obvious degradation. (d) is adapted from reference [107] *with permission.*

Written dots and nanowires (low voltage, short writing time) owe their enhanced conductance to anti-Frenkel pairs and were stable for 24 months, as shown in the previous study [107]. Here, we expanded the experiments towards time-dependent measurements of the dot-ring structures. The very different time evolution compared to the nanowire indicates that the dot-ring structure is less stable after the O_i'' and $V_O^{\bullet\bullet}$ that from the anti-Frenkel defect move far away from each other under the electric field. Based on our hypothesis that the dot-ring structure is evolved by the spatial splitting of oxygen vacancies and oxygen interstitials, a possible reason can be a lower backward migration barrier after splitting or the migration of oxygen interstitials in an ambient environment at room temperature due to its lower migration barrier [109,111,112]

4.2. Local response beyond conductance

To verify our hypothesis and acquire more information on the physical properties of the written dot-ring structure, we perform complementary surface characterization via SPM (scanning probe microscopy) and SEM methods, with cAFM results as the reference. Moreover, a numerical simulation is used to explain the evolving process, consistent with the work presented in reference [107].

4.2.1. Piezoresponse of dot-ring structures

To investigate the local piezoresponse and potential correlations with the local ferroelectric properties, we perform resonant PFM measurements (section 3.3.3).

Figure 4-7a displays a cAFM image of four dot-ring defect structures written on a single crystal sample $ErMnO_3$ surface with out-of-plane polarization following the same procedure as described in section 4.1.1. The lower two structures appear more blurry, which might be related to the surface contact during scanning. Figure 4-7 b and c present the vertical phase and amplitude channels of PFM, respectively, measured at the same position. The four dot-ring

structures are clearly visible in the PFM data as well. It is notable that the inner dots and the outer rings manifest differently in the PFM contrast. In Figure 4-7b, the inner dots exhibit a low phase (blue), while the outer rings show a larger phase (yellow) in the phase channel of PFM. This data reflects a locally altered piezoresponse, which we attribute to the local transport behavior. Note that this is different from switching-induced changes, which can also affect both the piezoresponse and conductance[18].

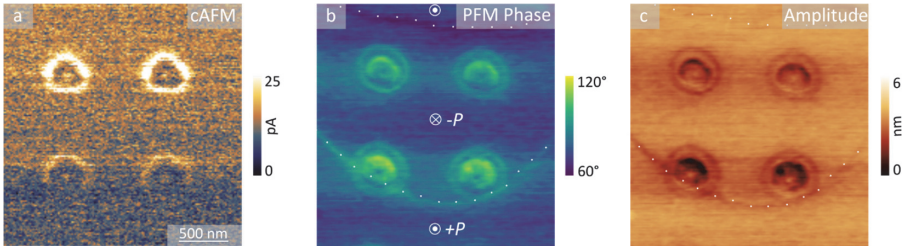

Figure 4-7. Resonant PFM results from a defect matrix. (a) cAFM image of the defects matrix. (b) PFM vertical phase channel from the same area as (a), two domain walls are marked by white dotted lines. The domain polarization is recongnised from the imprint in the sample topography and marked in white color. The imprint of the domain contrast in topography is caused during chemical-mechanical etching by domain-selective etching, during which the +P domain are etched stronger than -P domains[77]. (c) PFM vertical amplitude image from the same area, with the two white dashed lines highlighting the two domain walls. The scale bar in (a) is applied for all images here.

Switching and/or polarization-dependent contributions are excluded for the following reasons. Firstly, Figure 4-7 b and c show no pronounced contrast between +P and -P domains, which is typically seen on out-of-plane surfaces (see, e.g. Figure 2-10a). Instead, only the two domain walls are visible as faint lines, highlighted by white dashed lines. Thus, it is clear that the phase contrast and polarization direction are not one-to-one correlated in this data set. Moreover, as can be seen in the lower left of Figure 4-7 b and c, one of the defect structures expands over a +P and -P domain without any detectable impact on the domain wall position. Furthermore, ferroelectric domains written at room temperature are not stable in hexagonal mangnites[101] (see section 2.2.2.2). Thus, both our experimental observations and previous studies exclude the possibility that the electric field under the SPM tip can induce new domains on the $ErMnO_3$ surface in the same way as the conventional AFM-tip written domains in perovskite crystals [251,252]. Therefore, the primary conclusion gained from the PFM data in Figure 4-7 is that the piezoresponse change at the dot-ring structures is not a consequence of polarization switching. A possible explanation for the difference in the piezoresponse is non-piezoelectric effects [233], such as the ionic activity of the surface [253] and enhanced conductivity [112], which might disrupt the contact resonant frequency in resonance mode [254].

4.2.2. Scanning electron microscopy and numerical simulations

As a non-contact and high-resolution method that is sensitive to local variations in conductance [126], SEM (section 3.1) holds the potential to provide additional insight into the

electric conductivity of the dot-ring structure, offering a more comprehensive understanding of the dot-ring structures.

Figure 4-8a and b display cAFM and the SEM images of the same structure, respectively. The cAFM data displays the conductance contrast of the written dot-ring structure, as analyzed in section 4.1.1. In line with the cAFM data, the SEM shows a similar dot-ring structure with dark contrast. The graph in Figure 4-8c compares the current profile obtained from cAFM (dark gray) and the SEM intensity (orange) across the defect structure along the lines marked in Figure 4-8a and b.

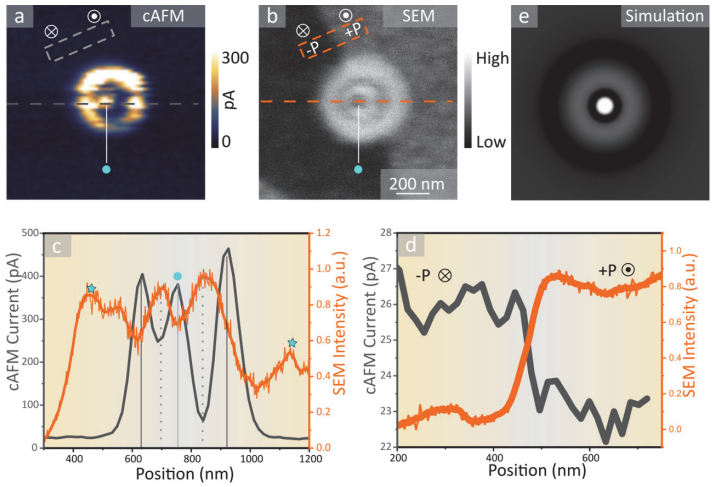

Figure 4-8. Overview of cAFM, SEM, and simulated data. (a) cAFM image of a written defect. (b) SEM image of the same defect as in a. (c) Comparing the cAFM current profile (dark gray) and the SEM intensity (orange) along the lines marked in (a) and (b), with the blue dot highlighting the position of the inner dot. The SEM curve is smoothed by the Savitzky-Golay method in Origin software with a window size of 20 and then normalized from 0 to 1. (d) Comparing the current profile (dark gray) and the SEM intensity (orange) of the background domains; both curves are averaged over the rectangle region highlighted in (a) and (b). The background domain contrast in cAFM image in (a) cannot be directly seen because of the pronounced enhancement of conductance at the dot-ring structure, but it can be seen from the raw data in the dark gray curve. (e) Simulation of the migration of two kinds of oppositely charged defects in one system, the white color indicates a higher concentration of defects (adopt from reference [107]).

The blue dot in Figure 4-8a, b, and c pinpoints the position of the inner dot. It is evident that the peak of the current profile aligns perfectly with the local minimum of the SEM intensity, corresponding to the inner conducting dot in cAFM. The two neighboring minima in the current profile match the peaks in SEM intensity, as indicated by the gray dotted lines in Figure 4-8c, correlating with the insulating intermediate region in cAFM. Likewise, the current profile's two maxima on the left and right sides, representing the conductive outer ring in the cAFM map, coincide with the local SEM intensity minima, as indicated by black lines in Figure 4-8c. (Note that an additional pair of peaks is resolved in SEM, indicated by two blue stars in Figure 4-8c, which will be discussed later). The similarity of the dot-ring structure in cAFM and SEM indicates a direct correlation, where the black inner dot in SEM corresponds to the conductive dot in the

cAFM image, and the black ring corresponds to the conductive outer ring. Qualitatively the same behavior, i.e., opposite contrast in cAFM and SEM, is observed for the background domain contrast, where the bright domain in cAFM corresponds to dark contrast in SEM (Figure 4-8d).

After establishing that regions with enhanced (suppressed) conductance appear dark (bright) in SEM, we turn to the additional contrast seen in the SEM map in Figure 4-8 b and c. As discussed above, the bright contrast within the dot-ring structure indicates lower conductance. In this context, the extra bright outer contrast in SEM hints at a more insulating ring at the periphery of the dot-ring structure, which is not resolved by cAFM and, hence, possibly below the detection limits of cAFM setup. To understand this additional feature, we revisit previous simulations.

In the previous studiey [107], it has been established that the formation of the initial conductive dot (see, e.g., Figure 4-5a) is due to the creation of anti-Frenkel defects under the influence of an electric field. This process and the subsequent migration of charged oxygen defects was modeled using a simple 2D numerical simulation. According to the model, in the presence of an electric field E, oxygen interstitials (O_i'') and oxygen vacancies ($V_O^{\bullet\bullet}$) are generated at a rate g. Meanwhile, due to their opposite electric charge, they move in opposite directions and recombine at a rate r.

This dynamic process can be expressed according to the following equations [107]:

$$\frac{\partial n_i}{\partial t} = \nabla\left(D\nabla n_i - n_i\mu E\right) + g|E| - r\left(n_i - n_i^0\right) \qquad \textit{Equation 4-2}$$

$$\frac{\partial n_o}{\partial t} = \nabla\left(D\nabla n_o + n_o\mu E\right) + g|E| - r n_o \qquad \textit{Equation 4-3}$$

where n_i and n_o represent the densities of O_i'' and $V_O^{\bullet\bullet}$, respectively. n_i^0 denotes the concentration of O_i'' in the absence of an electric field. In $ErMnO_3$, O_i'' are responsible for the majority carriers (holes) [109]. D is the coefficient of the defect diffusion, and μ is the relative mobility between O_i'' and $V_O^{\bullet\bullet}$.

For a non-zero electric field, O_i'' and $V_O^{\bullet\bullet}$ are generated and concentrate in the field-affected area, giving rise to the initial dot structure with enhanced conductance. Longer exposure causes a separation of the O_i'' and $V_O^{\bullet\bullet}$, influencing the conductivity distribution. This effect is represented in Figure 4-8e, where brighter colors indicate higher conductivity and defect concentration. This simulated result is in excellent agreement with the structure seen in SEM, but with inverted color schemes: the bright region in the simulation corresponds to the black region in SEM, and vice versa. Also the extra outer contrast observed in the SEM image, as mentioned before, is reproduced by the simulation, which can be explained by a minor defect concentration gradient due to the migration of the main defect species O_i'' from surrounding area into the high-field region.

This leads us to the conclusion that the origin of the dot-ring structure is a result of the spatial migration and splitting of O_i'' and $V_O^{\bullet\bullet}$. Their separation leads to the modified regions being spatially divided into regions accumulating different types of oxygen defects according to the direction of the electric field and the charge. In $ErMnO_3$, O_i'' and $V_O^{\bullet\bullet}$ are charge compensated by oxidation [109,255] and reduction [111] of Mn, acting as hole or electron donors, respectively, thereby enhancing p-type and n-type conductance, explaining the dot-ring structure measured by cAFM and SEM for high voltage and long exposure times.

4.3. Atomic-scale compositional and structural characterization

Having established that the dot-ring structure arises from the spatial separation of O_i'' and $V_O^{\bullet\bullet}$ under the electric field, this implies that the material close to the electrically biased tip separates into regions enriched with different defects, O_i'' or $V_O^{\bullet\bullet}$. To corroborate the separation into O_i'' and $V_O^{\bullet\bullet}$ rich regions and further investigate the experimental footprint of O_i'' and $V_O^{\bullet\bullet}$ within the dot-ring structure, we utilize atom probe tomography (APT) and high-angle annular dark-field scanning transmission electron microscopy (HAADF-STEM). The application of APT and HAADF-STEM allows for the analysis of the compositional variations and the local lattice arrangement in the modified area, respectively.

4.3.1. Atom probe tomography visualizing compositional variations

To perform the APT analysis, we extract a specimen from the modified region in the form of a needle, which is the standard shape required for the APT analysis as explained elsewhere [256]. This facilitates a comprehensive 3D analysis of the atomic positions with atomic-scale spatial resolution, enabling the visualization of variations in oxygen concentration from region to region. The APT experiments were conducted in collaboration with Kasper A. Hunnestad, who also provided the data in Figure 4-9 b and c.

Figure 4-9a illustrates the position at which the APT needle was extracted, which is perpendicular to the sample surface from the position of the conducting inner dot. To extract the APT needle, the inner dot of the dot-ring structure is first marked by an electron beam deposited marker and covered by a protective layer. A needle with a tip radius of less than 100 nm is extracted by FIB, as shown in Figure 4-9b. The “distance” indicates the direction away from the initial surface. Via electric field evaporation of the needle in a standard APT experiment, the 3D compositional data is obtained [205]. Selected compositional data from the APT analysis is presented in Figure 4-9 c (courtesy of Kasper A. Hunnestad).

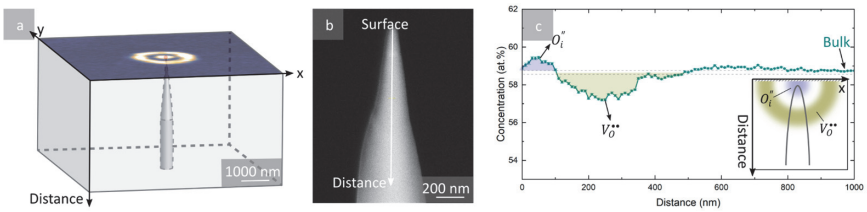

Figure 4-9. APT result from the dot-ring structure. (a) Illustration of the APT needle extracted from the region of interest. (b) SEM image of the APT needle. (c) Oxygen concentration profile along the long axis of the APT needle. Courtesy of Kasper A. Hunnestad.

The data points in Figure 4-9c display the oxygen concentration profile perpendicular to the surface under the inner conducting dot, extending from the surface to about 1 µm into the sample (indicated by the white arrow in Figure 4-9b). The plot is derived by integrating the data in the direction along the longitudinal axis of the needle. The region far away from the surface (from 600 nm to 1000 nm) is flat and serves as the benchmark for the oxygen concentration, representing the density within the unperturbed bulk area. Notably, distinct variations are resolved close to the surface, as illustrated in the inset of Figure 4-9c. Close to the surface, an increase in oxygen concentration is observed, hinting at the presence of O_i''. In contrast, a decrease in oxygen concentriation appears at a distance of 100 nm to 500 nm, indicating an accumulation of $V_O^{\bullet\bullet}$. The distance between the O_i''-rich region and the $V_O^{\bullet\bullet}$-rich region is very close, which may arise from an asymmetry of the dot-ring structure itself. The distance between two kinds of regions likely varies when observed from horizontal or vertical directions.

The APT analysis corroborates the simulated result shown in Figure 4-8e, indicating a separation of the regions within the dot-ring structure based on oxygen defects. Specifically, the inner dot region accumulates O_i'', followed by a recombination region and a $V_O^{\bullet\bullet}$-rich region. Furthermore, it indicates the dot-ring structure is actually a 3D structure with a depth of approximating 500 nm (illustrated in the inset of Figure 4-9c), as expected from the electric field-driven migration of charged oxygen defects.

4.3.2. HAADF-STEM characterizing the lattice structure

According to the simulations and the APT data, the dot-ring structure consists of different regions, each characterized by different defect accumulations extending hundreds of nanometers into the depth. To investigate potential structural change associated with the oxygen defects, we study the underlying atomic-scale structure in a FIB cut lamella using transmission electron microscopy (TEM) techniques.

Figure 4-10 presents the sample preparation process and provides a low-magnification overview image of the TEM lamella. Initially, a conducting dot-ring structure is created using U^{write}= -22.5 V and t^{write}= 60 s, analogous to section 4.1.1. Subsequently, SEM is used to image the same area, revealing the dot-ring structure with a darker contrast, as shown in Figure 4-10a.

Below the SEM image is a color bar, which serves as a reference for identifying different regions of the dot-ring structure, as indicated by the dashed lines. This color bar correlates with the color contrast in the SEM image: dark blue indicates conductive regions, while white represents insulating regions. This color index is consistently used throughout different stages of SEM and TEM/STEM imaging in the following for clarity to track each region.

After finding the written dot-ring structure in SEM, the next step is to mark its position. Considering the complexity of the structure, it is important to mark the exact position of the inner dot. This ensures that both the outer ring and the inner dot are included in the final lamella. To precisely mark the dot-ring defect, we zoom in on the electron beam channel, find the defect structure in high magnification using immersion mode, and deposit an “X” marker using Pt precursor gas with low electron beam current (50 pA). The center of the “X” marker sits on the inner dot (Figure 4-10b). In sequence, two additional “X” markers are deposited on the left and right side 1 µm away from the defect structure, aligning horizontally with the central marker. Figure 4-10b displays the SEM image of the markers, with the dot-ring structure highlighted by a red dot and circle. These markers offer an adequate reference system and ensure that the lamella undergoes straight milling in the preset direction (The rectangle in the center of the image results from carbon contamination [257] (section 3.1.2.6) after high-resolution SEM scans). The color bar under the SEM image is the same as in Figure 4-10a.

Following the marking, a standard extraction procedure for TEM lamellas [186] is conducted, and the milling processes for both sides of the lamella are guided by the markers. Figure 4-10c displays an SEM image of the final TEM lamella. Here, the bright contrast indicates a very thin region with electron transparency[258]. The red arrow marks the position of the dot-ring structure under the center of the middle marker. The inset presents an SEM image of the entire final TEM lamella, indicating a thinner area surrounding the target structure. The rest remains thicker to ensure optimal flatness of the defect structure region. The color bar below the SEM image represents a guide to the eye to the corresponding regions, as in (a) and (b).

After the sample preparation, STEM imaging was conducted by Dr. Ursula Ludacka using a Jeol JEM-ARM200F microscope. Figure 4-10d presents an overview STEM image captured with a CCD camera, showing the existence of different regions under the marker. Through careful comparison of size and relative positions to the marker in the SEM image, the bright region marked with a red dot aligns with the conducting inner dot region, which is the exact spot where the tip was placed during the writing process. The regions marked as regions ① and ② align with the insulating intermediate region and the conducting outer ring, respectively, as indicated by the dashed lines. The regions labeled as region ③ correspond to the outer ring observed at the periphery of the dot-ring structure in the SEM image. Consistent with Figure 4-10 a-c, the color bar under the STEM image indicates the different regions within the

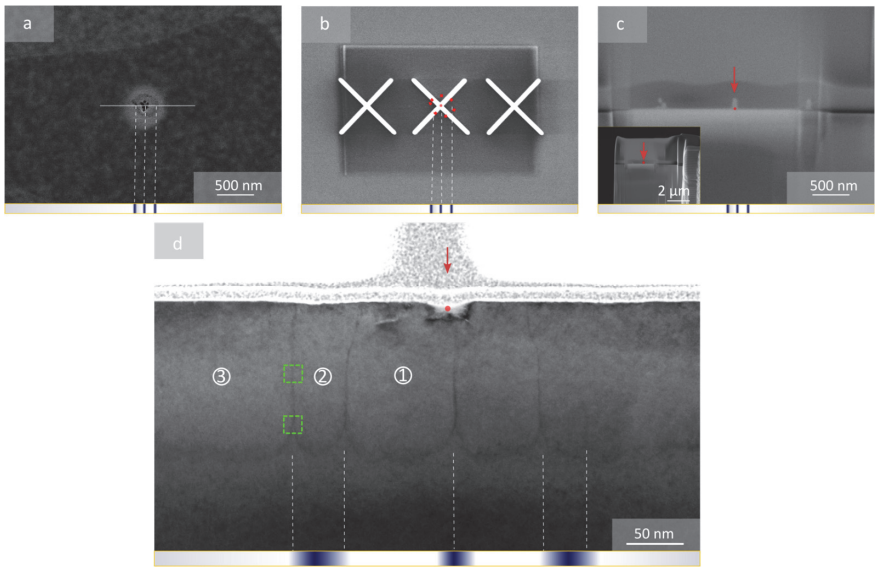

Figure 4-10. TEM sample preparation steps and overview TEM image. The color bar below each image serves as an index to different regions of the defect structure, with blue color representing enhanced conductance and white color denoting insulating regions according to the SEM contrast. (a) SEM image of the defect structure from the sample surface (1.25 kV, 0.1 nA, TLD). (b) SEM image of the defect structure marked by three electron-beam-deposited Pt "X" markers. (1.25 kV, 50 pA, TLD). (c) SEM image of the defect structure in the final TEM lamella, with the red arrow highlighting the location of the defect structure. Inset: SEM image of the final TEM lamella (4.00 kV, 0.1 n, ICE (section 3.1.3)). (d) STEM overview image of the defect structure area (200 kV, CCD), recorded by Ursula Ludacka. The red dot indicates the tip position during writing.

dot-ring structure,with dark blue indicating regions of enhanced conductance and white representing the regions of reduced conductance.

The bright region is indicative of structural difference, possibly dislocations, as discussed in reference [259]. Structural detail in this region is not further investigated. Here, focus on large length scales across which the O_i'' and $V_O^{\bullet\bullet}$ accumulation occurs as measured by APT.

High-angle annular dark-field scanning transmission electron microscopy (HAADF-STEM) images of the three regions, shown in Figure 4-11, show the atomic-scale structure. All HAADF-STEM images from the modified area reveal a highly ordered atomic arrangement. Specifically, the HAADF-STEM images in Figure 4-11 from regions ①, ②, and ③ as defined in Figure 4-10d all exhibit the typical down-up-up displacement pattern of the brighter Er atoms, alternating with layers of Mn atoms. This pattern, indicative of the ferroelectric polarization P pointing upwards [23], is highlighted and marked by the white arrows. The color bars under each image act as indicators of the respective conductance state of these regions.

Aside from the structural integrity and atomic displacement pattern, equivalent to the as-grown structure of $ErMnO_3$, Figure 4-11 shows that the variations in conductance within the dot-ring

structure are not controlled by the polarization as both regions with enhanced and reduced conductance exhibit the same polarization orientation.

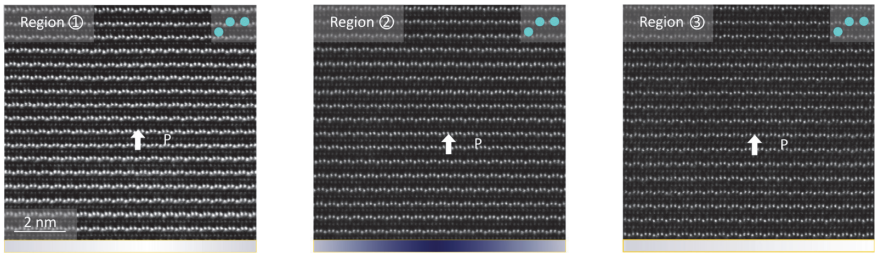

Figure 4-11. HAADF-STEM images from the different regions ①, ②, and ③ of the complex structure showing highly order lattice arrangement. The color bars below each HAADF-STEM image indicate the corresponding conductance states: blue represents enhanced conductance, and white insulates according to the SEM contrast.

In addition to the three regions marked as ①, ②, and ③ in Figure 4-11, distinct dark lines are observed in the low magnification TEM image of Figure 4-10d. These lines appear to arise in transition regions where the transport behavior changes from conducting to insulating or vice versa. This finding again excludes any direct correlation between the polarization direction and conductance state, as inferred above.

Figure 4-12a and b display representative HAADF-STEM images from the transition region between ② and ③ indicated by the green dashed squares in Figure 4-10. Inside the transition regions, the Er ions corrugate in a down-down-up pattern, as highlighted by the pink dots. This pattern indicates a downward polarization direction, as illustrated by the white arrow in the middle region. The color bar under the HAADF-STEM image shows that the transition region is located at a position where the conductance shifts from the conducting (dark) to the insulating (bright) region, as seen in the corresponding SEM image in Figure 4-10. Analysis of the Er ion corrugation in areas far below the modified region (not shown) reveals that the initial polarization of the domain points downward.

Figure 4-12c illustrates the observed polarization configuration at the topmost near-surface region, where the polarization inside the modified regions is upward. This change in polarization direction is, however, not favored by the electric field direction applied during the writing process. The observed polarization change aligns with the observations from Chen et al.[260], who reported that the initially downward-polarized domain in $YMnO_3$ was partially switched upward in the upper part of the irradiation area due to the electron beam illuminating in TEM. They attribute this phenomenon to the accumulation of positively trapped charges from the secondary electron emissions and oxygen vacancies introduced by the e-beam. This mechanism could also explain the polarization reorientation we observed here.

Similarly, damage from the TEM electron beam induced polarization change has also observed

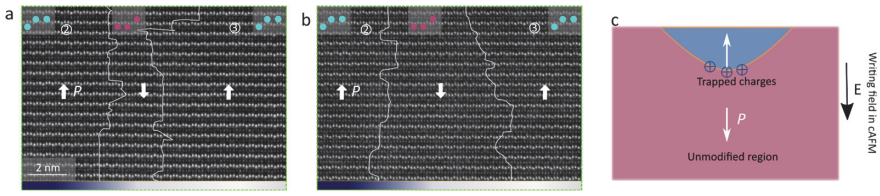

Figure 4-12. (a)-(b) HAADF-STEM images obtained from the transition region between regions ② and ③, corresponding to the regions, as indicated by the two green dashed squares in Figure 4-10d. The color bars under the HAADF-STEM images indicate the transition region located at the position where the conductance shifts from conducting (dark blue) to insulating (bright). (c) Illustration of the polarization configuration in TEM samples. The white arrows indicate the direction of polarization, and the black arrow indicates the direction of the electric field. Notably, the observed polarization change is not favored by the electric field direction given by the writing process in cAFM. Instead, it aligns with the effect of positive trapped charges induced by TEM beam irradiation.

elsewhere. Electron-stimulated desorption (ESD)[257] can cause oxygen atoms to be ejected into the vacuum, yielding a metal-rich surface in transition metal oxides[261]. Zhang et al. [262] observed that electron-beam-induced oxygen vacancies in TEM can disrupt ferroelectric displacement in $YMnO_3$.

Another possible explanation for the local polarization reorientation observed in the HAADF-STEM images is the sample preparation process. As observed by Cheng et al.[263], domain switching in $YMnO_3$ exclusively happened at the topmost surface upon the application of a bias voltage, which they ascribed to the electric field due to the trace amount of oxygen vacancies originating from the sample fabrication.

To identify the origin of the local polarization reorientation, additional studies are required which go beyond the scope of this work. Most importantly, the HAADF-STEM data shows that the changes in transport behavior in the dot-ring structure are not controlled by the ferroelectric polarization in the near-surface region.

Summarizing the HAADF-STEM results, a workflow has been demonstrated that allows for precise site-specific analysis of the lattice structure, correlated with electrical transport properties measured on the sample surface by SEM. The data confirm the structural integrity of the electrically modified region and decouple the emergent transport behavior from the ferroelectric properties.

4.4. Mechanism explanation

By combining the experimental and simulation results, we are able to outline the generation mechanism of the complex dot-ring structure, as illustrated in Figure 4-13a. Because of the electric field, anti-Frenkel defect pairs, i.e., O_i'' and $V_O^{\bullet\bullet}$, are created, leading to enhanced conductivity, as seen, e.g., in Figure 4-1 in the low field/ low exposure time regime. This result is in agreement with the previous study [107]. As described by the simulation (section 4.2.2), if the electric field is maintained for a longer time, the O_i'' and $V_O^{\bullet\bullet}$ will be generated, migrate, recombine, and eventually separate spatially, accumulating in different regions depending on

the sign of their charge. Consequently, the area under the tip is divided into an $V_O^{\bullet\bullet}$ rich region (pink frame), an O_i'' rich region (blue frame), and another $V_O^{\bullet\bullet}$ rich region (pink frame), with insulating regions of recombination in between, as illustrated in Figure 4-13a. APT results corroborate the presence of the O_i'' rich region and $V_O^{\bullet\bullet}$ rich region in the direction perpendicular to the sample surface. Furthermore, the size of the modified region can be tuned by adjusting the writing parameters U^{write}, t^{write}, and the radius of the probe tips.

Correspondingly, the respective regions within the modified area are dominated by n, p, and n-type conductivity, respectively, naturally forming a laterally n-p-n sequence, which has the potential to be used as bipolar junction structure, as shown in Figure 4-13b. n-p-n bipolar junctions are basic electronic components used for amplification and switching[264], enabling control of a substantial current flow from the collector (C) to the emitter (E) by a small current injected at the base (B). This provides a fascinating approach for fabricating bipolar junction transistors, in addition to traditional doping methods, going beyond just writing conducting wires as discussed earlier.

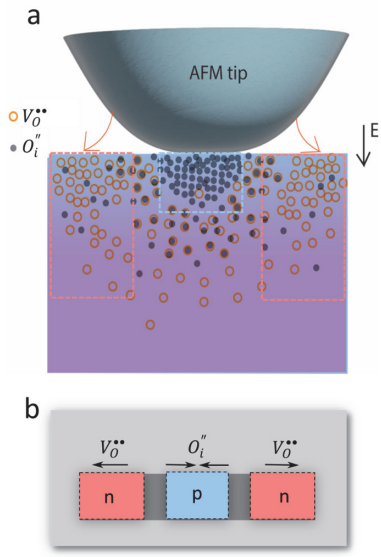

Figure 4-13. Mechanism and potential application. (a) Illustration of the generating mechanism of the complex dot-ring structure. Pink frame: $V_O^{\bullet\bullet}$-rich region; blue frame: O_i''-rich region. (b) Potential application of the complex structure as n - p - n bipolar junction according to the accumulated defects.

Contrary to preceding research [107], where anti-Frenkel defect pairs remained stable in an ambient environment for more than 24 months without significant degradation, our study reveals that the dot-ring structure degraded over time, and the enhanced conductance diminished, indicating temporary stability after defect pair separation. Interestingly, such temporary stability aligns with the concept of “transient electronics” – devices designed to

operate over a predefined duration of time and disintegrate fully or partially when longer needed [265], proposing a sustainable avenue for material recycling.

4.5. Summary

The experimental parameters for creating anti-Frenkel defects have been systematically investigated, including the writing voltages, exposure times, tip radii, sample atmospheric histories, and the writing environments. This exploration revealed a non-trivial evolution in the local electronic transport behavior. In contrast to the conducting dot structure obtained under low writing voltage and short exposure time, a more complex dot-ring structure with enhanced conductance is generated with higher writing voltages and longer exposure times. This evolution is interpreted based on the consistency of the SEM contrast at the dot-ring structure with the numerical simulation, suggesting the spatial separation of the initially paired oxygen interstitials and vacancies under the influence of the applied electric field. This hypothesis is supported by APT results, which show that the volume under the tip divides into regions with an accumulation of different types of oxygen defects. STEM data reveals the structural integrity of the modified region and decouples the observed electronic transport behaviors from the effect of electric polarizations.

Looking forward, utilizing the functionality of the modified area as bipolar n - p- n junction demands intensive efforts toward developing methods for establishing effective contacts for different regions. This would make it possible for comprehensive testing and demonstrations. Furthermore, considering the promising functionality of the domain walls in $ErMnO_3$, there lies an opportunity to incorporate such bipolar junction transistor into the framework of domain wall-based nanocircuitry, thereby propelling further innovations in the field.

5. Thickness-dependent electronic properties of ferroelectric domain walls in $ErMnO_3$

Ferroelectric domain walls in $ErMnO_3$ exhibit fascinating electronic properties[16,266], holding great promise for next-generation nanoelectronics [10,148,267], as described in section 2.2.3. So far, however, measurements of domain-wall-related electric outputs predominantly come from the surface of millimeter-thick bulk samples, with only a few examples from thin films [268,269] or FIB-cut lamella [200]. Consequently, it is often difficult to exclude effects from features within the material, which leads to uncertainties, including thickness effects and domain walls in the sub-surface region, leaving different fundamental properties of the domain walls to be explored.

For example, the sample thickness strongly influences the electric field distribution within the sample, thereby affecting the measured result. Furthermore, by combining cAFM and FIB 3D tomography, Roede et al. [96] identified the existence of a certain cutoff length, which is sample-specific and further complicates the problem. Beyond this specific depth, the current density quickly drops to zero, implying depth-dependent domain wall contributions. For a fully charged tail-to-tail domain wall, the cutoff length is about 50 nm. The value rapidly decreases when the domain wall deviates from a fully charged state, giving an additional degree of freedom. This reflects the need for careful studies, separating the different contributions and their impact.

In this chapter, the fundamental electronic properties of domain walls in samples of different thicknesses will be investigated systematically, to address the influence of spatial confinement. Understanding how the electrical properties vary with thickness, i.e., in confined geometries, is pivotal for both the technological device application and the fundamental science behind them.

The goal is to cover a broad range of thicknesses from 1000 nm to sub-10 nm. For this purpose, different preparation methods are developed to fabricate the samples. Subsequently, the electronic properties of the domain walls in these nano-structured samples are investigated using correlated SPM characterization, revealing thickness-dependent variations of the electronic properties at the domain walls.

5.1. Sample preparation methods

In order to investigate the domain wall properties within samples of varying thickness, thin lamellas are extracted from a high-quality $ErMnO_3$ bulk crystal sample. In a prior study from our group [28], a 700-nm-thick lamella extracted by FIB from a bulk sample was shown to retain the same electronic transport behavior as the bulk. Thus, this approach allows the extraction of lamellas with desired thicknesses from a targeted position, without obscuring the electronic domain wall response, enabling subsequent characterizations by, e.g., local probe techniques. It avoids the need for additional post-processing, such as heat treatment, to remove damaged

layers [270], foreshadowing the potential to extract individual domain walls for device applications. In this section, the sample preparation begins with the same procedure as in the previous study, supplemented by an additional final polishing step. With this preparation method, samples as thin as 200 nm can readily be manufactured. To achieve even thinner samples, further preparation strategies are developed, building up on this basic method.

This section describes the preparation methods of $ErMnO_3$ lamella samples with different thicknesses and geometries in detail, including FIB cutting and tripod polishing technique.

The model material for our study is $ErMnO_3$, as its domain walls have been widely investigated so that the fundamental domain wall properties are well-documented, providing an excellent basis for the advanced nanostructuring experiments presented here [16,21,69,266], see section 2.2for details. The $ErMnO_3$ single crystal was grown by Zewu Yan (ref [243]), using the pressurized floating-zone method. The sample was then oriented by Laue diffraction, and cut into 1mm-thick small pieces with polarization directions along one of the surface edges, which yields specimen with well-defined in-plane or out-of-plane polarization. Following this, the samples were lapped with an Al_2O_3 (9 µm grain size) fluid on a cast iron lapping plate, and polished with silica suspension (Logitech, SF1 polishing suspension, pH= 9.0-10.5) on a polyurethane plate, which obtains a smooth surface with a root mean square roughness of ~1 nm. Figure 5-1 shows a representative SEM image and cAFM image of the bulk sample surface for a specimen with in-plane polarization. The white arrows in Figure 5-1a indicate the polarization direction. The tail-to-tail walls appear as bright lines in SEM and exhibit enhanced conduction in cAFM. In contrast, the head-to-head domain walls correspond to dark lines in SEM and appear as insulating in cAFM. Lamella samples with different thicknesses are then subsequently extracted from the same bulk sample.

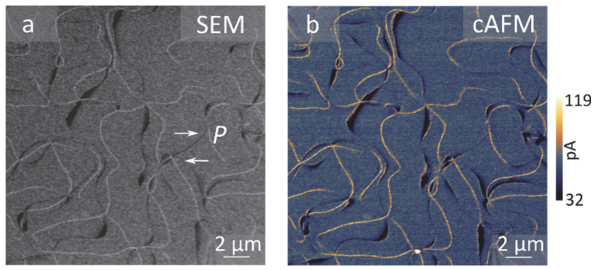

Figure 5-1. (a) SEM image from a spot on an in-plane $ErMnO_3$ bulk sample, with P lying in the surface plane as indicated by the white arrows. Taken by TLD detector (section 3.1.3) with 1.5 kV and 0.4 nA. (b) cAFM image recorded from the same spot as (a). Acquired with a CDT-NCR probe tip at a bias voltage of 13.5 V applied to the sample disk). Tail-to-tail domain walls exhibit enhanced conductance (bright) relative to the bulk, whereas reduced conductance (black) is observed in head-to-head domain walls.

For an overview, four important lamella sample geometries and preparation strategies used in this work are illustrated in Figure 5-2. For clarity, standard lamellas (Figure 5-2a) are referred to as free-standing lamellas (see section 5.1.1). The preparation process in this work is further

optimized compared to the initial method developed by Mosberg et al. [200], as explained in section 5.1.1. Going beyond previous work, we can now also access the so-called low voltage regime (section 2.2.3), reproducing the same properties in lamellas as observed in bulk samples. This approach allows for the reproducible preparation of lamellas that show the established electronic properties of ferroelectric domain walls in $ErMnO_3$.

In addition, new procedures for wedge-shaped lamellas are developed as part of this thesis: the back-electrode attached wedge lamella (Figure 5-2b) and back-electrode pre-tilt wedge lamella (Figure 5-2c), as detailed in section 5.1.2 and 5.1.3, respectively. These wedge-shaped FIB-cut lamellas are all mounted on a flat substrate (for detailed information, see section 5.1.1). Aside from the FIB-based approaches, wedge lamellas are achieved by tripod polishing (Figure 5-2d). The strategy of tripod-polished wedge lamella was developed and implemented in collaboration with Dr. Erik D. Roede and Dr. Kasper A. Hunnestad.

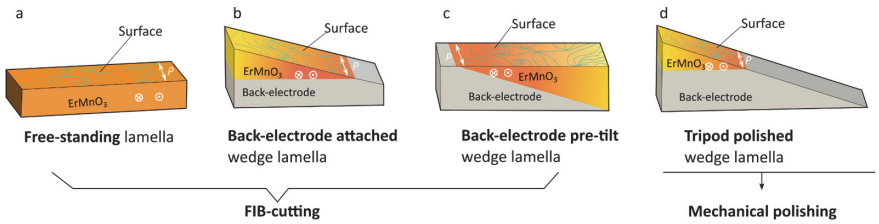

Figure 5-2. An overview of sample geometries used in this work. Four distinct geometries of lamellas prepared via FIB and mechanical polishing.

5.1.1. Flat free-standing lamellas

To prepare samples with thicknesses between 200 nm to 1000nm, a flat lamella sample is first extracted from the bulk sample and subsequently mounted onto a metal-coated Si wafer. Lamellas prepared by the simplest approach, which does not involve the deposition of any electrode on the back of lamella, will from now on be referred to as 'free-standing[1] lamellas'. The lift-out procedure of the free-standing lamella implemented here can be divided into three steps as follows:

Step 1: Lamella lift-out and landing

Analogous to standard TEM lamella cutting procedures [186], the extraction of a flat lamella begins with depositing (section 3.2.3) a protective layer of Pt on the target surface area (Figure 5-3a). Following this, a rough trench around the target region is milled, and the surrounding material is removed, leaving only a short bridge on the right to support the lamella until it is cut free from the bulk sample (red rectangle in Figure 5-3b).

Given that the backside of the lamella sample will not be accessible after landing, the lamella is trimmed before lift-out to ensure a flat high-quality surface and gain better contact between lamella and substrate. To do this, the backside is polished with stepwise reduced ion beam current down to 90 pA, yielding a domain wall contrast in the SEM image, as shown in Figure 5-3c.

To lift-out the lamella with the micromanipulator needle, the stage is rotated by 90° at 0° stage tilting, which allows attaching the micromanipulator needle to the front side (unpolished side, indicated by the red arrow in Figure 5-3d) of the lamella. The zero stage tilting angle is illustrated in the inset of Figure 5-3d, which corresponds to the geometry that the electron beam (e^-) perpendicularly incident to the stage plane. The lamella is attached to the needle by ion beam deposited platinum (Pt) and cut free using the ion beam. In this process, it is advised to leave a long bridge (≥ 5µm) during the rough trench milling (Figure 5-3b) to avoid unintended milling of the lamella material because of the special geometry.

Once the lamella is attached to the micromanipulator needle, the needle is moved to its park position (approximately 300 µm above the sample surface) and rotated by 180°. The lamella is now horizontal and can be easily placed on a flat substrate (Figure 5-3e; the red arrow indicates the unpolished side).

To mount the lamella on the substrate, a Si wafer coated with 100 nm Au is prepared beforehand and inserted into the chamber.

[1] In this context, 'free-standing' specifically refers to a lamella of $ErMnO_3$ that lacks an electrode deposited on its back side, serving to differentiate between lamellas with and without a back-electrode. This terminology differs from its typical use in the thin film field, where 'free-standing' describes a self-supporting thin film detached from the substrate, usually through dissolving or etching processes.

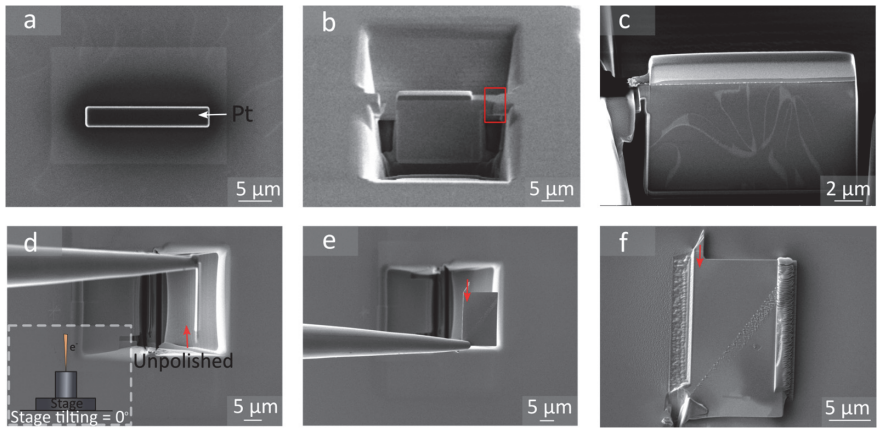

Figure 5-3. Detailed procedure of flat free-standing lamella lift-out from $ErMnO_3$ bulk sample. This involves extracting a flat lamella from a target region of a bulk sample and subsequently mounting it onto a flat substrate (100 nm Au-coated Si wafer). (a) A protective layer Pt is deposited on a designated region of the bulk sample surface by ion beam. (b) A rough trench is milled, leaving only a bridge to connect the lamella sample. The rectangle indicates the bridge. (c) Domain wall contrast on the finely polished side of the lamella, which will eventually serve as the backside of the lamella, facing the substrate. (d) Lamella sample is attached to the micromanipulator needle and cut free. The red arrow indicates the unpolished side. The cutting is performed after rotating the stage to a specific orientation of the trench. The inset illustrates the stage tilting angle of 0°. (e) Horizontally aligned lamella sample achieved by rotating the micromanipulator needle 180° at a safe height (park height). (f) The lamella sample is mounted on a flat substrate with the assistance of the micromanipulator needle. Re-deposition can be seen in a diagonal direction, which occurs during the deposition that attaches the lamella sample to the micromanipulator needle in the step shown in (d). The lamella surface now exhibits a rough texture due to high current ion beam milling.

The Au coating is performed by an electron-beam evaporator with 8 kV acceleration voltage and 25.3 mA current. This preparation method of the substrate is applied to all the FIB-cut samples. During the lamella landing, an ion beam-cut marker on the substrate is beneficial for beam alignment purposes. The subsequent step, at 0° stage tilt (illustrated in the inset of Figure 5-3), involves landing the lamella sample on the substrate surface, welding the right side of the lamella using ion beam deposited Pt, cutting away the micromanipulator needle, and welding the left side. The lamella sample is now securely mounted on the substrate (Figure 5-3f).

To optimize the landing process, first, a clean, neat edge positioned upstream of the ion beam is necessary to reduce the curtain effect (see section 3.2.4). Secondly, considering the special geometry during the upcoming polishing step and preventing any part of the disk from crashing the e-beam objective lens (see section 3.1.1.2), it is preferable to place the lamella close to one edge of the substrate. This edge will be positioned upstream of the ion beam later on.

Step 2: Lamella polishing

For the measurements of correlated SEM and SPM, a finely polished surface is essential. To achieve this, a 45° pre-tilt stub is required. This stub allows the lamella sample to be tilted at a glancing angle [271,272] with respect to the ion beam. In addition, a good electrical connection between the lamella, substrate, and the sample stub avoids ion beam drifting during polishing.

To realize this, the stub, including substrate and lamella, is sputter coated with 20 nm of Pt/Pd (80%/20%).

The polishing procedure begins by identifying the optimal polishing angle. Initially, the stage is tilted to 45° to find the coincidence position, where both the electron and ion beam can observe the same sample spot. Then, the stage is directly tilted back to 10°. As the stage tilts further down, the ion beam channel is used to monitor the geometry. The substrate disappears from the ion beam view, followed by the surface of the lamella, leaving only the protective layer visible, typically around 7°. Subsequently, the stage is tilted back by 2° to approximately 9° tilting, creating a glancing angle of 2° between the ion beam and the lamella surface. This alignment allows the ion beam to cut parallel to the substrate over a significant distance, ensuring a flat lamella surface. The electron beam channel can rapidly assess a trail cutting. If the cutting surface is not parallel to the substrate, the angle has to be fine-tuned until it is parallel, as depicted in Figure 5-4. The angle between the incident ion beam and the polished surface is described in section 3.2.3.3.

The lamella surface is then roughly trimmed using a high-current ion beam (2.8 nA is used here). Subsequently, the beam current is gradually decreased for cleanup line by line until it is down to a beam current of 90 pA. This yields a smooth surface with the desired lamella thickness. A crucial aspect of this step, different from cutting a TEM lamella, is setting the cutting depth of every line to cover the entire length of the lamella in order to minimize re-deposition (section 3.2.3.3). This corresponds to a z-value of above 20 µm or more, depending on the practical lamella size.

Step 3: Removing the ion beam-damaged layer

The issue of beam-damaged layers introduced by ion implantation in FIB-prepared samples is a persistent challenge within the community [171]. Over time, several methods have been explored to reduce the thickness of this damaged layer, as described in section 3.2.4. Here, we combine the advantages of low-energy ion beams and different ion sources to minimize the damage layer, using a 5 kV Ga^+ beam and an additional Argon beam for the final refinement.

For the 5 kV FIB polishing, the stage should be tilted two more degrees, leading to a tilt of 11° in total, to ensure the ion beam remains effective for milling. Figure 5-4b presents an SEM image of an in-plane lamella sample, in which the $ErMnO_3$ lamella and the welding material are indicated on the top of a substrate, which appears white in the image background). The $ErMnO_3$ lamella show pronounced domain wall contrast, similar to the bulk sample (Figure 5-1a), visible as bright and dark lines on a grey background, corresponding to the ferroelectric $\pm P$ domains. Up to this point, the lamella is adequately prepared for subsequent SPM measurements.

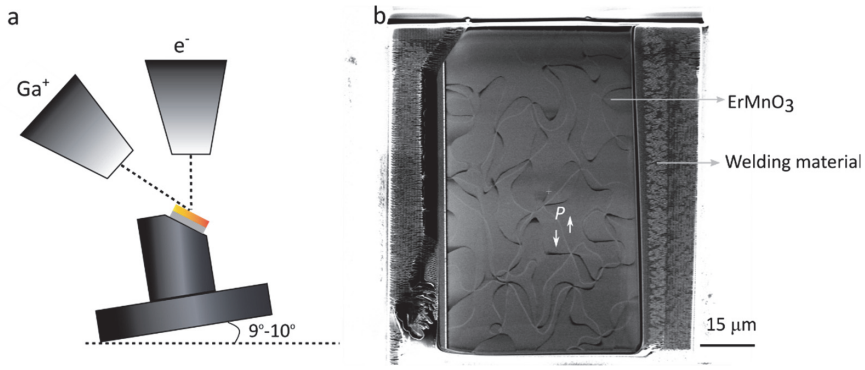

Figure 5-4. (a). Schematic representation of the lamella polishing configuration. The substrate holding the lamella sample is mounted to a 45°-pre-tilt stub, and visible for both the electron beam (e^-) and the gallium ion beam (Ga+). (b). SEM image (2.0 kV, 0.4 nA, TLD) of a finely polished lamella sample with pronounced domain wall contrast. The white arrows indicate the polarization direction. The polishing was first conducted using high-current beams, gradually reduced to a beam current as low as 90 pA, and a low-energy beam polishing at 5 kV.

The final optimized step is Argon polishing, conducted in an Argon ion beam polisher (GATAN PIPS II precision ion polishing system) at liquid N_2 temperature. The procedure uses a gun-operating angle of 6° and sequential milling at voltages of 1 keV, 0.5 keV, and 0.3 keV, each for a duration of one minute. This final step has proven to considerably improve the lamella quality, which is especially important for local transport measurements by cAFM, unlocking the access of intrinsic domain wall properties.

The 3-step preparation procedure is versatile and adaptable to various types of material. For ferroelectric materials as studied in this work, this approach offers two important degrees of flexibility:

(1) Orientation-dependent lamella preparation: From an in-plane single crystal bulk sample, lamellas with both in-plane or out-of-plane polarization can be obtained by cutting along or perpendicular to the polarization direction.
Figure 5-5a shows an in-plane $ErMnO_3$ lamella sample extracted by cutting along the polarization direction, displaying typical domain wall contrast with coexisting conducting (bright) and insulating (dark) domain walls, similar to bulk single crystal samples (Figure 5-1a).

Figure 5-5 b is an out-of-plane lamella sample lifted out perpendicular to the polarization direction. It exhibits domain contrast, with the upward polarized domains appearing bright and the downward polarized domains appearing dark. When utilizing an out-of-plane single crystal bulk sample, the polarization direction of the lamella can be controlled via plan-view (lamella surface parallel to the single crystal surface) or cross-sectional (lamella surface perpendicular to the single crystal surface) cutting. For plan-view lamella cutting, the basic process remains the same as described above. However, transfer via a TEM half-grid is necessary, as explained in ref. [28,185].

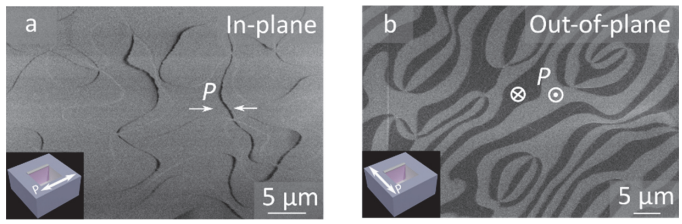

Figure 5-5. Lamellas with different polarization orientations extracted from the same $ErMnO_3$ single crystal bulk sample. (a) SEM image of an in-plane lamella sample extracted along the polarization direction, as sketched in the inset. (b) SEM image (2.0 kV, 0.1 nA, TLD) of an out-of-plane lamella extracted in a direction perpendicular to the polarization direction, as illustrated in the inset.

(2) Thickness control: The control over the lamella thickness can readily be achieved by the polishing process at 30 kV. Concerning the determination of the resulting lamella thickness, values from the top-view SEM/SIM (section3.2.3) images can serve as a reference. More precise values can be obtained via AFM topography measurements, particularly for lamellas with thicknesses less than 500 nm.

5.1.2. Back-electrode attached wedge lamellas

Going beyond the preparation of flat free-standing lamellas described in section 5.1.1, this section focuses on the preparation of wedge-shaped lamellas with electrodes attached to the back side. This approach allows for studying continuous thickness variations and offers certain advantages compared to free-standing lamellas. As the wedge lamellas are stabilized by the back-electrode, they are less susceptible to deformations and do not impose stringent requirements on the flatness of the backside when the thickness decreases below a certain thickness, as it is the case for free-standing lamellas. Another issue that can be bypassed is that the welding material (Pt) is milled faster than the $ErMnO_3$ material during polishing (step 2 in section 5.1.1). Because of this, often only insufficient welding material remains to secure the lamella, causing it to fall off during SPM scanning, which is no problem with wedge lamella on electrodes. Back-electrode attached wedge lamellas are thus perfectly aligned with the requirements for thickness-dependent studies also in ultra-thin samples. The attached back-electrode enhances the mechanical stability of the lamella sample, while the wedge shape allows the lamella thickness to decrease continuously from the micrometer regime approaching sub-10 nm.

Concerning the preparation of the back-electrode attached wedge sample, there are two main differences compared to the process of making free-standing lamellas (section 5.1.1), which are described in the following.

Back-electrode deposition

For the deposition of the back-electrode, conducting it directly after fine polishing and before lift-out (Figure 5-3c) is technically possible, yet it might lead to reconnection between the lamella and the bulk sample within the trench due to deposition/re-deposition. Alternatively,

the lamella is first extracted and fixed to a TEM half grid immediately after the trench milling (Figure 5-3b in section 5.1.1). Further steps, such as the lamella backside polishing (Figure 5-6a), back-electrode deposition (first electron beam deposition and then ion beam deposition) (Figure 5-6b), and the lift-out for landing on the flat substrate (Figure 5-6c), are then carried out on the TEM half grid.

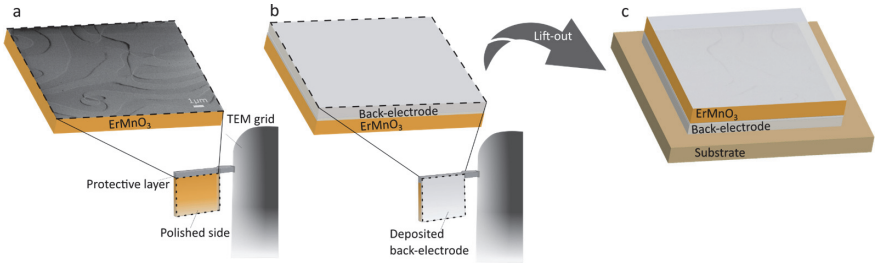

Figure 5-6. Back electrode deposition of the wedge lamella with the assistance of a TEM half lamella. (a) Fine polishing of the lamella backside, with the lamella being affixed to a TEM half grid. (b). Electron beam and ion beam deposition of the back electrode (grey) on the polished side in (a). (c) Lamella sample(orange) with the deposited back electrode(grey) being transferred and subsequently mounted onto a flat substrate(brown). The flat substrate is a 100 nm Au-coated Si wafer, the same as used in section 5.1.1.

Polishing angle

The second key difference relates to the polishing angle after the lamella landed on the substrate, i.e., the ion beam incident angle. Figure 5-7a depicts the polishing setup using the pre-tilted stub.

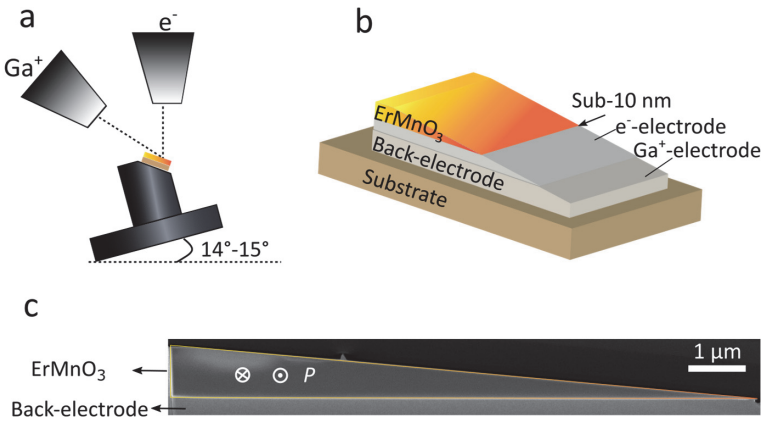

Figure 5-7. Depiction of the polishing process of back-electrode attached wedge lamellas I. (a) Configuration of the polishing angle. The stage is tilted to a larger angle to achieve an ion beam incident angle that allows the lower part to mill faster than the upper part. (b) Resulting wedge-shaped sample after the polishing process undertaken at the angle demonstrated in (a). (c) Cross-sectional SEM image (1.0 kV, 0.1 nA, TLD) of a wedge-shaped lamella sample using the aforementioned method. The $ErMnO_3$ material exhibits a wedge shape, with the left thicker part about 1.5 µm and the thinner part gradually approaching sub-10 nm, before the $ErMnO_3$ seamlessly transfers to the back-electrode on the right-hand side. The polarization directions are indicated in white color.

Compared to the flat lamella polishing, the stage is tilted an additional 5°, resulting in a total

tilting angle of 15° (a glancing angle of 7°). This adaptation results in an ion beam incident angle that allows more material to be milled away from the bottom compared to the upper side of the lamella, and the polishing thus leads to a wedge sample. As illustrated in Figure 5-7b, the thickness of the polished material can be controlled to sub-10 nm at the transition point to the back-electrode. This transition is made in such a way that the back-electrode material is partially milled away to align the back electrode with the lamella. In the end, the thickness of the $ErMnO_3$ material consistently decreases from the thicker part to the thinner part and seamlessly transfers to the back-electrode. Figure 5-7c presents a cross-section SEM image of a wedge-shaped $ErMnO_3$ lamella prepared via the outlined polishing approach. The $ErMnO_3$ material, highlighted by the orange triangle in Figure 5-7c, demonstrates a continuous decrease in thickness from approximately 1.5 µm at the thickest part to sub-10 nm at the junction with the back-electrode.

5.1.3. Back electrode pre-tilt wedge lamella

This section introduces a refined approach derived from the back-electrode attached wedge lamella described in section 5.1.2. The approach addresses two challenges of the back-electrode attached wedge lamella: Firstly, as mentioned above, the incident ion beam angle used during the polishing of the back-electrode attached wedge lamella can increase ion beam damage [194], which requires adequate control. Secondly, in the previous method, the direction of thickness variation is restricted to the polishing direction. Thus, when contrast variation (such as in Figure 5-11a) appears perpendicular to the polishing direction, it is challenging to determine if the contrast arises from polishing artifacts (such as the curtain effect, section 3.2.4.2) or inherent thickness variations of the sample.

The key difference to the approach discussed in section 5.1.2 is that it begins by defining the wedge angle, cutting a tilting angle into the attached back-electrode. This allows polishing at an ion beam incident angle that is the same as for the flat free-standing lamella in section 5.1.1, and the polishing direction becomes adjustable. To emphasize the difference between this approach and the method described in section 5.1.2, it is referred to as back electrode pre-tilt wedge lamella.

Similar to the method in section 5.1.2, the lamella sample is first transferred to a TEM half grid. The polishing of the lamella backside and the back-electrode deposition are then performed on the TEM half grid before the final transfer to the flat substrate. In this back electrode pre-tilt method, however, the back-electrode is cut into a wedge angle relative to the horizontal plane immediately after deposition. This wedge angle will eventually determine the lamella wedge angle. To obtain the pre-tilt back electrode, the stage is tilted a few degrees less than the glancing angle of the ion beam. This ensures that the lower part of the electrode is milled less than its upper part, establishing the pre-tilt angle (Figure 5-8a). The back-electrode is trimmed to attain a 5° pre-tilt angle, leaving thinner electrode material at the top and thicker electrode

material at the bottom. Figure 5-8b presents a side-view SEM image from the experimental process, showing an $ErMnO_3$ lamella with a pre-tilted electrode deposited on the back. A pronounced domain contrast is visible on the side of $ErMnO_3$, with the polarization directions indicated in white. The boundary between $ErMnO_3$ and the back-electrode is highlighted by a blue dotted line, corresponding to the blue dotted line in Figure 5-8a. The thicker region is intended to provide robust support for the thin part of the wedge lamella.

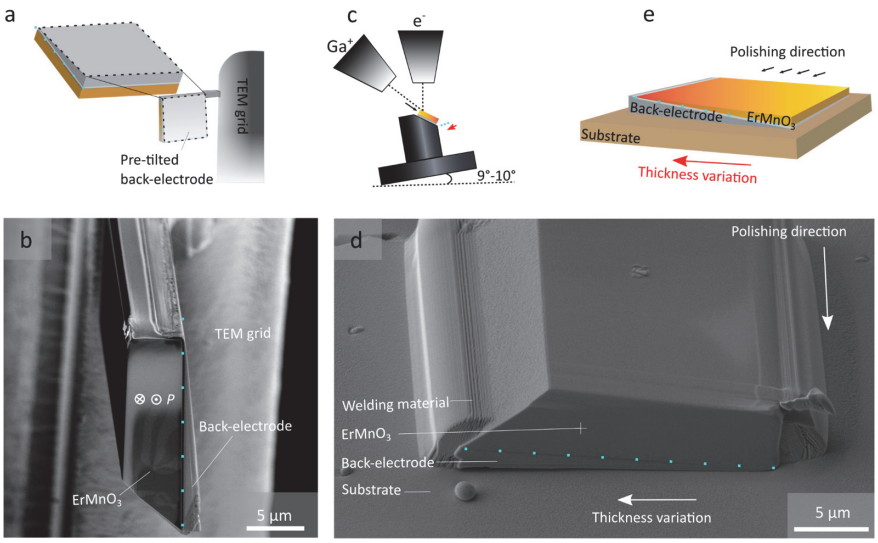

Figure 5-8. Depiction of the polishing process of the back-electrode pre-tilt wedge lamella. (a) illustration of Lamella sample covered by a wedge-shaped back-electrode with a pre-tilting angle of 5°. The back-electrode depositing and trimming to pre-tilt angle is executed on a TEM half grid. The blue dotted line highlighted the boundary between $ErMnO_3$ and the back-electrode. (b) SEM image (2.0 kV, 0.1 nA, TLD) of an $ErMnO_3$ lamella with pre-tilted back-electrode. The blue dotted line corresponds to the same positions highlighted in (a). (c) The setup for polishing. The lamella sample, accompanied by a wedge-shaped back electrode, is transferred and affixed to a flat substrate, which is then mounted to a 45°-pre-tilt stub. The ion beam incident angle is the same as the flat lamella sample. The polishing direction is illustrated by black arrows, and the thickness varying direction is indicated by the red arrow. (d) SEM image (2.0 kV, 0.1 nA, ICE) of the lamella shown in (b) landed on the substrate and is ready for polishing. The blue dotted line corresponds to the same position as indicated in (b). (e) The polishing ends with a wedge-shaped lamella sample, the thinner part compensated by a thicker back-electrode, and the thicker part supported by a thinner back electrode. The polishing direction is now perpendicular to the thickness variation direction.

Upon landing on a flat substrate, the sample is flipped over, exposing the unpolished side up. The polishing geometry is illustrated in Figure 5-8c. With the pre-tilt back-electrode, the wedge-shaped lamella can be polished at a beam incident angle that is identical to that of the flat lamellas (Figure 5-8c). Additionally, the pre-tilt back-electrode decouples the direction of polishing from the direction of thickness variation, permitting alternations in the polishing direction. In this work, the substrate is rotated 90° during landing compared to the previous method in section 5.1.2. As indicated by the black and red arrow in Figure 5-8c, the polishing direction (black) is now perpendicular to the thickness-varying direction(red).

Figure 5-8d displays an SEM image of the lamella in Figure 5-8b landed on the substrate and ready for polishing, with the same boundary as in Figure 5-8b marked by the blue dotted line. The varying direction of thickness and polarization direction are also marked in the image.

The subsequent polishing process is the same as for the flat lamella sample, described in section 5.1.1, resulting in a horizontal surface as illustrated in Figure 5-8e. In this setup, the thin part of the lamella is reinforced by a thicker back-electrode material, and a thin back electrode accompanies the thicker part. Importantly, the thickness variation is no longer restricted by the polishing direction.

5.1.4. Wedge-shaped sample preparation via tripod polishing

All approaches described so far rely on ion beam milling by FIB. Thus, a common disadvantage is the emergence of ion beam-induced amorphous/damaged layers, as described in section 3.2.4.4. The influence of the damaged layer becomes even larger when dealing with thinner samples due to the increase in volume fraction ratio. An alternative method that allows for bypassing this problem is tripod polishing. Tripod polishing, a conventional technique for preparing TEM samples [273], is a mechanical process of lapping and polishing, minimizing surface amorphization. Additionally, it yields a large transparent area that can, in ideal cases, match the lateral dimensions of the initial sample. Therefore, this approach represents a promising alternative for making wedge-shaped samples with a thickness ranging from a few hundred to sub-10 nanometers.

Building up on the plan-view TEM sample preparation method[274], a method that enables the preparation of a wedge-shaped sample with a very thin edge accessible to SPM measurements is developed using tripod polisher (Allied Multiprep™ polishing system). This method uses the same sample geometry as in FIB-prepared wedge lamellas in section 5.1.2, i.e., a conducting back electrode is deposited on one side of the sample before polishing. This back electrode ensures that the thinner edge of the wedge sample remains stable, avoids/suppresses deformation, and maintains a good electrical connection throughout the sample.

The workflow of the tripod polished wedge sample is outlined in Figure 5-9, in which no ion beam is involved. It starts from a polished single-crystal bulk sample using the standard sample preparation routines outlined in section 5.1. Subsequently, a 2 µm-thick Ti back-electrode with a 100 nm Au adhesion layer is deposited on the shiny polished side using an e-beam evaporator (Manufacturer: Pfeiffer, Model: Vacuum Classic 500), as illustrated in Figure 5-9a. The sample is then mounted on the edge of a wedge polishing stub, with the back electrode side facing the stub surface, and is subsequently loaded onto the tripod polisher (Figure 5-9b). This apparatus, equipped with Delrin-capped micrometers, allows for accurate lateral and longitudinal adjustments of the polishing plane [275]. The tilt-angle of the polishing plane is set to 2°, from left to right (Figure 5-9c). In this setup, the sample is lapped and polished continuously using a

succession of diamond films ranging in abrasive particle size from 15 to 0.1 µm. The final polishing step is executed using a felt cloth stained with colloidal silica suspension that contains 20 nm-sized particles, aiming to remove the polishing scratches as much as possible. Finally, the sample is cleaned with micro-organic soap (Allied Microorganic soap) and distilled water. Throughout the procedure, an optical microscope is used to inspect the surface roughness, with iterations of polishing and observation continuing until the thickness fringes are visible at the edge, which indicates the edge is thin enough[276].

Figure 5-9d displays an SEM image of a tripod-polished sample. The thickness varying direction is indicated by the white arrow. The boundary between the $ErMnO_3$ and the back-electrode is highlighted by the blue dotted line. The sample provides a large area for investigation. For a clearer view of the thinner edge, we zoom into the region marked by cobalt and pink frame, presenting them in Figure 5-9e and f. The blue dotted lines again indicate the $ErMnO_3$ and the back-electrode boundary. Both images exhibit that the sample smoothly transfers from $ErMnO_3$ to the back-electrode at the thin edge, suggesting a very thin edge of the $ErMnO_3$. In addition to the edge, many domain walls are visible in Figure 5-9e.

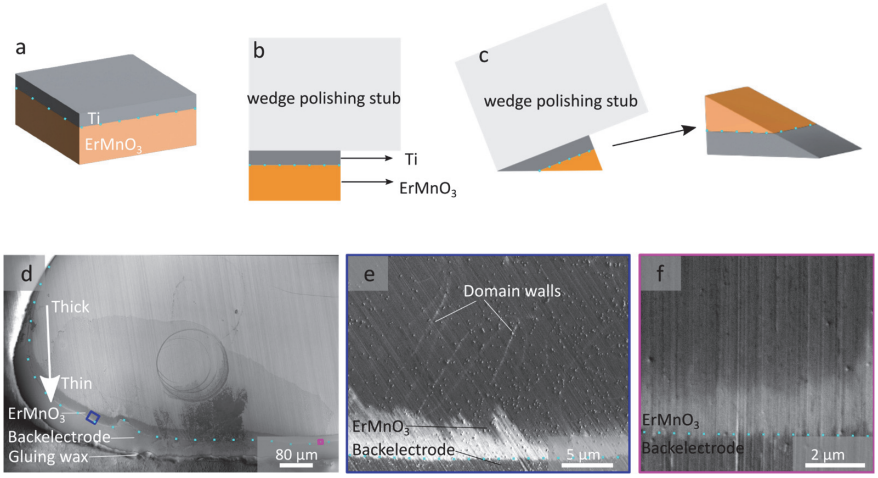

Figure 5-9 Schematic representation of the creation of a wedge-shaped sample via tripod polishing. (a) Ti electrode is deposited on the finely polished side of the single crystal surface. (b) Sample attached to a wedge polishing stub edge, ensuring the Ti side is positioned facing the stub. (c) The resultant wedge-shaped sample after tripod polishing at a sideways tilt-angle. (d) SEM image (1.0 kV, 0.1 nA, ICE) of a tripod polished $ErMnO_3$ sample. The thickness varying direction is indicated in the image. The edge of $ErMnO_3$ is marked by the blue dotted line. (e) SEM image(1.0 kV, 0.1 nA, ICE) of a region in tripod polished $ErMnO_3$ sample, highlighted by cobalt frame in (d). The boundary between $ErMnO_3$ and back-electrode is highlighted by the blue dotted line. Some domain walls are visible. (f) SEM image of the region highlighted by a small pink frame in (d). The blue dotted line highlighted the boundary between $ErMnO_3$ and the back-electrode, revealing a smooth transition and suggesting a very thin edge of $ErMnO_3$.

In summary, to probe the thickness-dependent properties of domain walls, it is imperative to devise methods capable of preparing lamella samples with thicknesses ranging from micrometers down to sub-10 nm. Each method described serves distinct purposes and allows for mitigating specific challenges in sample preparation. Altogether, these methods are

powerful toolkits for studying electronic properties at domain walls, going toward devices. They are applied in the following, specified in the text which method used.

5.2. Electronic domain walls response in confined geometries

In this section, the methods and strategies for making lamella samples of different thicknesses are applied to investigate the impact of thickness variations on the electronic properties of functional ferroelectric domain walls in the model system $ErMnO_3$. For example, it is expected that a reduction in thickness affects the electric field distribution, and interface effects related to the back electrode may play a much more pronounced role in the ultra-thin limit.

This section will present and analyze the characterization results of nano-structured samples of varying thicknesses cut from bulk single crystal $ErMnO_3$. For this purpose, two complementary approaches are used, addressing discrete stepwise changes and continuous variations in thickness. In the first case, a set of flat lamellas with thicknesses in the range from 200 to 1000 nm is realized; in the second experiment, wedge-shaped lamellas with a back-electrode are prepared. The latter allows a continuous change in sample thickness from more than 1000 nm to approaching 0 nm. SEM and correlated SPM are then used for characterization, revealing the domain wall behavior as a function of lamella thickness and the impact of the back electrode.

5.2.1. Electronic domain wall properties in flat free-standing lamellas

Flat free-standing lamellas with thicknesses of 1000 nm, 400 nm, and 200 nm, are fabricated by following the procedure described in section 5.1.1. Selected imaging results obtained from these flat lamellas are presented in Figure 5-10.

Figure 5-10a shows SEM and correlated cAFM images for the 1 µm thick lamella, revealing domain wall behavior similar to single crystal bulk samples [16]. Different types of domain walls are visible as bright, dark, and grey lines in the SEM image. These walls converge at distinctive six-fold points, corresponding to structural vortex and anti–vortex pairs as explained in section 2.2.2. The superimposed cAFM image on the SEM image reflects a one-to-one correspondence between the two data sets, showing that enhanced and reduced conductance probed at the domain walls by cAFM coincides with bright and dark contrast in SEM, respectively. It thus identifies domain walls in SEM as conducting tail-to-tail domain walls (bright) and insulating head-to-head walls for this setting. Therefore, both cAFM and SEM are applicable for the analysis of local transport behaviors [96]. Corresponding SEM images for the 400 nm and 200 nm flat lamellas are displayed in Figure 5-10.

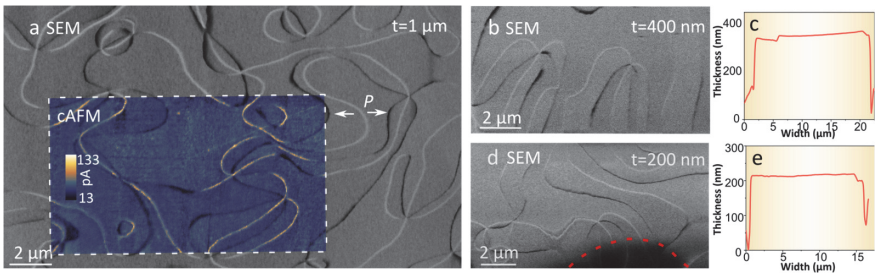

Figure 5-10. Flat free-standing lamella samples with different thicknesses (t). (a) SEM image of an in-plane lamella sample with a thickness of 1 µm (t= 1 µm), taken at 2.0 kV, 0.4nA using TLD detector. The insert shows the cAFM image acquired at the same position using a doped diamond tip HA_HR_DCP, with 22.5 V voltage applied to the sample disk. (b) SEM (2.0 kV, 0.2nA, TLD detector) image of the lamella with a thickness of 400 nm (t= 400 nm). (c) AFM measurement of the topography profile of the 400 nm-thick-lamella. The non-zero value on the side is attributed to the welding material on the side. (d) SEM (1.75 kV, 0.2nA, TLD detector) image of the lamella with a thickness of 200 nm (t= 200 nm). (e) Topography profile of the 200 nm -thick lamella, captured by AFM (AC-mode) height channel.

The SEM image of the 400 nm lamella is displayed in Figure 5-10b, which is supplemented by Figure 5-10c, showing an AFM topography profile to verify the thickness. Figure 5-10 d and e display the SEM image and the height profile of the 200 nm thick lamella. Notably, the domain walls in both lamellas exhibit qualitatively the same characteristics as observed in the bulk sample (see Figure 5-1). However, a deviation is discernible at the bottom part of the 200 nm lamella (Figure 5-10d), marked by the red dashed line, where the contrast appears darker. A possible explanation for this effect is local thickness variation, which impacts the contrast mechanism and /or the physical properties of the sample. To clarify the origin, we perform additional experiments on wedge-shaped samples and discuss in the next section 5.2.2.

In summary, the experiment demonstrates that the domain walls in $ErMnO_3$ lamellas preserve their functionality and stability analogous to their millimeter-thick counterparts down to about 200 nm in thickness, i.e., the thinnest samples produced at free-standing lamellas. The anomaly observed on the edge of the 200 nm lamella indicates the first deviations from the bulk-like behavior, which will be explored in more detail later. In order to investigate domain walls in thinner samples, wedge-shaped lamellas are utilized.

5.2.2. Domain and Domain wall behavior in wedge-shaped lamellas

To investigate the properties of domain walls in samples with a thickness under 200 nm, while ensuring good mechanical stability and electrical connection, wedge-shaped lamellas with electrode material attached to the back are fabricated as described in section 5.1.2. The configuration of wedge-shaped lamellas enables the comparison of a broad range of thicknesses, ranging from several hundred nanometers to the ultra-thin limit in the sub-10 nanometer range.

Figure 5-11 shows the example of a wedge-shaped lamella sample with a Pt electrode deposited on the back side, which is referred to as 'WL' in the following. Figure 5-11a displays

an SEM image of WL, with the thickness variation direction marked by the triangle on the right of the figure. Interestingly, the SEM data reveals two sections, distinguishable by their different contrast. The thicker part is brighter, displaying different domain walls similar to those found in single crystal bulk samples (Figure 5-1a). The thinner lower part exhibits a much darker contrast, with some domain walls appearing as fuzzy bright lines. This behavior is qualitatively different from the lamella with homogeneous thickness discussed in section 5.2.1.

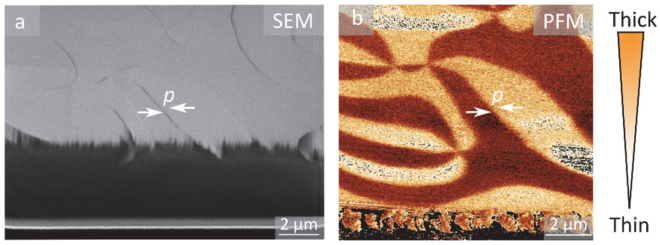

Figure 5-11. (a) SEM image (2.0 kV, 0.2 nA, TLD) and (b)PFM image of a back-electrode attached wedge lamella, WL. PFM image was obtained with a Ti/Ir probe tip using resonance PFM, drive amplitude 5V. The triangle on the right indicates the direction of thickness variation.

To understand the origin of the contrast, the lamella WL is probed by SPM. Figure 5-11b shows a subsequent PFM scan (resonant PFM). In contrast to the SEM image, the darker contrast is barely visible in the PFM image, only manifesting slightly in parts of the transition region. This indicates that the ferroelectric domain structure and piezoresponse are robust against the reduction in thickness, implying a different origin of the distinct SEM response of the thinner part.

The cAFM result of the same sample WL is presented in Figure 5-12. Consistent with SEM contrast in Figure 5-11a, a pronounced change in conduction contrast is observed in the cAFM scan (Figure 5-12a). Again, the direction of the thickness variation is marked on the left of the figure. The corresponding lamella thicknesses at the two positions marked by blue lines are specified on the left of the cAFM image. The upper thicker region exhibits qualitatively the same conductance as a bulk sample[243], showing conducting and insulating domain walls that meet in characteristic vortex structures, as highlighted by Figure 5-12b, cropped from the top region of Figure 5-12a. In the thinner, darker part, the domains are less conducting than in the normal area, and all the domain walls are somewhat more conductive than the domains, although the conductance varies from domain wall to domain wall. This is presented in Figure 5-12d, cropped from the bottom region of Figure 5-12a. Adjacent to the thin edge (in regions thinner than 110 nm), both the domains and domain walls become more conductive again. However, at the very edge, the material is observed to be destroyed, as evidenced at the bottom of the PFM image (Figure 5-11b). Notably, Figure 5-12c, cropped from the intermediate region of Figure 5-12a, displays a head-to-head domain wall transitioning from the normal region into the darker region. The conductance of this head-to-head domain wall changes from insulating to

conducting relative to the domains. To better visualize this effect, Figure 5-12e and f display respective current profiles, captured along the blue and pink lines marked in Figure 5-12c. In the upper region (blue line), the average current is roughly 50 pA, with the insulating domain wall descending to a minimum of 40 pA. In contrast, within the darker region, the domains only have a conductance of about 10 pA, whereas the head-to-head domain wall conductance is about 18 pA. This shows that although the conductance of both the domain walls and the domains is significantly reduced, the reduction is weaker at the domain wall, making it more conductive than the domains.

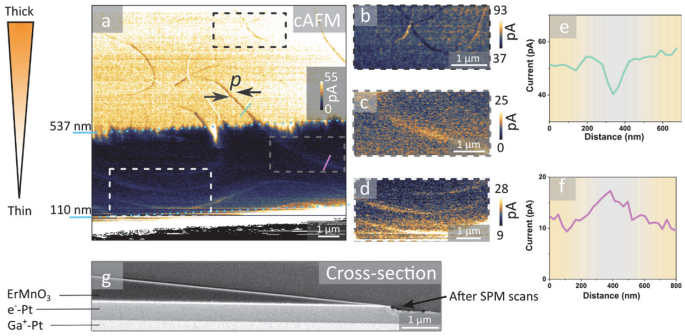

Figure 5-12 Domain wall conductance in back-electrode attached wedge lamella WL. (a) cAFM image of the whole WL lamella, recorded by a doped diamond tip HA_HR_DCP, with 15 V voltage applied to the back-electrode. The numbers on the left indicate the corresponding thicknesses of $ErMnO_3$ at indicated positions, determined by overlaying the cAFM and SEM images, using the thin edge in SEM image as the 0 nm reference point, and utilizing the wedge angle measured from the cross-section image in (g) for calculation. (b) cAFM image cropped from the thicker region. (c) cAFM image from the intermediate region. (d) cAFM image from the thin edge. (e) Current profile from the blue line marked region in (c). (f) Current profile from the pink line marked region in (c). (g) SEM image (1.0 kV, 0.1 nA, TLD) of the FIB cut cross-section on lamella WL after SPM scans.

In order to make sure that the geometry of the sample WL conforms to the desired wedge shape, with the thin edge approaching sub-10 nanometers, a FIB cut cross-section is performed on lamella WL after the SPM scans. The subsequent SEM image is shown in Figure 5-12g. The $ErMnO_3$ lamella (visible as the black triangular part in the middle) adopts a wedge shape, and the thickness changes from more than 1µm to sub-10 nm. The very edge of the $ErMnO_3$ is destroyed, which is consistent with the cAFM (Figure 5-12a) and PFM (Figure 5-11b)images. Furthermore, based on the size information obtained from the cross-section, the wedge angle is determined to be 6.2°. This value is used for the calculation of the corresponding thicknesses marked in Figure 5-12a. The onset of the darker contrast correlates with a thickness of approximately 537 nm. Note that this indicates a qualitative difference compared to the free-standing lamellas (without back-electrode) presented in Figure 5-10. Free-standing lamellas with 400 nm and 200 nm thicknesses still behaved the same as a normal bulk single crystal sample. This observation suggests that the darker contrast cannot be explained based only on the decrease in thickness, a point that will be discussed later.

In summary, in this section, two sets of lamellas were used to investigate thickness-dependent effects. For the flat-free standing $ErMnO_3$ lamellas with thicknesses ranging from 200 nm to 1000 nm, ferroelectric domain walls exhibit the same behavior as in bulk sample: conducting and insulating domain walls can readily be distinguished in SEM and cAFM, showing bright and dark contrast, respectively. In order to probe domain wall properties in samples thinner than 200 nm, a back-electrode attached wedge lamella is utilized. The cAFM result aligns with the SEM result, revealing two distinctive regions in the sample. While the thicker part behaves as a typical bulk sample, the thinner part exhibits a pronounced reduction in overall conductance. Interestingly, all the domain walls within this region are more conductive than the domains. After establishing the existence of two electrically different regions, which correlate with the sample thickness, the unusual domain wall behavior observed in the thin limit will be investigated in detail in the following section.

5.3. Unusual transport behavior in thin $ErMnO_3$ wedges

Section 5.2.2 revealed that domain walls in the thinner part of wedge lamellas with back-electrode exhibit behaviors distinctly different from bulk samples. Here, every domain wall, irrespective of head-to-head or tail-to-tail configuration, is more conductive than the domains. To understand this intriguing behavior, we first investigate the origin of the darker contrast and subsequently the characteristics of the domain walls.

Accordingly, this section consists of two subsections: the first part concerns the origin of the darker SEM contrast, and the second part explores domain wall properties inside the respective thickness regime. A summary part then collects the key findings.

5.3.1. Origin of the thickness-dependent SEM contrast

To reveal the origin of the step-like change in SEM contrast towards the thinner part of the wedge lamella, this subsection evaluates the sample preparation process, assesses different back electrode materials, and investigates potential extrinsic contributions.

5.3.1.1. Preparation process

We begin with an analysis of the process applied to achieve the wedge back-electrode attached lamella WL presented in Figure 5-11 and Figure 5-12. Lamella WL was fabricated following the procedure described in section 5.1.2, which implies that the backside of WL, which adheres to the substrate, underwent a fine polishing before the back-electrode deposition. Figure 5-13a shows the SEM image of the polished backside, where different types of domain walls meander, similar to the standard bulk sample and the flat free-standing lamellas. This side is then covered by the deposited back-electrode and mounted to the substrate. Figure 5-13b displays the SEM image of the subsequent wedge-shaped lamella surface. After the deposition of the electrode on the other side. The sample now clearly shows two contrast regimes, as described before. The red rectangles in Figure 5-13 a and b exhibit approximately the same domain wall configuration, although the data is recorded on the opposite side of the lamella, indicating that the sample is quite thin.

Based on the comparison of Figure 5-13 a and b, we can conclude that the contrast change likely arises due to either the polishing process, metal back electrode deposition, or thickness variation. On a closer inspection, many stripes (see the inset image marked by the white frame in Figure 5-13b) along the polishing direction are visible at the intermediate transitional zone so that polishing artifacts cannot be excluded. Coincidentally, the thickness variation (from thick to thin) is also along the same direction, as marked by the arrows on the right of the figure. Thus, distinguishing whether these stripes originate from thickness variation or polishing artifacts is difficult based on this experiment alone. To overcome this challenge, a new fabricating method is explored in the next step.

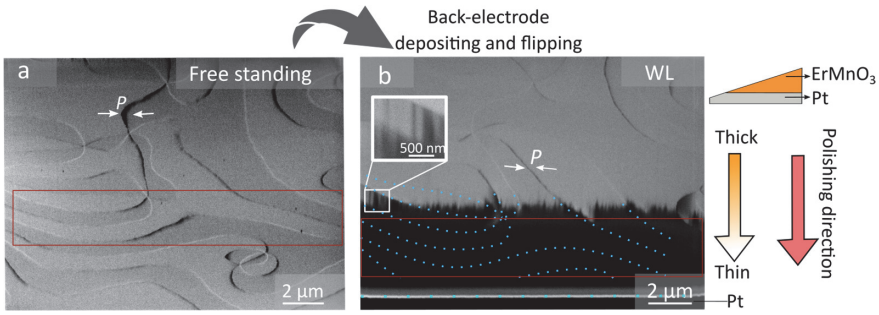

Figure 5-13. Wedge-shaped lamella sample WL. (a) SEM image (2 kV, 0.2 nA, TLD) of the backside of the lamella sample, taken before back electrode deposition and horizontally flipped from the raw image according to the geometry change. (b) SEM image (2 kV, 0.2 nA, TLD) of the front side of the sample with a Pt electrode attached to the back. Blue dotted lines indicate the domain wall configuration according to the PFM image in Figure 5-11b. The inset image, highlighted by the white frame, is a magnified SEM image from the marked region, showing stripes along the polishing direction. The red rectangle highlights the same domain wall configuration for images taken from the back and front sides, respectively, indicating the edge is very thin. Figure 5-13b *exhibits the SEM image of the wedge-shaped lamella WL.*

In order to separate potential effects caused by the polishing direction from thickness-related phenomena, a refined approach to making a pre-tile wedge lamella is applied, as outlined in section 5.1.3. Under this approach, the polishing direction can be along any of the edges, and this approach uses an ion beam incident angle that is the same as for the flat free-standing lamellas.

Unlike the prior method, this method first introduces a pre-tilt to the back-electrode by cutting at an angle relative to the horizontal plane before it is mounted on the substrate (denoted as 'PL' lamella in the following). The polishing direction is rotated by 90° with respect to the previous sample WL, making the polishing direction perpendicular to the direction of thickness variations.

Figure 5-14 shows the finished pre-tilted wedge lamella PL. The sample is clearly divided into two distinct parts again, similar to the WL sample. The thinner region exhibits a darker contrast with a fuzzy boundary. The onset of this darker contrast coincides with a thickness of approximately 830 nm. The stripes (see the inset image highlighted by the white frame.) again align with the direction of thickness variations and are perpendicular to the polishing direction. This finding effectively rules out polishing as the cause of stripes. However, potential damage from the ion beam cannot be entirely excluded since it is inevitable in FIB-structured samples. Thus, the possible influence of ion beam-induced damage layers remains a consideration.

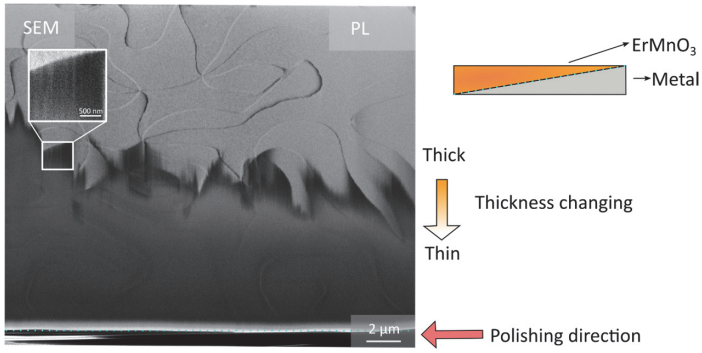

Figure 5-14. Back-electrode pre-tilt wedge lamella PL, polished at an orientation that is perpendicular to the thickness changing direction. The inset image, highlighted by the white frame, is a magnified SEM image from the marked region, showing stripes perpendicular to the polishing direction.

To exclude any FIB-related artifacts, the mechanical polishing method, tripod polishing, is used to fabricate an additional wedge lamella, as described in section 5.1.4. Figure 5-15 shows the SEM image of the wedge lamella fabricated via tripod polishing, labeled as 'TL'. Similar to the previous FIB cut lamellas, the SEM image reveals two regimes: a bright, thicker part and a darker, thinner part. Thus, this experiment clearly discards ion beam damage as the cause of the darker SEM contrast. Thus, although ion beam damage is present in all lamellas, it is clear that it is not the decisive factor for the emergence of the step-like change in contrast.

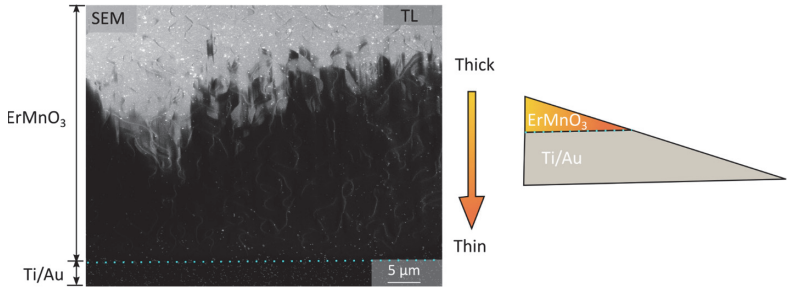

Figure 5-15. SEM image of the tripod polished sample TL. The thickness changing direction is indicated on the right. The blue dotted line indicates the edge of $ErMnO_3$.

In conclusion, by changing strategies of sample preparation to pre-tilt wedge lamella, the direction of thickness variation can be separated from the polishing direction, ruling out that the strips arise due to polishing artifacts. Importantly, the tripod polished sample still presents the same step-like change in contrast, corroborating that it is inherent to the $ErMnO_3$/electrode system.

5.3.1.2. Electrode-sample contact

In this section, the impact of the back-electrode on the transport behavior is studied. For this purpose, different back electrode materials are used, and SEM data gained on the respective wedge-shaped $ErMnO_3$ sample is compared.

For the wedge lamella labeled WL, platinum (Pt) was used as the back electrode (Figure 5-11), and for the pre-tilt lamella labeled as PL, Pt mixed with tungsten (W) was applied (Figure 5-14). Another available conducting material in the instrument is carbon (C), which is used as the back electrode on the wedge-shaped lamella labeled PL-C. For comparison, Figure 5-16a shows the wedge-shaped lamella WL, and Figure 5-16b displays the wedge-shaped lamella PL-C. A step-like change in SEM contrast is evident at the thin edge of both samples. Based on the pre-tilt angle, the thickness where the step-like change, in contrast, occurs in PL-C is approximately 255 nm, which is significantly less than that in WL and PL.

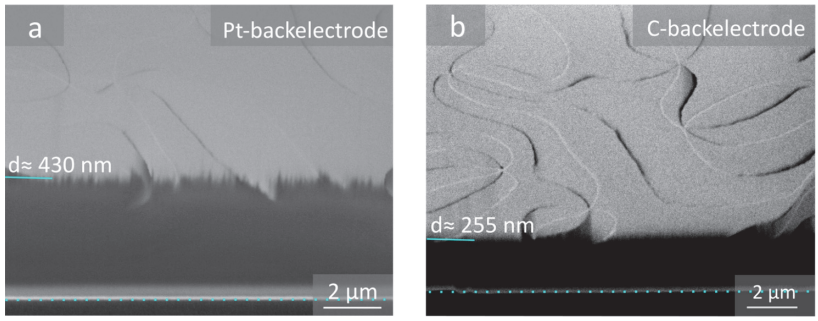

Figure 5-16. SEM images of back-electrode attached wedge lamellas with different electrode materials. (a) Lamella with platinum (Pt) as the back-electrode (labeled WL in section 5.2.2), wedge angle 6.2°. Taken by TLD at 2 kV, 0.2 nA. (b) Pretilted wedge lamella (PL-C), with Carbon (C) as the back-electrode material, wedge angle 6.6°. Image recorded by TLD at 2.0 kV, 0.2 nA. For both samples, the value of thickness (d), at which the step-like change occurs is indicated in the respective image.

Table 5-1 presents a summary of the thickness value at which the step-like contrast occurs in the SEM images of different lamella samples, including the information of the lamella name (labeled as 'Lamella'), back-electrode material ('Material'), and the corresponding thickness ('d_c'). This correlation suggests that the material of the back electrode plays a key role in the characteristic thickness at which the step-like change in contrast arises.

Table 5-1 Thicknesses of contrast change occurrence in different lamellas

Lamella	Material	d_c
PL	Pt+W	~830 nm
PL-C	C	255 nm
WL	Pt	~430 nm
Free-standing	---	Edge of 200 nm lamella

Different back electrode materials correlate with different thicknesses at which the step-like change in contrast emerges, and all these thicknesses were proved to exhibit bulk-like contrast in flat lamellas. A possible source is the nature of the metal-semiconductor contact between the back-electrode and our p-type semiconductor material $ErMnO_3$. To gain additional insight

and test this hypothesis, the next step will investigate the impact of a reduction in thickness after electrode deposition and voltage-driven effects.

5.3.1.3. Response to thickness-reduction and electrical biasing

In order to understand the physical origin and the properties of the low-contrast region, the position of the step-like change contrast is investigated in response to a reduction in thickness after deposition of the back-electrode, as well as changes caused by electrical bias.

First, we apply an iterative process of polishing by FIB, scanning by SPM, and re-polishing by FIB. For clarify, the corresponding procedure is sketched in Figure 5-17, illustrating the experimental process.

Here, the as-prepared wedge-shaped lamella is illustrated in blue color, and the surface of this lamella is denoted as 'State 1'. The position where the step-like change in SEM contrast is observed after the sample preparation. At this stage, the change in contrast on the surface occurs at a thickness of d_1. The lamella then undergoes several cAFM scans, which involve the application of a bias voltage to the back-electrode, resulting in the motion of the step-like change in SEM contrast towards the thicker end of the lamella and its corresponding position changes to the thickness d_1'.

In the next step, the lamella is re-polished using FIB to change the thickness and imaged again by SEM. The surface State 1 is milled away, leading to a thinner wedge-shaped sample (yellow color) with a new surface, 'State 2'. On this new surface, the darker contrast now appears at a different thickness, d_2.

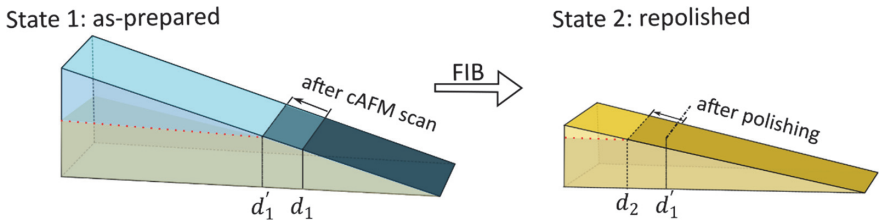

Figure 5-17. Schematic of the experimental procedure. State 1 (blue color) is the as-prepared lamella WL. State 2 is the lamella after being repolished by FIB. d is the corresponding thickness at which the step-like change in the contrast arises in the different states.

Corresponding SEM images tracking the evolution of the contrast are presented in Figure 5-18, showing how the contrast changes throughout this process on lamella WL. Figure 5-18a is the SEM image of State 1, in which the darker contrast only appears in the lower part, and the corresponding thickness d_1 is calculated as about 430 nm. The lamella is then transferred to an SPM and a cAFM scan, with a bias voltage of 15 V applied to the back-electrode (not shown). This way, it is possible to apply an electrical bias in a controlled way, reducing the risk of sample damage compared to macroscopic biasing experiments. After the SPM-controlled electrical

biasing, the darker contrast expands towards the thicker part, as shown in Figure 5-18b, in which the corresponding thickness d_1' is 710 nm.

By removing a layer of $ErMnO_3$ (about 150 nm) via FIB polishing, the lamella is thinned down. The contrast at the surface changes to State 2, causing the contrast to appear closer to the thicker edge, as shown in Figure 5-18c. The corresponding thickness, d_2, is calculated as 730 nm. Note that d_2 is similar to d_1', i.e., the value obtained after electrical biasing before repolishing, as illustrated by the red dashed lines in Figure 5-17. The latter suggests that the voltage-induced shift in d ($d_1 \rightarrow d_1'$) is quite robust and does not vanish under the applied procedure, which we will get back to later.

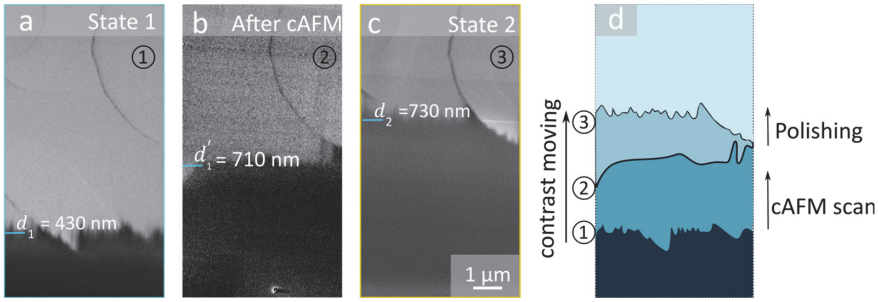

Figure 5-18. SEM images show the evolution of the contrast in response to the experiment outlined in Figure 5-17. (a) State 1, as-prepared lamella WL. (b) State 1 after applying an electrical bias, using the tip of cAFM; the darker contrast shifted towards the thicker end of the wedge-shaped lamella. (c) State 2, after FIB repolishing from State 1; a slight upward shift in the position of the darker contrast is observed. (d) A summary diagram depicting the position of the step-like change in contrast moving from image (a) to (b) and to (c).

Figure 5-18d summarizes the effect of the applied manipulation process illustrated in Figure 5-17. The position of the darker contrast moves upward after both the electrical biasing and FIB re-polishing, demonstrating that both the bias voltage and the thickness play an important role. Both processes will be investigated in more detail in the following two parts, with the goal of deconvoluting their contributions.

Thinning-dependent variations

To verify the effects from thinning and demonstrate that they generally arise in thin wedge-shaped lamellas with back-electrode, we repeat SEM imaging at different stages while reducing the thickness. Figure 5-19 illustrates the experiment, combining SEM imaging and FIB polishing. Figure 5-19a summarizes the thinning process of the lamella as described in section 5.1.3. The $ErMnO_3$ material is brought into a wedge shape and thinned down, as displayed from top to bottom. A representative SEM image showing the emergence of a region with reduced contrast is presented in Figure 5-19b. Here, the darker contrast only appears in the lower part, highlighted by a white dotted line.

As the milling continues and the back electrode material becomes visible, the thin edge of $ErMnO_3$ is approaching the sub-10 nm regime, as sketched at the bottom of Figure 5-19a. In the corresponding SEM image in Figure 5-19c, the back electrode material is now visible, giving rise to bright SEM contrast (bottom of the SEM image). Moreover, compared to Figure 5-19b, the starting position of the darker contrast has moved upwards, now situated in the middle of the imaged surface, which is also marked by the white dotted line.

Note that, the domain configuration varies between Figure 5-19b and c as the domain walls are not straight, forming a 3D network [96]. The position of the top line, however, remains constant and can hence be used as a reference position to verify that the step-like transition has moved.

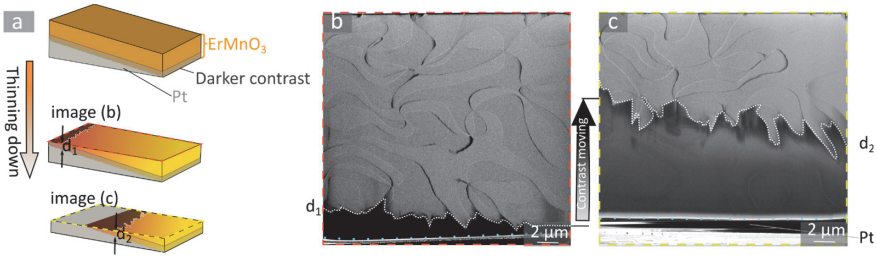

Figure 5-19. Expansion of the low-contrast regime after FIB polishing. (a) Illustration of the polishing process of the PL lamella. The thickness decreases from top to bottom, and the step-like contrast change is indicate. (b) SEM image of the lamella state in the middle of (a); the darker contrast is only visible at the very edge of the thinner part, and the value of the thickness (d_1) remains unmeasured and uncalculated due to the non-triangular cross-section of lamella at this stage. (c) SEM image of the state in the bottom of (a), the lamella is reduced in thickness, and the darker contrast becomes visible starting from the middle of the specimen, with corresponding thickness d_2= 830 nm.

The arrow between Figure 5-19b and Figure 5-19c indicates the distance the step-like change in the contrast moved during polishing, corresponding to a shift of about 9233 nm measured on the surface of the lamella. Most importantly, this shift is exclusively driven by the thinning of the lamella, without any other process involved. As the wedge is thinned down, the dark regime expands towards the top during polishing. This observation fits with the hypothesis that the onset of reduced SEM contrast relates to a specific thickness as sketched in Figure 5-17, where the red dotted line indicates the respective threshold thickness. Thus, as the thickness reduces, the portion of the surface with darker contrast gradually increases.

Electrical-bias driven effects

As shown in Figure 5-18, it was observed that the position where the darker contrast start shifted towards the thicker part after electrical biasing. To exclude that the shift is a general effect and not specific to the sample presented in Figure 5-18, different SPM techniques with and without a bias voltage applied to the lamella are conducted on a second lamella of PL type. Firstly, a non-contact technique, that is, Kelvin Probe Force Microscopy (KPFM)[277] (The working principle is described in section 3.3.4), is first performed on the new lamella PL with a sample voltage of zero. This approach allows for imaging differences in the electronic properties in a

non-invasive way and, most importantly, without the risk of modifying the low-contrast region via electrical biasing. Then, cAFM, which uses a bias voltage in contact mode, is conducted to reproduce the behavior seen in Figure 5-18. The results are presented in Figure 5-20.

Figure 5-20a is a zoom-in to the SEM image of the lamella PL from Figure 5-19c. The start of the darker contrast is outlined by the white dashed line. The KPFM image in Figure 5-20b shows the potential difference on the sample surface. The sample voltage was set as 0 V, and the tip-sample distance was 22 nm. Although the KPFM scan has a much lower resolution than the SEM image, it is clear that the thicker part with bright SEM contrast has a higher potential than the thinner part. The green dashed line is used to mark the approximate position of the dark region's edge in KPFM. By comparing the position in SEM and KPFM, we see that the contrast stays approximately at the same position as in the SEM image, which is also reflected by the line plot in Figure 5-21a, showing the intensity distribution integrated over the width of the SEM (Figure 5-20a) and KPFM (Figure 5-20b) images.

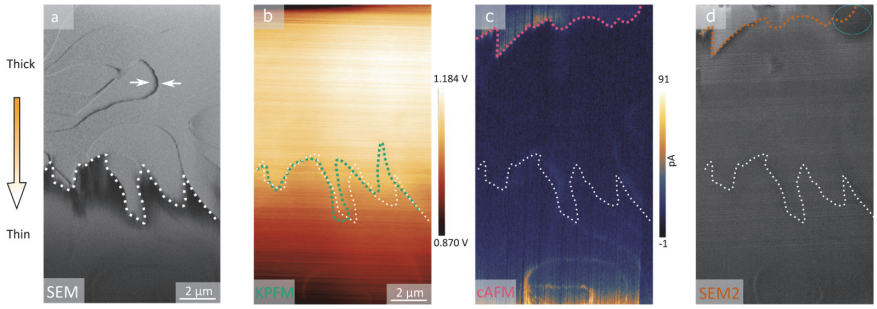

Figure 5-20. The position shift of darker contrast in SPM scans. The contrast only moves when the bias voltage is applied. (a) SEM image from part of the PL lamella. The position where the contrast starts is delineated by a white dotted line. 1.75 kV, 0.2 nA, by TLD. (b) KPFM image of the same area in (a). Green dots trace the contrast position. The white dots are the same as in SEM. The KPFM measurement was performed in two-pass mode using Cypher ES AFM (Oxford instruments) with a Ti/Ir coated Si tip (ASYELEC.01-R2, Oxford Instruments). The first pass recorded the topography in tapping mode (section 3.3.1) with a setpoint amplitude of 125.19 nm, oscillating frequency of 66.7 kHZ, and scanning height of 92 nm. On the second pass, the tip was about 22 nm above the sample surface, following the path of the first pass. The sample voltage was set to 0 V. An AC voltage of 3V with 66.7 kHz was applied to the tip. Simultaneously, a DC voltage was given to the tip by a feedback loop to nullify the cantilever oscillation. (c) cAFM image of the same region. The contrast position is now indicated by the red dots, and the white dots are from SEM. The cAFM image is acquired with a CDT-NCHR-10 probe tip with a bias voltage of 12.0 V applied to the back electrode. (d) SEM image (1.75 kV, 0.2 nA, by TLD) from the same spot after cAFM scan. Light red marked the contrast position.

Figure 5-20c is a cAFM image from the same spot, in which the red dashed line indicates the darker contrast position measured in cAFM. The thickness where the transition from dark to bright contrast occurs is approximately 1600 nm. When comparing the cAFM data with the initial SEM image (marked by the white dashed line), a substantial shift is seen. The change is even more pronounced than in lamella WL (see Figure 5-18). In addition, a small range of bias voltages (12.0 V, 13.5 V, and 16.5 V) are used for cAFM scans, with no detectable change in the position of the step-like change in contrast (not shown). It is important to note, based on our

experimental observation, that the contrast position shifts when a sufficiently high voltage is applied to the sample. For values in the order of about 10 V, no substantial changes in the position were resolved between different scans in the subsequent imaging experiments.

When a negative bias voltage (-15 V) is applied via the cAFM tip to the top welding material, Pt, for 5 minutes. In subsequent cAFM images recorded by the normal positive reading voltage it shows no detectable change.

Figure 5-20d shows an SEM image taken after the cAFM scan (Figure 5-20c) at the same spot, using identical imaging parameters as in Figure 5-20a. Although scan lines attributable to the SPM scans are present (e.g., the blue circle in the upper right highlights an area affected by the tip), it is evident that the darker contrast regime remains unchanged within the resolution of the experiment, showing the same position as in the initial cAFM scan in Figure 5-20c. This is further corroborated by the integrated data in Figure 5-21b, revealing that the step-like change in contrast has moved from about 10 µm to about 2µm toward the thicker region on the surface due to the electrical biasing.

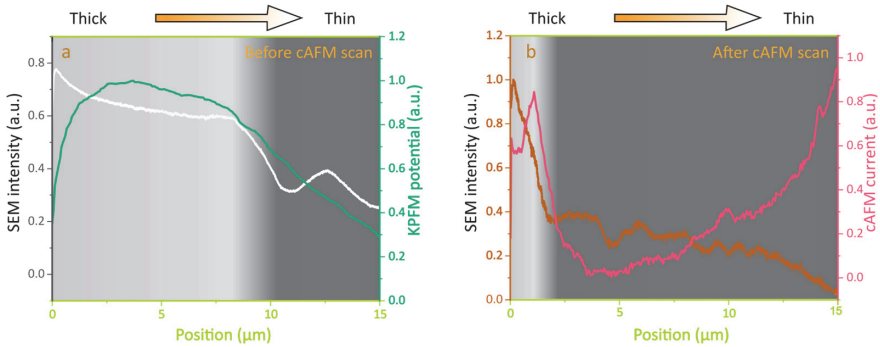

Figure 5-21. The position shift of the step-like change in contrast before and after electrical biasing. (a) Before the cAFM scan, the position of the step-like change in contrast in SEM and KPFM is located approximately 10 µm away from the top. The corresponding thickness of this position is approximately 800 nm. (b) After the cAFM scan, the contract change shift to a position located approximately 2 µm away from the top. The corresponding thickness of this position is approximately 1600 nm. All the values in these two graphs are integrated from the corresponding whole images shown in Figure 5-20 along the thickness variation direction. The integrated values are normalized from 0 to 1.

Figure 5-20 demonstrates that in the non-contact, zero-sample bias technique KPFM, the darker contrast remains at the same position as seen in the SEM image. However, in cAFM mode, where we apply a positive bias voltage to the metal, the darker contrast moves significantly toward the thicker part, while the negative voltage has no obvious effect. This result suggests that a positive bias voltage applied to the metal drives the contrast further toward the thicker part, where it remains as the bias is removed, reflecting a non-reversible change.

Discussion

In this section, by combining previous studies on $ErMnO_3$ and general semiconductor physics, the possible underlying mechanisms of the origin of the step-like change contrast are discussed, explaining the experimental observations.

In general, a Schottky barrier is formed at metal-semiconductor interfaces, creating a potential energy barrier between the metal and the semiconductor. The latter is induced by the mismatch of the work function between the metal and semiconductor [278]. When the metal and p-type semiconductor come into contact and form a Schottky barrier, this implies that the work function of the metal is lower than that of the semiconductor, in our case, p-type semiconductor $ErMnO_3$ [109,279,280]. In other words, the metal's Fermi level is higher than that of $ErMnO_3$, prompting an electron movement from the metal to the p-type semiconductor [281] $ErMnO_3$ until an equilibrium is reached. This electron migration leads to a depletion region, i.e., a zone within $ErMnO_3$ close to the interface where electron and hole carriers recombine, giving rise to a depletion region. A built-in potential manifests on both sides of the depletion region, counter-acting the electron movement from the metal to $ErMnO_3$ and holes diffusing from $ErMnO_3$ to the metal.

For a metal in contact with a p-type semiconductor, the Schottky barrier height can be calculated based on the difference in the work function of the two materials. $ErMnO_3$ has a band gap E_g of 1.6 eV and an electron affinity of 3.83 eV[282]. According to the definitions, this gives a work function $\emptyset_s(ErMnO_3) \leq 5.43$ eV, which is further dependent on the doping level. Pt is a relatively high work-function metal, for which the literature values range from 5.30 eV [283] to 5.65 eV [284]. In the fabrication process, Pt was, however, deposited by the Ga ion beam. This will lead to a Pt-Ga mixed material. Ga has been reported to have a work function of 4.20 eV [284]. The actual work function of Pt-Ga material $\emptyset_m$ is complicated to calculate, as the electronic levels and energies of a solid depend sensitively on the structure, surface morphology, and chemical composition of the system [285]. Based on this and our experimental observations, it is reasonable to assume that Ga reduces the work function below the value of $\emptyset_s(ErMnO_3)$. This assumption leads to the following band diagrams. As exact numbers are not available, we only qualitatively draw the band diagrams according to the experimental observations.

Figure 5-22a illustrates the band diagrams of a metal and a p-type semiconductor with higher work function, respectively, when they are sufficiently far apart. In these diagrams, E_{vac} denotes the energy level in vacuum. E_c represents the lowest energy level of the conduction band, and E_v is the highest energy level of the valence band. Fermi level is indicated by E_f. The term χ refers to the electron affinity, which is the energy difference between the semiconductor conduction band edge and the vacuum energy [286]. $\emptyset_m$ and $\emptyset_s$ are the work functions of metal and semiconductor, respectively. $\emptyset_B$ represents the Schottky barrier height. When the metal

comes into contact with the semiconductor, as in the wedge-shaped lamella, the electrons naturally move from the metal into the semiconductor until the Fermi levels are aligned. As shown in Figure 5-22b, this induces band bending and a depletion region in the semiconductor. In the wedge-shaped lamella, the metal is in direct contact with $ErMnO_3$, because the metal was deposited on the $ErMnO_3$ by ion beam deposition in high vacuum (~10^{-3} Pa). Thus, it is reasonable to assume that a depletion region with a certain thickness forms at the wedge-electrode interface, similar as discussed before concerning the regime marked by the red dotted line in Figure 5-17 and Figure 5-19. This leads to the conclusion that the observation of the step-like change in SEM contrast is due to the metal back-electrode contact. In contrast, for flat free-standing lamellas, the distance between the metal and semiconductor is not zero, leading to different charge carriers exchange dynamics and, consequently, different phenomena. This can explain the absence of the darker contrast in flat free-standing lamella of comparable thicknesses (200 nm, 400 nm).

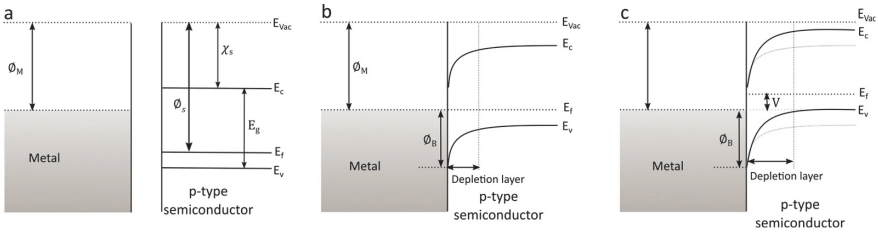

Figure 5-22. Sketches of the energy band diagram for a metal and semiconductor contact (p-type). (a) No contact; the work function of the p-type semiconductor is bigger than that of the metal. (b) Contact with zero bias voltage. The depletion appears.. (c) Contact and positive bias voltage given to the metal. The depletion region becomes wider.

If a positive bias voltage is applied to the metal, like in cAFM measurements we performed on wedge lamellas, the voltage adds to the build-in potential and increases the energy barrier that the holes need to overcome to diffuse from the semiconductor into the metal. The applied positive bias voltage add into the build-in potential[287], thereby expanding the width of the depletion region. This situation is illustrated in Figure 5-22c. Note that a second metal/semiconductor is formed at the tip/sample contact in our SPM experiments. In particular, in the cAFM scans, the Schottky barrier between the tip and the semiconductor surface plays an important role and has been widely investigated [282,288]. However, as the step-like change in contrast occurs at the same position in the SEM and cAFM scans, as shown in Figure 5-20d, one can exclude that the tip-sample contact plays an important role. This infers that the depletion region is mainly induced by the deposited back electrode, and the Schottky barrier between the tip and sample surface can be neglected here. Another effect we see is that the depletion region keeps its extended width after the bias voltage is removed. This behavior is different from an ideal Schottky barrier. A possible origin is the electric field-induced migration of oxygen defects. Oxygen defects play a key role for the conductivity of $ErMnO_3$ [109,111]. The oxygen

defects are rather mobile and migrate under the applied electric field. This result is in line with the result from Evans et al. [107], showing that the electric-field-induced oxygen defects persist on the timescale of years at room temperature, giving rise to irreversible changes in the transport behavior.

Thus, the experimental observations, including the emergence of the darker contrast, its correlation with the back electrode material, and the voltage-induced change of the depletion width, align well with the formation of a depletion region at the interface between wedge and back-electrode. From the experiments performed to characterize this depletion region, important material parameters can be extracted, such as the carrier density in the FIB-prepared $ErMnO_3$ lamella. According to Schottky barrier theory, the depletion width can be calculated as follows [289]:

$$d = \sqrt{\frac{2\varepsilon_0\varepsilon_r\phi_B}{n}}, \qquad \text{Equation 5-1}$$

where ε_0 is the vacuum permittivity, ε_r is the relative dielectric constant, ϕ_B is the Schottky barrier height in eV, and n is the density of free carriers.

From the measured thickness of approximately 430 nm for the depletion contrast in lamella WL (SEM image shown in Figure 5-16), the carrier density can then be calculated by Equation 5-1. According to literature, the dielectric constant of in-plane $ErMnO_3$ is about 11 [93]. In addition, we assume a Schottky barrier height ϕ_B= 1 eV based on the work function ($\emptyset_s(ErMnO_3) \approx 5.43$ eV, $\emptyset_s(\text{Pt}) = 5.30$ eV~5.65 eV, $\emptyset_s(\text{Ga}) = 4.20$ eV). Based on these numbers, the carrier density is calculated as 5.98×10^{15} carriers/cm^3. For reference, a carrier density of about 2×10^{19} carriers/cm^3 was previously assumed in calculations to rationalize the domain wall behavior in $ErMnO_3$ [282]. In addition, estimates have been made for the carrier density at tail-to-tail domain walls based on local Hall data, ranging from 10^{13} carriers/cm^3 [266] to $\sim 1 \times 10^{16}$ carriers/cm^3 [102]. Thus, the carrier density determined based on the wedge experiments is well within the discussed regime, providing a solid basis for the further analysis of the emergent domain wall contrasts in section 5.3.2.

The observation of abrupt changes in SEM contrasts due to the formation of a depletion region, together with the width of the depletion region, is actually not unprecedented and was observed in other systems. A brightly contrasted segment at the contact point between a metal and a single-walled carbon nanotube was observed by SEM image, extending up to micrometers in length. Here, the change in SEM contrast was attributed to the space charge distribution within the depletion region[290].

In our work, the depletion region itself is visible in SEM, which is a result of the lower concentration of the mobile carriers within this region, leading to a different conductivity that ultimately yields different secondary electron intensities in SEM. This mechanism is comparable

to the effect observed at charged domain walls in hexagonal manganites, where different SEM intensities arise compared to the domains due to a different charging effect [291].

Based on the experimental observation, the depletion width depends on the quality and nature of the contact between the semiconductor $ErMnO_3$ and the back electrode. This dependence explains the different behavior of the flat free-standing lamella and the back electrode attached wedge lamellas. The depletion happens at the entire interface where the metal contacts the $ErMnO_3$, as illustrated in Figure 5-17 and Figure 5-19. Therefore, in the wedge-shaped lamella, as the sample thickness decreases, a larger proportion of the depletion area becomes exposed and measurable at the surface. Moreover, as a bias voltage is applied to the metal, the depletion width increases because the build-in potential increases, again leading to a larger surface area at which the depletion layer is exposed.

The emergent depletion has not yet been discussed in literature for hexagonal manganites, but plays an important role in domain wall device applications where integration of domain walls into circuits is required. It presents a parameter that remains to be controlled and an opportunity to add new freedom into the device circuit by using different contact materials.

5.3.2. Domain walls in the depletion region

The origin of the step-like changes in SEM contrast can be explained by the depletion region that forms due to the Schottky barrier between the semiconducting $ErMnO_3$ and the metal back-electrode. This depleted region shows low conductance, whereas the domain walls within this region showed distinctly different behavior from the standard bulk sample. Here, all the domain walls are more conducting than the domains. In this section, SEM imaging in combination with different SPM methods is used to explore the origin of the intriguing domain wall behaviors.

In order to understand the domain wall properties within the depletion region in more detail, we investigate the domain wall conductance by means of voltage and temperature. For this, lamella PL is used, as it provides a broad depletion region, making it easier to monitor the change.

5.3.2.1. Domain wall conductance under different bias voltages

The conductance of the domain wall under different reading voltages is the first aspect to be evaluated. The accessible voltage range, however, is limited compared to previous bulk measurements: if the bias voltage is too low, no contrast can be obtained in the current channel of cAFM because of the reduced conductance, and if the voltage is too high and electric current flow, the thin part is easily destroyed. Reading voltages of 12.0 V, 13.5 V, and 16.5 V applied to the back-electrode turned out to be adequate, and the obtained cAFM images are presented in Figure 5-23. The figure on the right of Figure 5-23 illustrates that the scan area (indicated by the blue frame) is within the depletion region and close to the lamella wedge. Additionally, the

number on the right indicates the smallest thickness at which the cAFM data can be obtained without destroying the region. As the reading voltage increases, the thinner edge is increasingly destroyed, analogous to that observed in lamella WL shown in Figure 5-11 and Figure 5-12.

As shown in Figure 5-23, when a relatively low voltage (12 V) is used for the cAFM scan, only parts of the domain walls are conductive, most of which are head-to-head walls, as seen in the regime highlighted by the red rectangle. However, as voltage increases, all the domain walls exhibit enhanced conductance relative to the domains, as shown in Figure 5-23b. The effect becomes even more pronounced with a further increase in bias voltage to 16.5 V, as can be seen in the bottom of Figure 5-23c, which we attribute to the high electric field and currents. In addition, cAFM data can only be obtained from regions thicker than 202 nm, as more material has been compromised under a higher electric field.

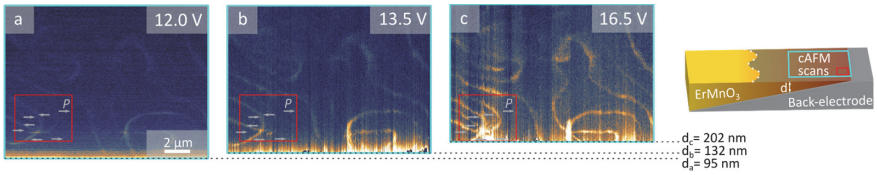

Figure 5-23. cAFM images of domain walls within the depletion region (marked by blue frame) in lamella PL under different reading voltages. (a) 12.0V; (b) 13.5V; (c) 16.5V. All the scans were performed with the same doped diamond tip CDT-NCR with the bias applied to the back electrode. The red rectangles highlight a region with a six-fold meeting point. The figure on the right illustrates that the scanned area displayed in (a)-(c) is within the depletion region and close to the thin edge of the lamella. The number below indicates the smallest corresponding lamella thickness at which the cAFM data can be obtained without destroying the region. As the reading voltage increases, the thinner edge is increasingly compromised.

It is known in p-type $ErMnO_3$ single crystal bulk samples that the tail-to-tail domain wall is usually conductive first when a voltage is applied [16], and only in the high-voltage regime the head-to-head domain walls also become conductive [21]. This is an intrinsic effect, due to the bound charges at the domain walls, inducing the accumulation of the hole carriers at tail-to-tail walls, as well as the inversion layer at head-to-head domain walls (see section 2.2.3 for detail). However, this explanation does not hold within the depletion region, where the effect is reversed and the head-to-head domain walls are conductive at lower bias voltages, whereas tail-to-tail domain walls only become visible at higher bias voltages, requiring further investigations/discussion. In general, the higher conductance of the domain walls compared to the domains in the depletion region is consistent with a locally different carrier density and different electrostatics, which will affect the interaction with the back-electrode and the local depletion process, as discussed later.

5.3.2.2. Domain wall conductance vs. temperature

In order to investigate the conductance at the domain walls in the depletion region in response to changes in temperature, the lamella PL is heated up to 100 °C. The heating process is performed in Cypher ES Environmental AFM at an ambient atmosphere with a ramp rate of

0.3 °C/s. Figure 5-24 shows cAFM images from the depletion region of sample PL, in which (a) is collected at room temperature and (b) at 100 °C. Figure 5-24a displays that only some of the domain walls are a bit more conducting than the domains. Figure 5-24c shows the current profile for a head-to-head domain wall marked by the blue line in Figure 5-24a. The domain wall is about 4 times more conductive than the domains. When the lamella is heated up to 100 °C, all the domain walls are significantly more conductive than the domains, as shown in Figure 5-24b. In addition, both domains and domain walls are much more conductive than at room temperature, consistent with the semiconducting behavior of $ErMnO_3$. Figure 5-24d shows the current profile along the same domain wall as in Figure 5-24c at 100 °C, marked by the red line in Figure 5-24b. Here, the overall current level of the domains is higher than at room temperature. Upon cooling the system back to room temperature with the same ramp rate, the current map returns to its initial state (not shown), which is the same as shown in Figure 5-24a.

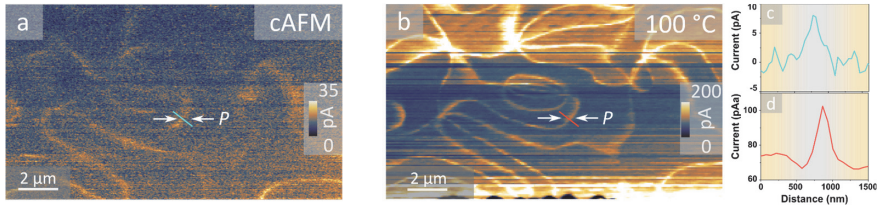

Figure 5-24. Variations in domain walls behavior under identical SPM parameters at different temperatures. (a) cAFM image acquired at room temperature under ambient atmosphere; recorded by doped diamond tip CDT-NCR with 12V bias applied to the back-electrode (b) cAFM image captured at 100 °C under ambient atmosphere; recorded by the same tip as (a) and 12 V voltage. (c) and (d): current profiles of the same spot (marked by the blue and red lines) at room temperature and 100 °C, respectively.

This observation reveals the significant influence of temperature on the conductivity of both domains and domain walls. As the number of available mobile carriers increases with the temperature, the overall conductance goes up. Moreover, this is consistent with the thermionic emission behavior in the depletion region of the Schottky barrier [292,293], as we concluded above.

5.3.2.3. Contact between back-electrode and domain walls

In $ErMnO_3$ bulk sample, the bound charges at the domain wall influence the distribution of the mobile carriers, i.e., holes [21]. In the depletion region seen in the thin part of our wedge-shaped samples, these bound charges are expected to also play a significant role in the redistribution of the holes. Figure 5-25 shows an SEM image of the FIB cutting cross-section on sample WL after performing different SPM scans. Here, it can be seen that many domain walls (three out of four) are in direct contact with the back electrode, while only one of the domain walls (the upper right) propagates almost parallel to the surface. Thus, it is reasonable to assume that for a substantial number of walls, the bound charges directly affect the depletion of the holes, as they affect the potential difference across the depletion region. This phenomenon is often referred to as Schottky barrier inhomogeneities and has been widely reported since it was first

observed by Werner et al.[294]. Interface roughness, metal dislocations, grain boundaries, and defects are common factors that induce such inhomogeneities [295].

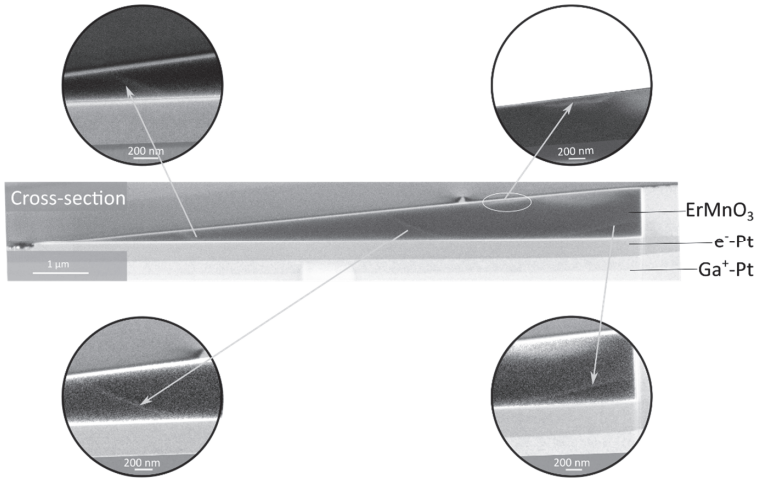

Figure 5-25. Representative SEM image (1.0 kV, 0.2 nA, TLD) of the FIB-cut cross-section on lamella WL. The middle triangular part (black) is the $ErMnO_3$. Three of the four domain walls are in contact with the back electrode (white). In the circled magnified SEM images, domain wall segments have been selectively enhanced to increase contrast and visibility. These enhanced segments are then seamlessly overlaid onto the original image, providing clear visual guidance to the domain walls.

Aside from the different conducting behavior at the domain walls relative to the domains due to the contact between the domain wall and the back electrode, another effect was observed at several head-to-head domain walls, i.e., the emergence of an additional contrast on only one side of the domain walls.

Figure 5-26 presents the SEM images of lamella PL-C (left) and PL (right), in which the white arrows indicate the polarization directions. The blue dotted lines in Figure 5-26b mark the position of the domain walls according to a correlated PFM image (not shown). As indicated both in Figure 5-26 a and b, the position of head-to-head domain walls influences the change in SEM contrast that reflects the onset of the fully depleted region. The domain walls appear to act as boundaries for the depletion region (darker contrast), which is observed only on one side of the domain wall in several places. In different places, the darker contrast next to the head-to-head domain walls can be observed to further extend towards the thicker part at head-to-head domain walls. A possible explanation for the latter is that the density of mobile holes is reduced at the head-to-head domain walls[21], resulting in a larger depletion width.

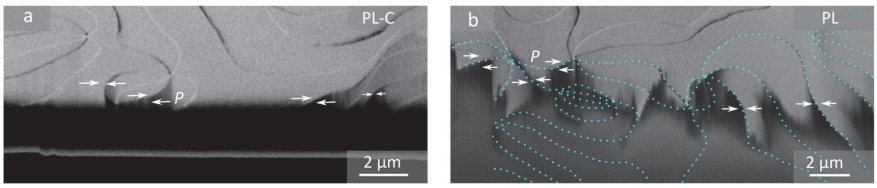

Figure 5-26. SEM images of the intermediate region between the normal and depleted regions, indicating the in-plane variation at the one end of the depletion region. (a) SEM image of PL-C (2.0 kV, 0.2 nA, TLD), with the white arrows representing the polarization direction. (b) SEM image of the PL lamella (1.75 kV, 0.2 nA, TLD). The blue dashed line indicates the domain walls positions.

To understand in detail how the bound charges affect the hole depletion, a KPFM scan on the lamella PL is used to analysis the emergent surface potential.

The KPFM image recorded on the new PL lamella provides additional evidence for the special role of the domain walls. Figure 5-27 summarizes the data addressing the surface potential variation at head-to-head domain walls in regions with different thicknesses. The domain wall charge states are identified through a combination of PFM and SEM.

Figure 5-27a presents the SEM images of the entire lamella, with the white arrows indicating the polarization direction. The colored rectangles highlight the regions for which corresponding KPFM images are presented in Figure 5-27c-e. Figure 5-27b shows a PFM scan (resonant PFM), with the white arrows indicating the polarization direction. Figure 5-27c, d, and e represent the potential map from the KPFM scan of the regions marked in the SEM image, as defined by the frame colors. Figure 5-27 (f)-(h) depict the potential profiles captured along the colored lines marked in Figure 5-27 (c)-(e). All the potential profiles are extracted from head-to-head domain walls, and are captured under the same potential scale from the raw data.

On closer inspection, it becomes apparent that the potential variation between the domain walls and domains varies as a function of the thickness.

Figure 5-27c shows KPFM data obtained from an area in the thicker part of the wedge-shaped lamella, indicated by the blue rectangle in the SEM image. In this area, two head-to-dead walls and one tail-to-tail wall are present. However, only the two head-to-head domain walls are visible in the KPFM scan, appearing as black lines. The corresponding potential profile in Figure 5-27f shows that the average potential of the domain is approximately 1.097 ± 0.001 V, while the lowest value measured at the head-to-head domain wall is 1.089 V.

In the transition region, where the step-like change in SEM contrast is observed, the KPFM image shows a substantial potential decrease from above 0.947 V in the top part to 0.912 V in the bottom (green rectangle) part. The potential profile along the green line across the head-to-head domain wall marked at the bottom of Figure 5-27d shows the domain having an average potential of 0.913 ± 0.002 V, whereas the domain wall's maximum potential value is

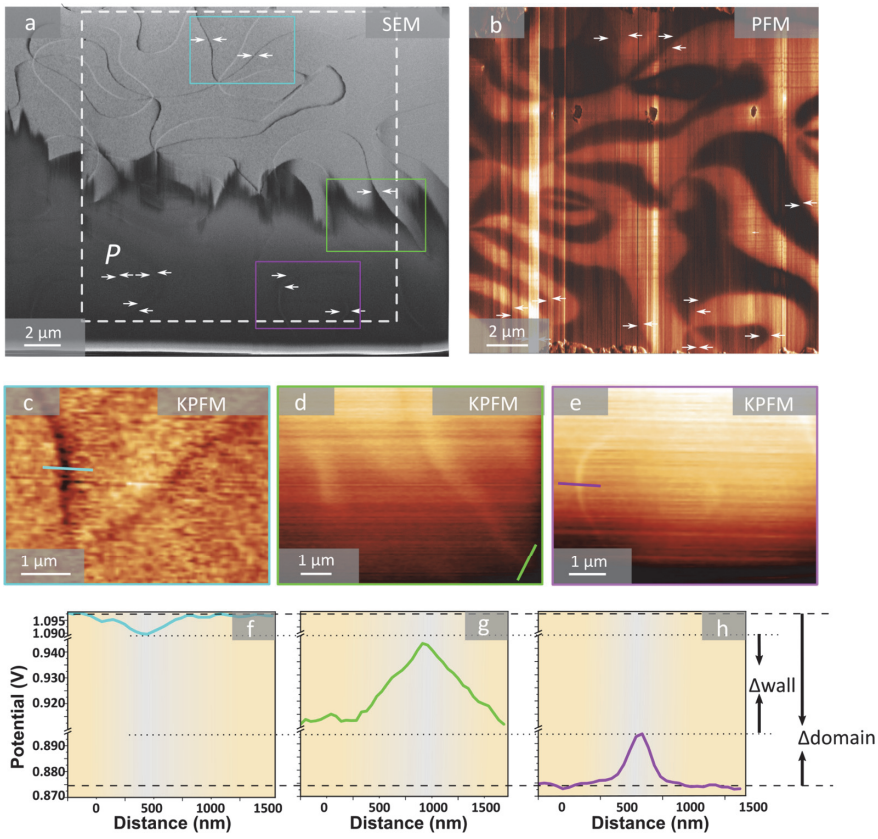

Figure 5-27. Comparison of potential variation at head-to-head domain walls and within domains as a function of thickness. (a) SEM image of the lamella PL. The three regions from the top, middle, and bottom highlighted by blue, green, and purple rectangles, correspond to the regions where the KPFM data are presented in (c)-(e), respectively. Domain polarizations are indicated by white arrows according to the PFM results. (b) PFM image of a part of lamella PL, with the white arrows indicating the polarization direction. The PFM image was obtained with a Ti/Ir probe tip using resonant PFM mode, drive amplitude 5V. (c)-(e) KPFM images recorded from the regions highlighted by colored rectangles in the SEM image. The KPFM image in (c) has been improved by a second-degree polynomial in the Gwyddion software. (f)-(h) Potential profiles along the lines marked in KPFM images in (c)-(e), respectively. The data are captured with a thickness of 10 pixels. The arrows on the right of (h) indicate the potential variations at head-to-head domain walls (Δ_{wall}) and within domains (Δ_{domain}), respectively, as the position moves from the normal region to the depletion region.

A similar behavior is observed at the head-to-head domain wall in the thinner part within the fully depleted region (purple rectangle), where the walls appear brighter than the domain, as shown in Figure 5-27e. The potential profile in Figure 5-27h shows the sharp peak at the head-to-head domain wall, where the domain has a potential of 0.874 ± 0.001 V, and the peak value at the head-to-head domain wall is 0.894 V.

Figure 5-28 summarizes the variations in surface potential over the entire lamella surface (ploted in dark green curve and denoted as Domain) and at head-to-head domain walls (scatter plot by stars and connected with bright green line) of different positions from the thick region

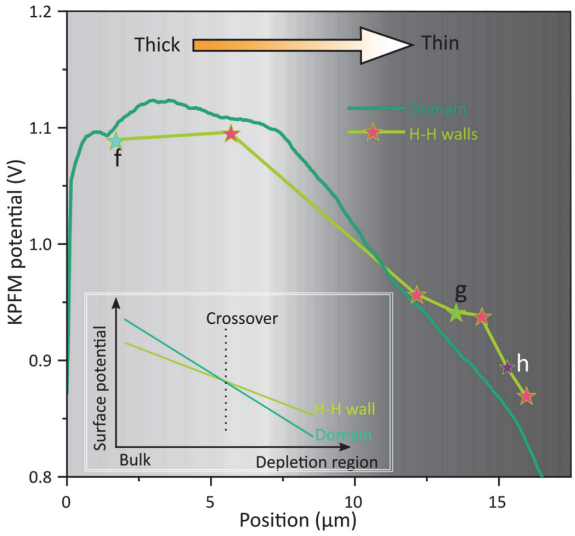

Figure 5-28 Summarizing the surface potential variation at head-to-head domain walls (H-H walls) and within domains (Domain) from the thick to thin region of lamella PL. The domain potential data (represented by the dark blue curve) is integrated over the entire surface, corresponding to the region shown in the SEM image in Figure 5-27a. The domain wall potential data are captured in the same way as the profiles shown in Figure 5-27 (f)-(h), with a thickness of ten pixels from raw data. Domain wall value are specifically marked by stars, using the minimum values of the profiles in the thick region and maximum values in the thin region. The inset demonstrates a critical crossover point where the potential at H-H wall changes from lower than the domains before it to higher than the domains after it.

to the thinner edge. The three specific positions, corresponding to the potential profiles shown in Figure 5-27 (f)-(h), are indicated by the stars with respective colors.

In summary, the KPFM measurements show a substantial potential drop from the top (thicker part) to the bottom (thinner part), which is more pronounced for the domains than the head-to-head domain walls. As a consequence, the head-to-head domain wall potential evolves from lower than the domain in the thick part to exceeding it in the thin part. The domain wall potential drops by Δ_{wall} = 0.218 V (from 1.089 at the top to 0.871 V), whereas the domain potential drops by Δ_{domain} =0.246 V (from 1.097 at the top to 0.851 V at the same position as the domain wall value), moving from the bulk-like region (top) to the depleted region (bottom). The inset in Figure 5-28 illustrates an intriguing crossover point where the potential at the head-to-head domain walls (H-H wall) transitions from being lower than the domains before it to higher than the domains after it.

This shows that the domain wall behaves differently from the domains also in the depletion region, corroborating its intrinsically different electronic properties. However, it is important to carefully analyze the KPFM contrast to understand its origin. Based on investigations of the charge dynamics in $BaTiO_3$ during heating and cooling across the Curie temperature, Kalinin and Bonnell [277,296] concluded that the KPFM surface potential they measured on the ferroelectric surface was due to screening charges in equilibrium, as well as polarization charge during the

dynamic process of the spontaneous polarization change. This is consistent with other published studies showing that the KPFM measured surface potential at grain boundary [297,298], ferroelectric domains[296,299], and charged domain walls [299] is opposite in sign to that of the bound charges. This phenomenon explains our observation: in the thicker region, head-to-head domain walls show lower potential due to the depletion of holes, and possibly, also the formation of an electronic inversion layer, which screens the positive domain wall bound charges [21]. However, in our KPFM data, the tail-to-tail domain walls, which exhibit an accumulation of holes, do not appear brighter than the domains. A possible reason can be the very small change in the electric potential at the tail-to-tail domain wall, according to the band diagram [21], possibly below the finite resolution[296] of the KPFM.

In the thin part, which is fully depleted region, the depletion results in a substantially lower hole density and, hence, overall lower potential. This leads to the potential drop within domains. At both head-to-head and tail-to-tail domain walls, the depletion leads to potential drops, which differ from those in the domains. At head-to-head domain walls, the depletion of initially dispersed holes leads to a slight decrease in surface potential. This, along with the localized electrons, which is not resolved in the experiment, results in a smaller potential drop compared to the domains. Tail-to-tail domain walls, on the other hand, demonstrate a small potential difference from the domains and, analogous to the thicker region, remain unresolved in the thin region.

Depletion significantly reduces the overall conductance, while the domain walls maintain relatively higher conductance than the domains. There are two possible reasons. Firstly, depletion leaves bound charge at the domain walls not fully compensated, inducing a depolarization field that prompts electrons/holes to transfer across the forbidden energy gap to screen the bound charge, thereby contributing to conductivity, as detailed by Sluka et al. [13]. Secondly, the interaction of head-to-head domain walls with the back-electrode could provide an n-type channel for electron flow, while bound charges at tail-to-tail domain walls only allow partial depletion of the hole, sustaining some conductivity at the walls.

Although the microscopic mechanism for the observed electrostatic response is not clear at this point, the data reveals a striking difference regarding the domain wall behavior between the normal bulk-like region and the depletion region. Most importantly, this finding gives new opportunities for the utilization of domain walls, showing that their electronic conductance is qualitatively different in depleted and non-depleted host materials. This distinction offers the potential to fine-tune the functionality of the pursuit domain wall-based circuity.

5.3.3. Summary

In the case of the back-electrode-attached wedge-shaped lamellas, a darker contrast appears close to the thinner edge. Due to its dependence on the lamella thickness, back electrode

material, and applied bias voltages, this darker contrast is attributed to the depletion region that forms when the metal back electrode comes into contact with our p-type $ErMnO_3$. Although the conductance across the whole region decreases strongly, the domain walls within this region remain more conductive than the domains. This enhanced conductance at the domain walls is driven by the bound charges at the domain wall, which lead to a redistribution/generation of mobile carriers.

To further explore the domain wall thickness-dependent properties and understand the electronic driving mechanism, we propose using FIB to deposit an insulating material to the back of the lamella to mitigate the depletion region we encountered here. This, however, would require a lateral electric connection between the $ErMnO_3$ and the metal disk for cAFM scanning.

Another promising approach to studying domain wall thickness-dependent properties without other interferences is to use SEM contrast. SEM has demonstrated its ability to provide a contrast correlatable with the cAFM image in our work. Specifically, by utilizing identical SEM image parameters, we can capture the contrast change of an $ErMnO_3$ lamella mounted on a TEM grid while using FIB to thin it down to electron transparent gradually. This strategy fully harnesses the capability of SEM and minimizes external factors such as the high electric field and Schottky barrier, thereby revealing the inherent properties of $ErMnO_3$ domain walls.

In general, experiments foreshadow so far unexplored domain wall properties in depleted systems, which is interesting from the fundamental point of view, but also highly relevant for domain wall-based device applications.

6. SEM non-destructive 3D imaging of ferroelectric domain walls for device fabrication

The ferroelectric domain walls in $ErMnO_3$ exhibit potential to be used as ultra-small functional units for next-generation nanoelectronics (section 2.2.3). However, determining the specific domain-wall properties, which are crucial for the subsequent device performance, remains a major challenge. This difficulty arises because the domain walls in $ErMnO_3$ are meandering, altering their charge states along their path on the nanometer length scale (see section 2.2.2). Furthermore, the domain wall structure in the near-surface region strongly influences the transport behavior[96], and, hence, needs to be characterized adequately. Established tomography techniques are either destructive or lack sufficient spatial resolution, highlighting the urgent need for 3D imaging methods that are compatible with future fabrication processes and capable of real-time monitoring of the electronic domain wall properties.

In this chapter, we demonstrate that secondary electrons (SE) carry rich information about the electronic material properties [94] at the surface and in near-surface regions. This sensitivity opens the door for SEM-tomography to monitor the position, orientation, and charge state of ferroelectric domain walls. The basic concept of SEM tomographic imaging is illustrated in Figure 6-1.

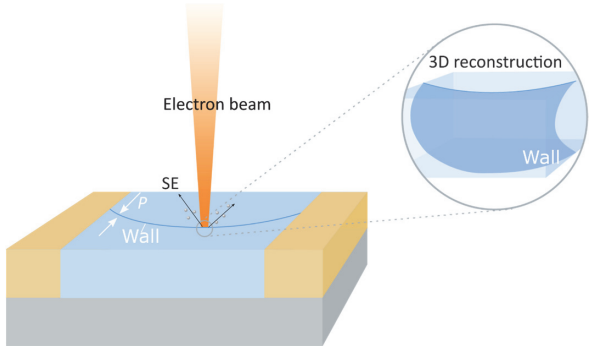

Figure 6-1. Concept of SEM tomographic imaging of ferroelectric domain walls. The surface SE intensity is measured to restructure the domain wall 3D structure in the near-surface region at a charged domain wall.

This chapter begins with an overview of the critical role of the domain wall sub-surface structure, summarizing previous findings and our experimental observations. We then demonstrate the capability of SEM to reveal the electronic properties at ferroelectric domain walls. Following this, our observation extends beyond the surface domain structure, showing that domain walls hidden below the surface can also cause noticeable variations in SEM surface intensity. A mathematical model is derived to correlate the SEM surface intensity variations with the domain wall properties in the near-surface region, including its location and orientation. Based on this model, it is possible to reconstruct the shape of ferroelectric domain

walls in near-surface regions using SEM surface images. The orientation angle and distance from the surface of hidden domain walls are derived by applying a reconstruction procedure that was developed in close collaboration with Manuel Zahn, who performed the respective calculations. The chapter is based on our manuscript [300].

6.1. The importance of the domain wall configuration in near-surface regions

The properties of domain walls are profoundly influenced by their local charge state, which is determined by their local orientation relative to the ferroelectric polarization. To display the crucial role of the subsurface configuration of the domain wall, this section begins with an overview of the definition of the domain wall charge state at the sample surface and, then, addresses the impact of the subsurface structure, drawing on insights from pioneering studies. Following this established knowledge, experimental data are presented, revealing the surface domain wall and the corresponding subsurface domain wall configurations via cross-sectional images.

6.1.1. Charge state and 3D domain wall structure

$ErMnO_3$ naturally forms a 3D network with neutral (side-by-side), positively (head-to-head), and negatively (tail-to-tail) charged domain walls [16]. The domain walls have been studied intensively, and their fundamental physical properties are well understood [16,21,22,25,63,69,84,86,96,102], which makes the material an ideal model system for exploratory studies as discussed here. At the tail-to-tail domain walls, mobile holes accumulate to screen the bound charges, ρ_b, and give rise to enhanced conductance, as shown in Figure 6-2. Figure 6-2b presents a conductive atomic force microscopy (cAFM) image, where tail-to-tail walls appear as bright lines, indicating about four times higher conductance than the ±*P* domains they separate. In contrast to the tail-to-tail walls, reduced conductance is observed at head-to-head domain walls (black lines in Figure 6-2b), owing to a depletion of hole carriers, as explained in detail in section 2.2.3. The local charge state of the domain walls can be estimated based on their orientation relative to the polarization $\vec{P}$ of the adjacent domains:

$$\rho_b = \left(\overrightarrow{P_1} - \overrightarrow{P_2}\right) \cdot \overrightarrow{n_1} = 2P \cdot \cos\alpha \,, \qquad \textit{Equation 6-1}$$

with $\overrightarrow{P_1} = P$ in domain 1, and $\overrightarrow{P_2} = -P$ in domain 2 (the domain wall normal unit vector $\overrightarrow{n_1}$ points from domain 2 to domain 1). α is the angle between the local wall normal $\vec{n}$ and $\overrightarrow{P_1}$, as illustrated in Figure 6-2a. In this approximation, however, the sub-surface structure of the domain wall is neglected, which can lead to substantial deviations between the calculated bound charge and the actual charge density. For example, it was observed that nominally neutral domain walls (i.e., $\alpha = 90°$) in $ErMnO_3$ [69] and $PbZr_{0.2}Ti_{0.8}O_3$ [18,59,60] can exhibit enhanced or even metallic conductance, which was attributed to a non-zero inclination angle relative to the surface (Figure 6-2b). By performing cross-sectional experiments on $LiNbO_3$ [71], the impact of the inclination angle on the domain wall conductance was demonstrated,

revealing that 10-15° tilting leads to a substantial enhancement. In addition, the domain wall curvature (Figure 6-2c) plays an important role, as shown by tomography-based 3D studies on $ErMnO_3$ [96]. In summary, these studies highlight the importance of the sub-surface structure of ferroelectric domain walls and the need for adequate characterization methods.

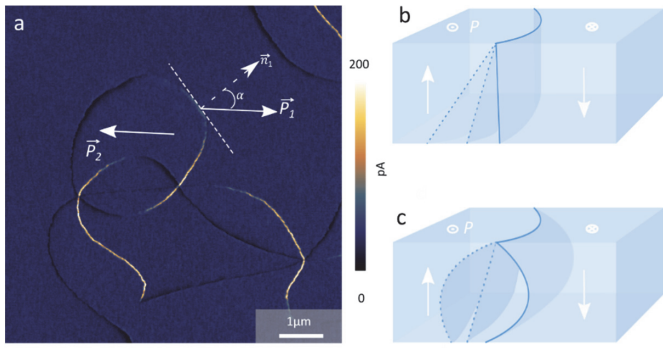

Figure 6-2. Domain wall conduction and orientation in surface-near regions. (a) cAFM image gained on the surface of an $ErMnO_3$ single crystal with in-plane polarization P as indicated by the white arrows (acquired with a CDT-NCHR-10 probe tip at a bias voltage of 3 V applied to the back electrode). Tail-to-tail domain walls exhibit enhanced conductance relative to the bulk (bright), whereas reduced conductance is observed at head-to-head domain walls (black). The local domain wall charge state can be estimated based on Equation 6-1 by measuring the angle α between the wall-normal n and the direction of P. b,c, Illustrations showing domain walls in the near-surface region. Domain walls can exhibit different inclination angles (b) or pronounced curvature effects (c) under the surface, which is not visible from surface-sensitive measurements alone.

6.1.2. Imaging domain walls in near-surface region

Some examples of how the domain walls vary their propagation direction in the near-surface region are displayed in Figure 6-3. Figure 6-3a shows an SEM image of an in-plane $ErMnO_3$ single crystal. Two domains separated by three domain walls are highlighted in the center, with the walls being approximately 4 µm apart, as indicated by the red dots. White arrows mark the direction of polarization. To facilitate the extraction of lamella samples with fewer domain walls, a FIB (focused ion beam) cut was performed along the red dashed line in Figure 6-3a. The resulting cross-sectional image, shown in Figure 6-3b, reveals that all three domain walls propagate toward the right side, forming horizontal walls in the near-surface region. Several additional horizontal walls are observed beneath the surface domain. The effort to obtain lamellas with fewer domain walls resulted in a much more complex structure than initially expected, demonstrating an extreme case of domain wall orientation changes in the subsurface region. This kind of situation is not rare.

In Figure 6-3c, another SEM image from the surface of an in-plane $ErMnO_3$ bulk sample is displayed, highlighting two domain walls that are separated by about 10 µm. The corresponding cross-sectional SEM image in Figure 6-3d reveals that these apparently distant head-to-head and tail-to-tail domain walls on the surface are actually connected in the region

about 500 nm under the surface. Additionally, a vortex structure is located at about 850 nm below the surface.

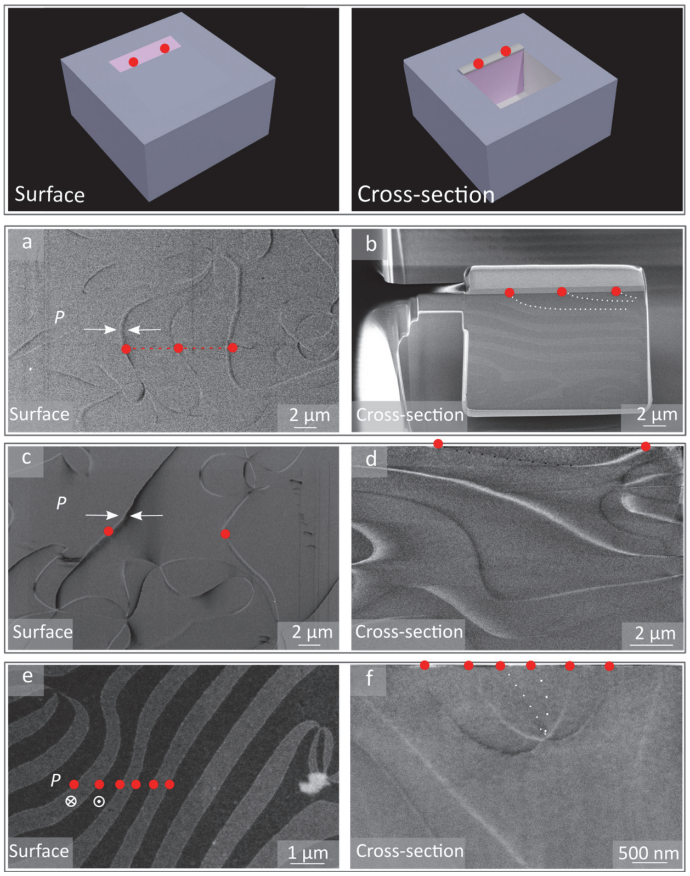

Figure 6-3. Propagation of domain walls beneath the surface. Top row: Surface SEM images. Bottom row: Corresponding cross-section SEM images. (a) SEM image showing three domain walls located between large domains on the surface of an in-plane $ErMnO_3$ single crystal bulk sample. The red dots highlight the domain wall positions. (b) Cross-sectional SEM image from the same region as in (a); the red dots correspond to the same position as in (a). (c-d) Surface SEM image and the corresponding cross-sectional SEM image from the same region on an in-plane $ErMnO_3$ bulk sample surface. Red dots in both images indicate the same spots. (e-f) Surface SEM image and the corresponding cross-sectional SEM image from an out-of-plane $Er(Mn,Ti)O_3$ single crystal. The six dots indicate the same spots in both images.

A similar scenario occurs also in out-of-plane samples. Figure 6-3e presents an SEM image from an out-of-plane $Er(Mn,Ti)O_3$ bulk sample surface, with six parallel neutral domain walls marked by red dots. The corresponding cross-sectional image in Figure 6-3f shows that these six parallel walls on the surface evolve into domain walls with varying charge states, converging at a vortex core approximately 1 µm below the surface. Although the meandering and changing orientations of domain walls in hexagonal manganites are expected due to the topologically protected vortex/antivortex structures (section 2.2.2), the rapid changes in orientations (charge states) within such a short distance away from the surface suggest the critical importance of the subsurface structure.

6.2. Probing electronic properties by SEM

SEM plays a vital role in this work, due to its capability to reveal the electronic properties of the domain walls. This section establishes a systematic correlation between SEM intensity contrast and the electronic properties of the domain walls in $ErMnO_3$, confirming SEM contrast as a reliable indicator of electronic transport phenomena associated with domain walls.

SEM has widely been applied for imaging domains and domain walls of ferroelectric materials, including $BaTiO_3$ [301], $Gd_2(MoO_4)_3$ [302], $LiNbO_3$ [303], and $RMnO_3$ (R = Y, Er) [100,304]. Although SEM is usually considered a surface-sensitive technique on account of the shallow escape depth of secondary electrons [305], it is also known that near-surface regions can play a crucial role for the emergent SEM contrast [122,306]. The latter provides an as-yet-unexplored opportunity for minimally invasive analysis of the near-surface nanostructure of ferroelectric domain walls and their electronic properties, that potentially allows to replace destructive measurements as presented, e.g., in Figure 6-3.

To explore this possibility, we perform correlated SEM and cAFM measurements on lamellas, which we extracted from an $ErMnO_3$ single crystal [243] with a FIB, applying the same procedure as outlined in section 5.1.1. Figure 6-4a and b show representative SEM images gained with the through-lens detector (TLD) detector (section 3.1.3.1) on lamellas with in-plane and out-of-plane polarization, respectively. Both lamellas have a thickness of about 1 µm and are mounted on a flat Si-wafer with 100 nm Au coating.

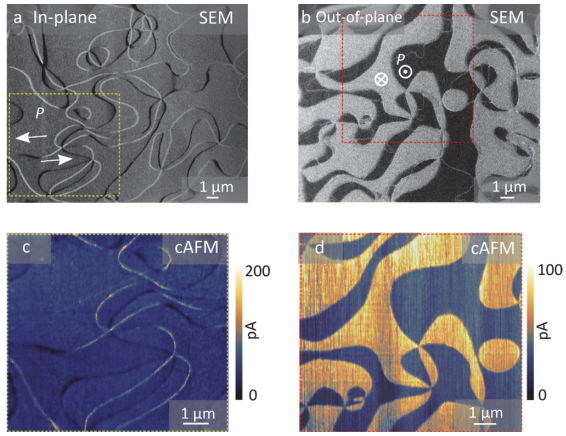

Figure 6-4. Correlated SEM and cAFM measurements on FIB-cut $ErMnO_3$ lamellas. (a) SEM image (2.0 kV, 0.4 nA, TLD) of a lamella with in-plane polarization (thickness ≈ 1 µm). Ferroelectric domain walls are visible as bright and dark lines. (b) SEM image (2.0 kV, 0.1 nA, TLD) of a lamella with out-of-plane polarization (thickness ≈ 1 µm), showing pronounced domain contrast. (c) cAFM image recorded in the region marked in a (yellow dashed rectangle). (d) cAFM image of the region marked by the red dashed rectangle in (b). The cAFM images in (c) and (d) are recorded with a doped diamond tip (HA_HR_DCP) and a bias voltage of 22.5 V applied to the back electrode.

For the sample with in-plane polarization (Figure 6-4a), domain walls are visible as bright and dark lines. The walls form characteristic six-fold meeting points, corresponding to structural

vortex/anti–vortex pairs as explained in section 2.2.2. A cAFM image from the region marked by the yellow dashed rectangle in Figure 6-4a is displayed in Figure 6-4c, showing the same domain wall pattern as the SEM image. Based on the cAFM data, we can identify the bright and dark lines in Figure 6-4a as conducting tail-to-tail and insulating head-to-head domain walls, respectively. Going beyond previous studies – which achieved contrast in FIB-cut lamellas only in the high-voltage regime where all walls are conducting [200] – we here access the low-voltage regime (section 2.2.3), where only the tail-to-tail walls exhibit enhanced conductance [21]. The latter is an important step, because it demonstrates that domain walls in lamellas and single crystals exhibit the same behavior, i.e., the applied nanostructuring by FIB does not alter the electronic properties of the domain walls. Figure 6-4b and d present analogous measurements for the lamella with out-of-plane polarization. Based on the comparison of the cAFM and SEM data, we find that the more conducting -*P* domains are brighter than the insulating +*P* domains in SEM (see, e.g., refs. [22,280] for details on the polarization-dependent transport behavior at the level of the domains). The data in Figure 6-4 allows for calibrating our SEM measurement (section 5.2.1), showing that (under the applied imaging conditions) bright/dark SEM contrast indicates enhanced/reduced conductance. Note that this calibration step is crucial as the domain wall contrast in SEM depends on the imaging parameters and can, e.g., invert depending on the acceleration voltage .

6.3. Surface SEM intensity variations induced by subsurface domain walls

This section demonstrates how surface SEM intensity variations can provide rich information about the electronic properties of both surface and subsurface regions. The experimental observation reveals that SEM intensity variation correlated with the domain walls under the surface, providing detailed information about the position and charge state of hidden walls. Utilizing both surface and cross-sectional data, a simple model that correlates the observed SEM surface contrast with the location and orientation of the subsurface domain walls is derived and refined.

6.3.1. Experimental observation

On a closer inspection of the SEM data in Figure 6-4a, we observe gradual changes in intensity on one side for several of the domain walls. This behavior is presented in Figure 6-5a, showing a head-to-head domain wall with an asymmetric intensity distribution in the adjacent domains as marked by the blue dashed line. Occasionally, gradual intensity variations also occur within the domains as seen in Figure 6-5b. Qualitatively the same features arise in SEM measurements on millimeter-thick single crystals (Figure 6-5c). Analogous to Figure 6-5a, several head-to-head domain walls exhibit a distinct contrast on one side (marked by the yellow dashed line in Figure 6-5c). Furthermore, we observe distinct intensity variations within one of the domains,

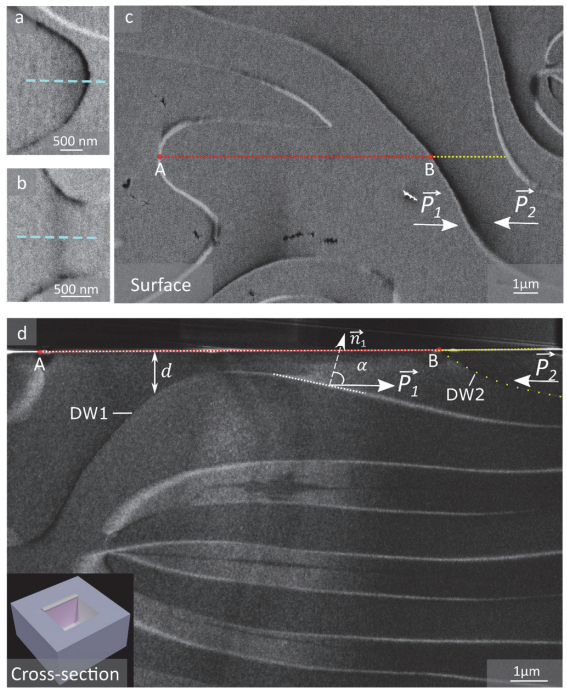

Figure 6-5. Correlated surface and cross-sectional SEM data. (a,b) Zoom-ins to the SEM image in Figure 6-4 present examples of gradually varying SEM intensity in the vicinity of a domain wall (a) and within a domain (b). (c) SEM data (1.5 kV, 0.1 nA, TLD) recorded on the surface of an $ErMnO_3$ single crystal. The image shows qualitatively similar features as in (a) and (b). Along the red dashed line, a change in contrast is observed within the domain, whereas a gradual change in intensity on one side of the wall is measured in the region marked by the yellow dashed line. Labels A and B correspond to two positions where domain walls intersect with the surface, and white arrows show the polarization direction within the domains. (d) Cross-sectional SEM image(2.0 kV, 0.1 nA, TLD) taken after FIB cutting a trench as sketched in the inset to (d). Labels A and B mark the same positions as seen in (c). Two domain walls in the near-surface region are highlighted (DW1 and DW2), and key parameters are presented (d distance from the surface, $\vec{n_1}$ local normal to the domain wall, α angle between $\vec{n_1}$ and $\vec{P_1}$).

As indicated by the red dashed line. These contrast variations cannot be explained based on the nominal charge state of the walls at the surface alone (as defined in Figure 6-2), indicating additional contributions.

To understand the origin of such additional contrast contributions, we use the FIB to cut a cross-section parallel to the white line in Figure 6-5c as illustrated in the inset to Figure 6-5d. Figure 6-5d presents the corresponding cross-sectional SEM image, where letters A and B indicate the same positions as in Figure 6-5c. Consistent with the SEM data gained on the surface, the cross-sectional measurement shows a conducting tail-to-tail wall (bright) that reaches the surfaces at point A and an insulating head-to-head wall (dark) that surfaces at point B. The head-to-head wall (DW2, yellow dots) has a surface inclination angle of about 25.2° and propagates in the direction in which the gradual contrast change is observed in Figure 6-5c. Furthermore, the cross-sectional image reveals an additional domain wall in the near-surface region (DW1), as well as several domain walls deeper in the bulk (i.e., $\gtrsim 3$ µm away from the surface) that run almost parallel to the surface until they merge in a vortex-like meeting point,

analogous to the results presented in Figure 6-3. Interestingly, we find that DW1 changes its charge state, going from insulating (dark) to conducting (bright), and the respective turning point coincides with the position where we observed the change in SEM intensity on the surface (see Figure 6-5c and d). These observations indicate a close relationship between the SEM contrast measured at the surface and the (hidden) charged domain walls in the near-surface region.

6.3.2. Relation between SEM intensity and hidden domain walls

To relate the intensity measured at the surface to the position and structure of the domain walls in the near-surface region, we build a simple model (the model has been developed in close collaboration with Manuel Zahn, who constructed and tested the mathematical framework). Based on the SEM data, within the first order Taylor expansion in ρ_{b} and multipole-like expansion in d, we assume that variations in SEM intensity, ΔI, scale with the density of bound charges ($\propto \rho_{\mathrm{b}}$) and that related effects decrease with increasing distance between the wall and the surface ($\propto d^{-n}, n \in \mathbb{N}$), leading to

$$\Delta I \propto \frac{\rho_b}{d^n} \propto \frac{cos\,\alpha}{d^n}, \qquad \textit{Equation 6-2}$$

$$\Delta I = \frac{A}{d^n} \cdot \cos\alpha \;\; (A = \mathrm{const}) \qquad \textit{Equation 6-3}$$

($\cos\alpha > 0$ and $\cos\alpha < 0$ give tail-to-tail and head-to-head configurations, respectively).

To derive the value of n, we extract the SEM intensity measured at the surface ($I_{\mathrm{SEM}} = I_0 + \Delta I$) and the parameters α and d from the SEM data in Figure 6-5c and d, respectively, considering two domain walls (DW1 and DW2) as explained in the following.

To determine the exponent n in Equation 6-2 and test if the ansatz describes the measured SEM intensity variations, we extract the parameters α, d and I_{exp} for the domain walls DW1 and DW2 in Figure 6-5d. The change in intensity is $\Delta \mathrm{I}_{\mathrm{exp}} = I_{\mathrm{exp}} - I_{\mathrm{exo,bg}}$, where $I_{\mathrm{exp,bg}}$ denotes the background intensity. Equation 6-3 can be brought into the following form, leading to a linear relation with respect to n:

$$\ln \Delta I_{\mathrm{exp}} - \ln\cos\alpha = \ln A - n \cdot \ln d, \qquad \textit{Equation 6-4}$$

The obtained representation is visualized for DW1 and DW2 in Figure 6-6. In both cases, the data is reasonably well described by the ansatz, demonstrating its general validity. Based on the slope, we find $\mathrm{n} = 2.31 \pm 0.09$ for DW1 and $\mathrm{n} = 2.35 \pm 0.08$ for DW2. We thus conclude that $n = 2$ is a good approximation, while the numerical uncertainties are underestimated. For the intensity amplitudes, we find $A = 0.726 \pm 0.019$ for DW1 and $A = 1.169 \pm 0.030$ for DW2.

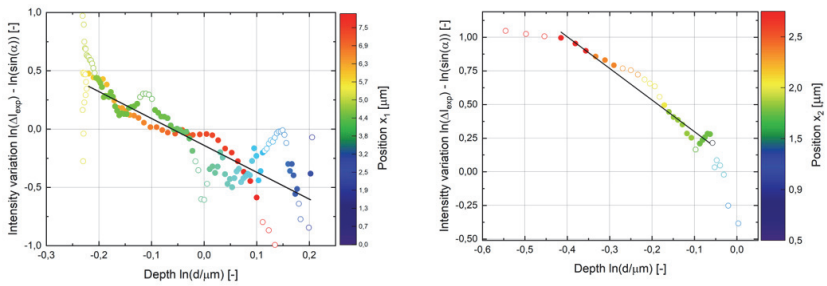

Figure 6-6. Determination of exponent n based on two datasets for the quantitative model. Based on the cross-section shown in Figure 6-5d, the different parameters describing the domain-wall shape are determined for two domain walls, i.e., DW1 (left panel) and DW2 (right panel). Datapoints that have been excluded from the linear fitting process as they aren't part of the linear regime are visualized with open circles. Graphs are a courtesy of Manuel Zahn.

This approach leads us to the conclusion that the experimentally observed dependence of ΔI on the distance between the wall and the surface is reproduced best for $n = 2$, i.e.,

$$\Delta I = \frac{A}{d^2} \cdot \cos\alpha \;\; (A = \text{const}) \qquad \textit{Equation 6-5}$$

A possible physical explanation for this relationship is the electrostatic effect of the domain wall bound charges on the secondary electrons [307]. As the CASINO simulations [308] shown in Figure 6-7, incident primary electrons (E = 1.5 keV at 0° tilt) lose 75% of their energy in the near-surface region with a depth of about 6.6 nm (maximum penetration depth $\lesssim$ 30 nm). The latter implies that the majority of secondary electrons is generated close to the surface, i.e., at a distance comparable to the parameter d that describes the wall–surface distance in our model. One possible physical mechanism that leads to the domain-wall-related SEM contrast is electrostatic interaction. Considering secondary electrons and domain wall bound charges as points charges, q_1 and q_2, their interaction is described by Coulomb's law, $F \propto \frac{q_1 \cdot q_2}{d^2}$. When neglecting the impact of the free charge carriers and considering only the bound charge carriers at the domain wall, q_2, this translates into an electric field $E = -\frac{\partial F}{\partial q_1} \propto \frac{\rho_b}{d^2}$ from the bound charges that acts on the secondary electrons via electrostatic induction and, hence, influences the secondary electron yield [307]. It is important to note, however, that the SEM contrast formation is highly non-trivial in ferroelectrics with multiple possible contributions [94]; to clarify the microscopic origin, additional studies are required, which is beyond the scope of this thesis.

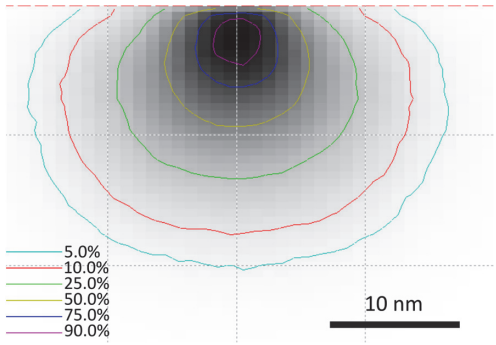

Figure 6-7. CASINO Monte Carlo simulation of the energy loss fraction in the electrons-sample interaction process under the SEM imaging parameters. Beam energy: 1.5 keV; sample composition: $ErMnO_3$; sample density: 7.39 g/cm³; sample tilting: 0°; numbers of electrons to simulate: 200,000; beam radius: 10 nm; number of displayed trajectories: 200; software: CASINO v2.42 [308].

6.3.3. Direct calculation of surface intensity

To verify the agreement of the experimental data with the (specified) model developed in a direct way, the resulting intensities I_{calc} (black), calculated based on Equation 6-5 ($I_{\mathrm{calc}} \equiv \Delta I$), are plotted together with the experimental SEM intensity I_{exp} data in Figure 6-8. Values for α and d are extracted from the data in Figure 6-5d. The experimental SEM intensity data, obtained between points A and B in Figure 6-5c (red dotted line, 50 pixels) was smoothed using the Savitzky-Golay method with a window size of 40 and polynomial order of 2. Subsequently, the subsequent was normalized between 0 to 1 ($\mathrm{x}_{\mathrm{normalized}} = \frac{\mathrm{x}-\mathrm{x}_{\mathrm{min}}}{\mathrm{x}_{\mathrm{max}}-\mathrm{x}_{\mathrm{min}}}$; x represents individual data points, $\mathrm{x}_{\mathrm{min}}$ and $\mathrm{x}_{\mathrm{max}}$ denote the dataset's minimum and maximum value).

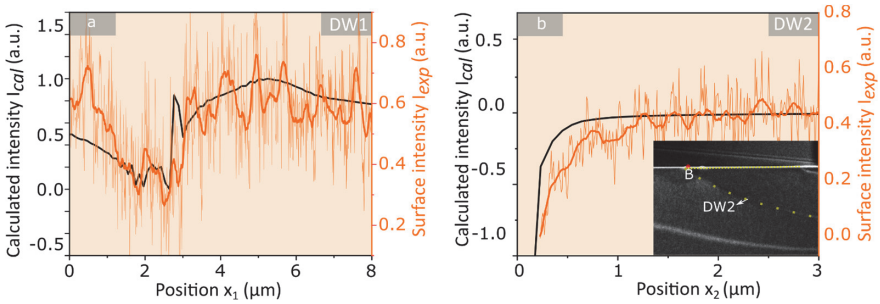

Figure 6-8. Comparison of measured and calculated SEM surface intensity. (a) Comparison of the SEM intensity I_{exp} measured along the red dashed line between A and B in Figure 6-5c in the main text, and the calculated intensity I_{calc} for DW1 based on direct numerical calculation. (b) Same as in a for the yellow dashed line in Figure 6-5 and DW2 (see also inset to b).

Importantly, our simple model reproduces the experimental data remarkably well (Figure 6-8), corroborating that domain wall bound charges play a key role for the intensity distribution in SEM measurements. Most interestingly, the experiments demonstrate that Equation 6-5 holds for domain walls at distances up to ≈ 1.5 μm away from the surface, which is much larger than the penetration depth of the incident primary electrons. This finding reflects an outstanding

sensitivity toward otherwise hidden domain walls and enables nanoscale 3D imaging of domain walls as discussed in the following.

6.4. Reconstruction of near-surface domain wall geometry from surface SEM contrast

This section explores the possibility of inferring the subsurface domain wall information from the surface SEM intensity variations, building upon the model developed in section 6.3.2. We begin with the theoretical framework developed by Manuel Zahn and Ivan Ushakov, that underpins this approach, followed by its application to an experimental domain wall and a hypothetical domain wall.

The domain wall shape was expanded in a fourth-order Taylor series $d(x) = \sum_{k=0}^{4} a_k x^k$. The coefficients a_k, as well as the intensity change prefactor A and the background intensity I_0, were optimized with a basin-hopping algorithm to yield a similar SEM intensity as in the experiment as:

$$I(x) = I_0 + \frac{A}{d^2(x)} \underbrace{\frac{d'(x)}{\sqrt{1 + [d'(x)^2]}}}_{=\cos\alpha(x)} \qquad \textit{Equation 6-6}$$

The basin approach is required to avoid trapping in local minima due to the noisy experimental data. In general, fitting a_k and A simultaneously overparameterizes the problem. Under ideal experimental conditions this can, in principle, be bypassed by determining the parameter A from calibration. Instead, in this study, one point of the domain wall (x_f, d_f) was determined from the cross-sectional data (Figure 6-5d) and used as an additional constraint on the a_k coefficients.

Figure 6-9a presents the SEM intensity (orange) measured at the surface above DW1. A zoom-in to the area of interest from which the line plot is generated is shown in the inset of Figure 6-9a. To derive a mathematical representation for ΔI, we optimize a low order Taylor expansion of the domain wall shape *d*(*x*), utilizing a basin-hopping optimization algorithm. This approach leads to the fit (back line) that is shown along with the SEM data in Figure 6-9a. The fit captures the main features seen in the SEM data and allows for calculating the domain-wall structure based on Equation 6-5. The result is displayed in Figure 6-9b, where the black curve represents the reconstructed domain wall. The orange curve corresponds to d-values extracted from the cross-sectional data (Figure 6-5d), which is shown for comparison to evaluate the quality of the reconstructed domain-wall structure. We find that based on the SEM map gained at the surface, we can determine the sign of higher derivatives $\mathrm{d}^{(n)}\, d/\mathrm{d}x^{(n)}$, which reveals whether the domain wall curvature is convex or concave in the near-surface region (the uncertainty of the Taylor coefficients a_n is about $(n+1)^2 \cdot 3\%$, yielding good precision for the low-order coefficients, which are the most relevant ones for the reconstruction).

To go beyond the specific case of DW1, we next consider a hypothetical domain wall of arbitrary shape, corresponding to the profile (orange) shown in Figure 6-9d. Figure 6-9c presents the calculated SEM intensity (orange) with random Gaussian noise to emulate experimental fluctuations. Applying the same approach as for DW1, we fit the noisy intensity data, which leads to the black curve in Figure 6-9c. Based on this fit, we calculate the domain wall structure using Equation 6-5 (black reconstructed profile in Figure 6-9d). The reconstructed structure is in excellent agreement with the hypothetical domain wall of arbitrary shape that was used as input data, demonstrating the general validity of our reconstruction approach.

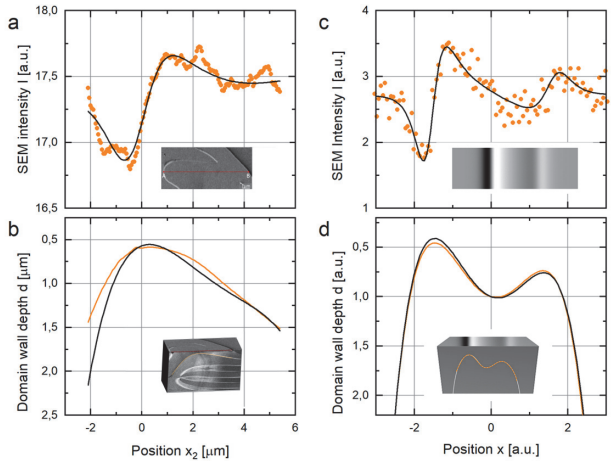

Figure 6-9. Reconstruction of the near-surface domain wall geometry from SEM intensity data. (a) SEM intensity recorded along the red dashed line (between A and B) shown in the inset and Figure 6-5c and calculated SEM intensity (black) based on the reconstructed domain wall in b. (b) Shape of DW1 (see Figure 6-5d and inset) as measured from the cross-section (orange) and reconstructed shape based on the SEM surface intensity (black). (c) Simulated SEM intensity of an artificial domain wall of arbitrary shape overlayed with random noise for the reconstruction process to simulate random experimental fluctuations (orange) and SEM intensity from the reconstructed domain wall shape (black). (d) Arbitrarily generated structure of the simulated domain wall (orange, input data) and its reconstructed shape (black). Courtesy of Manuel Zahn.

Our results demonstrate the possibility of reconstructing the shape of ferroelectric domain walls in near-surface regions with nanoscale spatial resolution based on SEM maps. Key parameters of otherwise hidden domain walls, such as curvature and local charge state, thus become readily accessible within a single scan. In contrast to previously applied techniques with comparable resolution (e.g., 3D imaging by tomographic PFM or FIB), the SEM-based reconstruction process is non-destructive and much faster, allowing for image acquisition and data analysis on a time scale of seconds. On the one hand, this enables correlated experiments on individual domain walls or domain-wall networks with well-known orientation, curvature, and charge state, providing new opportunities for fundamental domain wall studies. Combined with machine learning and faster evaluation algorithms, dynamical electric-field, pressure- or

temperature-driven changes in the 3D structure may be investigated in real-time along with changes in the electronic domain wall response. On the other hand, SEM-tomography is of interest for domain-wall nanoelectronics, facilitating non-destructive high-throughput screening of materials with functional charged domain walls and domain-wall-based devices, which is essential for monitoring during the production of device architectures and quality control in real-time.

6.5. Summary

Domain walls hidden in the near-surface region play an important role for the surface electronic properties. Based on this observation, an SEM-based tomographic method is developed to map the 3D structure of domain walls in the near-surface region. SEM has proven capable of probing the electronic properties of domain walls, both at the surface and in the near-surface region. By using the surface SEM image and the corresponding cross-sectional data, a simple model that correlates the observed surface SEM intensity variation with the location and orientation of the otherwise hidden domain walls was derived. Furthermore, it is possible to reconstruct the shape of ferroelectric domain walls in near-surface regions with nanoscale resolution. This offers a non-destructive method for real-time monitoring of the production of device architectures, paving the way for high-throughput screening of individual domain walls for device application.

7. Toward ferroelectric domain wall device applications

Ferroelectric domain walls in $ErMnO_3$ demonstrated the capability to emulate the behavior of electrical components, such as digital switches [3] and rectifiers [4], effectively controlling electric signals at the nanometer scale. Such findings hint the possibility of using the domain walls themselves as ultra-small devices. To realize such transformative device applications, it is imperative to develop strategies that enable building up domain wall-based circuitry to control electronic signals using the intrinsic domain wall properties. The ultimate goal is to create electronic 2D devices using individual domain walls at the atomic scale and subsequently integrate them into complex functional networks. As a first step in this direction, we aim to build up elementary two-terminal devices using domain walls with a known propagating path. The latter make domain walls accessible in device-relevant geometries, allowing to transfer previous results [21,22] obtained based on microscopy measurements on bulk samples to individual domain walls.

In previous chapters, the capability to extract domain walls with well-defined charge states and reshape the host system into different geometries and sizes was demonstrated. The domain walls exhibited excellent stability in flat free-standing lamellas with a thickness above 200 nm. Continuing with this geometry, in this chapter, flat free-standing thin lamella samples are extracted from single crystal $ErMnO_3$ samples, and then integrated into a setup of electrodes that bridges different length scales, e.g., allowing to contact domain wall by conventional wire-bonding approaches. With this, the domain walls become accessible to electronic measurements under ambient conditions.

7.1. System setup

After establishing the possibility to extract domain walls with a well-defined charge state using FIB, the next step is to move away from c-AFM-based measurements and towards relevant geometries for electric circuits, making the domain walls accessible for electronic signal control and measurements. To achieve this, a nanoelectronic setup is further developed starting from the thesis work of Dr. E. Lysne [27] and Dr. E. D. Roede [28]. This setup consists of three core elements: the lamella, the lamella carrier chip, and the printed circuit board (PCB), as shown in Figure 7-1.

A flat thin $ErMnO_3$ lamella with well-defined domain walls extracted by FIB. The lamella serves as the functional unit of the setup. At the current stage, there are still multiple domain walls within the lamella. However, future iterations will utilize a lamella with a single domain wall, which can be achieved by thermal annealing of the bulk crystal to generate larger domains [309].

A custom lamella carrier chip is used to hold the $ErMnO_3$ lamella. The chip is manufactured via photolithography using the pattern shown in Figure 7-1a. This pattern is composed of 100 nm

e-beam evaporated gold (Au) with a 5 nm titanium (Ti) adhesion layer. The substrate beneath the pattern is a Si wafer covered with a 1 µm layer of insulating oxide. The pattern consists of four gold terminal pads, labeled A^+, A^-, B^+, and B^-, interconnected with wires to a central pad that can be patterned by FIB as demand. To be able to control the current flow direction, the connection of the four gold terminal pads is isolated by milling away the conducting layer of the central pad with a size a bit smaller than the lamella, as shown in the inset of Figure 7-1a. Ideally, the lamella should be landed at an angle that places two of the chip pads along the target domain wall, realizing a two-terminal setup. Ion beam deposited Pt is used to connect the lamella to the specific wire that connected to the terminal pad. Thus, the carrier chip works as the first bridge between the nanoscaled lamella and the millimeter-scaled circuit/electrodes. The carrier chips were fabricated by NTNU Nanolab according to the layout developed by Dr. E. Lysne [27].

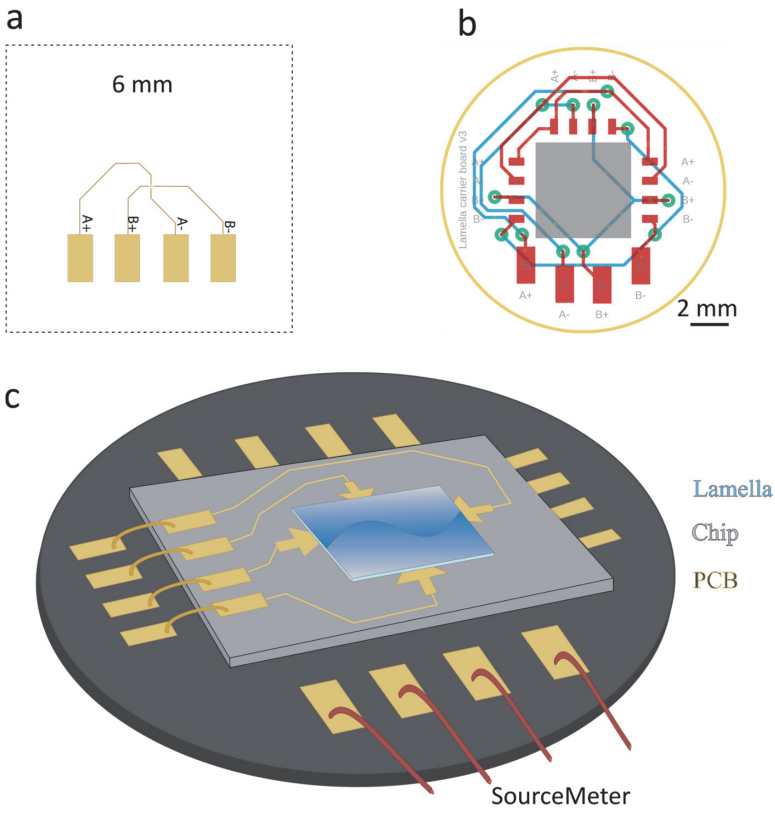

Figure 7-1. Schematic of the elementary domain wall device setup. (a): Mask pattern used for creating the carrier chip via photolithography. The size of the big dashed rectangle frame is 6 mm×6 mm. The inset shows the central part after FIB tailoring. (b): PCB schematic, courtesy of Dr. E. Lysne. Red and blue lines are connections on the top and bottom sides of the PCB, and green circles are vias. (c): Sketch of the entire elementary domain wall device stack. The top blue block represents the $ErMnO_3$ lamella with a domain wall, the middle grey block is the carrier chip, and the bottom black circle is the PCB.

A custom-printed circuit board (PCB) links the source measure unit (SMU) and the carrier chip. As shown by the schematic in Figure 7-1b, the PCB is designed with four channels labeled as A^+,

A^-, B^+, and B^-, corresponding to the four Au pads on the carrier chip. This design enables us to control of the current flow direction. Four equivalent groups of Au pads (red rectangles in Figure 7-1b), one big and three small, are placed around the central grey area. The larger group is designed to connect to the voltage source by soldering regular wires. The repetition of the three smaller groups is intended to provide flexibility in the geometry, avoiding any wire across the central chip. Usually, only one of the smaller groups is connected to the Au pads on the carrier chip by wire bonding using Au wires with a diameter of 20 µm. The PCB is manufactured by *Seeedstudio* and uses ENEPIG (Ni/Pd/Au) for the contact pads, which makes wire bonding easier.

Figure 7-1c illustrates the entire stack of the setup. By connecting to the source meter, the current can go either along the domain wall or across the domain wall. The target domain wall is now directly accessible for electrical measurement at different length scales, including probe station and SPM-based experiments.

7.2. Fabrication process of the device

With the PCB and the carrier chip prepared, our major challenge of the fabrication process lies in landing the lamella onto the carrier chip. 'Landing' in this context refers not merely to transferring a lamella from a bulk sample to a flat substrate, but it also includes positioning and contact of the lamella within the setup.

The integration of the lamella into the system is highly non-trivial due to its microscopic dimension and the exact placement within the device structure.

The lamella is easily damaged or completely destroyed when connecting it with cables to the larger pads of the PCB when the soldering is done after the lamella landing, as it is very sensitive to electrical discharging. For example, the probing voltage that is applied when checking the electric connection is sufficient to destroy the lamella. Furthermore, the charging difference induced by electron/ion beam in FIB between the four Au pads on the chip can also led to lamella destruction. These seemingly minor effects at the macroscopic level have significant implications at the microscopic scale, necessitating the development of a reliable workflow to ensure the smooth and successful progression of the fabrication process.

To ensure this, the entire stack is first assembled (Figure 7-2), with the lamella landing process being the final step. The assembling starts with soldering the cable to the larger Au pads on the PCB. Subsequently, the chip is fixed to the central area using carbon tape. Following this, the Au pads on the carrier chip are connected to one group of small Au pads on the PCB by wire bonding. The wire bonding is done with an TPT HB05 wire bonder with a 20 µm Au wire. Up to this point, a voltmeter can be used for checking the connections.

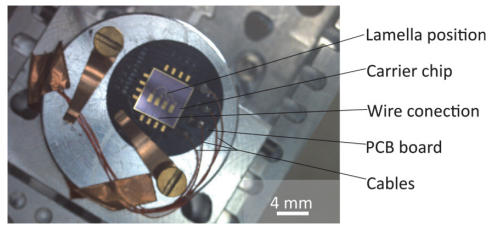

Figure 7-2 Photograph of the assembled stack in the chamber of FIB before lamella landing. This image, captured by the nav-cam in FIB, shows the entire stack is carefully grounded to ensure stability during FIB process.

After successful connection, the setup is ready for landing the FIB lamella on the chip. To reduce charging effects, the entire stack needs to be grounded properly. Figure 7-2 shows a photo taken by the nav-camera in the FIB chamber. Here, the entire stack is mounted onto a sample stub, with the cable soldered to the PCB larger pads neatly wrapped around the stub. All the cables are twisted together to short-circuit and grounded to the stage, ensuring the safe processing of the landing.

The procedure of landing a lamella onto the carrier chip is essentially the same as landing a flat lamella on a substrate, as described in section 5.1.1. However, the lamella sample should be finely polished on both sides before landing on the carrier chip. This step is necessary to ensure that the pattern on the chip is preserved and not milled away, including the wires or terminal pads. To facilitate careful polishing for both sides and prevent the aforementioned ion milling of device components, we transfer the lamella to a TEM grid. The preparation steps are the same as before, beginning with the deposition of a protective layer, cutting a rough trench, and then lifting out the lamella to attach it to a TEM grid, as shown in Figure 7-3a. Following this, a standard polishing procedure with a large depth value ($Z \geq 20$ µm) (see, section 5.1.1 step 2) is performed on both sides.

After that, the material in the region between the TEM grid and the $ErMnO_3$ is partly milled away, leaving only a thin bridge to stabilize the lamella sample, as shown in Figure 7-3b.

In order to lift off the lamella in a horizontal position for an easy transfer to the flat carrier chip, it is necessary to open the chamber and manually flip the holder of the TEM grid to a horizontal position. As shown in Figure 7-3c, the lamella now aligns parallel to the horizontal plane and is ready for its transfer in the next step.

In addition, the chip has to be prepared for the lamella landing. As shown in Figure 7-3d, FIB cutting is used to isolate the four wires, leaving an insulating region in the center of the chip pattern, as indicated by the blue dashed square. The size of this region is slightly smaller than the lamella to ensure good contact to all four pads.

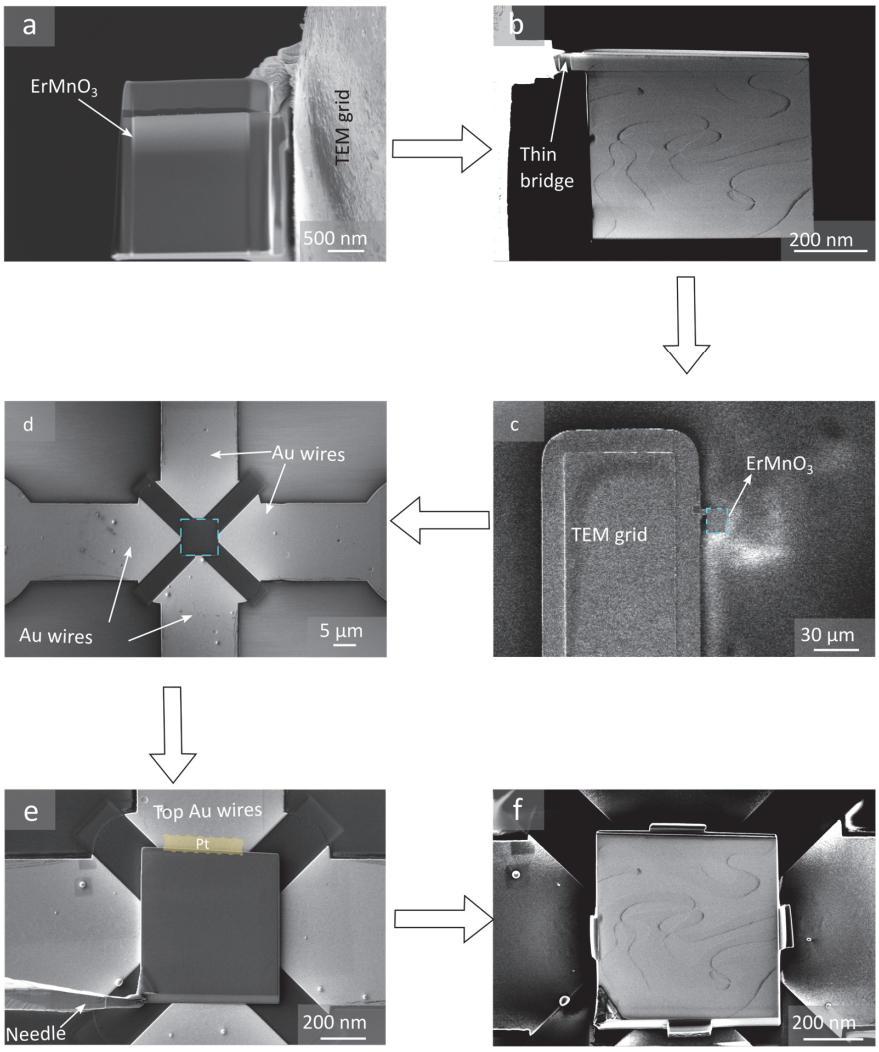

Figure 7-3 Fabrication process of elementary domain wall device using FIB. (a) Lamella attached to a TEM grid. The lamella has been polished, leaving only a thin bridge connected to the grid. (c) Lamella flipped to a horizontal orientation alongside the TEM grid and is ready for transfer. (d) The carrier chip after FIB patterning of the central area, which is indicated by the blue dashed square. (e) Lamella landed on the chip with the aid of the micromanipulator needle. (f) Finished lamella on the carrier chip, exhibiting domain wall contrast.

The lamella sample is then landed on the target region using the micromanipulator needle, with ion beam deposited Pt as the welding material between the $ErMnO_3$ and the top Au wire. After these steps, the micromanipulator needle should be located in the lower left corner, corresponding to the downstream of the ion beam, to prevent milling of the lamella during removal of the needle, as shown in Figure 7-3e. After carefully detaching the micromanipulator needle, the deposition of the welding material on the remaining three Au wire is carried out. To ensure optimal utilization and precise control of the ion beam, the deposition is conducted for each wire when it is located at the top edge, which requires a 90-degree rotation of the

stage for each deposition step. During the process, the lamella sample should be irradiated by the ion beam as little as possible to avoid damage.

The main objective of the deposition of the welding material currently is to fix the lamella to the carrier chip and ensure a good electrical connection between the lamella surface and the Au wires on the chip. In future iterations, when the lamella includes only a single domain wall, the targeted deposition of welding material will allow for connecting the two terminals to an individual domain wall.

After deposition, the lamella sample is typically contaminated due to the precursor gas injection and redeposition. Therefore, a low-energy ion beam milling is used to clean the surface, using a 5 kV ion beam with the stage tilted at -10.4°, which is the smallest angle our instrument can reach to decrease the ion beam incident angle, and thus reducing beam damage.

Figure 7-3f displays an SEM image of a finished lamella landed on the chip. With the bridging of the carrier chip and PCB, the domain wall networks and, in principle, individual domain walls as sketched in Figure 7-1c, become available for testing of electronic properties in a device-relevant geometry, going beyond previous microscopy-based approaches.

As a first step into this direction and to demonstrate the general feasibility of the established approach for device design, we contacted the PCB to a source measure unit and performed basic SPM measurements on the lamella in the fully connected device structure. The experiment worked, showing the general possibility to build domain-wall-based two-terminal devices. However, the procedure is time-consuming and the development of devices is challenging. In total, 6 devices were produced following the process described in this section, out of 6 got destroyed during our proof-of-concept experiments due to the electrical discharges and other challenges.

To ensure the lamella is not destroyed during the measurement, it is vital to ground the device in alignment with the instrument before testing. Figure 7-4a shows an artistic image in which a cAFM image is overlayed on to an SEM image of a lamella sample. This artistic image provides an illustration of the device setup. This design enables the control of the current flow between domain walls with different orientations, which will be utilized in follow-up studies, aiming at the realization of fully functional two-terminal devices.

By utilizing thermally treated samples with domain sizes in the order of up to 5 µm [309], the same device design can be utilized to work with individual domain walls with well-defined charge states in the near future. Figure 7-4b illustrates a two-terminal device using a single domain wall with lateral contact pads, allowing ex-situ measuring of the current flow along the domain wall under realistic ambient conditions.

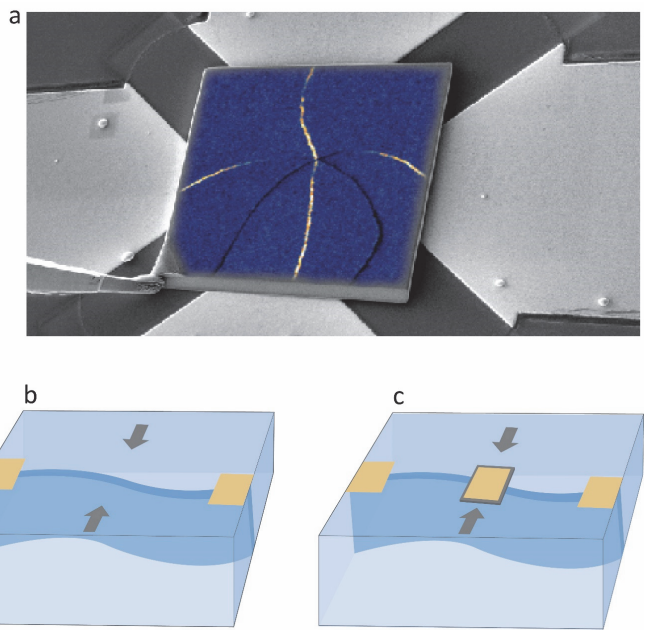

Figure 7-4. (a): Artistic illustration of an elementary domain wall device, showing a cAFM image overlayed over an SEM image. Artistic image overlayed by Ivan Ushakov. (b): Illustration of a two-terminal device. (c): Illustration of a three-terminal device. The third terminal is composed of a dielectric layer(shown in grey) situated on top of the $ErMnO_3$, with a metal layer (shown in gold) covering the dielectric layer.

Another possibility is to introduce a third terminal as gate, realizing a field-effect transistor using a single domain wall, as depicted in Figure 7-4c. This configuration potentially allows for controlling the electric signal between the source and the drain using the gate as a valve.

Beyond these device geometries, there are further possibilities that remain to be explored. For instance, arranging the contact pads in top-bottom geometry could minimize the distance between the input and output terminals, leading to reduced energy consumption. Here, the thickness-dependent experiments discussed in section 5.2 provide important guidelines concerning the choice of dimensions and physical thickness limits.

7.3. Summary and outlook

The results discussed in this section represent an important milestone for the ATRONICS project, which aims to develop electronic components using improper ferroelectric domain walls to control electronic signals at the atomic scale and with low energy consumption. To achieve this goal, the creation of basic domain wall-based device architectures is crucial. By integrating an $ErMnO_3$ lamella with functional domain walls into a carrier chip and PCB, we made the system compatible with conventional circuitry. Preliminary tests by SPM were conducted, showing the general feasibility of our approach. Our result thus set the stage for the interesting and challenging next step: testing and exploring the elementary device properties and potential application opportunities and limits. During this process, the material that connects the domain

walls to the carrier chip may influence the device performance and deserves a closer inspection based on the observed Schottky barrier contrast in section 5.2.2. The setup enables the integration of lamellas with a single domain wall, facilitating the control of electrical current flowing either along the domain wall or across the domain wall. Functional properties previously observed bulk samples [21,22] thus can be tested on individual domain walls. The results open the door to two-terminal and three-terminal devices and networks with varied contact pad configurations. This will facilitate the development of functional units based on individual domain walls, thereby fostering the advancement of next-generation domain wall nanoelectronics.

8. Conclusions and outlook

Ferroelectric domain walls in hexagonal manganites exhibit unusual electronic properties that are of interest for device application in next-generation nanotechnology. Proof-of-concepts foreshadow the possibility of using the intrinsic physical properties of stationary ferroelectric domain walls to control electrical signals at the nanoscale. Building up on a robust theoretical and experimental foundation for $ErMnO_3$ bulk systems, advancements in imaging techniques, and methodologies established in previous works in our group, the overall aim of this work was to develop and establish strategies to create systems with reduced dimensions and study the impact on the functional domain walls, getting an important step closer to devices that utilize the intrinsic electronic properties of the walls. The local conductance at domain walls in $ErMnO_3$ was systematically investigated, laying the groundwork for more complex functional networks and circuitry in the future.

Furthermore, as discussed in the different chapters, open fundamental questions have been addressed in this thesis, and novel non-invasive techniques have been demonstrated for 3D imaging, providing a possible approach for device testing/characterization. Several important challenges have been identified that will be tackled in the final project phase of our EU project ATRONICS, giving input and clear guidelines for the follow-up experiments and next steps.

Controlling local electronic transport phenomena by oxygen defects

The creation and evolution of anti-Frenkel defects have been systematically investigated by varying the electric field strength, exposure time, probe tip radii, sample atmospheric histories, and environmental conditions. By looking at the local electronic transport behavior after applying the electric field, a uniform non-trivial evolution trend was observed. The modified regions evolved from an enhanced conducting dot structure under low applied voltage and short exposure time into a more complex dot-ring structure with enhanced conductance for high voltage and longer exposure times. This evolution was attributed to the spatial separation of anti-Frenkel defects, i.e., initially paired oxygen vacancies and interstitials. In contrast to the initial anti-Frenkel defects[107], the dot-ring structures are less stable, vanishing on the time scale of about six months. PFM was conducted to exclude local polarization switching effects. cAFM and numerical simulation were used to explain the evolving process. APT provided direct evidence for the concentration change of oxygen interstitials and oxygen vacancies along the direction perpendicular to the surface, penetrating to a depth of approximately 400 nm. This finding corroborated the hypothesis that the observed dot-ring structure arises from the spatial separation of anti-Frenkel defects. This separation resulted in different areas rich in oxygen interstitials and oxygen vacancies, respectively. HAADF-STEM images confirmed the structural integrity of the modified region, and revealed the possibility of local polarization switching

independent of the transport behavior, which shows that the induced changes in local conductance are not controlled by the ferroelectric properties.

The evolved dot-ring structure presents interesting possibilities for new functionality in complex domain wall networks, going beyond just acting as nanoscale wires [107], which initially motivated this part of the thesis work. To move toward practical applications, however, additional work is required. For example, the 3D conductance profile of the dot-ring structure remains an open question due to the lack of distinct contrast in SEM imaging. To address this challenge, preparing a plan-view lamella sample would be a promising next step, in which we progressively thin the lamella after each cAFM scan, allowing for the reconstruction of the 3D conductance profile and the development of potential device concepts.

Thickness-dependent electronic properties of ferroelectric domain walls in $ErMnO_3$

Understanding how the electrical properties vary with thickness in confined geometries is crucial for both technological device applications and the understanding of the underlying physics. For this purpose, the electronic properties of domain walls in samples of different thicknesses have been investigated systematically.

To cover a broad range of thicknesses ranging from 1000 nm to sub-10 nm, different preparation methods were applied to fabricate the samples, including FIB cutting and tripod polishing. In the FIB-cutting lamella process, an extra final polishing step using Ar polishing to remove the damaged layer has been implemented. This additional step significantly enhances the ability to reproducibly make lamellas that show the inherent electronic properties of ferroelectric domain walls in $ErMnO_3$. Benefitting from this improvement, two complementary approaches were established: a set of flat lamellas with thicknesses in the range from 200 to 1000 nm and a set of back-electrode attached wedge-shaped lamellas with a thickness continuously changing from more than 1000 nm to sub-10 nm. The results from SEM and correlated SPM revealed that the domain walls in $ErMnO_3$ lamellas preserve their functionality and stability analogous to their millimeter-thick counterparts down to about 200 nm in thickness. In the case of the back-electrode-attached wedge-shaped lamellas, a depletion region was observed in the thinner edge, which was attributed to a Schottky barrier that forms at the interface between the p-type semiconductor $ErMnO_3$ sample and the metal back-electrode. Notably, all the domain walls in this depletion region were conducting, especially the head-to-head domain walls, which in this region exhibited conduction at a lower reading voltage compared to the tail-to-tail domain walls. These findings reveal the outstanding stability of the functional domain walls, which behave differently from the domains even within the depletion region. On the one hand, this behavior foreshadows yet-to-be-utilized properties that could be useful for future device applications.

On the other hand, the emergence of the depletion region causes fundamental unexplored challenges regarding the application of domain walls in devices. To address this and learn more about related effects, two possible solutions are proposed. Firstly, utilizing the full capabilities of SEM contrast. This would involve using SEM images to directly compare the effect of thickness, achieved by gradually thinning down the lamella without involving any external impact. Secondly, fabricate an insulating back side supporting material to avoid direct contact of the metal electrode with the lamella samples. These experiments will help to clarify the physical phenomena driven by the electrode, separating them from the intrinsic domain wall behavior.

SEM non-destructive 3D imaging of ferroelectric domain walls for device fabrication

With the advancement of characterization techniques, the important role of the subsurface domain walls has become increasingly evident. Thus 3D imaging method that is compatible with future fabrication processes, non-destructive, and capable of real-time monitoring of the domain wall properties has become highly desirable.

The thesis work show that secondary electrons carry rich information about the electronic material properties at the surface and, importantly, in the near-surface regions. This sensitivity opened the door for SEM-based tomography to monitor the position, orientation, and charge state of ferroelectric domain walls. The experiments revealed that SEM intensity variation arise from domain walls hidden under the surface, providing detailed information about the charge state of the hidden walls. Utilizing both surface and cross-sectional data, a simple model that correlates the observed SEM surface contrast with the location and orientation of otherwise hidden domain walls has been derived. Furthermore, our results demonstrated the possibility of reconstructing the shape of ferroelectric domain walls in near-surface regions with nanoscale spatial resolution based on SEM maps. Such SEM-tomography is of interest for domain-wall nanoelectronics, facilitating non-destructive high-throughput screening of materials with functional charged domain walls and domain-wall-based devices, which is essential for monitoring the production of device architectures and quality control in real-time.

Towards ferroelectric domain wall device applications

With the capability of extracting specific domain walls with defined geometry, the real-time monitoring method, and the setup for bridging the gap between the macroscale and nanoscale, the workflow for fabricating elementary domain wall devices has been built up. First attempts to test the devices in a standard SPM setting failed, leading to the destruction of several devices, possibly due to the ground of the elementary device being not perfectly aligned with the instrument. Despite this setback, the preliminary experiments provided valuable insights, setting the stage for device testing in the next step. Future device testing can essentially start

from the electric field-controlled and frequency-controlled test in SPM, similar to those conducted on bulk samples, progressing to more current/voltage and frequency response characterization using a probe station. These steps will not only validate the previous device-like behavior on domain walls with fully known configuration but also confirm the applicability of the device setup. This thus provides an important basis for the final phase of ATRONICS, fabricating elementary devices with individual domain walls. By selecting the voltage supply pads that are connected to the domain walls, the current can be controlled to flow along or perpendicular to the domain wall. Combined with the known domain wall path, this allows for controlling the domain wall electronic transport with high precision. Further advancements include utilizing the established oxygen defect strategy to control local conductance, thereby building up more complex functional domain wall circuitry and network, enabling a significant leap towards ultra-small and energy-efficient electronics with domain walls acting as atomic-scale devices.

Summary

A comprehensive FIB routine for the fabrication of a domain wall-based device has been established. This process has opened avenues to explore several open questions, including the influence of sample geometry and thickness on domain wall electronic properties and the method for real-time domain wall property visualization. Additionally, a systematic investigation of anti-Frenkel-based local conductance control has been conducted, following the idea to eventually combine this strategy with the domain-wall-based concepts, giving a new direction to the development of nanoscale circuits and networks. These findings lay a robust foundation for the next step: fabricating domain wall devices using individual domain walls and, ultimately, extended complex networks.

On the way, several challenges have been identified that require adequate control. Firstly, understanding the 3D profile of the complex dot-ring structure is important for practical applications. Secondly, the intrinsic thickness-dependent domain wall properties without the disturbance of depletion regions remain uncertain. Thirdly, the influence of Ga implantation/amorphous layer on the domain wall properties warrants further investigation, based on the observation that the domain wall properties evolved from the so-called high voltage regime to low voltage after Ar polishing and the comparative analysis of domain wall conductance with and without 5 kV ion beam polishing in the previous publication[200]. Lastly and most importantly, identifying appropriate materials for connecting domain walls into the circuit is a pressing need.

All these findings inform the experiments and research performed as part of the ATRONICS project in the next years, which will be continued by two PhD students and two postdocs.

It is clear that the physics of functional domain walls and their utilization in devices will keep the community busy in the coming years. The results presented in this thesis contribute to the field in different key aspects, and it is expected that several of the concepts are transferable to other material systems, stimulating new follow-up studies in the years to come.

Bibliography

[1] Kroemer, H., "Quasi-Electric Fields and Band Offsets: Teaching Electrons New Tricks". In: *Selected Works of Professor Herbert Kroemer* (**2008**) 22–42. Doi: 10.1142/9789812709028_0004.

[2] Mannhart, J., Schlom, D.G., "Oxide Interfaces - An opportunity for electronics". In: *Science (1979)* 327 (**2010**) 1607–1611. Doi: 10.1126/science.1181862.

[3] Zubko, P., Gariglio, S., Gabay, M., et al., "Interface physics in complex oxide heterostructures". In: *Annu Rev Condens Matter Phys* 2 (**2011**) 141–165. Doi: 10.1146/annurev-conmatphys-062910-140445.

[4] Hwang, H.Y., Iwasa, Y., Kawasaki, M., et al., "Emergent phenomena at oxide interfaces". In: *Nat Mater* 11 (**2012**) 103–113. Doi: 10.1038/nmat3223.

[5] Bert, J.A., Kalisky, B., Bell, C., et al., "Direct imaging of the coexistence of ferromagnetism and superconductivity at the LaAlO3/SrTiO3 interface". In: *Nat Phys* 7 (**2011**) 767–771. Doi: 10.1038/nphys2079.

[6] Ohtomo, A., Hwang, H.Y., "A high-mobility electron gas at the LaAlO3/SrTiO3 heterointerface". In: *Nature* 427 (**2004**) 423–427.

[7] Förg, B., Richter, C., Mannhart, J., "Field-effect devices utilizing LaAlO3-SrTiO3 interfaces". In: *Appl Phys Lett* 100 (**2012**) 1–4. Doi: 10.1063/1.3682102.

[8] Stemmer, S., James Allen, S., "Two-dimensional electron gases at complex oxide interfaces". In: *Annu Rev Mater Res* 44 (**2014**) 151–171. Doi: 10.1146/annurev-matsci-070813-113552.

[9] Ramesh, R., Schlom, D.G., "Creating emergent phenomena in oxide superlattices". In: *Nat Rev Mater* 4 (**2019**) 257–268. Doi: 10.1038/s41578-019-0095-2.

[10] Meier, D., Selbach, S.M., "Ferroelectric domain walls for nanotechnology". In: *Nat Rev Mater* 7 (**2022**) 157–173. Doi: 10.1038/s41578-021-00375-z.

[11] Vul, B.M., Guro, G.M., Ivanchik, I.I., "Encountering domains in ferroelectrics". In: *Ferroelectrics* 6 (**1973**) 29–31. Doi: 10.1080/00150197308237691.

[12] Yang, S.Y., Seidel, J., Byrnes, S.J., et al., "Above-bandgap voltages from ferroelectric photovoltaic devices". In: *Nat Nanotechnol* 5 (**2010**) 143–147. Doi: 10.1038/nnano.2009.451.

[13] Sluka, T., Tagantsev, A.K., Damjanovic, D., et al., "Enhanced electromechanical response of ferroelectrics due to charged domain walls". In: *Nat Commun* 3 (**2012**) Doi: 10.1038/ncomms1751.

[14] Lorenz, M., Ramachandra Rao, M.S., Venkatesan, T., et al., "The 2016 oxide electronic materials and oxide interfaces roadmap". In: *J Phys D Appl Phys* 49 (**2016**) Doi: 10.1088/0022-3727/49/43/433001.

[15] Seidel, J., Martin, L.W., He, Q., et al., "Conduction at domain walls in oxide multiferroics". In: *Nat Mater* 8 (**2009**) 229–234. Doi: 10.1038/nmat2373.

[16] Meier, D., Seidel, J., Cano, A., et al., "Anisotropic conductance at improper ferroelectric domain walls". In: *Nat Mater* 11 (**2012**) 284–288. Doi: 10.1038/nmat3249.

[17] Guyonnet, J., Gaponenko, I., Gariglio, S., et al., "Conduction at domain walls in insulating Pb(Zr 0.2Ti 0.8)O 3 thin films". In: *Advanced Materials* 23 (**2011**) 5377–5382. Doi: 10.1002/adma.201102254.

[18] Maksymovych, P., Morozovska, A.N., Yu, P., et al., "Tunable metallic conductance in ferroelectric nanodomains". In: *Nano Lett* 12 (**2012**) 209–213. Doi: 10.1021/nl203349b.

[19] Schröder, M., Haußmann, A., Thiessen, A., et al., "Conducting domain walls in lithium niobate single crystals". In: *Adv Funct Mater* 22 (**2012**) 3936–3944. Doi: 10.1002/adfm.201201174.

[20] Sharma, P., Zhang, Q., Sando, D., et al., "Nonvolatile ferroelectric domain wall memory". In: *Sci Adv* 3 (**2017**) 1–9. Doi: 10.1126/sciadv.1700512.

[21] Mundy, J.A., Schaab, J., Kumagai, Y., et al., "Functional electronic inversion layers at ferroelectric domain walls". In: *Nat Mater* 16 (**2017**) 622–627. Doi: 10.1038/nmat4878.

[22] Schaab, J., Skjærvø, S.H., Krohns, S., et al., "Electrical half-wave rectification at ferroelectric domain walls". In: *Nat Nanotechnol* 13 (**2018**) 1028–1034. Doi: 10.1038/s41565-018-0253-5.

[23] Holtz, M.E., Shapovalov, K., Mundy, J.A., et al., "Topological Defects in Hexagonal Manganites: Inner Structure and Emergent Electrostatics". In: *Nano Lett* 17 (**2017**) 5883–5890. Doi: 10.1021/acs.nanolett.7b01288.

[24] Lilienblum, M., Lottermoser, T., Manz, S., et al., "Ferroelectricity in the multiferroic hexagonal manganites". In: *Nat Phys* 11 (**2015**) 1071–1074. Doi: 10.1038/NPHYS3468.

[25] Schoenherr, P., Shapovalov, K., Schaab, J., et al., "Observation of Uncompensated Bound Charges at Improper Ferroelectric Domain Walls". In: *Nano Lett* 19 (**2019**) 1659–1664. Doi: 10.1021/acs.nanolett.8b04608.

[26] Schaab, J., Shapovalov, K., Schoenherr, P., et al., "Electrostatic potential mapping at ferroelectric domain walls by low-temperature photoemission electron microscopy". In: *Appl Phys Lett* 115 (**2019**) Doi: 10.1063/1.5117881.

[27] Lysne, E., Novel Topological Spin Solitons for Spintronics Applications, Norwegain University of Science and technology, 2021. https://hdl.handle.net/11250/2760659.

[28] Roede, E.D., FIB and Functional Ferroics: Structuring and Correlated Microscopy, Norwegian University of Science and Technology, 2022. https://ntnuopen.ntnu.no/ntnu-xmlui/handle/11250/3005099.

[29] Brennecka, G., Sherbondy, R., Schwartz, R., et al., "Ferroelectricity - A revolutionary century of discovery". In: *American Ceramic Society Bulletin* 99 (**2020**) 24–30.

[30] Salje, E., Zhang, H., "Domain boundary engineering". In: *Phase Transitions* 82 (**2009**) 452–469. Doi: 10.1080/01411590902936138.

[31] Salje, E.K.H., "Multiferroic domain boundaries as active memory devices: Trajectories towards domain boundary engineering". In: *ChemPhysChem* 11 (**2010**) 940–950. Doi: 10.1002/cphc.200900943.

[32] Schultheiß, J., Rojac, T., Meier, D., "Unveiling Alternating Current Electronic Properties at Ferroelectric Domain Walls". In: *Adv Electron Mater* 8 (**2022**) Doi: 10.1002/aelm.202100996.

[33] Catalan, G., Seidel, J., Ramesh, R., et al., "Domain wall nanoelectronics". In: *Rev Mod Phys* 84 (**2012**) 119–156. Doi: 10.1103/RevModPhys.84.119.

[34] Meier, D., "Functional domain walls in multiferroics". In: *Journal of Physics Condensed Matter* 27 (**2015**) Doi: 10.1088/0953-8984/27/46/463003.

[35] Rabe, K.M., Ahn, C.H., Triscone, J.-M., Physics of Ferroelectrics, Springer Berlin Heidelberg New York, 2007.

[36] Vinod K.Wadhawan, Introduction To Ferroic Materials, Taylor & Francis Group, 2000. https://www.ptonline.com/articles/how-to-get-better-mfi-results.

[37] Tagantsev, A.K., Cross, L.E., Fousek, J., Domains in ferroic crystals and thin film, Springer Science+Business Media, 2010 Doi: 10.1007/ 978-1-4419-1417-0.

[38] Seidel, J., Topological Structures in Ferroic Materials: Domain Walls, Vortices and Skyrmions, Springer International Publishing Switzerland, 2016 Doi: 10.1007/978-3-319-25301-5.

[39] Cohen, R.E., "Origin of ferroelectricity in perovskite pxides". In: *Nature* 358 (**1992**) 136–138. Doi: 10.1038/358136a0.

[40] Seshadri, R., Hill, N.A., "Visualizing the role of Bi 6s “lone pairs” in the off-center distortion in ferromagnetic $BiMnO_3$". In: *Chemistry of Materials* 13 (**2001**) 2892–2899. Doi: 10.1021/cm010090m.

[41] Wang, J., Neaton, J.B., Zheng, H., et al., "Epitaxial $BiFeO_3$ multiferroic thin film heterostructures". In: *Science (1979)* 299 (**2003**) 1719–1722. Doi: 10.1126/science.1080615.

[42] Dvořák, V., "Improper ferroelectrics". In: *Ferroelectrics* 7 (**1974**) 1–9. Doi: 10.1080/00150197408237942.

[43] Levanyuk, A.P., Sannikov, D.G., "Improper ferroelectrics". In: *Soviet Physics - Uspekhi* 17 (**1974**) 276–282. Doi: 10.1070/PU1974v017n02ABEH004336.

[44] Cheong, S.-W., Mostovoy, M., "Multiferroics: a magnetic twist for ferroelectricity". In: *Nat Mater* 6 (**2007**) 13–20. Doi: doi.org/10.1038/nmat1804.

[45] Damjanovic, D., "Ferroelectric, dielectric and piezoelectric properties of ferroelectric thin films and ceramics". In: *Rep Prog Phys* 61 (**1998**) 1267–1324. Doi: 10.1088/0034-4885/61/9/002.

[46] Arlt, G., "Twinning in ferroelectric and ferroelastic ceramics: stress relief". In: *J Mater Sci* 25 (**1990**) 2655–2666. Doi: 10.1007/BF00584864.

[47] Kittel C., "Physical theory of ferromagnetic domains". In: *Phys Rev* 21 (**1949**) 541–583. Doi: 10.1103/PhysRev.79.745.2.

[48] Catalan, G., Schilling, A., Scott, J.F., et al., "Domains in three-dimensional ferroelectric nanostructures: Theory and experiment". In: *J Phys Condens Matter* 19 (**2007**) Doi: 10.1088/0953-8984/19/13/132201.

[49] Li, L., Xie, L., Pan, X., "Real-time studies of ferroelectric domain switching: A review". In: *Rep Prog Phys* 82 (**2019**) Doi: 10.1088/1361-6633/ab28de.

[50] Schultheiß, J., Picht, G., Wang, J., et al., "Ferroelectric polycrystals: Structural and microstructural levers for property-engineering via domain-wall dynamics". In: *Prog Mater Sci* 136 (**2023**) 1–41. Doi: 10.1016/j.pmatsci.2023.101101.

[51] Ishiwara, H., "Ferroelectric random access memories". In: *J Nanosci Nanotechnol* 12 (**2012**) 7619–7627. Doi: 10.1166/jnn.2012.6651.

[52] Nataf, G.F., Guennou, M., Gregg, J.M., et al., "Domain-wall engineering and topological defects in ferroelectric and ferroelastic materials". In: *Nat Rev Phys* 2 (**2020**) 634–648. Doi: 10.1038/s42254-020-0235-z.

[53] Evans, D.M., Garcia, V., Meier, D., et al., "Domains and domain walls in multiferroics". In: 5 (**2020**) 1–23. Doi: 10.1515/psr-2019-0067.

[54] Cherifi-Hertel, S., Bulou, H., Hertel, R., et al., "Non-Ising and chiral ferroelectric domain walls revealed by nonlinear optical microscopy". In: *Nat Commun* 8 (**2017**) 15768. Doi: 10.1038/ncomms15768.

[55] Acevedo-Salas, U., Croes, B., Zhang, Y., et al., "Impact of 3D Curvature on the Polarization Orientation in Non-Ising Domain Walls". In: *Nano Lett* 23 (**2023**) 795–803. Doi: 10.1021/acs.nanolett.2c03579.

[56] Jia, C.L., Mi, S.B., Urban, K., et al., "Atomic-scale study of electric dipoles near charged and uncharged domain walls in ferroelectric films". In: *Nat Mater* 7 (**2008**) 57–61. Doi: 10.1038/nmat2080.

[57] Holstad, T.S., Emergent nanoscale functionality in uniaxial ferroelectrics, Norwegian University of Science and Technology (NTNU), 2020. https://hdl.handle.net/11250/2652259

[58] Bednyakov, P.S., Sturman, B.I., Sluka, T., et al., "Physics and applications of charged domain walls". In: *NPJ Comput Mater* 4 (**2018**) Doi: 10.1038/s41524-018-0121-8.

[59] Sluka, T., Tagantsev, A.K., Bednyakov, P., et al., "Free-electron gas at charged domain walls in insulating $BaTiO_3$". In: *Nat Commun* 4 (**2013**) Doi: 10.1038/ncomms2839.

[60] Crassous, A., Sluka, T., Tagantsev, A.K., et al., "Polarization charge as a reconfigurable quasi-dopant in ferroelectric thin films". In: *Nat Nanotechnol* 10 (**2015**) 614–618. Doi: 10.1038/nnano.2015.114.

[61] Rojac, T., Bencan, A., Drazic, G., et al., "Domain-wall conduction in ferroelectric $BiFeO_3$ controlled by accumulation of charged defects". In: *Nat Mater* 16 (**2017**) 322–327. Doi: 10.1038/nmat4799.

[62] Moore, K., Conroy, M., O'Connell, E.N., et al., "Highly charged 180 degree head-to-head domain walls in lead titanate". In: *Commun Phys* 3 (**2020**) 1–7. Doi: 10.1038/s42005-020-00488-x.

[63] Wu, W., Horibe, Y., Lee, N., et al., "Conduction of topologically protected charged ferroelectric domain walls". In: *Phys Rev Lett* 108 (**2012**) 077203. Doi: 10.1103/PhysRevLett.108.077203.

[64] Du, Y., Wang, X., Chen, D., et al., "Manipulation of domain wall mobility by oxygen vacancy ordering in multiferroic $YMnO_3$". In: *Phys Chem Chem Phys* 15 (**2013**) 20010–20015. Doi: 10.1039/c3cp52892h.

[65] Oh, Y.S., Luo, X., Huang, F.T., et al., "Experimental demonstration of hybrid improper ferroelectricity and the presence of abundant charged walls in $(Ca,Sr)_3Ti_2O_7$ crystals". In: *Nat Mater* 14 (**2015**) 407–413. Doi: 10.1038/nmat4168.

[66] Lindgren, G., Canalias, C., "Domain wall conductivity in $KTiOPO_4$ crystals". In: *APL Mater* 5 (**2017**) Doi: 10.1063/1.4995651.

[67] McQuaid, R.G.P., Campbell, M.P., Whatmore, R.W., et al., "Injection and controlled motion of conducting domain walls in improper ferroelectric Cu-Cl boracite". In: *Nat Commun* 8 (**2017**) 1–7. Doi: 10.1038/ncomms15105.

[68] Ghara, S., Geirhos, K., Kuerten, L., et al., "Giant conductivity of mobile non-oxide domain walls". In: *Nat Commun* 12 (**2021**) 1–8. Doi: 10.1038/s41467-021-24160-2.

[69] Schultheiß, J., Schaab, J., Småbråten, D.R., et al., "Intrinsic and extrinsic conduction contributions at nominally neutral domain walls in hexagonal manganites". In: *Appl Phys Lett* 116 (**2020**) 262903. Doi: 10.1063/5.0009185.

[70] Sharma, P., Sando, D., Zhang, Q., et al., "Conformational Domain Wall Switch". In: *Adv Funct Mater* 29 (**2019**) 1–10. Doi: 10.1002/adfm.201807523.

[71] McConville, J.P.V., Lu, H., Wang, B., et al., "Ferroelectric Domain Wall Memristor". In: *Adv Funct Mater* 30 (**2020**) 2000109. Doi: 10.1002/adfm.202000109.

[72] Boyn, S., Grollier, J., Lecerf, G., et al., "Learning through ferroelectric domain dynamics in solid-state synapses". In: *Nat Commun* 8 (**2017**) Doi: 10.1038/ncomms14736.

[73] Chai, X., Jiang, J., Zhang, Q., et al., "Nonvolatile ferroelectric field-effect transistors". In: *Nat Commun* 11 (**2020**) 1–9. Doi: 10.1038/s41467-020-16623-9.

[74] Jiang, J., Bai, Z.L., Chen, Z.H., et al., "Temporary formation of highly conducting domain walls for non-destructive read-out of ferroelectric domain-wall resistance switching memories". In: *Nat Mater* 17 (**2018**) 49–55. Doi: 10.1038/NMAT5028.

[75] Van Aken, B.B., Palstra, T.T.M., Filippetti, A., et al., "The origin of ferroelectricity in magnetoelectric $YMnO_3$". In: *Nat Mater* 3 (**2004**) 164–170. Doi: 10.1038/nmat1080.

[76] Lorenz, B., "Hexagonal Manganites-($RMnO_3$): Class (I) Multiferroics with Strong Coupling of Magnetism and Ferroelectricity". In: *ISRN Cond Matter Phys* (**2013**) 1–43. Doi: 10.1155/2013/497073.

[77] Lilienblum, M., Ferroelectric Order in Multiferroic Hexagonal, ETH Zürich, 2016.

[78] Chae, S.C., Lee, N., Horibe, Y., et al., "Direct observation of the proliferation of ferroelectric loop domains and vortex-antivortex pairs". In: *Phys Rev Lett* 108 (**2012**) 1–5. Doi: 10.1103/PhysRevLett.108.167603.

[79] Momma, K., Izumi, F., "VESTA 3 for three-dimensional visualization of crystal, volumetric and morphology data". In: *J Appl Crystallogr* 44 (**2011**) 1272–1276. Doi: https://doi.org/10.1107/S0021889811038970.

[80] Jeong, I.-K., Hur, N., Proffen, Th., "High-temperature structural evolution of hexagonal multiferroic $YMnO_3$ and $YbMnO_3$". In: *J Appl Crystallogr* 40 (**2007**) 730–734. Doi: 10.1107/S0021889807025101.

[81] Aken, B.B. van, Meetsma, A., Palstra, T.T.M., "Hexagonal $YMnO_3$". In: *Acta Crystallographica Section C* 57 (**2001**) 230–232. Doi: 10.1107/S0108270100015663.

[82] Fiebig, M., Lottermoser, T., Meier, D., et al., "The evolution of multiferroics". In: *Nat Rev Mater* 1 (**2016**) Doi: 10.1038/natrevmats.2016.46.

[83] Fennie, C.J., Rabe, K.M., "Ferroelectric transition in YMnO3 from first principles". In: *Phys Rev B* 72 (**2005**) 1–4. Doi: 10.1103/PhysRevB.72.100103.

[84] Kumagai, Y., Spaldin, N.A., "Structural domain walls in polar hexagonal manganites". In: *Nat Commun* 4 (**2013**) 1–8. Doi: 10.1038/ncomms2545.

[85] Artyukhin, S., Delaney, K.T., Spaldin, N.A., et al., "Landau theory of topological defects in multiferroic hexagonal manganites". In: *Nat Mater* 13 (**2014**) 42–49. Doi: 10.1038/nmat3786.

[86] Choi, T., Horibe, Y., Yi, H.T., et al., "Insulating interlocked ferroelectric and structural antiphase domain walls in multiferroic $YMnO_3$". In: *Nat Mater* 9 (**2010**) 253–258. Doi: 10.1038/nmat2632.

[87] Zhang, Q., Tan, G., Gu, L., et al., "Direct observation of multiferroic vortex domains in $YMnO_3$". In: *Sci Rep* 3 (**2013**) 1–5. Doi: 10.1038/srep02741.

[88] Han, M.G., Zhu, Y., Wu, L., et al., "Ferroelectric switching dynamics of topological vortex domains in a hexagonal manganite". In: *Adv Mater* 25 (**2013**) 2415–2421. Doi: 10.1002/adma.201204766.

[89] Artyukhin, S., Delaney, K.T., Spaldin, N.A., et al., "Landau theory of topological defects in multiferroic hexagonal manganites". In: *Nat Mater* 13 (**2014**) 42–49. Doi: 10.1038/nmat3786.

[90] Zhang, J.X., He, Q., Trassin, M., et al., "Microscopic origin of the giant ferroelectric polarization in tetragonal-like $BiFeO_3$". In: *Phys Rev Lett* 107 (**2011**) 1–5. Doi: 10.1103/PhysRevLett.107.147602.

[91] Wang, Y., Zhang, L., Wang, J., et al., "Chemical-pressure-modulated $BaTiO_3$ thin films with large spontaneous polarization and high curie temperature". In: *J Am Chem Soc* 143 (**2021**) 6491–6497. Doi: 10.1021/jacs.1c00605.

[92] Vrejoiu, I., Rhun, G. Le, Pintilie, L., et al., "Intrinsic ferroelectric properties of strained tetragonal $PbZr_{0.2}Ti_{0.8}O_3$ obtained on layer-by-layer grown, defect-free single-crystalline films". In: *Adv Mate* 18 (**2006**) 1657–1661. Doi: 10.1002/adma.200502711.

[93] Holstad, T.S., Evans, D.M., Ruff, A., et al., "Electronic bulk and domain wall properties in B-site doped hexagonal $ErMnO_3$". In: *Phys Rev B* 97 (**2018**) 1–7. Doi: 10.1103/PhysRevB.97.085143.

[94] Hunnestad, K.A., Roede, E.D., Helvoort, A.T.J. van, et al., "Characterization of ferroelectric domain walls by scanning electron microscopy". In: *J Appl Phys* 128 (**2020**) 191102. Doi: 10.1063/5.0029284.

[95] Jungk, T., Hoffmann, Á., Fiebig, M., et al., "Electrostatic topology of ferroelectric domains in $YMnO_3$". In: *Appl Phys Lett* 97 (**2010**) 012904. Doi: 10.1063/1.3460286.

[96] Roede, E.D., Shapovalov, K., Moran, T.J., et al., "The Third Dimension of Ferroelectric Domain Walls". In: *Adv Mater* 34 (**2022**) 1–13. Doi: 10.1002/adma.202202614.

[97] Schultheiß, J., Xue, F., Roede, E., et al., "Confinement-Driven Inverse Domain Scaling in Polycrystalline $ErMnO_3$". In: *Adv Mater* 34 (**2022**) Doi: 10.1002/adma.202203449.

[98] Sandvik, O.W., Müller, A.M., Ånes, H.W., et al., "Pressure Control of Nonferroelastic Ferroelectric Domains in $ErMnO_3$". In: *Nano Lett* 23 (**2023**) 6994–7000. Doi: 10.1021/acs.nanolett.3c01638.

[99] Safranhova, M., Fousek, J., Kizaev, S.A., "Domains in ferroelectric $YMnO_3$". In: *Czechoslovak Journal of Physics B* 17 (**1967**) 559–560. Doi: doi.org/10.1007/BF01695179.

[100] Roede, E.D., Mosberg, A.B., Evans, D.M., et al., "Contact-free reversible switching of improper ferroelectric domains by electron and ion irradiation". In: *APL Mater* 9 (**2021**) 021105. Doi: 10.1063/5.0038909.

[101] Kuerten, L., Krohns, S., Schoenherr, P., et al., "Local control of improper ferroelectric domains in $YMnO_3$". In: *Phys. Revi. B* 102 (**2020**) 94108. Doi: 10.1103/PhysRevB.102.094108.

[102] Campbell, M.P., McConville, J.P.V., McQuaid, R.G.P., et al., "Hall effect in charged conducting ferroelectric domain walls". In: *Nat Commun* 7 (**2016**) 13764. Doi: 10.1038/ncomms13764.

[103] Hassanpour, E., Wegmayr, V., Schaab, J., et al., "Robustness of magnetic and electric domains against charge carrier doping in multiferroic hexagonal $ErMnO_3$". In: *New J Phys* 18 (**2016**) Doi: 10.1088/1367-2630/18/4/043015.

[104] Asokan, K., Chen, Y.S., Pao, C.W., et al., "Effect of Co, Ni, and Cu substitution on the electronic structure of hexagonal $YMnO_3$ studied by x-ray absorption spectroscopy". 95 (**2009**) 1–3. Doi: 10.1063/1.3224905.

[105] Levin, I., Krayzman, V., Vanderah, T.A., et al., "Oxygen-storage behavior and local structure in Ti-substituted $YMnO_3$". In: *J Solid State Chem* 246 (**2017**) 29–41. Doi: 10.1016/j.jssc.2016.10.029.

[106] Asaka, T., Nemoto, K., Kimoto, K., et al., "Crystallographic superstructure of Ti-doped hexagonal $YMnO_3$". In: *Phys. Rev. B* 71 (**2005**) 014114. Doi: 10.1103/PhysRevB.71.014114.

[107] Evans, D.M., Holstad, T.S., Mosberg, A.B., et al., "Conductivity control via minimally invasive anti-Frenkel defects in a functional oxide". In: *Nat Mater* 19 (**2020**) 1195–1200. Doi: 10.1038/s41563-020-0765-x.

[108] Rathod, K.N., Gadani, K., Dhruv, D., et al., "Effect of oxygen vacancy gradient on ion-irradiated Ca-doped $YMnO_3$ thin films". In: *J. Vac. Sci. Technol. B* 38 (**2020**) 062208. Doi: 10.1116/6.0000507.

[109] Skjaervø, S.H., Wefring, E.T., Nesdal, S.K., et al., "Interstitial oxygen as a source of p-type conductivity in hexagonal manganites". In: *Nat.Commun.* 7 (**2016**) 13745. Doi: 10.1038/ncomms13745.

[110] Småbråten, D.R., Charged domain walls in improper ferroelectric hexagonal manganites and gallates, Norwegian University of Science and Technology, 2018.

[111] Skjærvø, S.H., Småbråten, D.R., Spaldin, N.A., et al., "Oxygen vacancies in the bulk and at neutral domain walls in hexagonal $YMnO_3$". In: *Phys. Revi. B* 98 (**2018**) 184102. Doi: 10.1103/PhysRevB.98.184102.

[112] Wang, X., Yang, D., Zhang, H.-M.M., et al., "Anisotropic resistance switching in hexagonal manganites". In: *Phys Rev B* 99 (**2019**) 1–6. Doi: 10.1103/PhysRevB.99.054106.

[113] Overton, A.J., Best, J.L., Saratovsky, I., et al., "Influence of topotactic reduction on the structure and magnetism of the multiferroic $YMnO_3$". In: *Chemistry of Materials* 21 (**2009**) 4940–4948. Doi: 10.1021/cm9021276.

[114] Angoshtari, A., Yavari, A., "Effect of strain and oxygen vacancies on the structure of 180° ferroelectric domain walls in $PbTiO_3$". In: *Comput Mater Sci* 48 (**2010**) 258–266. Doi: 10.1016/j.commatsci.2010.01.006.

[115] Chandrasekaran, A., Damjanovic, D., Setter, N., et al., "Defect ordering and defect-domain-wall interactions in $PbTiO_3$: A first-principles study". In: *Phys. Revi. B* 88 (**2013**) 214116. Doi: 10.1103/PhysRevB.88.214116.

[116] Yang, C., Sun, E., Liu, Z., et al., "Phase-field simulation on the interaction of oxygen vacancies with charged and neutral domain walls in hexagonal $YMnO_3$". In: *J. Phys.: Condens. Matter* 34 (**2022**) 165401. Doi: 10.1088/1361-648X/ac50d8.

[117] Wang, X., Huang, F.T., Hu, R., et al., "Self-poling with oxygen off-stoichiometry in ferroelectric hexagonal manganites". In: *APL Mater* 3 (**2015**) Doi: 10.1063/1.4908159.

[118] Cen, C., Thiel, S., Hammerl, G., et al., "Nanoscale control of an interfacial metal-insulator transition at room temperature". In: *Nat Mater* 7 (**2008**) 298–302. Doi: 10.1038/nmat2136.

[119] Du, N., Manjunath, N., Li, Y., et al., "Field-Driven Hopping Transport of Oxygen Vacancies in Memristive Oxide Switches with Interface-Mediated Resistive Switching". In: *Phys. Rev. Applied* 10 (**2018**) 054025. Doi: 10.1103/PhysRevApplied.10.054025.

[120] Rao, C.N.R., S., F.R., Gopalakrishnan, J., New directions in solid state chemistry, Second edi, (**1997**) Doi: 10.1063/1.2811679.

[121] Pettersen, S.R., Stokkeland, A.E., Kristiansen, H., et al., "Electrical four-point probing of spherical metallic thin films coated onto micron sized polymer particles". In: *Appl Phys Lett* 109 (**2016**) Doi: 10.1063/1.4959783.

[122] Goldstein, J.I., Newbury, D.E., Michael, J.R., et al., Scanning electron microscopy and X-Ray Microanalysis, Fourth Edi, Springer Science+Business Media, (**2018**) Doi: 10.1007/978-1-4939-6676-9_20.

[123] Ludwig Reimer, Scanning electron microscopy. physics of image formation and microanalysis, Springer-Verlag Berlin Heidelberg, (**1998**) Doi: 10.1007/978-3-540-38967-5.

[124] Ul-Hamid, A., A Beginners' Guide to Scanning Electron Microscopy, Springer Nature Switzerland AG, (**2018**) Doi: 10.1007/978-3-319-98482-7.

[125] Yang, D.S., Mohammed, O.F., Zewail, A.H., "Scanning ultrafast electron microscopy". In: *4d Visualization of Matter: Recent Collected Works of Ahmed H Zewail, Nobel Laureate* 2010 (**2014**) 138–143. Doi: 10.1073/pnas.1009321107.

[126] Goldstein, J.I., Newbury, D.E., Michael, J.R., et al., Scanning electron microscopy and X-Ray Microanalysis, Fourth Edi, Springer Science+Business Media, (**2018**) Doi: 10.1007/978-1-4939-6676-9_20.

[127] Heinrich, K.F.J., Newbury, D.E., Yakowitz, H., Use of Monte Carlo calculations in electron probe microanalysis and scanning electron microscopy:, National Institute of Standards, (**1975**) Doi: https://doi.org/10.6028/NBS.SP.460.

[128] Kanaya, K., Okayama, S., "Penetration and energy-loss theory of electrons in solid targets". In: *J Phys D Appl Phys* 5 (**1972**) 43–58. Doi: 10.1088/0022-3727/5/1/308.

[129] T Koshikawa and R Shimizu, "Secondary electron and backscattering measurements for polycrystalline copper with a spherical retarding-field analyser". In: *J. Phys. D: Appl Phys* 6 (**1973**) 1369. Doi: 10.1088/0022-3727/6/11/312.

[130] Seiler, H., "Secondary electron emission in the scanning electron microscope". In: *J. Appl. Phys.* 54 (**1983**) R1. Doi: 10.1063/1.332840.

[131] Lin, Y., Joy, D.C., "A new examination of secondary electron yield data". In: *Surf. Interface Anal.* 37 (**2005**) 895. Doi: 10.1002/sia.2107.

[132] Paul L. Copeland, "Correlation between variation of secondary electron emission and atomic number". In: *Phys. Rev.* 46 (**1934**) 167. Doi: https://doi.org/10.1103/PhysRev.46.167.

[133] Joy, D.C., Prasad, M.S., Meyer, H.M., "Experimental secondary electron spectra under SEM conditions". In: *J Microsc* 215 (**2004**) 77–85. Doi: 10.1111/j.0022-2720.2004.01345.x.

[134] Joy, D.C., Joy, C.S., "Low voltages scanning electron microscopy". In: *Micron* 27 (**1996**) 247. Doi: doi.org/10.1016/0968-4328(96)00023-6.

[135] Chen, H., Liu, D., "Advances in scanning electron microscope moiré". In: *Exp Mech* 41 (**2001**) 165–173. Doi: 10.1007/BF02323193.

[136] Bihan, R. Le, "Study of ferroelectric and ferroelastic domain structures by scanning electron microscopy". In: *Ferroelectrics* 97 (**1989**) 19–46. Doi: 10.1080/00150198908018081.

[137] Postek, M.T., "An approach to the reduction of hydrocarbon contamination in the scanning electron microscope". In: *Scanning* 18 (**1996**) 269–274. Doi: 10.1002/sca.1996.4950180402.

[138] Postek, M.T., Vladár, A.E., Purushotham, K.P., "Does your SEM really tell the truth? How would you know? Part 2". In: *Scanning* 36 (**2014**) 347. Doi: 10.1002/sca.21124.

[139] Hugenschmidt, M., Adrion, K., Marx, A., et al., "Electron-Beam-Induced Carbon Contamination in STEM-in-SEM: Quantification and Mitigation". In: *Microscopy and Microanalysis* 29 (**2023**) 219–234. Doi: 10.1093/micmic/ozac003.

[140] Everhart, T.E., Thornley, R.F.M., "Wide-band detector for micro microampere low-energy electron currents". In: *J. Sci. Instrum.* 37 (**1960**) 246. Doi: 10.1088/0950-7671/37/7/307.

[141] Gerlach, R., Mountain, E., Maazouz, M., et al., Patent application publication, US 2008/0308742 A1,In-chanmber electronic detector, 2008.

[142] Zhou, W., Apkarian, R., Wang, Z.L., et al., "Fundamentals of scanning electron microscopy (SEM)". In: *Scanning Microscopy for Nanotechnology: Techniques and Applications* (**2007**) 1–40. Doi: 10.1007/978-0-387-39620-0_1.

[143] Robinson, G.Y., White, R.M., "Scanning electron microscopy of ferroelectric domains in barium titanate". In: *Appl Phys Lett* 10 (**1967**) 320–323. Doi: 10.1063/1.1754829.

[144] Bihan, R.L., Maussion, M., "Study of the Surface of Ferroelectric Crystals with the Scanning Electron Microscope". In: *Ferroelectrics* 7 (**1974**) 307–308. Doi: 10.1080/00150197408238029.

[145] Bihan, R.L., Maussion, M., "Direct observation of ferroelectric domains in triglycine sulphate (TGS) using the scanning electron microscope (SEM)". In: *J. Phys. Colloques* 33 (**1972**) C2-217-C2-219. Doi: 10.1051/jphyscol:1972275.

[146] Maussion, M., Bihan, R. Le, "Study of ferroelectric domains on KD2PO4 and BaTiO3 crystals with the scanning electron microscope". In: *Ferroelectrics* 13 (**1976**) 465. Doi: 10.1080/00150197608236642.

[147] Aristov, V. V., Kokhanchik, L.S., Voronovskii, Y.I., "Voltage contrast of ferroelectric domains of lithium niobate in SEM". In: *Phys Status Solidi (A)* 86 (**1984**) 133–141. Doi: 10.1002/pssa.2210860113.

[148] Schaab, J., Skjærvø, S.H., Krohns, S., et al., "Electrical half-wave rectification at ferroelectric domain walls". In: *Nat Nanotechnol* 13 (**2018**) Doi: 10.1038/s41565-018-0253-5.

[149] Ruff, A., Li, Z., Loidl, A., et al., "Frequency dependent polarisation switching in h-$ErMnO_3$". In: *Appl Phys Lett* 112 (**2018**) Doi: 10.1063/1.5026732.

[150] Leson, A., "There is plenty of room at the bottom". In: *Vakuum in Forschung Und Praxis* 17 (**2005**) 123. Doi: 10.1002/vipr.200590035.

[151] Giannuzzi Lucille A., S.F.A., Introduction to Focused Ion Beams, 2005 Doi: 10.1201/b16235-24.

[152] Orloff, J., Utlaut, M., Swanson, L., High Resolution Focused Ion Beams: FIB and Its Applications, 2003 Doi: 10.1007/978-1-4615-0765-9.

[153] Liu, Y., King, H.E., van Huis, M.A., et al., "Nano-tomography of porous geological materials using focused ion beam-scanning electron microscopy". In: *Minerals* 6 (**2016**) Doi: 10.3390/min6040104.

[154] Bassim, N., Scott, K., Giannuzzi, L.A., "Recent advances in focused ion beam technology and applications". In: *MRS Bull* 39 (**2014**) 317–325. Doi: 10.1557/mrs.2014.52.

[155] Antoniou, N., Rykaczewski, K., Uchic, M.D., "In situ FIB-SEM characterization and manipulation methods". In: *MRS Bull* 39 (**2014**) 347–352. Doi: 10.1557/mrs.2014.58.

[156] Holzer, L., Indutnyi, F., Gasser, PH., et al., "Three-dimensional analysis of porous BaTiO3 ceramics using FIB nanotomography". In: *J Microsc* 216 (**2004**) 84. Doi: 10.1111/j.0022-2720.2004.01397.x.

[157] J. Orloff, Handbook of charged particle optics, second edi, Taylor & Francis Group, 2009 Doi: 10.1002/9781118557662.ch5.

[158] Yau, Y.W., Groves, T.R., Pease, R.F.W., "Space Charge Effects in Focused Ion Beams.". In: *J. Vac. Sci. Technol B* 1 (**1983**) 1141. Doi: 10.1116/1.582652.

[159] Davies, N., Weibel, D.E., Blenkinsopp, P., et al., "Development and experimental application of a gold liquid metal ion source". In: *Appl Surf Sci* 203–204 (**2003**) 223–227. Doi: 10.1016/S0169-4332(02)00631-1.

[160] Tajmar, M., Vasiljevich, I., Grienauer, W., "High current liquid metal ion source using porous tungsten multiemitters". In: *Ultramicroscopy* 111 (**2010**) 1–4. Doi: 10.1016/j.ultramic.2010.09.005.

[161] Bischoff, L., Mazarov, P., Bruchhaus, L., et al., "Liquid metal alloy ion sources—An alternative for focussed ion beam technology". In: *Appl Phys Rev* 3 (**2016**) 21101. Doi: 10.1063/1.4947095.

[162] Emmrich, D., Beyer, A., Nadzeyka, A., et al., "Nanopore fabrication and characterization by helium ion microscopy". In: *Appl Phys Lett* 108 (**2016**) Doi: 10.1063/1.4947277.

[163] Smith, N.S., Skoczylas, W.P., Kellogg, S.M., et al., "High brightness inductively coupled plasma source for high current focused ion beam applications". In: *J Vac Sci Technol B:* 24 (**2006**) 2902–2906. Doi: 10.1116/1.2366617.

[164] McClelland, J.J., Steele, A. V, Knuffman, B., et al., "Bright focused ion beam sources based on laser-cooled atoms". In: *Appl Phys. Rev.* 3 (**2016**) 011302. Doi: 10.1063/1.4944491.

[165] Yanagisawa, J., Kito, K., Monden, K., "Low-energy focused ion beam system and direct deposition of Au and Si". In: *J. Vac. Sc. Technol. B* 13 (**1995**) 2621.

[166] Pak, K., Saitoh, I., Ohshima, N., et al., "In-situ maskless selective area epitaxy of GaAs using a low-energy Ga focused ion beam". In: *J Cryst Growth* 140 (**1994**) 244–247. Doi: 10.1016/0022-0248(94)90518-5.

[167] Cai, S., Wang, K., Huang, W., et al., "Design of a beam line for simultaneous dual-beam ion implantation". In: *AIP Adv* 13 (**2023**) Doi: 10.1063/5.0144431.

[168] Michael Rauscher, Development of an Advanced Low Energy Focused Ion Beam System Based on Immersion Optics, University of Tubingen, 2006.

[169] Pillatsch, L., Östlund, F., Michler, J., "FIBSIMS: A review of secondary ion mass spectrometry for analytical dual beam focussed ion beam instruments". In: *Prog Cryst Growth Charact Mater* 65 (**2019**) 1–19. Doi: 10.1016/j.pcrysgrow.2018.10.001.

[170] Ziegler, J.F., Ziegler, M.D., Biersack, J.P., "Nuclear Instruments and Methods in Physics Research B SRIM – The stopping and range of ions in matter (2010)". In: *Nucl Insrumt. Methods Phys Res, B* 268 (**2010**) 1818–1823. Doi: 10.1016/j.nimb.2010.02.091.

[171] Giannuzzi, L.A., Stevie, F.A., Introduction to foucused ion beams. Instrumentation, theory, techniques and practice, Springer, 2005 Doi: 10.1201/b16235-20.

[172] Thompson, K., Gorman, B., Larson, D.J., et al., "Minimization of Ga induced FIB damage using low energy clean-up". In: *Microscopy and Microanalysis* 12 (**2006**) 1736–1737. Doi: 10.1017/S1431927606065457.

[173] Phaneuf, M.W., FIB for Materials Science Applications - a Review, in: L.A. Giannuzzi, F.A. Stevie (Eds.), Introduction to Focused Ion Beams: Instrumentation, Theory, Techniques and Practice, Springer US, Boston, MA, 2005: pp. 143–172 Doi: 10.1007/0-387-23313-X_8.

[174] Volkert, C.A., Minor, A.M., "Focused Ion Beam Micromachining". In: *MRS Bull* 32 (**2007**) 389. Doi: doi.org/10.1557/mrs2007.62.

[175] Melngailis, J., "Focused ion beam induced deposition: a review". 1465 (**1991**) 36–49. Doi: 10.1117/12.47341.

[176] Shedd, G.M., Lezec, H., Dubner, A.D., et al., "Focused ion beam induced deposition of gold". In: *Appl Phys Lett* 49 (**1986**) 1584–1586. Doi: 10.1063/1.97287.

[177] Utke, I., Moshkalev, S., Russell, P., Nanofabrication using focused ion and electron beams, Oxford University Press, 2012.

[178] Langford, R.M., Wang, T.X., Ozkaya, D., "Reducing the resistivity of electron and ion beam assisted deposited Pt". In: *Microelectron Eng* 84 (**2007**) 784–788. Doi: 10.1016/j.mee.2007.01.055.

[179] De Teresa, J.M., Cárdoba, R., Fernández-Pacheco, A., et al., "Origin of the difference in the resistivity of as-grown focused-ion- and focused-electron-beam-induced Pt nanodeposits". In: *J Nanomater* 2009 (**2009**) 936863. Doi: 10.1155/2009/936863.

[180] Kwong, W.Y., Zhang, W.Y., "Electron-beam assisted platinum deposition as a protective layer for FIB and TEM applications". In: *IEEE Int Sympo Semicond Manuf Conf Pro* (**2005**) 469–471. Doi: 10.1109/issm.2005.1513408.

[181] Thompson, K., Lawrence, D., Larson, D.J., et al., "In situ site-specific specimen preparation for atom probe tomography". In: *Ultramicroscopy* 107 (**2007**) 131–139. Doi: 10.1016/j.ultramic.2006.06.008.

[182] Li, P., Chen, S., Dai, H., et al., "Recent advances in focused ion beam nanofabrication for nanostructures and devices: fundamentals and applications". In: *Nanoscale* 13 (**2021**) 1529–1565. Doi: 10.1039/d0nr07539f.

[183] Brogden, V., Johnson, C., Rue, C., et al., "Material Sputtering with a Multi-Ion Species Plasma Focused Ion Beam". In: *Adv Mater Sci Eng* 2021 (**2021**) 8842777. Doi: 10.1155/2021/8842777.

[184] Lindsey, S., Hobler, G., "Sputtering of silicon at glancing incidence". In: *Nucl Instrum Methods Phys Res B* 303 (**2013**) 142–147. Doi: 10.1016/j.nimb.2012.12.087.

[185] Li, C., Habler, G., Baldwin, L.C., et al., "An improved FIB sample preparation technique for site-specific plan-view specimens: A new cutting geometry". In: *Ultramicroscopy* 184 (**2018**) 310–317. Doi: 10.1016/j.ultramic.2017.09.011.

[186] Schaffer, M., Schaffer, B., Ramasse, Q., "Sample preparation for atomic-resolution STEM at low voltages by FIB". In: *Ultramicroscopy* 114 (**2012**) 62–71. Doi: 10.1016/j.ultramic.2012.01.005.

[187] Hofmann, F., Harder, R.J., Liu, W., et al., "Glancing-incidence focussed ion beam milling: A coherent X-ray diffraction study of 3D nano-scale lattice strains and crystal defects". In: *Acta Mater* 154 (**2018**) 113–123. Doi: 10.1016/j.actamat.2018.05.018.

[188] Li, C., Habler, G., Baldwin, L.C., et al., "An improved FIB sample preparation technique for site-specific plan-view specimens: A new cutting geometry". In: *Ultramicroscopy* 184 (**2018**) 310–317. Doi: 10.1016/j.ultramic.2017.09.011.

[189] Lid, M.J., Afif, A. Bin, Torgersen, J., et al., "Finish-pass strategy to improve sidewall angle and processing time in FIB milled structures". In: *Procedia Struct Integrity* 34 (**2021**) 266–273. Doi: 10.1016/j.prostr.2021.12.038.

[190] Schankula, C.W., Anand, C.K., Bassim, N.D., "Multi-angle plasma focused Ion Beam (FIB) curtaining artifact correction using a fourier-based linear optimization model". In: *Microsc Microanal* 24 (**2018**) 657–666. Doi: 10.1017/S1431927618015234.

[191] Allen, F.I., Velez, N.R., Thayer, R.C., et al., "Gallium, neon and helium focused ion beam milling of thin films demonstrated for polymeric materials: Study of implantation artifacts". In: *Nanoscale* 11 (**2019**) 1403–1409. Doi: 10.1039/c8nr08224c.

[192] Burnett, T.L., Kelley, R., Winiarski, B., et al., "Large volume serial section tomography by Xe Plasma FIB dual beam microscopy". In: *Ultramicroscopy* 161 (**2016**) 119–129. Doi: 10.1016/j.ultramic.2015.11.001.

[193] Huang, Z., "Combining Ar ion milling with FIB lift-out techniques to prepare high quality site-specific TEM samples". In: *J Microsc* 215 (**2004**) 219. Doi: 10.1111/j.0022-2720.2004.01376.x.

[194] McCaffrey, J.P., Phaneuf, M.W., Madsen, L.D., "Surface damage formation during ion-beam thinning of samples for transmission electron microscopy". In: *Ultramicroscopy* 87 (**2001**) 97–104. Doi: 10.1016/S0304-3991(00)00096-6.

[195] Saad, M.M., Bowman, R.M., Gregg, J.M., "Characteristics of single crystal “thin film” capacitor structures made using a focused ion beam microscope". In: *Appl Phys Lett* 84 (**2004**) 1159–1161. Doi: 10.1063/1.1645318.

[196] Nagarajan, V., Stanishevsky, A., Ramesh, R., "Ferroelectric nanostructures via a modified focused ion beam technique". In: *Nanotechnology* 17 (**2006**) 338–343. Doi: 10.1088/0957-4484/17/1/058.

[197] Kato, N.I., Kohno, Y., Saka, H., "Side-wall damage in a transmission electron microscopy specimen of crystalline Si prepared by focused ion beam etching". In: *J Vac Sci Technol A*17 (**1999**) 1201–1204. Doi: 10.1116/1.581795.

[198] Turner, E.M., Sapkota, K.R., Hatem, C., et al., "Wet-chemical etching of FIB lift-out TEM lamellae for damage-free analysis of 3-D nanostructures". In: *Ultramicroscopy* 216 (**2020**) 113049. Doi: 10.1016/j.ultramic.2020.113049.

[199] Kelley, R.D., Song, K., Van Leer, B., et al., "Xe+ FIB Milling and Measurement of Amorphous Silicon Damage". In: *Microsc and Microanal* 19 (**2013**) 862–863. Doi: 10.1017/s1431927613006302.

[200] Mosberg, A.B., Roede, E.D., Evans, D.M., et al., "FIB lift-out of conducting ferroelectric domain walls in hexagonal manganites". In: *Appl Phys Lett* 115 (**2019**) 122901. Doi: 10.1063/1.5115465.

[201] Xia, D., Jiang, Y.B., Notte, J., et al., "GaAs milling with neon focused ion beam: Comparison with gallium focused ion beam milling and subsurface damage analysis". In: *Appl Surf Sci* 538 (**2021**) 147922. Doi: 10.1016/j.apsusc.2020.147922.

[202] Preiß, E.I., Merle, B., Xiao, Y., et al., "Applicability of focused Ion beam (FIB) milling with gallium, neon, and xenon to the fracture toughness characterization of gold thin films". In: *J Mater Res* 36 (**2021**) 2505–2514. Doi: 10.1557/s43578-020-00045-w.

[203] Nowakowski, P., Bonifacio, C.S., Campin, M.J., et al., "Accurate Removal of Implanted Gallium and Amorphous Damage from TEM Specimens after Focused Ion Beam (FIB) Preparation". In: *Microsc and Microanal* 23 (**2017**) 300–301. Doi: 10.1017/s1431927617002185.

[204] Burns, S.R., Gregg, J.M., Nagarajan, V., "Nanostructuring Ferroelectrics via Focused Ion Beam Methodologies". In: Adv. Funct Mater 26 (**2016**) 8367–8381. Doi: 10.1002/adfm.201603812.

[205] Hunnestad, K.A., Schultheiß, J., Mathisen, A.C., et al., "Quantitative Mapping of Chemical Defects at Charged Grain Boundaries in a Ferroelectric Oxide". In: *Adv Mater* 2302543 (**2023**) 1–8. Doi: 10.1002/adma.202302543.

[206] Gao, P., Nelson, C.T., Jokisaari, J.R., et al., "Revealing the role of defects in ferroelectric switching with atomic resolution". In: *Nat Commun* 2 (**2011**) Doi: 10.1038/ncomms1600.

[207] Zhong, Q., Wang, Y., Cheng, Y., et al., "Optimization of the In Situ Biasing FIB Sample Preparation for Hafnia-Based Ferroelectric Capacitor". In: Micromachines 12 (**2021**) 1436. Doi: 10.3390/mi12121436.

[208] Schilling, A., Adams, T.B., Bowman, R.M., et al., "Scaling of domain periodicity with thickness measured in $BaTiO_3$ single crystal lamellae and comparison with other ferroics". In: *Phys. Rev. B* 74 (**2006**) 024115. Doi: 10.1103/PhysRevB.74.024115.

[209] Schilling, A., Bowman, R.M., Gregg, J.M., et al., "Ferroelectric domain periodicities in nanocolumns of single crystal barium titanate". In: *Appl Phys Lett* 89 (**2006**) Doi: 10.1063/1.2393145.

[210] Schilling, A., Bowman, R.M., Catalan, G., et al., "Morphological control of polar orientation in single-crystal ferroelectric nanowires". In: *Nano Lett* 7 (**2007**) 3787–3791. Doi: 10.1021/nl072260l.

[211] Schilling, A., Byrne, D., Catalan, G., et al., "Domains in ferroelectric nanodots". In: *Nano Lett* 9 (**2009**) 3359–3364. Doi: 10.1021/nl901661a.

[212] McMillen, M., McQuaid, R.G.P., Haire, S.C., et al., "The influence of notches on domain dynamics in ferroelectric nanowires". In: *Appl Phys Lett* 96 (**2010**) 2008–2011. Doi: 10.1063/1.3300638.

[213] McQuaid, R.G.P., Chang, L.W., Gregg, J.M., "The effect of antinotches on domain wall mobility in single crystal ferroelectric nanowires". In: *Nano Lett* 10 (**2010**) 3566–3571. Doi: 10.1021/nl101830d.

[214] Whyte, J.R., McQuaid, R.G.P., Sharma, P., et al., "Ferroelectric domain wall injection". In: *Adv Mater* 26 (**2014**) 293–298. Doi: 10.1002/adma.201303567.

[215] Whyte, J.R., Gregg, J.M., "A diode for ferroelectric domain-wall motion". In: *Nat Commun* 6 (**2015**) 1–5. Doi: 10.1038/ncomms8361.

[216] McGilly, L.J., Yudin, P., Feigl, L., et al., "Controlling domain wall motion in ferroelectric thin films". In: *Nat Nanotechnol* 10 (**2015**) 145–150. Doi: 10.1038/nnano.2014.320.

[217] McGilly, L.J., Sandu, C.S., Feigl, L., et al., "Nanoscale Defect Engineering and the Resulting Effects on Domain Wall Dynamics in Ferroelectric Thin Films". In: *Adv Funct Mater* 27 (**2017**) Doi: 10.1002/adfm.201605196.

[218] Chouprik, A., Kirtaev, R., Spiridonov, M., et al., "Nanoscale Tailoring of Ferroelectricity in a Thin Dielectric Film" In: ACS Appl. Mater. Interfaces 12 (**2020**) 50 Doi: 10.1021/acsami.0c16741.

[219] Li, P., Chen, S., Dai, H., et al., "Recent advances in focused ion beam nanofabrication for nanostructures and devices: Fundamentals and applications". In: *Nanoscale* 13 (**2021**) 1529–1565. Doi: 10.1039/d0nr07539f.

[220] McQuaid, R.G.P., McGilly, L.J., Sharma, P., et al., "Mesoscale flux-closure domain formation in single-crystal $BaTiO_3$". In: *Nat Commun* 2 (**2011**) Doi: 10.1038/ncomms1413.

[221] Voigtländer, B., Atomic force microscopy, second edition, Springer Nature Switzerland AG, 2015 Doi: 10.1007/978-3-030-13654-3_12.

[222] Bian, K., Gerber, C., Heinrich, A.J., et al., "Scanning probe microscopy". In: *Nature Reviews Methods Primers* 1 (**2021**) Doi: 10.1038/s43586-021-00033-2.

[223] Characterization, M., David, E., Kaplan, W.D., Microstructural Characterization of Materials Microstructural Characterization of Materials 2nd Edition, 2008.

[224] Lanza, M., Conductive Atomic Force Microscopy, Wiley-VCH Verlag GmbH & Co. KGaA, 2017 Doi: 10.1007/978-981-10-6156-1_9.

[225] Asylum Research, SPM-AFM Cypher applications guide, 2018.

[226] Murrell, M.P., Welland, M.E., O'Shea, S.J., et al., "Spatially resolved electrical measurements of SiO2 gate oxides using atomic force microscopy". In: *Appl Phys Lett* 62 (**1993**) 786–788. Doi: 10.1063/1.108579.

[227] Yang, Z., Zhang, Z., Li, C., et al., "Probing switching mechanism of memristor for neuromorphic computing". In: *Nano Express* 4 (**2023**) Doi: 10.1088/2632-959X/acd70c.

[228] Molotskii, M., "Generation of ferroelectric domains in atomic force microscope". In: *J Appl Phys* 93 (**2003**) 6234–6237. Doi: 10.1063/1.1567033.

[229] Rieck, J.L., Cipollini, D., Salverda, M., et al., " Ferroelastic Domain Walls in BiFeO 3 as Memristive Networks ". In: *Adv Intell Syst* 5 (**2023**) 1–9. Doi: 10.1002/aisy.202200292.

[230] Schultheiß, J., Lysne, E., Puntigam, L., et al., "Charged Ferroelectric Domain Walls for Deterministic ac Signal Control at the Nanoscale". In: *Nano Lett* 21 (**2021**) 9560–9566. Doi: 10.1021/acs.nanolett.1c03182.

[231] Wu, W., Guest, J.R., Horibe, Y., et al., "Polarization-modulated rectification at ferroelectric surfaces". In: *Phys Rev Lett* 104 (**2010**) 1–4. Doi: 10.1103/PhysRevLett.104.217601.

[232] Soergel, E., "Piezoresponse force microscopy (PFM)". In: *J Phys D Appl Phys* 44 (**2011**) Doi: 10.1088/0022-3727/44/46/464003.

[233] Seol, D., Kim, B., Kim, Y., "Non-piezoelectric effects in piezoresponse force microscopy". In: *Curr Appl Phys* 17 (**2017**) 661–674. Doi: 10.1016/j.cap.2016.12.012.

[234] Melitz, W., Shen, J., Kummel, A.C., et al., "Kelvin probe force microscopy and its application". In: *Surf Sci Rep* 66 (**2011**) 1–27. Doi: 10.1016/j.surfrep.2010.10.001.

[235] Liscio, A., Palermo, V., Müllen, K., et al., "Tip - Sample interactions in Kelvin probe force microscopy: Quantitative measurement of the local surface potential". In: *J Phys Chem C* 112 (**2008**) 17368–17377. Doi: 10.1021/jp806657k.

[236] Axt, A., Hermes, I.M., Bergmann, V.W., et al., "Know your full potential: Quantitative Kelvin probe force microscopy on nanoscale electrical devices". In: *Beilstein J Nanotechnol* 9 (**2018**) 1809–1919. Doi: 10.3762/bjnano.9.172.

[237] Kondratenko, S. V., Lysenko, V.S., Kozyrev, Y.N., et al., "Local charge trapping in Ge nanoclustersdetected by Kelvin probe force microscopy". In: *Appl Surf Sci* 389 (**2016**) 783–789. Doi: 10.1016/j.apsusc.2016.07.148.

[238] Du, Y., Kumar, A., Pan, H., et al., "The resistive switching in TiO2 films studied by conductive atomic force microscopy and Kelvin probe force microscopy". In: *AIP Adv* 3 (**2013**) Doi: 10.1063/1.4818119.

[239] Meng, H., Huang, S., Jiang, Y., "The role of oxygen vacancies on resistive switching properties of oxide materials". In: *AIMS Mater Sci* 7 (**2020**) 665–683. Doi: 10.3934/matersci.2020.5.665.

[240] Lim, J.S., Yang, C.H., "Charge-neutral defects control conductivity". In: *Nat Mater* 19 (**2020**) 1132–1133. Doi: 10.1038/s41563-020-0772-y.

[241] Wang, X., Yang, D., Zhang, H.M., et al., "Anisotropic resistance switching in hexagonal manganites". In: *Phys Rev B* 99 (**2019**) 1–6. Doi: 10.1103/PhysRevB.99.054106.

[242] Du, Y., Wang, X., Chen, D., et al., "Manipulation of domain wall mobility by oxygen vacancy ordering in multiferroic $YMnO_3$". In: *Phys Chem Chem Phys* 15 (**2013**) 20010–20015. Doi: 10.1039/c3cp52892h.

[243] Yan, Z., Meier, D., Schaab, J., et al., "Growth of high-quality hexagonal ErMnO3 single crystals by the pressurized floating-zone method". In: *J Cryst Growth* 409 (**2015**) 75–79. Doi: 10.1016/j.jcrysgro.2014.10.006.

[244] Yang, C.H., Seidel, J., Kim, S.Y., et al., "Electric modulation of conduction in multiferroic Ca-doped BiFeO 3 films". In: *Nat Mater* 8 (**2009**) 485–493. Doi: 10.1038/nmat2432.

[245] Zhang, Z.L.P.G.X.B.D.C.J.Z., "Evidence for electric-field-driven migration and diffusion of oxygen vacancies in Pr0.7 Ca0.3 MnO3". In: *J Appl Phys* 111 (**2012**) 114506. Doi: https://doi.org/10.1063/1.4724333.

[246] Holzlechner, G., Kastner, D., Slouka, C., et al., "Oxygen vacancy redistribution in $PbZr_xTi_{1-x}O_3$ (PZT) under the influence of an electric field". In: *Solid State Ion* 262 (**2014**) 625–629. Doi: 10.1016/j.ssi.2013.08.027.

[247] Popov, V.L., Heß, M., Willert, E., Handbook of Contact Mechanics, 2019 Doi: 10.1007/978-3-662-58709-6.

[248] Chadli, A., Halit, M., Lagoun, B., et al., "Structural and Anisotropic Elastic Properties of Hexagonal $YMnO_3$ in Low Symmetry Determined by First-Principles Calculations.". In: *Solid State Phenom* 297 (**2019**) 120–130. Doi: doi.org/10.4028/www.scientific.net/ssp.297.120.

[249] Nardi, F., Deleruyelle, D., Spiga, S., et al., "Switching of nanosized filaments in NiO by conductive atomic force microscopy". In: *J Appl Phys* 112 (**2012**) Doi: 10.1063/1.4752032.

[250] Abughayada, C., Dabrowski, B., Avdeev, M., et al., "Structural, magnetic, and oxygen storage properties of hexagonal $Dy_{1-x}Y_xMnO_{3+\delta}$". In: *J Solid State Chem* 217 (**2014**) 127–135. Doi: 10.1016/j.jssc.2014.05.017.

[251] Volk, T.R., Gainutdinov, R. V., Zhang, H.H., "Domain-wall conduction in AFM-written domain patterns in ion-sliced $LiNbO_3$ films". In: *Appl Phys Lett* 110 (**2017**) Doi: 10.1063/1.4978857.

[252] Gainutdinov, R. V., Bodnarchuk, Y. V., Volk, T.R., et al., "AFM-tip written normal and anomalous domains in PMN-0.4PT crystals". In: *J Appl Phys* 126 (**2019**) 0–7. Doi: 10.1063/1.5092569.

[253] Enriquez, E., Li, Q., Bowlan, P., et al., "Induced ferroelectric phases in $SrTiO_3$ by a nanocomposite approach". In: *Nanoscale* 12 (**2020**) 18193–18199. Doi: 10.1039/d0nr03460f.

[254] Uršič, H., Prah, U., "Investigations of ferroelectric polycrystalline bulks and thick films using piezoresponse force microscopy". In: *Proc R Soc A:* 475 (**2019**) Doi: 10.1098/rspa.2018.0782.

[255] Selbach, S.M., Løvik, A.N., Bergum, K., et al., "Crystal structure, chemical expansion and phase stability of $HoMnO_3$ at high temperature". In: *J Solid State Chem* 196 (**2012**) 528–535. Doi: 10.1016/j.jssc.2012.07.024.

[256] Gault, B., Chiaramonti, A., Cojocaru-Mirédin, O., et al., Atom probe tomography, 2021 Doi: 10.1038/s43586-021-00047-w.

[257] Egerton, R.F., Li, P., Malac, M., "Radiation damage in the TEM and SEM". In: *Micron* 35 (**2004**) 399–409. Doi: 10.1016/j.micron.2004.02.003.

[258] Minenkov, A., Šantić, N., Truglas, T., et al., "Advanced preparation of plan-view specimens on a MEMS chip for in situ TEM heating experiments". In: *MRS Bull* 47 (**2022**) 359–370. Doi: 10.1557/s43577-021-00255-5.

[259] Evans, D.M., Småbråten, D.R., Holstad, T.S., et al., "Observation of Electric-Field-Induced Structural Dislocations in a Ferroelectric Oxide". In: *Nano Lett* 21 (**2021**) 3386–3392. Doi: 10.1021/acs.nanolett.0c04816.

[260] Chen, Z., Wang, X., Ringer, S.P., et al., "Manipulation of Nanoscale Domain Switching Using an Electron Beam with Omnidirectional Electric Field Distribution". In: *Phys Rev Lett* 117 (**2016**) 1–5. Doi: 10.1103/PhysRevLett.117.027601.

[261] McCartney, M.R., Crozier, P.A., Weiss, J.K., et al., "Electron-beam-induced reactions at transition- metal oxide surfaces". In: *Vacuum* 42 (**1991**) 301.

[262] Zhang, Q.H., Shen, X., Yao, Y., et al., "Oxygen vacancy ordering and its mobility in $YMnO_3$". In: *J Alloys Compd* 648 (**2015**) 253. Doi: 10.1016/j.jallcom.2015.07.032.

[263] Cheng, S., Meng, Q., Han, M.G., et al., "Revealing the Effects of Trace Oxygen Vacancies on Improper Ferroelectric Manganite with In Situ Biasing". In: *Adv Electron Mater* 5 (**2019**) Doi: 10.1002/aelm.201800827.

[264] Habeb, A., Fouzeyah, R., "Bipolar junction transistor as a switch". In: *IOSR J Electr Electron Eng* 13 (**2018**) 52–57. Doi: 10.9790/1676-1301015257.

[265] Jamshidi, R., Taghavimehr, M., Chen, Y., et al., "Transient Electronics as Sustainable Systems: From Fundamentals to Applications". In: *Adv Sustain Syst* 6 (**2022**) 1–13. Doi: 10.1002/adsu.202100057.

[266] Turner, P.W., McConville, J.P.V., McCartan, S.J., et al., "Large Carrier Mobilities in ErMnO3 Conducting Domain Walls Revealed by Quantitative Hall-Effect Measurements". In: *Nano Lett* 18 (**2018**) 6381. Doi: 10.1021/acs.nanolett.8b02742.

[267] Mundy, J.A., Schaab, J., Kumagai, Y., et al., "Functional electronic inversion layers at ferroelectric domain walls". In: *Nat Mater* 16 (**2017**) 622–627. Doi: 10.1038/nmat4878.

[268] Pang, H., Zhang, F., Zeng, M., et al., "Preparation of epitaxial hexagonal $YMnO_3$ thin films and observation of ferroelectric vortex domains". In: *NPJ Quantum Mater* 16015 (**2016**) 1. Doi: 10.1038/npjquantmats.2016.15.

[269] Chen, Y., Li, Y., Zheng, D., et al., "Domain structure and multiferroic properties of epitaxial hexagonal $ErMnO_3$ films". In: *J Alloys Compd* 821 (**2020**) 3–8. Doi: 10.1016/j.jallcom.2019.153529.

[270] Schilling, A., Adams, T., Bowman, R.M., et al., "Strategies for gallium removal after focused ion beam patterning of ferroelectric oxide nanostructures". In: *Nanotechnology* 18 (**2007**) Doi: 10.1088/0957-4484/18/3/035301.

[271] Shen, Y.Q., Chen, Y., Lee, K.W., et al., "Glancing angle fib de-layering for embedded defect and pvc fault isolation analysis". In: Proc Int Symp Phys Fail Anal Integr Circuits, *IPFA* 2018-July (**2018**) 1–5. Doi: 10.1109/IPFA.2018.8452503.

[272] Ishitani, T., Umemura, K., Ohnishi, T., et al., "Improvements in performance of focused ion beam cross-sectioning: Aspects of ion-sample interaction". In: *J Electron Microsc (Tokyo)* 53 (**2004**) 443–449. Doi: 10.1093/jmicro/dfh078.

[273] Neumayer, S.M., Fisslthaler, E., Feistritzer, S., et al., "TEM Sample Preparation of a Hard Metal by Semiautomatic Wedge Polishing". In: *Pract Metallogr* 50 (**2013**) 304–317. Doi: 10.3139/147.110224.

[274] Cha, H.-W., Kang, M.-C., Shin, K., et al., "Transmission Electron Microscopy Specimen Preparation of Delicate Materials Using Tripod Polisher". In: *Appl Microsc* 46 (**2016**) 110–115. Doi: 10.9729/am.2016.46.2.110.

[275] Benedict, J., Klepeis, S.J., Anderson, R., "The Development and Application of the Tripod Polishing Technique". In: *Microsc and Microanal* 3 (**1997**) 339. Doi: 10.1017/s1431927600008588.

[276] Eberg, E., Monsen, Å.F., Tybell, T., et al., "Comparison of TEM specimen preparation of perovskite thin films by tripod polishing and conventional ion milling". In: *J Electron Microsc (Tokyo)* 57 (**2008**) 175–179. Doi: 10.1093/jmicro/dfn018.

[277] Kalinin, S. V., Bonnell, D.A., "Local potential and polarization screening on ferroelectric surfaces". In: *Phys Rev B Condens Matter Mater Phys* 63 (**2001**) 1–13. Doi: 10.1103/PhysRevB.63.125411.

[278] Li, S.S., Semiconductor Physical Electronics, second edi, Springer Science+Business Media, 2006 Doi: https://doi.org/10.1007/0-387-37766-2.

[279] G.V. Subba Rao, B.M. Wanklyn, C.N.R.R., "Electrical transport in rare-earth orthochromites". In: *J Phys Chem Solids* 32 (**1971**) 345–358. Doi: doi.org/10.1016/0022-3697(71)90019-9.

[280] Wu, W., Guest, J.R., Horibe, Y., et al., "Polarization-modulated rectification at ferroelectric surfaces". In: *Phys Rev Lett* 104 (**2010**) 217601. Doi: 10.1103/PhysRevLett.104.217601.

[281] Lüth, H., Solid Surfaces, Interfaces and Thin Films sixth edition, Sixth Edit, Springe, 2014 Doi: 10.1007/978-3-319-10756-1.

[282] Schaab, J., Electronic transport and correlation phenomena at improper ferroelectric domain walls, ETH Zurich, 2017.

[283] Han, H., Song, S., Lee, J.H., et al., "Switchable Photovoltaic Effects in Hexagonal Manganite Thin Films Having Narrow Band Gaps". In: *Chem Mater* 27 (**2015**) 7425–7432. Doi: 10.1021/acs.chemmater.5b03408.

[284] Michaelson, H.B., "The work function of the elements and its periodicity". In: *J Appl Phys* 48 (**1977**) 4729–4733. Doi: 10.1063/1.323539.

[285] Kahn, A., "Fermi level, work function and vacuum level". In: *Mater Horiz* 3 (**2016**) 7. Doi: 10.1039/C5MH00160A.

[286] Evstigneev, M., Introduction to Semiconductor Physics and Devices, Springer Nature Switzerland AG, 2022 Doi: 10.1007/978-3-031-08458-4.

[287] An, Y., Behnam, A., Pop, E., et al., "Metal-semiconductor-metal photodetectors based on graphene/p-type silicon Schottky junctions". In: *Appl Phys Lett* 102 (**2013**) Doi: 10.1063/1.4773992.

[288] Giannazzo, F., Fisichella, G., Piazza, A., et al., "Nanoscale inhomogeneity of the Schottky barrier and resistivity in MoS_2 multilayers". In: *Phys Rev B Condens Matter Mater Phys* 92 (**2015**) 1–4. Doi: 10.1103/PhysRevB.92.081307.

[289] Shu, L., Ke, S., Fei, L., et al., "Photoflexoelectric effect in halide perovskites". In: *Nat Mater* 19 (**2020**) 605–609. Doi: 10.1038/s41563-020-0659-y.

[290] He, Y., Zhang, J., Li, D., et al., "Evaluating bandgap distributions of carbon nanotubes via scanning electron microscopy imaging of the Schottky barriers". In: *Nano Lett* 13 (**2013**) 5556–5562. Doi: 10.1021/nl403158x.

[291] Hunnestad, K.A., Roede, E.D., Van Helvoort, A.T.J., et al., "Characterization of ferroelectric domain walls by scanning electron microscopy". In: *J Appl Phys* 128 (**2020**) Doi: 10.1063/5.0029284.

[292] Maeda, T., Okada, M., Ueno, M., et al., "Temperature dependence of barrier height in Ni/n-GaN Schottky barrier diode". In: *Applied Physics Express* 10 (**2017**) Doi: 10.7567/APEX.10.051002.

[293] Akkal, B., Benamara, Z., Boudissa, A., et al., "Modelization and characterization of Au/InSb/InP Schottky systems as a function of temperature". In: *Mater Sci Eng* B55 (**1998**) 162–168. Doi: 10.1016/s0921-5107(98)00168-8.

[294] Jürgen H. Werner; Herbert H. Güttler, "Barrier inhomogeneities at Schottky contacts". In: *J Appl* Phys 69 (**1991**) 1522–1533. Doi: 10.1063/1.347243.

[295] Al-Ahmadi, N.A., "Schottky barrier inhomogeneities at the interface of different epitaxial layer thicknesses of n-GaAs/Ti/Au/Si: $Al_{0.33}Ga_{0.67}As$". In: *Heliyon* 6 (**2020**) e04852. Doi: 10.1016/j.heliyon.2020.e04852.

[296] Kalinin, S. V., Bonnell, D.A., "Screening phenomena on oxide surfaces and its implications for local electrostatic and transport measurements". In: *Nano Lett* 4 (**2004**) 555–560. Doi: 10.1021/nl0350837.

[297] Cao, J., Ekren, D., Peng, Y., et al., "Modulation of Charge Transport at Grain Boundaries in $SrTiO_3$: Toward a High Thermoelectric Power Factor at Room Temperature". In: *ACS Appl Mater Interfaces* 13 (**2021**) 11879–11890. Doi: 10.1021/acsami.0c21699.

[298] Kalinin, S. V., Suchomel, M.R., Davies, P.K., et al., "Potential and impedance imaging of polycrystalline $BiFeO_3$ ceramics". In: J Am Ceram Soc 85 (**2002**) 3011–3017. Doi: 10.1111/j.1151-2916.2002.tb00571.x.

[299] Maguire, J.R., Waseem, H., McQuaid, R.G.P., et al., "Imaging Ferroelectrics: Reinterpreting Charge Gradient Microscopy as Potential Gradient Microscopy". In: *Adv Electron Mater* 8 (**2022**) 1–7. Doi: 10.1002/aelm.202101384.

[300] He, J., Zahn, M., Ushakov, I.N., et al., "Non-destructive tomographic nanoscale imaging of ferroelectric domain walls". In: *ArXiv* (**2023**) Doi: https://doi.org/10.48550/arXiv.2311.00139.

[301] Robinson, G.Y., White, R.M., "Scanning electron microscopy of ferroelectric domains in barium titanate". In: *Appl Phys Lett* 10 (**1967**) 320–323. Doi: 10.1063/1.1754829.

[302] Meyer, K.P., Blumtritt, H., Szczesniak, L., "Visualization of domain boundaries in Gd2(MoO4)3 single crystals by scanning electron microscope potential contrast". In: *Ultramicroscopy* 6 (**1981**) 67. Doi: 10.1016/S0304-3991(81)80178-7.

[303] Aristov, V. V., Kokhanchik, L.S., Voronovskii, Y.I., "Voltage contrast of ferroelectric domains of Lithium Niobate in SEM". In: *Phys Status Solidi (a)* 86 (**1984**) 133–141. Doi: 10.1002/pssa.2210860113.

[304] Li, J.Q., Yang, H.X., Tian, H.F., et al., "Scanning secondary-electron microscopy on ferroelectric domains and domain walls in $YMnO_3$". In: *Appl Phys Lett* 100 (**2012**) 152903. Doi: 10.1063/1.4704165.

[305] Zou, Y.B., Mao, S.F., Da, B., et al., "Surface sensitivity of secondary electrons emitted from amorphous solids: Calculation of mean escape depth by a Monte Carlo method". In: *J Appl Phys* 120 (**2016**) Doi: 10.1063/1.4972196.

[306] Zhao, M., Ming, B., Kim, J.W., et al., "New insights into subsurface imaging of carbon nanotubes in polymer composites via scanning electron microscopy". In: *Nanotechnology* 26 (**2015**) Doi: 10.1088/0957-4484/26/8/085703.

[307] Srinivasan, A., Han, W., Khursheed, A., "Secondary electron energy contrast of localized buried charge in metal-insulator-silicon structures". In: *Microsc and Microanal* 24 (**2018**) 453–460. Doi: 10.1017/S1431927618015052.

[308] Drouin, D., Couture, A.R., Joly, D., et al., "CASINO V2.42 - A fast and easy-to-use modeling tool for scanning electron microscopy and microanalysis users". In: *Scanning* 29 (**2007**) 92. Doi: 10.1002/sca.20000.

[309] Q. N. Meier, M. Lilienblum, S. M. Griffin, et al., "Global Formation of Topological Defects in the Multiferroic Hexagonal Manganites". In: *Phys Rev X* 7 (**2017**) 041014. Doi: 10.1103/PhysRevX.7.041014.

AFM probe information

Name	DCP 20	HA_HR_DCP	ASYELEC.01-R2	DEP-01	CDT-NCHR-10
Company	K-TEK nano	NT-MDT	Oxford Instruments	Tips Nano	Nanosensor
Tip coating	N-Diamond	B-Diamond	Ti/Ir	B-Diamond	Doped Diamond
Tip radius (nm)	100 nm	100 nm	25 ± 10 nm	<10 nm	100 ~200 nm
Force constant (N/m)	28-91	68-102	1.4-5.8	1.2-4.5	23-225

ISBN 978-82-326-7798-6 (printed ver.)
ISBN 978-82-326-7797-9 (electronic ver.)
ISSN 1503-8181 (printed ver.)
ISSN 2703-8084 (online ver.)